ABSTRACT

Title of dissertation: A PORTRAIT OF THE BINARY COMPACT MERGER AS A YOUNG: SHORT GRB, GRAVITATIONAL WAVE AFTERGLOW, AND KILONOVA

Tomás Ahumada-Mena,
Doctor of Philosophy, 2022

Dissertation directed by: Dr. Leo P. Singer
NASA Goddard Space Flight Center

Both binary neutron star (BNS) and neutron star–black hole (NSBH) mergers radiate gravitational waves (GWs) as they gradually spiral inwards. Once they merge, they emit electromagnetic (EM) radiation that is potentially detectable across the entire EM spectrum, from hours to years after the coalescence. Right after the merger, a short burst of gamma-rays is followed by an hours to days long optical/near infrared (NIR) transient (i.e. kilonova (KN)), which is powered by the decay of the r-process nucleosynthesis elements. Depending on the angle of the gamma-ray burst (GRB) relative to Earth, a seconds to years long afterglow can be detected from radio to X-rays. The EM radiation from these mergers has shed light into different fields of physics and astronomy: they are sources of GWs, a site of rapid neutron-capture process (r-process) nucleosynthesis, and promising standard candles. However only one BNS merger has been studied in detail: AT2017gfo, the EM counterpart to GRB 170817A/GW170817. This thesis focuses on the optical

searches of these multi-messenger sources using wide field of view (FOV) telescopes.

The first chapter of this thesis describes the systematic search for optical counterparts to short gamma-ray bursts (SGRBs). We used the Zwicky Transient Facility (ZTF) to follow-up 10 short duration GRBs detected by the *Fermi* Gamma-ray Burst Monitor (GBM). We covered areas between 250 and 3000 deg^2, and followed-up more than 60 objects, photometrically and spectroscopically. While we did not find a counterpart to a compact binary merger, we used the ZTF magnitude limits (i.e. ~ 21 mag in the r-band) to compare to SGRB afterglows and KN models, to show that our searches are sensitive to most KN models up to 200 Mpc. However, the majority of SGRB afterglows in the literature have been found at relatively high redshifts (i.e. mean $z \sim 0.5$), making them fainter than our magnitude limits. Moreover, we explore the efficiency of our searches and we determine our searches have probed between redshift 0.16-0.4, depending on the energy models assumed for the SGRBs. Future campaigns can expand the horizon to redshift 0.2-0.7.

The second part of this thesis is about the discovery of the shortest gamma-ray burst coming from a collapsing massive star. In the context of the optical follow-up of short GRBs with ZTF, we triggered target-of-opportunity (ToO) observations in the error region of GRB 200826A, a 1.13 sec duration GRB. There we found the afterglow of the burst, ZTF20abwysqy, with an optical decay rate ~ 1 mag/day. The afterglow was additionally X-ray and radio bright. At the redshift of the host galaxy $z = 0.74$, its hardness - intensity relation (i.e. $E_{peak,z} - E_{\gamma,iso}$) is consistent with the long GRB population, puzzling the community. We present the afterglow and host galaxy analysis, along with Gemini Multi-Object Spectrograph (GMOS)

observations that show a rising source in the i-band that could only be explained by an underlying supernova.

The third chapter of the thesis describes the optical follow-up of gravitational wave events using the ZTF. We describe the observing strategy, as well as the selection and monitoring of GW counterpart candidates. Our ToO strategy allowed us to sift through $\sim$ 2 million sources to select $\sim$ 160 candidates for follow-up. We apply this strategy to search for 13 GW alerts during the third LIGO/Virgo observing run (O3). Particularly, we describe the case of the first BNS merger in O3, S190425z, and two NSBH mergers, S200105ae and S200115j. As no counterpart was found for any of the GW events, we use the photometric limits of our searches to compare to KN models.

Finally, we explore how the upcoming Rubin Observatory will be able to serendipitously find KNe, independently from GW or SGRB triggers. For this, we simulated the universe accessible to the survey and use it to derive contamination rates for different classes of transients. When using a filtering scheme based on the magnitude evolution of the sources, we find that $\sim$90% of the sources that fade faster than 0.4 mag/day are either GRB afterglows or supernova (SN) IIb shock breakout. This strategy is only capable of retrieving $\sim$3% of the generated KNe, mainly due to the fast fading nature of the KNe and their intrinsic low luminosity. We propose that future filtering schemes should take into consideration not just the detections, but the difference in magnitudes, Δm, between the last detection, m_{last}, and the subsequent limiting magnitude, m_{lim}. Additional information as color, host galaxy or NIR counterparts on future NIR surveys could also improve the selection.

A portrait of the binary compact merger as a young: Short GRB, Gravitational wave, Afterglow, and Kilonova

by

Tomás Ahumada-Mena

Dissertation submitted to the Faculty of the Graduate School of the
University of Maryland, College Park in partial fulfillment
of the requirements for the degree of
Doctor of Philosophy
2022

Advisory Committee:
Dr. Leo P. Singer, Advisor/Co-Chair
Professor Sylvain Veilleux, Co-Chair
Professor Peter Shawhan, Dean's Representative
Professor Cole Miller
Dr. S. Brad Cenko
Dr. Daniel Kocevski

Preface

The research presented in this dissertation has been conducted in collaboration with multiple co-authors, including my advisor. Most of this research has been published, and here I describe my contribution in detail to each of these articles.

Chapter 1 is an introduction to the relevant concepts, processes, and an overview of the thesis. I was the sole author of this chapter.

Chapter 2 is presented with only minimal modification since appearing in the Astrophysical Journal (ApJ) as "In search of short gamma-ray burst optical counterpart with the Zwicky Transient Facility" (Ahumada et al., 2022). I am the first and corresponding author of this publication, as I led the Target of Opportunity campaing, I got awarded time to observe candidates, I analyzed the data products, and I led the simulations and its analysis. I wrote the majority of the article.

Chapter 3 is also presented with minimal modification since appearing in Nature Astronomy as "Discovery and confirmation of the shortest gamma ray burst from a collapsar" (Ahumada et al., 2021). I am the first and corresponding author of this work, as I discovered the afterglow, lead the optical follow-up that revealed the supernova, and performed the host galaxy analysis. I wrote the sections related to these topics. I completed the section on the modeling of the afterglow light-curve with the help of co-authors V. Cunningham, G. Ryan, M. Coughlin, and L. Singer.

Chapter 4 is presented with extracts from three different works. They all showcase our collaboration efforts to find the optical counterpart to a gravitational wave events, and the extracts shown in this thesis are my contribution to these searches. This corresponds mainly to the discovery and monitoring of the counterpart candidates. In Sec. 4.2 I show my contributions to the searches with ZTF towards finding the optical counterpart of the first BNS merger during O3. Specifically, I contributed in the design of the observing plan, I lead the galaxy targeted follow-up with Kitt Peak Electron multiplying CCD Demonstrator (KPED), and analyzed the photometric follow-up of the candidates, along with the writing of these sections. This work titled "GROWTH on S190425z: Searching thousands of square degrees to identify an optical or infrared counterpart to a binary neutron star merger with the Zwicky Transient Facility and Palomar Gattini IR" was published in ApJ (Coughlin et al., 2019b). In Sec. 4.3, I present my contributions to the work published in Nature Astronomy titled "Optical follow-up of the neutron star-black hole mergers S200105ae and S200115j" (Anand et al., 2021). Similarly to the case of S190425z, I contributed to the photometric follow-up and analysis of the candidates, as well as the writing of these sections. Finally in Sec. 4.4 and the Apendix A contain sections from the ApJ paper titled "Kilonova Luminosity Function Constraints based on Zwicky Transient Facility Searches for 13 Neutron Star Mergers" (Kasliwal et al., 2020b), where I contributed in the light-curve analysis of the candidates and for which I compiled and wrote the summary for all the candidates shown in the appendix of the paper. In Sec. 4.4.1 I show new analysis I solely wrote for this thesis.

Chapter 5 is a first author publication that is in preparation for submission to the Monthly Notices of the Royal Astronomical Society journal, for which I was the main writer and contributor. This includes the simulations of the Rubin Observatory, the development of the transient database, and the analysis of the results.

Finally, in Chapter 6 I summarize the conclusions of the thesis and previous chapters, and venture into future endeavors. I was the sole author if this chapter.

Throughout the thesis I use the pronoun "we" instead of "I", for work where I was a contributor and for work I was the sole author.

Dedication

I dedicate this work the ones that shine in my life.

Acknowledgments

The journey that took me to another hemisphere to do science is closing a chapter. In this few paragraphs, I would like to acknowledge the large list of people that have helped me along the way:

The first in my list is my advisor, Dr. Leo P. Singer. I am grateful for his support and for for the way he took the guided me when I felt lost. Even though he likes to remind me he is not an astronomer (his PhD is in physics, so I guess he's technically correct), he is a very kind, approachable and knowledgeable scientist. I am grateful for the times he let me take the lead, and for his assertiveness when things needed to get sorted out. He allowed me to carve a space in the multi-messenger astronomy community and has always advocated for me.

The next in my list is Dr. S. Bradley Cenko. The first time we met was in Stockholm, during a ZTF team meeting. Brad, kind and welcoming as always, introduced me to collaborators and allowed me to feel part of a community. Throughout my PhD, he has been a constant presence, commenting on my paper drafts and including me in projects. Brad is reliable and responsible, as well as extremely knowledgeable. I think we all should strive to be more like Brad.

Let's keep going with the list, because the next is Prof. Mansi Kasliwal. Although Mansi is at Caltech, she has managed to be extremely present during all

these years. She has always made time to hear my questions, and has supported me in multiple ways throughout my PhD. We met in the summer of 2018, when I visited Caltech to work with Michael Coughlin (spoiler alert, he's the next in my acknowledgment list). Mansi was kind and made me feel part of the group immediately. She has a very contagious curiosity, and from that very first meeting I realized she was someone I wanted to learn from. A little bit of her drive and science enthusiasm lives now in me and for that I am thankful.

The next one is Prof. Michael Coughlin (how did you know?!). I met Michael around the same time I met Mansi, during the summer of 2018. Ever since, he took me under his wing, and taught me how to be a scientist. From starting an idea, to executing, testing and troubleshooting it, Michael has made me part of many projects. He has deposited trust and treated me like an equal from the very beginning. Our many interactions have shaped the scientist I am today.

The constellation of Leo, Brad, Mansi, and Michael has guided me throughout this journey, as the stars in the night-sky have guided sailors throughout history.

Where am I going?

Where will I land?

Not sure, I only hope there is gelato.

And talking about gelato, I cannot forget to mention Dr. Igor Andreoni. I met Igor in India, during a GROWTH conference. Igor and I have similar scientific interests and I am grateful of all the discussions, as these have positively impacted my work. After Igor moved to UMD, our scientific collaboration blossomed and we ended

up involved on a project that took me to Rome. Working there I met Dr. Silvia Piranomonte and Dr. Fabio Ragosta, two OAR-INAF astronomers that welcomed me in Italy. I am grateful to them for all the ideas, opportunities, and gelato we shared while working on the last chapter of my thesis.

A separate paragraph needs to be dedicated to my partner in gravitational waves astronomy crimes, Shreya Anand. Shreya and I are both academic children of Dr. Leo Singer, as she worked with him during her time as and undergraduate at UMD. So naturally, we have a lot of similar scientific interests, and have spent an eternity (maybe two eternities) sifting through ZTF data , looking for kilonova candidates, acquiring photometric and spectroscopic data, writing proposals, papers, troubleshooting, and brainstorming. For all that I am grateful to Shreya.

My adventures in the multi-messenger realm would not have been as enjoyable without the support of the ZTF multi-messenger group. The atmosphere in our meetings definitely fostered a productive environment and I am grateful of the people that made that possible: Dan Perley, David Kaplan, Jesper Sollerman, Robert Stain, Ana Sagues-Carracedo, Anna Frankowiak, Simeon Rausch, among others.

I think I mentioned the list was long.

I have yet to mention people at UMD! Thankful I am for the support my committee has given me during these years, particularly Prof. Sylvain Veilleux and Prof. Cole Miller. Cole additionally was part of the volleyball branch of the Dirty Snowballs, our UMD astronomy team that along with Massimo, Milena, Harrison, and Andrei won the second place in the intramural league! The interactions with

other faculty have also been pleasant and encouraging: thanks Alberto, Stuart, Andy, and generally all the faculty. Thank you to the business office and professional staff at UMD who always keep things running so smoothly.

You might be puzzled after reading the names of Milena and Harrison in the paragraph above. Who are they? What role did they play in this journey? Good question, dear reader. They are part of my lovely cohort. Along with Ramsey, Charlotte, Julian, Guangwei and Sergio, we survived classes, exams, and even living together. Friends, roommates, and co-workers: dangerous combination. However, after multiple years, we are all alive and *thriving*.

The list keeps growing, as I keep diving into my memories. I hope all the incoming and future astronomy UMD graduate students have a student body as amazing as I had. I could mention basically all the grad students I got the chance to meet throughout these years, because in one way or another I am grateful to all of them. The fabulous Ginny, the supportive Carrie, and Liz the fantastic. Since I'll run out of adjectives, pick one of these (kind, bold, resilient) and attach it to your name: Erica (from Michigan), Pradip, Drew, Arnab, Dana, Sara, Ben, Vicente, Rye, Chongchong, Weizhe, Gabe, Katya, Arjun, Ell, Jialu, and all the ones I forgot to mention. Thank you all.

Of course this list has not yet ended.

I will be eternally grateful of the support my family gave me these years. There are close to 8000 km (many many miles) between my home in Santiago, Chile and UMD. Somehow, my parents Mónica and Héctor, have managed to be present every step of the way. I do not think there are words to describe how important they

have been. My sister Macarena and my brother Matías have also been there for me. My nephew Joaquín, my cousins Francisco and Fernando, as well as my aunt Azucena would constantly and relentlessly support me. I am thankful of both my grandmothers, María and Azucena, for their thoughts and their wisdom. Thanks to Claudio, Mónica, Constanza, Rodrigo, and Laura as well.

Finally, to my chosen family. To my friends I am most grateful. For keeping me sane and on track, while allowing me to enjoy life by their side. For the company, the adventures, and the long hours spent eating, cooking and enjoying life. To my Chilean friends Gonzalo, Perry, Joyce, Martina, Javiera, Amelia, Victoria, Enriqueta, Valentina, Hannes, Jorge, Francisca, and Matias. To my DC friends Carolina, Laura, Amanda, Lambrini, Romina, Damareus, and Allen. To my Rome friends Gabriela and Federica. To Mathilde, Mela, and to all the ones that shine in my life, thank you.

I told you the list was long and I am sure I forgot to mention people. But if you read this entire hefty section, I am grateful for you too.

Gracias.

Table of Contents

List of Tables

List of Figures

List of Abbreviations

2MASS	Two Micron All Sky Survey
AGN	Active Galactic Nuclei
AGILE	Astro rivelatore Gamma a Immagini Leggero
ALeRCE	Automatic Learning for the Rapid Classification of Events
AMPEL	Alert Management, Photometry, and Evaluation of Light curves
ATLAS	Asteroid Terrestrial-impact Last Alert System
ApJ	Astrophysical Journal
BALROG	BAyesian Location Reconstruction Of GRBs
BAT	Burst Alert Telescope
BATSE	Burst and Transient Source Explorer
BAYESTAR	BAYESian TriAngulation and Rapid localization
BeppoSAX	*Beppo* Satellite for X-ray Astronomy
BH	Black Hole
BNS	Binary Neutron Star
CASA	Common Astronomy Software Applications
CBC	Compact Binary Coalescence
CCD	Charge-Coupled Device
CLU	Census of the Local Universe
CR	Credible Region
CRTS	Catalina Real-time Transient Survey
CTA	Cherenkov Telescope Array
CV	Cataclysmic Variable
CIFT	CZTI Interface for Fast Transients
CZTI	Cadmium Zinc Telluride Imager
DBSP	Double Spectrograph
DDT	Director's Discretionary Time
DECam	Dark Energy Camera
DR	Data Release
DRAGONS	Data Reduction for Astronomy from Gemini Observatory North and South
DREAMS	Dynamic REd All-sky Monitoring Survey
EM	Electromagnetic
EOS	Equation Of State
ePESSTO	enhanced Public ESO Spectroscopic Survey for Transient Objects
ESO	European Southern Observatory

FAR	False Alarm Rate
FBOT	Fast Blue Optical Transient
FOV	Field Of View
FP	Forced Photometry
FPipe	Fremling Automated Pipeline
FTN	Faulkes Telescope North
FWHM	Full Width at Half-Maximum
GALEX	Galaxy Evolution Explorer
GBM	Gamma-ray Burst Monitor
GCN	Gamma-ray Coordinates Network
GIT	GROWTH India Telescope
GMOS	Gemini Multi-Object Spectrograph
GMRT	Giant Metrewave Radio Telescope
GOTO	Gravitational wave Optical Transient Observer
GRANDMA	Global Rapid Advanced Network Devoted to Multi-messenger Addicts
GRB	Gamma-ray Burst
GROWTH	Global Relay of Observatories Watching Transients Happen
GTC	Gran Telescopio Canarias
GW	Gravitational Wave
GWB	GMRT Wideband Backend
HCT	Himalayan Chandra Telescope
HEALPix	Hierarchical Equal Area isoLatitude Pixelisation
HEND	High-Energy Neutron Detector
HETE	High Energy Transient Explorer Mission
HOTPANTS	High Order Transform of Psf ANd Template Subtraction
IFU	Integral Field Unit
IMF	Initial Mass Function
INAF	National Institute for Astrophysics
INTEGRAL	International Gamma-Ray Astrophysics Laboratory
IPAC	Infrared Processing and Analysis Center
IPN	InterPlanetary Network
iPTF	intermediate Palomar Transient Factor
IR	Infrared
IRAF	Image Reduction and Analysis Facility
JD	Julian Day
KN	Kilonova
KPED	Kitt Peak EMCCD Demonstrator
KW	Konus-Wind
LAL	LSC Algorithm Library
LBTO	Large Binocular Telescope Observatory

LCO	Las Cumbres Observatory Global Telescope
LCOGT	Las Cumbres Observatory
LDT	Lowell Discovery Telescope
LGRB	Long Gamma-ray Burst
LIGO	Laser Interferometer Gravitational-Wave Observatory
llGRB	low-luminosity GRB
LMC	Large Magellanic Cloud
LMI	Large Monolithic Image
LOT	Lulin One-meter Telescope
LRIS	Low Resolution Imaging Spectrograph
LSC	LIGO Scientific Collaboration
LSST	Large Synoptic Survey Telescope
LS	Legacy Survey
LT	Liverpool Telescope
LVC	LIGO/Virgo Collaboration
MCMC	Markov chain Monte Carlo
MPC	Minor Planet Center
ML	Machine Learning
NASA	National Aeronautics and Space Administration
NED	NASA Extragalactic Database
NGC	New General Catalogue
NIR	Near Infrared
NIRES	Near-Infrared Echellete Spectromete
NS	Neutron Star
O3	third Observing run
O4	fourth Observing run
OAR	Astronomical Observatory of Rome
OSIRIS	Optical System for Imaging and low-Intermediate-Resolution Integrated Spectroscopy
P48	Palomar 48 inch Oschin telescope
P60	Palomar 60 inch Oschin telescope
P200	Palomar 200 inch Hale telescope
Pan-STARRS	Panoramic Survey Telescope and Rapid Response System
PESSTO	Public ESO Spectroscopic Survey for Transient Objects
POSSIS	POlarization Spectral Synthesis In Supernovae
pPFX	Penalized Pixel-Fitting
PSF	Point Spread Function
PSR	Pulsating Source of Radiation
PRLS	Photometric Redshifts Legacy Survey
PTF	Palomar Transient Factor

RA	Right Ascension
RB	Real-Bogus
RSS	Robert Stobie Spectrograph
SALT	Southern African Large Telescop
SBO	Shock Breakout
SED	Spectral Energy Distribution
SEDM	Spectral Energy Distribution Machine
SDSS	Sloan Digital Sky Survey
SFH	Star Formation History
SFR	Star Formation Rate
SGRB	Short Gamma-ray Burst
SN	Supernova
SN Ic-BL	Supernova type Ic Broad-Line
SNID	SuperNova IDentification
SPRAT	Spectrograph for the Rapid Acquisition of Transients
TDE	Tidal Disruption Event
TNS	Transient Name Server
ToO	Taget of Opportunity
uGMRT	upgraded Giant Metrewave Radio Telescope
UMD	University of Maryland
UVOT	UV/Optical Telescope
WD	White Dwarf
WINTER	Wide-field INfrared Transient ExploreR
WMAP	Wilkinson Microwave Anisotropy Probe
WRIC	Wide Field Infrared Camera
WISE	Wide-field Infrared Survey Explorer
XRF	X-ray flash
XRT	X-ray Telescope
ZADS	Zwicky Transient Facility Alert Distribution System
ZAL	ZTF Alert Lab
ZTF	Zwicky Transtient Facility
ZTFReST	ZTF REaltime Search and Triggering
ZUDS	ZTF Uniform Depth Survey

Chapter 1: Introduction

Compact binaries composed of neutron stars (NSs) and/or black holes (BHs) have long captivated physicists and astronomers. These provide a natural environment where it is possible to test high energy phenomena, as well as a place to study the late evolution of a star. More relevant to this thesis, is the fact that these binaries are sources of gravitational waves (GWs) and their mergers can be detected with current GW observatories. Furthermore, these events are expected to illuminate the entire electromagnetic spectrum, from radio to gamma-rays. Commonly, a compact binary coalescence (CBC) refers to a merger that involves either a binary neutron star (BNS), a binary black hole (BBH) or a neutron star and a black hole (NSBH). Typically, the concept of CBC excludes white dwarfs (WD) as compact objects.

Walter Baade and Fritz Zwicky proposed neutron stars as they were exploring ways to explain the origin of supernovae (Baade & Zwicky, 1934), soon after Sir James Chadwick (Chadwick, 1932) discovered the neutron as a particle. Supernovae (SNe) are extremely bright transients, most times outshining an entire galaxy. It is currently understood that they are linked to the death of a star. In their work, Baade and Zwicky proposed that the release of the gravitational binding energy of the neutron star powers the supernova. It took years to discover the first neutron star and

the journey began in 1965, when Antony Hewish and Samuel Okoye discovered the first pulsar while monitoring the radio sky (Hewish & Okoye, 1965). The Crab Nebula had been associated to the great supernova of 1054 C.E., which was documented by multiple communities across the globe. Later, in 1967, Jocelyn Bell and Antony Hewish discovered radio pulses coming from the Crab Nebula (Hewish et al., 1968). The radio emission originated from an isolated, rotating neutron star. Although most known neutron stars are thought to be isolated, there are neutron stars (and black holes) that have been observed with a companion star, usually from the main sequence. These have been discovered in X-rays, as the material from the companion star falls into an accretion disk around the compact object, either through Roche-lobe overflow or through direct impact of a stellar wind onto the compact object (Shklovsky, 1967). In 1975, Hulse and Taylor discovered PSR B1913+16, the first binary neutron star (Hulse & Taylor, 1975). The observations of this pulsar allowed Taylor and Weisberg to calculate the rate at which the orbital period should decay as energy is lost from the system via gravitational radiation (Taylor & Weisberg, 1982), providing the first evidence of the existence of gravitational-wave radiation.

Black holes, on the other side, were first theorized in 1783 by J. Michell, based on Newton's laws (Schaffer, 1979). He described them as volumes of space where gravity is so strong that nothing could escape from it. However, no one believed that these objects would actually exist and it took centuries to develop a better understanding of these objects. In 1915, A. Einstein presented his theory of General Relativity (Einstein, 1922), which served as a base for black hole studies, cosmology, and gravitational waves among other topics. Not long after, K. Schwarzschild found

a solution to the equations and was able to determine the radius for a non-spinning black hole (Schwarzschild, 1916), and in 1963 R. Kerr was able to find a solution to the rotation of a black hole (Kerr, 1963). Around that time, M. Schmidt discovered quasars, targeting radio sources in the optical and unveiling extremely energetic outflows from the distant universe (Schmidt, 1963). This discovery fueled the search for black holes and now it is understood that quasars are active galactic nuclei (AGN) powered by super-massive black holes undergoing accretion. Today, supermassive black holes are known to exist at the center of almost all galaxies, even our own (Akiyama et al., 2022), although not all are actively accreting. The search for stellar-sized black holes made a breakthrough thanks to X-ray observations in the early 1970s, when Cygnus X–1 was discovered by Webster & Murdin (Webster & Murdin, 1972), and Bolton (Bolton, 1972) . The second binary black hole, LMC X–3, was identified by Cowley et al. (1983). Both of these systems are bright objects in the X-ray sky and their luminosity is driven by accretion from a companion star.

Compact binaries have been inferred from the energy output, luminosities, and orbital decay rate associated to their observed electromagnetic emission. These type of binaries are gravitationally bounded and it is expected that they will be strong gravitational wave emitters. Gravitational waves are directly derived from Einstein's equations, and even though they were originally controversial, today they are widely accepted, and have been observed from compact binary mergers. In fact the Laser Interferometer GW Observatory (LIGO) (Abbott et al., 2009) was built to accomplish this goal. LIGO is composed of two Fabry-Perot-Michelson interferometers located in Hanford (WA) and Livingston (LA), 3000 kilometers apart. These

"L" shaped 1.2m-wide steel vacuum tubes are covered with concrete, and they shelter interferometers that are sensitive to gravitational waves in the frequency range from 10 Hz to 7 kHz (LIGO Scientific Collaboration et al., 2015). LIGO was the first gravitational wave observatory to detect GWs coming from a binary black hole merger in 2015 (Abbott et al., 2016). Furthermore, this groundbreaking discovery granted the 2017 Nobel Prize in Physics to the LIGO Founders, Kip S. Thorne, and Rainer Weiss, along with Caltech professor Barry C. Barish. Following that first detection, currently, more than 85 binary black hole mergers have been detected, two binary neutron star mergers, and five neutron star - black hole mergers (Abbott et al., 2019a; The LIGO Scientific Collaboration et al., 2021a).

On August 17th, 2017, the first - and so far the only - electromagnetic counterpart to a binary neutron star merger was found (Abbott et al., 2017a,b; Arcavi et al., 2017; Chornock et al., 2017; Côté et al., 2018; Cowperthwaite et al., 2017; Drout et al., 2017; Goldstein et al., 2017; Kasliwal et al., 2017b; Savchenko et al., 2017; Soares-Santos et al., 2017). This event was detected by LIGO Livingston and Hanford, and 1.7 sec after, the *Fermi* and *INTEGRAL* spacecraft detected a short burst of gamma-rays. The combination of LIGO and Virgo data allowed to localize the source of GWs to a 28 deg^2 sky area. The electromagnetic follow-up campaign that multiple teams carried out found AT2017gfo, the optical counterpart of the BNS merger, 2.0 kpc from the galaxy NGC 4993. This was a turning point moment in astrophysics, as for the first time the optical emission from a compact binary merger was unambiguously discovered, and a new window in multi-messenger astronomy was opened. Unlike for BNS or NHBH mergers, an electromagnetic counterpart to

a BBH merger is not expected.

The localization of the optical counterpart allowed for a detailed study, some would even say a portrait, of a binary neutron star merger. This event, first discovered in gravitational waves and later detected in gamma-rays, was followed by a week-long r-process powered KN, and a years-long X-ray and radio afterglow. All these components, together and separately, gave an immense insight into numerous fields as diverse as jet physics (Bromberg et al., 2018; Granot et al., 2018), general relativity (Abbott et al., 2019b; Shibata et al., 2017), r-process nucleosynthesis (Chornock et al., 2017; Côté et al., 2018; Drout et al., 2017; Pian et al., 2017), the measurement of the equation of state (EOS) of neutron stars (Abbott et al., 2018), and the expansion of the universe (Abbott et al., 2017a; Fishbach et al., 2019; Hotokezaka et al., 2019). The scientific bounty is still giving, as to this day ($\sim$4.8 years after the merger), the latest observations with the *Chandra* X-ray Observatory (Weisskopf et al., 2000) show a source with a flux of 0.6 $\times 10^{-15}$ erg/cm^2/s in the 0.3-10 keV energy range (O'Connor & Troja, 2022).

In the next following sections I aim to broadly describe gamma-ray bursts, the kilonova emission, and the state-of-the-art instruments that are being used to optically search for compact binary mergers.

1.1 Gamma-ray bursts

GRBs are amongst the most energetic explosions known to exist in the Universe and their current rate is close to one event per day, over the entire sky (von

Kienlin et al., 2020). These events were first detected by the Vela satellites in the 1960's, and their cosmological origin was not confirmed until 1973 (Klebesadel et al., 1973). GRBs are jets of collimated radiation, typically confined to a width between 1–10° (Rhoads, 1999; Sari et al., 1999). As the jet interacts with the circumburst material, it powers a multi-wavelength afterglow that ranges from X-rays to radio frequencies and can be detected even months after the onset of the gamma radiation (Costa et al., 1997; Frail et al., 1997; van Paradijs et al., 1997).

The events detected by the Burst and Transient Source Experiment (BATSE), on board the Compton Gamma Ray Observatory (Fishman et al., 1989) showed for the first time a bimodal distribution in the duration of the event. The two distributions peaked at 0.3 and 30 seconds, and a separation threshold was set to 2 seconds (Kouveliotou et al., 1993). The duration of the burst, T_{90}, was defined as the time in which the 90% of the radiation is emitted in the prompt emission. Throughout the years, the association to host galaxies and the finding of afterglows at lower energies, allowed for the study of these two populations separately. The current understanding of long bursts is that they are produced as the core of a massive star collapses onto a compact object, which powers a ultra-relativistic jet that drills through the stellar material and emerges as a collimated structure (MacFadyen et al., 2001). Current gamma-ray instruments are only able to detect these jets if they point towards Earth, or if they are close enough. In 1998, a SN was discovered following the long-duration GRB 980425, providing direct evidence of the relationship between long GRBs and SN (Galama et al., 1998; Kulkarni et al., 1998). Although detecting SNe after long gamma-ray bursts (LGRBs) has proven to be challenging (mainly due

to optical constraints), numerous SNe have been found in association with LGRBs. The SN type associated to them usually shows broad lines on its spectrum, and lacks H, He and Si, making them of the type Ic (Hjorth & Bloom, 2012).

On the other hand short GRBs were originally defined as the bursts lasting less than 2 seconds. Their origin is still under debate, however short GRBs have been observed coming from a binary neutron star merger (Goldstein et al., 2017), bursting magnetars (Burns et al., 2021), and lately collapsars (see Chapter 3 and Ahumada et al. 2021). Models predicted short gamma-ray bursts as a product of the merger of compact objects long before GW170817 (Eichler et al., 1989). These binary systems can originate from the evolution of massive stars in a primordial binary (Narayan et al., 1992) or dynamically, due to three-body interactions in globular clusters (Grindlay et al., 2006; Salvaterra et al., 2008).

The Neil Gehrels *Swift* Observatory (Gehrels et al., 2004) has provided the community with a large number of precisely localized SGRBs. The systematic study of their afterglows has led to better understanding of multiple features (Fong et al., 2015): SGRBs have on average less energetic afterglows and lower associated isotropic gamma-ray energies than long bursts, their hosts tent to have lower star formation rate (SFR) and occur at a lower redshifts than LGRBs, and generally they are not found in association with SNe (except from Ahumada et al. 2021). Although different in many ways, it has been shown that SGRBs and LGRBs follow a hardness-intensity correlation (i.e. a relationship between the isotropic energy, E_{iso}, and the GRB rest-frame peak energy, $E_{z,p}$) (Amati et al., 2002; Yonetoku et al., 2004), and their X-ray absorbing column densities (N_H) do not differ significantly

up to redshift ~ 1.2. When looking into the prompt emission properties, short GRBs show almost no spectral lag (Norris & Bonnell, 2006; Norris et al., 2000) in contrasts to LGRBs (Norris et al., 2000), and normally a harder spectrum (Kouveliotou et al., 1993) compared to LGRBs.

The original classification based on the duration of the burst has been challenged several times (Lü et al., 2010; Zhang et al., 2009), and a different classification has been proposed based on the progenitor of the GRB. It has proven challenging to cement the progenitor type using solely the GRB data, however, it is useful when combined with the afterglow emission and host galaxy properties. In Zhang et al. 2009 two progenitor types of GRBs were proposed: the core collapse of a massive star, and the merger of a compact binary. However the number of types is expected to increase, as more objects such as magnetars (Burns et al., 2021) and merger-triggered core collapses (Dong et al., 2021) have been associated to GRBs.

1.1.1 GRB Afterglows

On February 28, 1997, the *Beppo* Satellite for X-ray Astronomy (BeppoSAX) (Boella et al., 1997), discovered for the first time an X-ray counterpart of a GRB (Costa et al., 1997). This afterglow showed a rapidly fading X-ray and optical emission, and its detection helped determine the redshift of the burst. This marked the beginning of an era of GRB afterglow detections, providing more data to understand these explosions and to test different theories (Frontera et al., 1998; van Paradijs et al., 1997).

Most afterglow models are a generic explanation of jets interacting with matter at ultra-relativistic speeds, specifically between the *fireball* (Dermer et al., 1999; Rhoads, 2003) moving with a given Lorentz factor Γ_0 and a given isotropic energy E, with the circumburst density, normally described with a density profile that is a function of the radius $n(R)$. These models normally do not depend on the details of the central engine, which has proven to be convenient, as the fireball-circumburst medium interaction is expected for all cases. The models predict a power-law decaying multi-wavelength afterglow (Mészáros & Rees, 1997; Paczynski & Rhoads, 1993), first observed in 1997 as mentioned above.

The current models predict that the rotational spindown of the neutron star, or the accretion onto the black hole accelerates the material to ultra-relativistic speeds. This produces a collimated outflow with a typical opening angle of $\theta \sim 10^{\circ}$ and an initial Lorentz factor $\Gamma_0 \sim 100$. This outflow drills through the star, and eventually collides with the circumstellar medium, producing an afterglow that is bright across the electromagnetic spectrum (Panaitescu & Kumar, 2002; van Eerten, 2018).

The afterglow of SGRBs showed to be a bit more elusive. Only in 2005, and thanks to the re-pointing capabilities of the *Swift* observatory, the first afterglow of a short GRB was detected in the X-rays, optical, near-infrared and radio (Castro-Tirado et al., 2005; Fox et al., 2005; Gehrels et al., 2005)

Since then, *Swift* has enabled dozens of discoveries (Fong et al., 2015; Rastinejad et al., 2021), allowing for the systematic characterization of the afterglows and their hosts. These studies have shown that, compared to LGRB afterglows, SGRB

afterglows have a lower luminosity across the entire EM spectrum, a lower circum-burst density and can occur in galaxies with lower star-formation rate (Fong et al., 2022; Rastinejad et al., 2021).

1.2 Kilonova emission

During a compact binary coalescence (CBC), some matter from the NS will unbind from the central remnant and will be ejected at mildly relativistic velocities. The nature of the composition of the ejecta is mainly neutrons, creating a natural environment to synthesize elements via rapid neutron capture. The r-process nucleosynthesis leads to the formation of heavy, unstable elements, that through α-decay, β-decay and fission, deposit energy into the ejecta. This is what powers a thermal transient commonly known as kilonova (KN) (Kulkarni, 2005; Li & Paczynski, 1998; Metzger et al., 2010).

Generally, there are two main flavors of KN: blue and red. The matter that gets tidally disrupted from the NS is neutron-rich (with an electron fraction $Y_e < 0.25$), and allows for the creation of lanthanide-bearing material, that eventually falls into the accretion disk. The thermalized emission is heavily suppressed in the UV and optical bands due to the high opacity of these lanthanides, creating a red KN. A blue KN is produced when the unbound ejecta has a lower neutron abundance ($Y_e > 0.3$), as the resulting material is lanthanide-free. This low-opacity material is produced by the shock generated after the two neutron stars make contact, as this heats the material and leads to pair production and positron capture. Additional low opacity

material is ejected once (if) the remnant NS is formed and launches baryon-loaded winds. The shocked and wind ejecta sits in the polar regions and its not opaque to UV/optical wavelengths allowing for a bluer emission Ascenzi et al. (2021); Foucart et al. (2014); Rosswog (2005, 2015).

It is expected that as a result of the high and low electron fraction material distribution, KNe will normally be a combination of both the red and blue components. This creates an angular dependence in the emission as a redder KN will be seen if the viewer is closer to the equatorial plane of the merger, while a bluer KN will be visible from angles closer to the poles (Metzger, 2017)

A diagram from Ascenzi et al. 2021 summarizing the GRB, afterglow and KN emission is shown in Fig. 1.1.

1.3 ZTF and the *Rubin* observatory

Before diving into serendipitous detections, I will describe the instruments and projects that have enabled these searches during my stay at UMD. The Zwicky Transient Facility (Bellm et al., 2019a) mounted in the Palomar 48-inch telescope, at Palomar Observatory, is a state-of-the-art camera is capable of imaging 47 $\deg^2$ in one exposure. It is the successor of the Palomar Transient Factory (PTF) (Law et al., 2009), a 7 $\deg^2$ camera used to monitor the dynamic optical sky in the northern hemisphere. Currently, ZTF monitors the night sky taking 30 seconds exposures in g-, r- and sometimes in i-band, reaching on average a limit of 20.5 mag. Once an exposure finishes, a pipeline reduces and calibrates the image, to later

perform image subtraction using references of the field (Masci et al., 2019) previously acquired. To account for the chip gaps and cover the totality of the sky, ZTF has two grids of fields that tessellate the sky. After the subtraction, any 5σ changes in brightness generates an *alert* that contains information about its current brightness, real-bogus classification, previous detections, features of neighboring sources, as well as a cross-match with solar-system objects. The Zwicky Transient Facility Alert Distribution System (ZADS) (Patterson et al., 2019) is responsible for streaming in near-real-time the alerts to the alert brokers, as *avro* packages. There are nine official Rubin alert brokers and some of them, such as the Automatic Learning for the Rapid Classification of Events (ALeRCE) (Förster et al., 2021), Lasair (Smith et al., 2019a), or Fink (Möller et al., 2021), are constantly listening to the ZTF alert stream and they provide interfaces for scientists to interact with the data. This allows scientists to perform real-time time-domain astronomy, and tackle science cases as different as the follow-up of gravitational waves and the identification of near-Earth asteroids. Normally, ZADS distributes $\sim 10^5$ alerts each night, making the search of interesting sources incredibly hard. For this purpose, multiple brokers have enabled alert filtering schemes, enhancing the search of transient and allowing for an efficient selection of sources. Even though the alert filtering schemes can be quite effective at selecting transients, the volume of astronomically interesting sources normally surpasses the ability to study them individually. Multiple groups within ZTF have started tackling this issue by using to robotic telescopes, such as Las Cumbres Observatory (LCO) or Spectral Energy Distribution Machine (SEDM). For example, the SN ZTF group is tackling this problem by automating the entire process: from

the discovery with ZTF, to the spectroscopic classification, with SEDM (Fremling et al., 2020; Perley et al., 2020).

The *Rubin* Observatory is expected to start operations in early 2024, beginning the 10-year Legacy Survey of Space and Time (LSST) (Ivezić et al., 2019). The *Rubin* camera will be mounted on a 8.4 m telescope in Cerro Pachon, Chile, and it was designed to image 9.6 deg^2 on each exposure. Similarly to ZTF, *Rubin* will monitor the dynamic optical sky multiple times each night and in multiple filters (i.e. *ugrizy*). This system will reach a typical magnitude depth of 24.7 mag in the r band on a 30 seconds exposure, exploring a much larger volume than ZTF. It is expected that the number of alerts generated by LSST will be ∼10-100 times the current number of alerts generated by ZTF, raising not only technical challenges, but also defying current strategies to filter alerts and follow-up transients. It is expected that *Rubin* will discover 10^5 SNe per year (The LSST Dark Energy Science Collaboration et al., 2018), however most of them will be spectroscopically inaccessible, as they will be in the 0.5-0.7 redshift range and hence too faint. Multiple efforts have been carried out to try to classify these objects using uniquely their photometric light curves. Currently, *Rubin* has produced simulated data (LSST Dark Energy Science Collaboration (LSST DESC) et al., 2021) over 300 deg^2, including galaxies, type Ia SNe, stars, and variable stars to allow the community to explore science cases and get familiarized with the facilities.

1.4 Serendipitous findings

Above, I have discussed a few distinctive features of BNS and NSBH mergers: the production of gravitational waves, the gamma-ray radiation that follows the merger, and the optical and near-infrared kilonova powered by the r-process nucleosynthesis. In order to discover a compact binary merger, then it is possible to act upon GW alerts or short GRBs, because they provide a defined merger time and a direction in the sky to point optical telescopes. Thus, there are many Target of Opportunity (ToO) programs active in multiple telescopes, to rapidly target these areas. However, unless extremely close, the detailed study of one of these objects is quite challenging. Additionally, when GW observatories are offline, or if the GRB jet does not point towards earth, it is virtually impossible to receive a compact binary merger alert.

Nonetheless, the KN radiation following the merger is nearly isotropic although it is expected to show different features deppending on the viewing angle (see Sec. 1.2). The current models for these mergers predict a fast fading transient in the UV/optical/NIR: regardless of its original composition $\sim 80\%$ of the models fade at a rate greater than 0.3 mag/day in the r-band. This fact has motivated the search of KNe in wide field of view surveys, like ZTF, the Asteroid Terrestrial-impact Last Alert System (ATLAS ; Tonry et al. 2018) and the Panoramic Survey Telescope and Rapid Response System (Pan-STARRS ; Chambers et al. 2016a; Kaiser et al. 2010) (see Andreoni et al. 2020b; McBrien et al. 2021). These unbiased searches are independent from GW or GRB detections, and they have helped discover collapsars

with dirty fireballs and 'orphan afterglows' (i.e. afterglows without GRB counterparts) (Cenko et al., 2015; Ho et al., 2022). No KN has been found through these searches, however it has been possible to constrain the rate of KN, with the most recent upper limit being of 900 Gpc^{-3} yr-1 (Andreoni et al., 2021). However, the hope it is not yet lost, as it recently has been shown that *Rubin* will uncover at least a few tens of kilonovae (Andreoni et al., 2019; Cowperthwaite et al., 2019; Setzer et al., 2019).

There are still a number of questions opened, as up until the time I am writing this introduction, it is uncertain how much will the kilonova detection improve by implementing a ToO strategy for Rubin, or how can the different cadences proposed for the main survey impact the detection rate of serendipitous KN. There are further implications to these issues, as a late archival KN detection would probably not allow for an in-depth study of the source as the acquisition of a spectrum is essential to classify them, and to study their composition and evolution.

1.5 Thesis outline

This thesis aims to serve as a portrait of the search of the optical counterpart of a compact binary merger. I start with the searches for afterglows and KNe signatures over *Fermi*-GBM short GRBs in Chapter 2. During this campaign, we discovered the shortest gamma-ray emission coming from a collapsing massive star. In Chapter 3 we describe the afterglow, host galaxy, and the observations that led to the discovery of a rising SN. In Chapter 4, I present a summary of the searches

for GW optical counterparts using ZTF. In this chapter I describe the observing strategy and the candidate selection and vetting strategy. The last piece of this portrait involves the optical search for the radioactively powered KN. In Chapter 5 I describe the approach to searching for serendipitously detected KNe with the *Rubin* Observatory. In Chapter 6, I summarize the main results of the thesis and discuss future plans to expand on each of the fields.

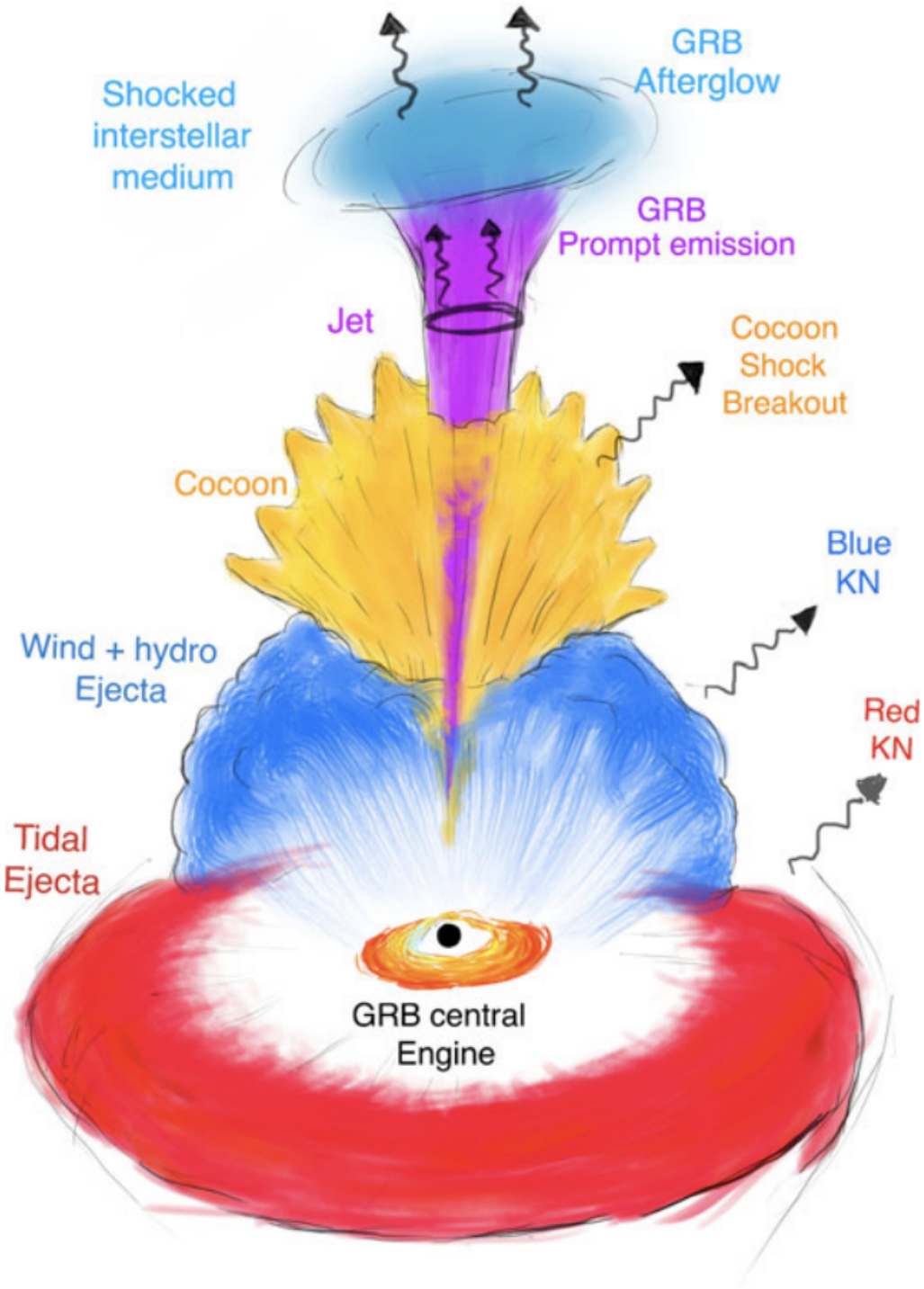

Figure 1.1: Artistic representation of the scenario following an NS–NS/NS–BH merger, when an accreting BH is formed. The red component denotes the tidal ejecta, the blue component the shock and wind ejecta, the purple component the GRB jet and the yellow component the matter of the ejecta heated by the jet (cocoon). The light blue component represents the afterglow emission generated by the interaction between the jet and the circumburst material. The different components are not represented in scale. From Ascenzi et al. 2021.

Chapter 2: In search of short gamma-ray bust optical counterparts with the Zwicky Transient Facility

2.1 Abstract

The *Fermi* Gamma-ray Burst Monitor (GBM) triggers on-board in response to ~ 40 short gamma-ray bursts (SGRBs) per year; however, their large localization regions have made the search for optical counterparts a challenging endeavour. We have developed and executed an extensive program with the wide field of view of the Zwicky Transient Facility (ZTF) camera, mounted on the Palomar 48 inch Oschin telescope (P48), to perform target-of-opportunity (ToO) observations on 10 *Fermi*-GBM SGRBs during 2018 and 2020-2021. Bridging the large sky areas with small field of view optical telescopes in order to track the evolution of potential candidates, we look for the elusive SGRB afterglows and kilonovae (KNe) associated with these high-energy events. No counterpart has yet been found, even though more than 10 ground based telescopes, part of the Global Relay of Observatories Watching Transients Happen (GROWTH) network, have taken part in these efforts. The candidate selection procedure and the follow-up strategy have shown that ZTF is an efficient instrument for searching for poorly localized SGRBs, retrieving a

reasonable number of candidates to follow-up and showing promising capabilities as the community approaches the multi-messenger era. Based on the median limiting magnitude of ZTF, our searches would have been able to retrieve a GW170817-like event up to ~ 200 Mpc and SGRB afterglows to $z = 0.16$ or 0.4, depending on the assumed underlying energy model. Future ToOs will expand the horizon to $z = 0.2$ and 0.7 respectively.

2.2 Introduction

Between the years 1969–1972, the Vela Satellites discovered gamma-ray bursts (GRBs) and further analysis confirmed their cosmic origin (Klebesadel et al., 1973). These GRBs are among the brightest events in the universe, and have been observed both in nearby galaxies as well as at cosmological distances (Metzger et al., 1997). The data collected over the years suggest a bimodal distribution in the time duration of the GRB that distinguishes two groups: long GRBs (LGRB; $T_{90} > 2s$) and short GRBs (SGRB; $T_{90} < 2s$) (Kouveliotou et al., 1993), where T_{90} is defined as the duration that encloses the 5th to the 95th percentiles of fluence or counts, depending on the instrument.

LGRBs have been associated with supernova (SN) explosions (Bloom et al., 1999; Woosley & Bloom, 2006) and a large number of them have counterparts at longer wavelengths (Cano et al., 2017). On the other hand only $\sim$ 35 SGRBs have optical/NIR detections (Fong et al., 2015; Rastinejad et al., 2021), thus their progenitors are still an active area of research. SGRBs have been shown to occur in

environments with old populations of stars (Berger et al., 2005; D'Avanzo, 2015) and have long been linked with mergers of compact binaries, such as binary neutron star (BNS) and neutron star–black hole (NSBH) (Narayan et al., 1992). The discovery of the gravitational wave event GW170817 coincident with the short gamma-ray burst GRB 170817A, unambiguously confirmed BNS mergers as at least one of the mechanisms that can produce a SGRB (Abbott et al., 2017b). However, compact binary mergers might not be the only source of SGRBs, as collapsars (Ahumada et al., 2021; Zhang et al., 2021) and giant flares from magnetars (Burns et al., 2021) can masquerade as short duration GRBs. Hence, the traditional classification of a burst based solely on the time duration is subject to debate (Amati, 2021; Bromberg et al., 2013; Zhang & Choi, 2008). For example, other gamma-ray properties (i.e. the hardness ratio) can cluster the bursts in different populations (Nakar, 2007), and there are a couple of examples for which the time classification of the burst has been questioned due to the presence or lack of SN emissions (Ahumada et al., 2021; Gal-Yam et al., 2006; Rossi et al., 2021; Zhang et al., 2021). In this context, the search for the optical counterparts of SGRBs is essential to unveil the nature of their progenitors and the underlying physics.

Not all SGRBs show similar gamma-ray features and different models have tried to explain the observations. For example, the "fireball" model (Mészáros & Rees, 1998; Wijers et al., 1997) describes a highly relativistic jet of charged particle plasma emitted by a compact central engine as a result of a BNS or NSBH merger. The model predicts the production of gamma rays and hard X-rays within the jet. The interaction of the jet and the material surrounding the source produces

synchrotron emission in the X-ray, optical, and radio wavelengths. This "afterglow" lasts from days to months depending on the frequency range.

Different models have been applied to the observations that followed GW170817. Among the most popular is the classical case of a narrow and highly relativistic jet powered by a compact central engine (Goldstein et al., 2017). Deviations in the light-curves derived from classical models have motivated further developments (Cannizzo & Gehrels, 2009; Duffell & MacFadyen, 2015; Metzger et al., 2011; Willingale et al., 2007), including Gaussian structured jets (Abbott et al., 2017c; Kumar & Granot, 2003; Troja et al., 2017) that can be detected off-axis and do not require the jet to point directly to Earth. Other models predict a more isotropic emission profile, produced by an expanding cocoon formed as the jet makes its way through the ejected material, reaching a Lorentz factor on the order of a few (i.e. $\Gamma \sim 2$ to 3) (Kasliwal et al., 2017b; Lazzati et al., 2017; Mooley et al., 2017; Nagakura et al., 2014).

In addition to the GRB afterglow, in the event of a BNS or NSBH merger, the highly neutron rich material undergoes rapid neutron capture (r-process), which creates heavy elements and enriches galaxies with rare metals (Côté et al., 2018). Some of the products of the r-process include radioactive elements; the decay of these newly created elements can energize the ejecta. The produced thermal radiation eventually powers a transient known as a *kilonova* (KN) (Kasen et al., 2017; Lattimer & Schramm, 1974; Li & Paczynski, 1998; Metzger et al., 2010; Rosswog, 2015). In the case of an on-axis SGRB, in most cases the optical emission is expected to be dominated by the afterglow and not by the KN. (Gompertz et al., 2018; Zhu et al.,

2021). There have been attempts to separate the light of the SGRB afterglow and the KN (Ascenzi et al., 2019; Fong et al., 2016, 2021; O'Connor et al., 2021; Rossi et al., 2020; Troja et al., 2019), however this still presents a number of challenges.

Identifying optical counterparts to compact binary mergers can provide a rich scientific output, as demonstrated by the discovery of AT2017gfo (Chornock et al., 2017; Coulter et al., 2017; Cowperthwaite et al., 2017; Drout et al., 2017; Evans et al., 2017; Kasliwal et al., 2017b; Kilpatrick et al., 2017; Lipunov et al., 2017; McCully et al., 2017; Nicholl et al., 2017; Pian et al., 2017; Shappee et al., 2017; Smartt et al., 2017) which led to discoveries in areas as diverse as r-process nucleosynthesis, jet physics, host galaxy properties, and even cosmology (Arcavi et al., 2017; Chornock et al., 2017; Drout et al., 2017; Kasen et al., 2017; Kasliwal et al., 2017b; Pian et al., 2017; Smartt et al., 2017; Tanvir et al., 2017; Troja et al., 2017). Previous studies have used the arcminute localizations achieved with the Neil Gehrels *Swift* Observatory Burst Alert Telescope (BAT) to find and characterize SGRBs optical counterparts (Fong et al., 2015; Rastinejad et al., 2021), however the number of associations is still only a few dozens. Others have tried following-up thousands of square degrees of the LIGO-Virgo Collaboration (LVC) maps (Anand et al., 2021; Andreoni et al., 2019, 2020; Coughlin et al., 2019b; Goldstein et al., 2019; Hosseinzadeh et al., 2019; Kasliwal et al., 2020b; Vieira et al., 2020) in the hopes of localizing EM counterparts to gravitational wave events, to no avail. Moreover, other studies have tried to serendipitously find the elusive KN (Andreoni et al., 2020b; Andreoni et al., 2021; Chatterjee et al., 2019b), but they have so far only been able to constrain the local rate of neutron star mergers using wide field of view (FOV) synoptic

surveys.

In this paper we present a summary of the systematic and dedicated optical search of *Fermi*-GBM SGRBs using the Palomar 48-inch telescope equipped with the 47 square degree Zwicky Transient Facility camera (Bellm et al., 2019a; Graham et al., 2019) over the course of ~ 2 years. Previous studies (Singer et al., 2013, 2015) have successfully found optical counterparts to GBM LGRBs using the intermediate Palomar Transient Factory (iPTF) (Law et al., 2009; Rau et al., 2009), and other searches have serendipitously found orphan afterglows and LGRBs using ZTF (Andreoni et al., 2021; Ho et al., 2022). There are ongoing projects like Global MASTER-Net (Lipunov et al., 2005), and the Gravitational-Wave Optical Transient Observer (GOTO; Mong et al. 2021) that are using optical telescopes to scan the large regions derived by GBM. We note that the optical afterglows of LGRBs are usually brighter than of SGRBs, thus the ToO strategy might differ from the one presented in this paper. We base our triggers on GBM events since GBM is more sensitive to higher energies than *Swift* and it detects SGRBs at four times the rate of *Swift*, making it the most prolific compact binary merger detector.

In section 2.3 we describe the facilities involved along with the observations and data taken during the campaign. We describe our filtering criteria and how candidates are selected and followed up in section 2.4, and detail the *Fermi* events we followed up in section 2.5. In section 2.6 we compare our observational limits to SGRB transients in the literature. In section 2.7 we discuss the implications of the optical non-detection of a source and we explore the sensitivity of our searches. Using the lightcurves of the transients generated for our efficiency analysis, we put

the detection of an optical counterpart in context for future ToO follow-up efforts in section 2.8. We summarize our work in section 2.9.

2.3 Observations and Data

In this section we will broadly describe the characteristics of the telescopes and instruments involved in this campaign, as well as the observations. We start with the *Fermi*-GBM, our source of compact mergers, followed by ZTF, our optical transient discovery engine, and finally describe the facilities used for follow-up.

2.3.1 *Fermi* Gamma-ray Burst Monitor

The Gamma-ray Burst Monitor (GBM) is an instrument on board the *Fermi* Gamma-ray Space Telescope sensitive to gamma-ray photons with energies from 8 keV to 40 MeV (Meegan et al., 2009). The average rest frame energy peak for SGRBs ($E_{p,i} \sim 0.5$ MeV; Zhang et al. 2012) is enclosed in the observable GBM energy range and not in the *Swift* BAT energy range (5-150 keV). Additionally, any given burst should be seen by a number of detectors, as GBM is sensitive to gamma-rays from the entire unocculted sky.

The low local rate of *Swift* SGRBs has impeded the discovery of more GW170817-like transients (Dichiara et al., 2020). On the other hand, GBM detects close to 40 SGRBs per year (von Kienlin et al., 2020), four times the rate of *Swift*. However, the localization regions given by GBM usually span a large portion of the sky, going from a few hundred sq. degrees to even a few thousand square degrees. These large

regions make the systematic search for counterparts technically challenging and time consuming (Goldstein et al., 2020; von Kienlin et al., 2020).

Our adopted strategy prioritizes *Fermi*-GBM GRB events visible from Palomar that present a hard spike, that are classified as SGRBs by the on-board GBM algorithm, and that are not detected by *Swift*. During the first half of our campaign (2018), we did not have any constraints on the size of the GRB localization region. However, during the second half of our campaign, we restricted our triggers to the events for which more than 75% of the error region could be covered twice in $\sim$2 hrs. With ZTF this corresponds to a requirement that 75% of the map encloses less than $\sim$500 deg^2, which explains the difference in the number of triggers between the first and second half of our campaign.

For each GRB, we calculate the probability of belonging to the population that clusters the SGRBs based on their comptonized energy peak E_{peak} and their duration T_{90}. For this, we fit two log-normal distributions (representing the long and short classes) to a sample of $\sim$ 2300 GRBs. We derive and color code the probability P_{SGRB} by assessing where each GRB falls in the distribution (see Fig. 2.1, and Ahumada et al. 2021 for more details). In Table 2.1 we list the relevant features of the SGRBs selected for follow-up.

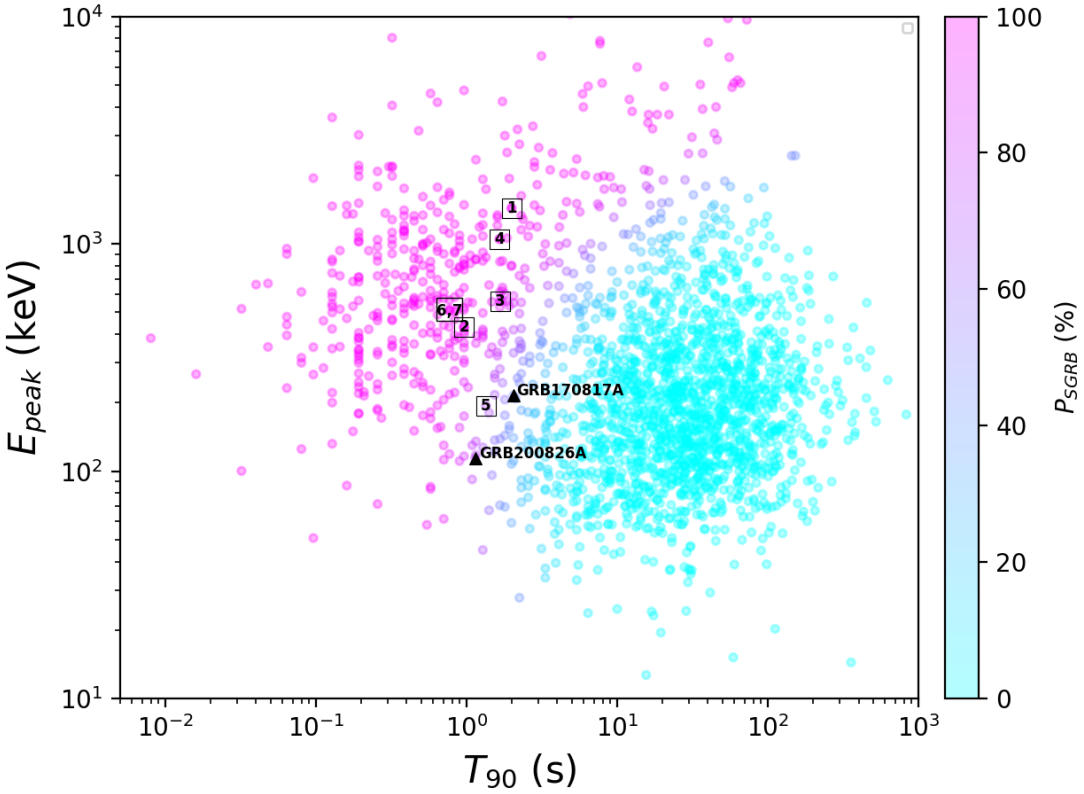

Figure 2.1: The peak energy based on a Comptonized fit, E_{peak} (keV), versus the time-integrated T_{90} (s), for 2,310 *Fermi* GBM GRBs. The data are fit with two log-normal distributions for the two GRB classes. The colour of the data points indicates the probability, with magenta being 100% SGRB and cyan being 100% LGRB. We show in squares numbered from 1 to 7 the following SGRBs: GRB 180523B, GRB 180626C, GRB 180715B, GRB 181126B, GRB 210510A, GRB 180913A and GRB 180728B. Note that the GRB 180728B and GRB 180913A share the same location in this parameter space. The bursts GRB 200514B and GRB 201130A are not shown as the power-law model is preferred over the Comptonized fit, thus there is no E_{peak} parameter associated to them. For context, we show in triangles GRB 170817A and GRB 200826A.

GRB	Fermi Trigger	Time [JD]	T_{90} [s]	90% (50%) C.R. [deg^2]	. S/N	E_{peak} [keV]	Fluence [10^{-8} erg/cm^2]	P_{SGRB}
GRB 180523B	548793993	2458262.2823	2.0 ± 1.4	5094 (852)	6.9	1434 ± 443	25.7± 2.3	0.99
GRB 180626C	551697835	2458295.8916	1.0 ± 0.4	5509 (349)	7.1	431 ± 81	49.1 ± 3.8	0.97
GRB 180715B	553369644	2458315.2412	1.7 ± 1.4	4383 (192)	12.5	560 ± 89	52.0 ± 1.7	0.92
GRB 180728B	554505003	2458328.3819	0.8 ± 0.6	397 (47)	20.2	504 ± 61	130.9 ± 2.0	0.99
GRB 180913A	558557292	2458375.2834	0.8 ± 0.1	3951 (216)	10.0	508 ± 90	79.1 ± 2.0	0.99
GRB 181126B	564897175	2458448.6617	1.7 ± 0.5	3785 (356)	7.5	1049 ± 241	48.3 ± 3.2	0.99
GRB 200514B	611140062	2458983.8802	1.7 ± 0.6	590 (173)	5.1	†	17.8 ± 1.1	–
GRB 201130A	628407054	2459183.7297	1.3 ± 0.8	545 (139)	5.3	†	37.0 ± 5.2	–
GRB 210510A	642367205	2459345.3055	1.3 ± 0.8	1170 (343)	5.6	194 ± 60	23.2 ± 1.4	0.74
GRB 200826A	620108997	2459087.6874	1.1 ± 0.1	339 (63)	8.1	88.9 ± 3.2	426.5 ± 2.2	0.74

Table 2.1: Global features of the *Fermi*-GBM SGRB followed-up with ZTF. The peak energies come from the public Fermi catalog (von Kienlin et al., 2020) for GRB 180523B, GRB 180626C, GRB 180715B, GRB 180913A and GRB 181126B. Additionally, we compiled E_p listed in Hamburg et al. (2018) for GRB 180728B, and independently provide time-integrated fits for GRB 200514B, GRB 201130A, and GRB 210510A over the T_{90}. We list the GRB name, their trigger number, the Julian day (JD) of each event, the T_{90} duration, the area encompassed by the 90% (50%) credible region (C.R.), the signal-to-noise ratio from the Fermi detection, the peak energy of the gamma-ray spectrum (E_{peak}), the fluence of the burst, and the probability of the burst to belong to the SGRB population (see Sec. 2.3.1). The area associated to a given C.R. is derived by calculating the number of pixels that cumulatively sum a specific percentage, using the HEALPix map of each GRB. For events with a †, the power-law model is preferred over the comptonized model, thus there is no E_p parameter. We show separately the parameters of GRB 200826A, as it was not related to a compact binary merger (see Chapter 3, or Ahumada et al. 2021)

2.3.2 The Zwicky Transient Facility

We have used ZTF to scan the localization regions derived by the *Fermi*-GBM. ZTF is a public-private project in the time domain realm which employs a dedicated camera (Dekany et al., 2020) on the Palomar 48-inch Schmidt telescope. The ZTF field of view is 47 deg^2, which usually allows us to observe more than 50% of the SGRB error region in less than one night. The public ZTF survey (Bellm et al., 2019b) covers the observable northern sky every two nights in g- and r-bands with a standard exposure time of 30 s, reaching an average 5σ detection limit of $r = 20.6$.

Two ToO strategies were tested during this campaign, one during 2018 and the second during 2020-2021. Most modifications came after lessons learned during the follow-up efforts of gravitational waves in 2019 (Anand et al., 2021; Coughlin et al., 2019b; Kasliwal et al., 2020b). The original ToO observing plan allowed us to start up to 36 hrs from the SGRB GBM trigger. However, since the afterglow we expect is already faint ($m_r > 19$ mag) and fast fading ($\Delta m/\Delta t > 0.3$ mag per day), our revised strategy only includes triggers that can be observed from Palomar within 12 hrs. The exposure time for each trigger ranges from 60 s to 300 s depending on the size of the localization region, as there is a trade-off between exposure time and coverage. We generally prioritized coverage over depth, and for the second half of our campaign, we only triggered on maps where more than 75% of the region could be covered. The same sequence is repeated a second time the following night, unless additional information from other spacecraft modifies the error region. Generally, fields with an airmass > 2.5 are removed from the observing plan.

We schedule two to three sets of observations depending on the visibility of the region, using the ZTF r- and g-bands. The combination of r- and g-band observations was motivated by the need to look for afterglows and KNe, which are both fast evolving red transients. In fact, the SGRB afterglows in the literature show red colors (i.e. $g - r > 0.3$ mag) and a rapid evolution, fading faster than $\Delta m_r/\Delta t > 0.5$ mag per day. On the other hand, GW170817 started off with bluer colors and evolved dramatically fast in the optical during the first days, with $g - r = 0.5$ mag 1 day after the *Fermi* alert and $\Delta m_g/\Delta t > 1$ mag per day. Even though we expect a fast fading transient, if we assume conservative fading rates of 0.3-0.5 mag per day, we would need observations separated by 8 to 5 hrs respectively to detect the decline using ZTF data with photometric errors of the order of 0.1 mag. This ToO strategy thus relies on the color of transients for candidate discrimination, as this is easier to schedule than multi-epoch single-band photometry within the same night and with sufficient spacing between observations.

We followed up on 10 *Fermi*-GBM SGRBs, and we show 9 skymaps and their corresponding ZTF footprints in Fig. 2.2 through Fig. 2.10. Please refer to Chapter 3 or Ahumada et al. 2021 for details on GRB 200826A, the only short duration GRB followed up during our campaign that is not shown here. As listed in Table 2.1, all of the events span more than 100 deg^2, which is the average localization region covered during previous LGRBs searches (Singer et al., 2015). Moreover, in many cases, the 90% credible region (C.R.) spans more than 1000 deg^2, which is challenging even for a 47 deg^2 field of view instrument such as ZTF.

Triggering ToO observations for survey instruments like ZTF and Palomar

Gattini-IR (De et al., 2020b) halts their ongoing survey observations and redirects them to observe only certain fields as directed by an observation plan. We have used `gwemopt` (Coughlin et al., 2018, 2019a), a code intended to optimize targeted observations for gravitational wave events, to achieve an efficient schedule for our ToO observations. The similarities between LVC and GBM skymaps allow us to apply the same algorithm, which involves slicing the skymap into the predefined ZTF tiles and determining the optimal schedule by taking into consideration the observability windows and the need for a repeated exposure of the fields. In order to prioritize the fields with the highest enclosed probability, we used the "greedy" algorithm described in Coughlin et al. (2018) and Almualla et al. (2020). As `gwemopt` handles both synoptic and galaxy-targeted search strategies, we employed the former to conduct observations with some of our facilities, Palomar Gattini-IR, GROWTH-India and ZTF, and the latter for scheduling observations with the Kitt Peak EMCCD Demonstrator (KPED; Coughlin et al. 2019b).

2.3.3 Optical follow-up

Following the identification of candidate counterparts with ZTF, subsequent optical follow-up of these transients is required to characterize and classify them. For the candidates that met the requirements described in section 2.4, mainly that they showed interesting light-curve history and magnitude evolution, we acquired additional data. To obtain these data, the GROWTH multi-messenger group relies on a number of telescopes around the globe. Most of these facilities are strategi-

cally located in the Northern Hemisphere, enabling continuous follow-up of ZTF sources. The follow-up observations included both photometric and spectroscopic observations. Even though the spectroscopic classification is preferable, photometry was essential to rule out transients, based on their color evolution and fading rates. The telescopes involved in the photometric and spectroscopic monitoring are briefly described in the following paragraphs.

We used the KPED on the Kitt Peak 84 inch telescope (Coughlin et al., 2019b) to obtain photometric data. The KPED is an instrument mounted on a fully robotic telescope and it has been used as a single-band optical detector in the Sloan $g-$ and $r-$ bands and Johnson $UVRI$ filters. The FOV is $4.4' \times 4.4'$ and the pixel size is $0.259''$.

Each candidate scheduled for photometry was observed in the g- and r- band for 300 s. The data taken with KPED are then dark subtracted and flat-field calibrated. After applying astrometric corrections, the instrumental magnitudes were determined using Source Extractor (Bertin & Arnouts, 1996). To calculate the apparent magnitude of the candidate, the zero-point of the field is calibrated using Pan-STARRS 1 (PS1) and Sloan Digital Sky Survey (SDSS) stars in the field as standards. Given the coordinates of the target, an on-the-fly query to PAN-STARRS1 and SDSS retrieves the stars within the field that have a minimum of 4 detections in each band.

Additionally, sources were photometrically followed-up using the Las Cumbres Observatory Global Telescope (LCOGT) (PI: Coughlin, Andreoni) (Brown et al., 2013). We used the 1-m and 2-m telescopes to schedule sets of 300 s in the g-, r-

and i-band. The LCOGT data come already processed and in order to determine the magnitude of the transient, the same PS1/SDSS crossmatching strategy used for KPED was implemented for LCOGT images.

We used the Spectral Energy Distribution Machine (SEDM) on the Palomar 60-inch telescope (Blagorodnova et al., 2018) to acquire g-, r-, and i- band imaging with the Rainbow Camera on SEDM in 300 s exposures. Images were then processed using a python-based pipeline that performs standard photometric reduction techniques and uses an adaptation of `FPipe` (Fremling Automated Pipeline; described in detail in Fremling et al. 2016) for difference imaging. Moreover, we employed the Integral Field Unit (IFU) on SEDM to observe targets brighter than $m_{AB} < 19$ mag. Each observation is reduced and calibrated using the `pysedm` pipeline (Rigault et al., 2019), which applies standard calibrations using standards taken during the observing night. Once the spectra are extracted we use the `SuperNova IDentification`[1] software (`SNID`; Blondin & Tonry, 2007) for spectroscopic classification.

We obtained spectra for six candidates using the Double Spectrograph (DBSP) on the Palomar 200-inch telescope during classical observing runs. The data were taken using the 1.5 arcsec slit and reduced following a custom PyRAF pipeline[2] (Bellm & Sesar, 2016).

The other telescopes used for photometric follow-up are the GROWTH India telescope (GIT) in Hanle, India, the Liverpool Telescope (Steele et al., 2004) in La Palma, Spain, and the Akeno telescope (Kotani et al., 2005) in Japan. The requested

[1]https://people.lam.fr/blondin.stephane/software/SNID/
[2]https://github.com/ebellm/pyraf-dbsp

observations in the g-, r- and i-band varied between 300s and 600s depending on the telescope.

We obtained spectra with the DeVeny Spectrograph at the Lowell Discovery Telescope (LDT) (MacFarlane & Dunham, 2004) and the 10m Keck Low Resolution Imaging Spectrograph (LRIS) (Oke et al., 1995). We reduced these spectra with PyRAF following standard long-slit reduction methods.

We used the Gemini Multi-Object Spectrograph (GMOS-N) mounted on the Gemini-North 8-meter telescope on Mauna Kea to obtain photometric and spectroscopic data (P.I. Ahumada, GN-2021A-Q-102). Our standard photometric epochs consisted of four 180s exposures in r-band to measure the fading rate of the candidates, although we included g-band when the color was relevant. These images were processed using Data Reduction for Astronomy from Gemini Observatory North and South (DRAGONS) (Labrie et al., 2019) and the magnitudes were derived after calibrating against PS1. When necessary and possible, we used PS1 references to subtract the host, using High Order Transform of Psf ANd Template Subtraction (HOTPANTS). For spectroscopic data, our standard was four 650 s exposures using the 1" long-slit and the R400 grating and we used PyRAF standard reduction techniques to reduce the data.

2.4 Candidates

After a given ZTF observation finishes, the resulting image is subtracted to a reference image of the field (Masci et al., 2019; Zackay et al., 2016). The latter

process involves a refined PSF adjustment and a precise image alignment in order to perform the subtraction and determine flux residuals. Any 5σ difference in brightness creates an '*alert*' (Patterson et al., 2019), a package with information describing the transient. The alerts include the magnitude of the transient, proximity to other sources and its previous history of detections among other features. ZTF generates around 10^5 alerts per night of observation, which corresponds to $\sim 10\%$ of the estimated Vera Rubin observatory alert rate. The procedure to reduce the number of alerts from $\sim 10^5$ to a handful of potential optical SGRB counterparts is described in this section.

In general terms, the method involves a rigid online alert filtering scheme that significantly reduces the number of sources based on image quality features. Then, the selection of candidates takes into consideration the physical properties of the transient (i.e. cross-matching with AGN and solar system objects), as well as archival observations from different surveys. After visually inspecting the candidates that passed the preliminary filters, scientists in the collaboration proceed to select sources based on their light-curves, color and other features (i.e. proximity to a potential host, redshift of the host, etc.). This method allows us to recover objects that are later scheduled for further follow-up.

The candidate selection and the follow-up are coordinated via the GROWTH marshal (Kasliwal et al., 2019a) and lately through the open-source platform and alert broker Fritz[3].

[3] `https://github.com/fritz-marshal/fritz`

2.4.1 Detection and filtering

In the searches for the optical counterpart for SGRBs, we query the ZTF data stream using the GROWTH marshal (Kasliwal et al., 2019a), the `Kowalski` infrastructure (Duev et al., 2019)[4], the `NuZTF` pipeline (Stein et al., 2021; Stein et al., 2021) built using `Ampel` (Nordin et al., 2019) [5], and Fritz. The filtering scheme restricted the transients to those with the following properties:

- **Within the skymap:** To ensure the candidates are in the GBM skymap, we implemented a cone search in the GBM region with `Kowalski` and `Ampel`. With the GROWTH marshal approach, we retrieve only the candidates in the fields scheduled for ToO. We note that a more refined analysis on the coordinates of the candidates is done after this automatic selection.

- **Positive subtraction:** After the new image is subtracted, we filter on the sources with a positive residual, thus the ones that have brightened.

- **It is real:** To distinguish sources that are created by ghosts or artifacts in the CCDs, we apply a random-forest model (Mahabal et al., 2019) that was trained with common artifacts found in the ZTF images. We restrict the Real-Bogus score to > 0.25 as it best separates the two populations. For observations that occurred after 2019, we used the improved deep learning real-bogus score `drb` and we set the threshold to sources with `drb` score > 0.15 (Duev et al., 2019).

- **No point source underneath:** To rule out stellar variability we require the

[4] `https://github.com/dmitryduev/kowalski`
[5] `https://github.com/AmpelProject`

transient to have a separation of 3 arcsec from any point source in the PS1 catalog based on Tachibana & Miller (2018).

- **Two detections:** We require a minimum of two detections separated by at least 30 min. This allows us to reject cosmic rays and moving solar system objects.

- **Far from a bright star:** To further avoid ghosts and artifacts, we require the transient to be > 20 arcsec from any bright ($m_{\rm AB} < 15$ mag) star.

- **No previous history:** As we do not expect the optical counterpart of a SGRB to be a periodic variable source, we restrict our selection to only sources that are detected after the event time and have no alerts generated for dates prior to the GRB.

As a reference, this first filtering step reduced the total number of sources to a median of $\sim 0.03\%$ of the original number of alerts. The breakdown of each filter step is shown in Table 2.2. A summary of the numbers of followed-up objects for each trigger is in Table 2.3 and the details of the filtering scheme are described below. More than 3×10^5 alerts were generated during the 9 ToO triggers, while $\sim$80 objects were circulated in the Gamma-ray Coordinates Network (GCN).

GRB	SNR>5	Positive subtraction	Real	Not star underneath	Far from bright star	Two detections	Circulated in GCNs
GRB 180523B	67614	17374	12117	687	669	297	14
GRB 180626C	10602	5040	4967	1582	1377	214	1
GRB 180715B	33064	7611	7515	6941	5509	104	14
GRB 180728B	18488	1450	1428	859	739	51	7
GRB 180913A	25913	12105	12077	6284	5145	372	12
GRB 181126B	40342	30455	30416	22759	21769	340	11
GRB 200514B	20610	10983	10602	4502	4422	1346	14
GRB 200826A	13488	8142	7744	3892	3785	464	14
GRB 201130A	1972	1045	990	647	637	43	0
GRB 210510A	41683	27229	28940	16977	16973	1562	1
Median reduction		50.27%	48.53%	23.05 %	20.66%	1.73%	0.03%

Table 2.2: Summary of the efficiency of our vetting strategy. For each GRB we list the number of alerts that survives after a given filtering step. The first column (SNR>5) shows the total number of alerts in the GRB map. The next column displays the number of alerts that show an increase in flux (Positive subtraction). The 'Real' column shows the number of sources considered as real using either the real-bogus index(RB) or `drb` scores. We set the thresholds to RB>0.25 and `drb`>0.5. The next columns show the number of sources that are not related to a point source, nor close to a bright star, to avoid artifacts. To avoid moving objects, we show the number of sources with two detections separated by at least 30 min. The last column shows the number of sources we circulated as potential candidates for each trigger. For each step, we calculate the median reduction of alerts and list this number at the end of each column.

2.4.2 Scanning and selection

Generally, after the first filter step, the number of transients is reduced to a manageable amount $\sim O(100)$. These candidates are then cross-matched with public all-sky surveys such as *Wide-field Infrared Survey Explorer* (*WISE*; Cutri et al., 2013), Pan-STARRS 1 (PS1; Chambers et al., 2016a), Sloan Digital Sky Survey (SDSS; Ahumada et al., 2020a), the Catalina Real-time Transient Survey (CRTS; Drake et al., 2009), and the Asteroid Terrestrial-impact Last Alert System (ATLAS; Tonry, 2011). We use the *WISE* colors to rule out candidates, as active galactic nuclei (AGN) are located in a particular region in the *WISE* color space (Stern et al., 2012; Wright et al., 2010). If a candidate has a previous detection

in ATLAS or has been reported to the Transient Name Server (TNS) before the event time it is also removed from the candidate list. We additionally crossmatch the position of the candidates with the Minor Planet Center (MPC) to rule out any other slow moving object. We use the PS1 DR2 [6] to query single detections at the location of the transients, and we use this information to rule out sources based on serendipitous previous activity.

One of the most important steps in our selection of transients is the rejection of sources using forced photometry (FP) on ZTF images. For this purpose we run two FP pipelines: ForcePhotZTF[7] (Yao et al., 2019) and the ZTF FP pipeline (Masci et al., 2019). We limit our search to 100 days before the burst and reject sources with consistent $\geq 4\sigma$ detections.

Finally, we manually scan and vet candidates passing those cuts, referring to cutouts of the science images, photometric decay rates, and color evolution information in order to select the most promising candidates (see Fig. 2.11).

Detailed tables with the candidates discovered by ZTF for the SGRB campaign are shown in Table 2.4 and 2.5.

2.4.3 Rejection Criteria

In order to find an optical counterpart, further monitoring of the discovered transients is needed. We have taken spectra for the most promising candidates to classify them. Most of the spectra acquired correspond to bright SNe (as in Fig.

[6] https://catalogs.mast.stsci.edu/panstarrs/
[7] https://github.com/yaoyuhan/ForcePhotZTF

2.12) and a few Cataclysmic Variables (CVs) and an AGN. After the 9 SGRBs follow-ups, we obtained 19 spectra, however none of them exhibited KN features. We have used the 'Deep Learning for the Automated Spectral Classification of Supernovae and Their Hosts' or `dash` (Muthukrishna et al., 2019) to determine the classification of the candidates with SN spectral features. CVs were recognized as they show H features at redshift $z = 0$.

For the sources that do not have spectra available, we monitored their photometric evolution with the facilities described in Section 2.3. Even though the photometric classification cannot be entirely conclusive, there are characteristic features shared between afterglows and KNe. On one side, afterglows are known to follow a power-law decay of the form $F \sim t^{-\alpha}$. On the other hand, most KN models (Bulla, 2019) show evolution faster than 0.3 mag per day (Anand et al. 2021; Andreoni et al. 2020b). As a reference, GW170817 faded over ~ 1 mag over the course of 3 days and other SGRB optical counterparts have shown a rapid magnitude evolution as well (Fong et al., 2015; Rastinejad et al., 2021). The astrophysical events that most contaminated our sample are SNe, but they normally show a monotonic increase in their brightness during their first tens of days, to later decline at a slower rate than expected for afterglows or KNe. Other objects like slow-moving asteroids and flares are less common and can be removed inspecting the images or performing a detailed archival search in ZTF and other surveys.

To illustrate the photometric rejection, we show two transients in Fig. 2.11 with no previous activity in the ZTF archives previous to the SGRB. As their magnitude evolution in both $r-$ and $g-$ band does not pass our threshold, we

conclude that they are not related to the event. This process was repeated for all candidates without spectral information, using all the available photometric data from ZTF and partner telescopes.

2.5 SGRB events

2.5.1 GRB 180523B

The first set of ToO observations of this program was taken 9.1 hours after GRB 180523B (trigger 548793993). We covered $\sim$ 2900 deg^2, which corresponds to 60% of the localization region after accounting for chip gaps in the instrument (Coughlin et al., 2018c). The median 5σ upper limit for an isolated point source in our images was r $>$ 20.3 mag and g $>$ 20.6 mag and after 2 days of observations we arrived at 14 viable candidates that required follow-up. We were able to spectroscopically classify 4 transients as SNe and photometrically follow-up sources with KPED to determine that the magnitude evolution was slower than our threshold. This effort was summarized in Coughlin et al. (2019c) and the list of transients discovered is displayed in Table 2.4.

2.5.2 GRB 180626C

The SGRB GRB 180626C (*Fermi* trigger 551697835) came in the middle of the night at Palomar. We started observing after 1.5 hours and were able to cover 275 deg^2 of the GBM region. The localization, and hence the observing plan, was later updated as the region of interest was now the overlap between the *Fermi* and

the newly arrived InterPlanetary Network (IPN)[8] map. The observations covered finally 230 deg^2, corresponding to 87% of the intersecting region. After two nights of observations, with a median 5-sigma upper limit of r $>$ 21.1 mag and g $>$ 21.0 mag, only one candidate was found to have no previous history of evolution and be spatially coincident with the SGRB (Coughlin et al., 2018a).

The transient ZTF18aauebur was a rapidly evolving transient that faded from g = 18.4 to g = 20.5 in 1.92 days. This rapid evolution continued during the following months, fluctuating between r $\sim$ 18 mag and r $\sim$ 19 mag. It was interpreted as a stellar flare, as it is located close to the Galactic plane and there is an underlying source in the PS1 and *Galaxy Evolution Explorer (GALEX)* (Morrissey et al., 2007) archive. Additionally, its SEDM spectrum showed a featureless blue spectrum and Hα absorption features at redshift $z = 0$, so it is an unrelated Galactic source. The rest of the candidates can be found in Table 2.4.

2.5.3 GRB 180715B

We triggered ToO observations to follow-up GRB 180715B (trigger 553369644) 10.3 hours after the GBM detection. We managed to observe $\sim$ 36% of the localization region which translates into 254 deg^2. The median limiting magnitude for these observations was r $>$ 21.4 mag and g $>$ 21.3 mag.

During this campaign, we discovered 14 new transients (Cenko et al., 2018) in the region of interest. We were able to spectroscopically classify 2 candidates using instruments at the robotic Palomar 60 inch telescope (P60) and Palomar 200 inch

[8] `http://www.ssl.berkeley.edu/ipn3/index.html`

Hale telescope (P200). The SEDM spectrum of ZTF18aauhpyb showed a stellar source with Balmer features at redshift $z = 0$ and a blue continuum. The DBSP spectrum of ZTF18abhbfqf was best fitted by a SN Ia-91T. We show the rejection criteria used to rule-out associations with the SGRB in Table 2.4. Generally, most candidates showed a slow magnitude evolution. Furthermore, three candidates (ZTF18abhhjyd, ZTF18abhbfoi and ZTF18abhawjn) matched with an AGN in the Milliquas (Flesch, 2019) catalog. A summary of the candidates can be found in Table 2.4.

2.5.4 GRB 180728B

The ToO observations of GRB 180728B (trigger 554505003) started ~ 8 hours after the *Fermi* alert, however, it did not cover the later updated IPN localization. The following night and 31 hours after the *Fermi* detection we managed to observe the joint GBM and IPN localization, covering 334 deg^2 which is $\sim 76\%$ of the error region. The median upper limits for the scheduled observations were r > 18.7 mag and g > 20.0 mag (Coughlin et al., 2018a). As a result of these observations, no new transients were found.

2.5.5 GRB 180913A

We triggered ToO observations with ZTF to follow-up the *Fermi* event GRB 180913A (trigger 558557292) about ~ 8 hours after the GBM detection. The first night of observations covered 546 deg^2. The schedule was adjusted as the localiza-

tion improved once the IPN map was available. During the second night we covered 53% of the localization, translated into 403 deg^2. After a third night of observations, 12 transients were discovered and circulated in Coughlin et al. (2018b). The median upper limits for this set of observations were r $>$ 21.9 and g $>$ 22.1 mag.

We obtained a spectrum of ZTF18abvzfgy with LDT, a fast rising transient ($\Delta m/\Delta t \sim -0.2$ mag per day) in the outskirts of a potential host galaxy. It was classified as a SN Ic at a redshift of $z = 0.04$. The rest of the transients were follow-up photometrically with KPED and LCO, but generally showed a flat evolution. The candidate ZTF18abvzsld had previous PS1 detections, thus ruling it out as a SGRB counterpart. The rest of the candidates are listed in Table 2.4.

2.5.6 GRB 181126B

The last SGRB we followed-up before the start of the 2019 O3 LIGO/Virgo observing run was of the *Fermi*-GBM event GRB 181126B (trigger 564897175). As this event came during the night at the ZTF site, the observations started $\sim$ 1.3 hours after the *Fermi* alert, and we were able to cover 1400 deg^2, close to 66% of the GBM localization. After the IPN localization was available the next day, the observations were adjusted and we used ZTF to cover 709 deg^2, or $\sim$ 76% of the overlapped region. The mean limiting magnitude of the observations was r $>$ 20.8 mag (Ahumada et al., 2018). After processing the data, we discovered 11 new optical transients timely and spatially coincident with the SGRB event. We took spectra of 7 of them with the Keck LRIS, discovering 6 SNe (ZTF18acrkkpc, ZTF18aadwfrc,

ZTF18acrfond, ZTF18acrfymv, ZTF18acptgzz, ZTF18acrewzd) and 1 stellar flare (ZTF18acrkcxa). All of the candidates are listed in Table 2.5, and none of them showed rapid evolution.

2.5.7 GRB 200514B

We resumed the search for SGRB counterparts with ZTF once LIGO/Virgo finished O3. On 2020-05-14 we used ZTF to cover over 519.3 deg^2 of the error region of GRB 200514B (trigger 611140062). This corresponds to $\sim$ 50% of the error region. After the first night of observations, 7 candidates passed our filters and were later circulated in Ahumada et al. (2020). The observations during the following night resulted in 7 additional candidates (Reusch et al., 2020a). The depth of these observations reached 22.4 and 22.2 mag in the $g-$ and $r-$band respectively. After IPN released their analysis (Svinkin et al., 2020), 9 of our candidates remained in the localization region. Our follow-up with ZTF and LCO showed that none of these transients evolved as fast as expected for a GRB afterglow (see Table 2.5).

2.5.8 GRB 200826A

This burst is discussed extensively in Chapter 3, as well as in other works (Rhodes et al., 2021; Rossi et al., 2021; Zhang et al., 2021). It was the only short duration GRB in our campaign with an optical counterpart association. However, despite its short duration (T_{90} = 1.13s), it showed a photometric bump in the i-band that could only be explained by an underlying SN (Ahumada et al., 2020c).

This makes GRB 200826A the shortest-duration long gamma-ray burst (LGRB), presented in detail in Ahumada et al. 2021.

2.5.9 GRB 201130A

The ZTF trigger on GRB 201130A reached a depth of r = 20.5 mag in the first night of observations after covering 75% of the credible region. No optical transient passed all our filtering criteria (Reusch et al., 2020b).

2.5.10 GRB 210510A

We triggered optical observations on GRB 210510A (trigger 642367205) roughly 10 hrs after the burst. The second night of observations helped with vetting candidates based on their photometric evolution, at least a 0.3 mag per day decay rate is expected for afterglows and KNe. The only candidate that passed our filtering criteria was ZTF21abaytuk (Anand et al., 2021), however its Keck LRIS spectrum showed Hβ, [O II], and [O III] emission features and Mg II absorption lines at redshift of $z = 0.89$ (see Table 2.5 and Fig. 2.12). Its spectrum, summed with its *WISE* colors, are consistent with an AGN origin.

2.6 ZTF upper limits

It is possible to compare the search sensitivity, both in terms of depth and timescale, to the expected afterglow and kilonova light-curves. In Fig. 2.13, the median limits for ZTF observations are shown with respect to known *Swift* SGRB

afterglows with measured redshift from Fong et al. (2015). The yellow light-curve corresponds to GW170817 (Abbott et al., 2017d) and the red line is the same GW170817 light-curve scaled to a distance of 200 Mpc (see below). Along with GW170817, we show a collection of KN light-curves from a BNS grid (Bulla, 2019; Dietrich et al., 2020) scaled to 200 Mpc. The regions of the light-curve space explored by each ZTF trigger are represented as grey rectangles and the more opaque region corresponds to their intersection. Even though ZTF has the ability to detect a GW170817-like event and most of the KN lightcurves, most of the SGRB afterglows observed in the past are below the median sensitivity of the telescope. On the other hand, the counterpart of the GRB 200826A would have been detected in six of our searches, even though it is on the less energetic part of the LGRB distribution. When scaled to 200 Mpc, the GW170817 light-curve overlaps with the region of five of our searches, suggesting that the combination of depth and rapid coverage of the regions could allow us to detect an GW170817-like event. The searches that do not overlap with the scaled GW170817 have either fainter median magnitude upper limits (< 20 mag) or late starting times (> 1 day).

We used the redshifts of the SGRBs optical counterparts to determine their absolute magnitudes, which is plotted in Fig. 2.15, along with GRB 200826A and GW170817. In order to compare with the ZTF searches and constrain the observations, the median ZTF limits were scaled to a fiducial distance of 200 Mpc, the O3 LIGO/Virgo detection horizon (Abbott et al., 2018) for binary neutron star (BNS) mergers. The range of 200 Mpc is coincidentally approximately the furthest distance as to which ZTF can detect a GW170817-like event based on the median limiting

magnitudes of this experiment. Moreover, the ZTF region covers most of the KNe models (blue shaded region) scaled to 200 Mpc. In contrast to Fig. 2.13, most of the SGRB optical afterglows fall in the region explored by ZTF. Therefore, if any similar events happened within 200 Mpc, the current ZTF ToO depth plus a rapid trigger of the observations should suffice to ensure coverage in the light-curve space. Previous studies (Dichiara et al., 2020) have come to the conclusion that the low rate of local SGRB is responsible for the lack of detection GW170817-like transients. In fact, the probability that one of the SGRBs in our sample is within 200 Mpc is 0.3, given the rate derived in Dichiara et al. (2020) of 1.3 SGRB within 200 Mpc per year, assuming an average of 40 SGRBs per year. In Fig. 2.15 we show the same SGRB absolute magnitude light-curves, but in this case we compared them to the ZTF limits scaled to the median redshift of $z = 0.47$ from Fong et al. (2015). The ZTF search is still sensitive to SGRB afterglows at these distances within the first day after the GRB event.

2.7 Efficiency and joint probability of non-detection

In this section we determine the empirical detection efficiency for each of our searches, and use these efficiencies to calculate the likelihood of detecting a SGRB afterglow in our ToO campaign. With this approach we are able to set limits on the ZTF's ability of detecting SGRB afterglows as a function of the redshift of the SGRB. To accomplish this, we take each GRB we followed-up and inject afterglow light-curves in the GRB maps at different redshifts. We derive efficiencies using

the ZTF observing logs, since these logs contain the coordinates of each successful ZTF pointing and the limiting magnitude of each exposure. This already takes into consideration weather and other technical problems with the survey. In this section we describe the computational tools used in this endeavor and the results derived from these simulations.

We use `simsurvey` (Feindt et al., 2019) to inject afterglow-like light-curves into the GBM skymaps. We distributed the afterglows according to the GBM probability maps and within the 90% credible region of each skymap. We slice the volume into seven equal redshift bins, from $z = 0.01$ to $z = 2.1$, and injected 7000 sources in each slice. For each injected transient, `simsurvey` employs light-curve models to derive the magnitude of the source at different times (see below for the models used). `simsurvey` uses the ZTF logs to determine if the simulated source was in an observed ZTF field and whether the transient would have been detected given the upper limits of that ZTF field.

One of the driving features of an afterglow model is its isotropic-equivalent energy, E_{iso}, as it sets the luminosity of the burst and hence its magnitude and light-curve. The information provided by the *Fermi*-GBM gamma-ray detections does not give insights on the distance to the event or the energies associated with the SGRBs. For this reason, and to get a sense on the E_{iso} associated with each burst we take two approaches: using the gamma-ray energy peak, E_{peak}, and the average kinetic isotropic energy, $E_{K,iso}$ to estimate E_{iso}. *First*, we assume that our population of SGRBs follows the isotropic energy (E_{iso}) - rest-frame peak energy (E_z, p) relationship (see Eq. 2.1), postulated in Equation 2 of Tsutsui et al. (2013).

This relationship requires the peak energies of the bursts, E_p, which can be obtained by fitting a Band model (Band et al., 1993) to the gamma-ray emission over the duration of the burst. The results of this modelling are usually listed in the public GBM catalog (von Kienlin et al., 2020) and online[9]. The compilation of E_p for our SGRBs sample is listed in Table 2.1.

$$E_{iso} = 10^{52.4\pm0.2}\ erg\ \left(\frac{E_{z,p}}{774.5\ keV}\right)^{1.6\pm0.3} \tag{2.1}$$

The energy derived with this equation is related to the prompt emission phase of the GRB, and not to the burst kinetic energy remaining during the afterglow phase. Lloyd-Ronning & Zhang 2004 defines

$$\zeta \equiv E_{iso}/(E_k + E_{iso})$$

as parameter that related the gamma-ray energy of the burst, E_{iso}, and the kinetic energy powering the afterglow, E_k. By modeling X-ray data, they find that ζ varies from 0.1 to 0.99, reflecting an order of magnitude variation. The median $\zeta \sim 0.7$ reflects a ratio of $E_k/E_{iso} \sim 2.4$. However, for simplicity, in this work we assumed a one-to-one relationship between E_k and E_{iso}.

We additionally use the average kinetic isotropic energy, $E_{K,iso}$, presented in Fong et al. (2015) as a representative value for E_{iso}. Particularly, for this *second* E_{iso} approach, we assume $E_{K,iso} \sim E_{iso} = 2.9 \times 10^{51}$ ergs.

We used the python module `afterglowpy` (Ryan et al., 2020) to generate after-

[9] `https://heasarc.gsfc.nasa.gov/W3Browse/fermi/fermigbrst.html`

glow light-curve templates. Due to the nature of the relativistic jet, we constrained the viewing angle to $\theta < 20°$. We assume a circumburst density of $5.2 \times 10^{-3}\ cm^{-3}$, chose a Gaussian jet, and fixed other `afterglowpy` parameters to standard values: the electron energy distribution index $p = 2.43$, as well as the fraction of shock energy imparted to electrons, $\epsilon_E = 0.1$, and to the magnetic field, $\epsilon_B = 0.01$. For E_{iso} we used the relation in Eq. 2.1 and the mean $E_{K,iso}$ mentioned in the paragraph above. Additionally for E_{iso} as a function of $E_{z,p}$, we took the gamma-ray $E_{z,p} = E_p(1+z)$, with the redshift varying for each simulated source.

We feed `simsurvey` light-curves generated with `afterglowpy` assuming the two separate E_{iso} distributions described above. We note that these two approaches are based on conclusions drawn from *Swift* bursts, since the bulk of the SGRB afterglow knowledge comes from *Swift* bursts. We calculated the efficiency as a function of redshift by taking the ratio of sources detected *twice* over the number of generated sources within a redshift volume. We require two detections as our ToO strategy relies on at least two data points.

The efficiencies vary depending on a few factors. The total coverage and the limiting magnitude of the observations limit the maximum efficiency, which then decays depending on the associated E_{iso}. For larger energies, the decay is smoother. In Fig. 2.16, we show the efficiencies for the 9 GRBs that had no discovered counterpart. We exclude GRB 200826A as the energies used to model the afterglow follow the SGRB energy distribution, while GRB 200826A was proven to be part of the LGRB population. The energies derived from the Tsutsui et al. (2013) relationship are larger than the mean $E_{K,iso}$ derived from Fong et al. (2015).

This increases the efficiencies at larger redshifts assuming the Tsutsui et al. (2013) relationship, as the transients are intrinsically more energetic.

For both of the energies used, we calculate the joint probability of non-detection by taking the product of the SGRB ToO efficiencies as a function of redshift. Similar to the analysis in Kasliwal et al. (2020b), we define

$$(1 - CL) = \prod_{i=0}^{N} (1 - p_i) \tag{2.1}$$

with CL as the credible level and p_i the efficiency of the ith burst as a function of redshift. We show in the bottom panel of Fig. 2.17 the result for the afterglows with energies following Tsutsui et al. (2013) (blue) and Fong et al. (2015) (orange). The lower energies associated with Fong et al. (2015) afterglows only allow us to probe the space up to $z = 0.16$, considering a $CL = 0.9$, while SGRBs with energies following the $E_{iso} - E_{z,p}$ relationship can be probed as far as $z = 0.4$. To look into the prospects of the SGRB ToO campaign, we model a scenario with 21 additional ToO campaigns, each with a median efficiency based on the results presented here. These results are shown as dashed lines in Fig. 2.17, and show that for $E_{iso} \sim E_{K,iso}$, the improvement after thirty ToOs can only expand our searches (i.e. $CL = 0.9$) up to $z = 0.2$, while if the GRBs follow the $E_{iso} - E_{z,p}$ relationship, our horizon expands to $z = 0.7$.

Finally, when comparing our limits to the redshift distribution of SGRB afterglows found in the literature (Fong et al., 2015) (green histogram in Fig. 2.17), our searches show that we are probing (and could probe) volumes that contain 10-40%

of the observed afterglows, depending on the E_{iso} assumption.

2.8 Proposed follow-up strategy

The current ToO strategy aims for two consecutive exposures in two different filters, prioritizing the color of the source as the main avenue to discriminate between sources. This helps confirming the nature of the transient as an extragalactic source. In some cases, it can lead to problems as the source might not be detected at shorter wavelengths, due to either the extinction along the line of sight or its intrinsically fainter brightness. If there is no second detection at shorter wavelengths, there is the risk of ignoring a potential counterpart as a single detection can be confused as a slow moving object or an artifact. The standard strategy considers a second night of ZTF observations in the same two filters, to measure the magnitude and color evolution. However, a number of sources did not have a second detection in the same filter after the second night, impeding the measurement of the decline rate. For these two reasons, for afterglow searches with ZTF (and possibly other instruments with similar limiting magnitudes), it is more informative to observe the region at least twice in the same filter during the first night. By separating the two same-filter epochs by at least $2\sigma \times 24/\alpha$, where σ is the typical error of the observations and α is the power-law index of the afterglow decline, we can possibly measure the decay rate of sources, or at least set a lower limit for α. For ZTF, two epochs separated by 6 hours would suffice for afterglows with a typical $\alpha \sim 1$, assuming $\sigma = 0.12$.

This scenario is unlikely to happen often, as it requires that the region is visible during the entire night and that the night is long enough to allow for two visits separated by a number of hours. In any case, the standard ToO strategy for the second night of observation (two visits in two different filters) should help determine the color and magnitude evolution.

For the third day of follow-up, there will be two kinds of candidates: (a) confirmed fast fading transients, and (b) transients with unconstrained evolution, that likely only have data for the first night. For (a) it is important to get spectra as soon as possible before the transients fade below the spectroscopic limits. Ideally, observations in other wavelengths should be triggered to cement the classification and begin the characterization of the transient. For candidates in situation (b), the fast evolution of the transients requires the use of larger facilities. From our experience, this is feasible as only a handful of candidates will fall in this category. In both cases, (a) and (b), photometric follow-up using facilities different than ZTF are needed, as any afterglow detected by ZTF will likely not be detectable three days after the burst. In Fig. 2.18 we show the magnitude distribution of all the transients that `simsurvey` detected, independent of redshift, as a function of how many days passed after the burst. This figure illustrates the need for other telescopes to monitor the evolution of the transient, as for example, only $\sim$30% of the transients that we can detect with ZTF will be brighter than $r > 22$ mag. Additionally, Fig. 2.18 shows that spectroscopy of the sources becomes harder after day 2, as only 20% of the detected transients will be brighter than $r = 21.5$ mag.

Since spectroscopic data will be challenging to acquire for faint sources, the

panchromatic follow-up, from radio to x-rays, will help to confirm the classification of the transient.

2.9 Conclusions

During a period of ∼2 years, a systematic, extended and deep search for the optical counterparts to *Fermi*-GBM SGRBs has been performed employing the Zwicky Transient Facility. The ZTF observations of 10 events followed-up are listed in Table 2.3 and no optical counterpart has yet been associated to a compact binary coalescence. However, our ToO strategy led to the discovery of the optical counterpart to GRB 200826A, which was ultimately revealed as the shortest-duration LGRB found to date (Ahumada et al., 2021).

This experiment complements previous studies (Coughlin et al., 2019c; Singer et al., 2013, 2015), and demonstrates the feasibility of studying the large sky areas derived from *Fermi* GBM by exploiting the wide field of view of ZTF. The average coverage was $\sim 60\%$ of the localization regions, corresponding to ~ 950 deg^2. The average amount of alerts in the targeted regions of the sky was over 20000, and we were able to reduce this figure to no more than 20 candidates per trigger. Thanks to the high cadence of ZTF we were able to achieve a median reduction in alerts of 0.03%. The effectiveness of the filtering criteria is comparable with the median reduction reached in Singer et al. (2015), even when the areas covered are almost orders of magnitude larger. The iPTF search for the optical counterparts to the long gamma-ray burst GRB 130702A covered 71 deg^2 and yielded 43 candidates (Singer

et al., 2013).

This campaign has utilized ZTF capabilities to rapidly follow-up SGRB trigger, which has allowed us to explore the magnitude space and set constraints on SGRB events. The average depth for ZTF 300s exposures is $r \sim 20.8$ which has allowed us to look for SGRB afterglows and GW170817-like KNe. From Fig. 2.18, it can be seen that future follow-ups would benefit both from a more rapid response and longer exposures.

By using computational tools like `afterglowpy` and `simsurvey`, we have quantified the efficiency of our ToO triggers. The ZTF efficiency drops quickly as the transient is located at further distances, and the magnitude limits only allow for detections up to $z = 0.4$, for energies following the Tsutsui et al. (2013) relation and $z = 0.16$ for bursts with energies equal to the mean E_{iso} found by Fong et al. (2015), for a $CL = 0.9$. Furthermore, when repeating the experiment 21 times (to complete 30 ToOs) and assuming a median efficiency p_{med} for each new event, the horizons of our searches increase to $z = 0.2$ and 0.72 respectively.

Additionally, our simulations show that ZTF is no longer effective at following-up afterglows after three days following the burst. The fast fading nature of these transients requires deeper observations, and spectroscopic and panchromatic observations are helpful to reveal the nature of the candidates. Ideally, at least two observations in the same filter should be taken during the first night of observation, as afterglows and KNe fade extremely rapidly and they might not be observable 48 hrs after the burst. With this strategy we can hope to find another counterpart.

2.10 Acknowledgements

Based on observations obtained with the Samuel Oschin Telescope 48-inch and the 60-inch Telescope at the Palomar Observatory as part of the Zwicky Transient Facility project. ZTF is supported by the National Science Foundation under Grants No. AST-1440341 and AST-2034437 and a collaboration including current partners Caltech, IPAC, the Weizmann Institute for Science, the Oskar Klein Center at Stockholm University, the University of Maryland, Deutsches Elektronen-Synchrotron and Humboldt University, the TANGO Consortium of Taiwan, the University of Wisconsin at Milwaukee, Trinity College Dublin, Lawrence Livermore National Laboratories, IN2P3, University of Warwick, Ruhr University Bochum, Northwestern University and former partners the University of Washington, Los Alamos National Laboratories, and Lawrence Berkeley National Laboratories. Operations are conducted by COO, IPAC, and UW. This work was supported by the GROWTH (Global Relay of Observatories Watching Transients Happen) project funded by the National Science Foundation under PIRE Grant No 1545949. GROWTH is a collaborative project among California Institute of Technology (USA), University of Maryland College Park (USA), University of Wisconsin Milwaukee (USA), Texas Tech University (USA), San Diego State University (USA), University of Washington (USA), Los Alamos National Laboratory (USA), Tokyo Institute of Technology (Japan), National Central University (Taiwan), Indian Institute of Astrophysics (India), Indian Institute of Technology Bombay (India), Weizmann Institute of Science (Israel), The Oskar Klein Centre at Stockholm University (Sweden), Humboldt University

(Germany), Liverpool John Moores University (UK) and University of Sydney (Australia).

The material is based on work supported by NASA under award No. 80GSFC17M0002. Based on observations obtained at the international Gemini Observatory, a program of NSF's NOIRLab, which is managed by the Association of Universities for Research in Astronomy (AURA) under a cooperative agreement with the National Science Foundation on behalf of the Gemini Observatory partnership: the National Science Foundation (United States), National Research Council (Canada), Agencia Nacional de Investigación y Desarrollo (Chile), Ministerio de Ciencia, Tecnología e Innovación (Argentina), Ministério da Ciência, Tecnologia, Inovações e Comunicações (Brazil), and Korea Astronomy and Space Science Institute (Republic of Korea). The observations were obtained as part of Gemini Director's Discretionary Program GN-2021A-Q-102. The Gemini data were processed using DRAGONS (Data Reduction for Astronomy from Gemini Observatory North and South). This work was enabled by observations made from the Gemini North telescope, located within the Maunakea Science Reserve and adjacent to the summit of Maunakea. We are grateful for the privilege of observing the Universe from a place that is unique in both its astronomical quality and its cultural significance. The ZTF forced-photometry service was funded under the Heising-Simons Foundation grant No. 12540303 (PI: Graham). These results also made use of Lowell Observatory's Lowell Discovery Telescope (LDT), formerly the Discovery Channel Telescope. Lowell operates the LDT in partnership with Boston University, Northern Arizona University, the University of Maryland and the University of Toledo. Partial support

of the LDT was provided by Discovery Communications. LMI was built by Lowell Observatory using funds from the National Science Foundation (AST-1005313). The Liverpool Telescope is operated on the island of La Palma by Liverpool John Moores University in the Spanish Observatorio del Roque de los Muchachos of the Instituto de Astrofisica de Canarias with financial support from the UK Science and Technology Facilities Council. SED Machine is based upon work supported by the National Science Foundation under Grant No. 1106171. GIT is a 70-cm telescope with a 0.7 field of view, set up by the Indian Institute of Astrophysics (IIA) and the Indian Institute of Technology Bombay (IITB) with funding from DST-SERB and IUSSTF. It is located at the Indian Astronomical Observatory, operated by IIA. We acknowledge funding by the IITB alumni batch of 1994, which partially supports operations of the telescope. Telescope technical details are available at `https://sites.google.com/view/growthindia/`.

GRB	Area covered	C.R. covered	Time delay in triggering ZTF	Exposure time (sequence)	$r-$band 5σ limit	Objects followed-up
GRB 180523B	2900 deg^2	60%	9.1h	60s(rgr), 90s(rgr)	r > 20.3 mag	14
GRB 180626C	275 deg^2	87%	1.5h	120s(rgr), 240s(grg)	r > 20.9 mag	1
GRB 180715B	254 deg^2	37%	10.3h	180s(rgr), 240s(rg)	r > 21.4 mag	14
GRB 180728B	334 deg^2	76%	31h	180s(rgr), 180s(rgr)	r > 18.7 mag	7
GRB 180913A	546 deg^2	53%	8.3h	180s(grg), 300s(grg)	r > 22.2 mag	12
GRB 181126B	1400 deg^2	66%	1.3h	180s(rr), 300s (r)	r > 20.5 mag	11
GRB 200514B	519 deg^2	49%	0.9h	300s(gr)	r > 22.2 mag	14
GRB 201130A	400 deg^2	75%	7h	300s(grg),300s(gr)	r > 20.3 mag	0
GRB 210510A	1105 deg^2	84%	10h	180(gr),240(r)	r > 22.1 mag	1

Table 2.3: Summary of the ZTF ToO triggers. We list the area covered with ZTF, as well as the corresponding credible region (C.R.) of the GBM map. We shown our time delay between the burst and the start of ZTF observations. For each trigger, we list the exposure time for night 1 and nigth 2, along with the filter sequence in parenthesis. The last two columns show the median $r-$band 5σ limit and the number of objects followed-up with other facilities.

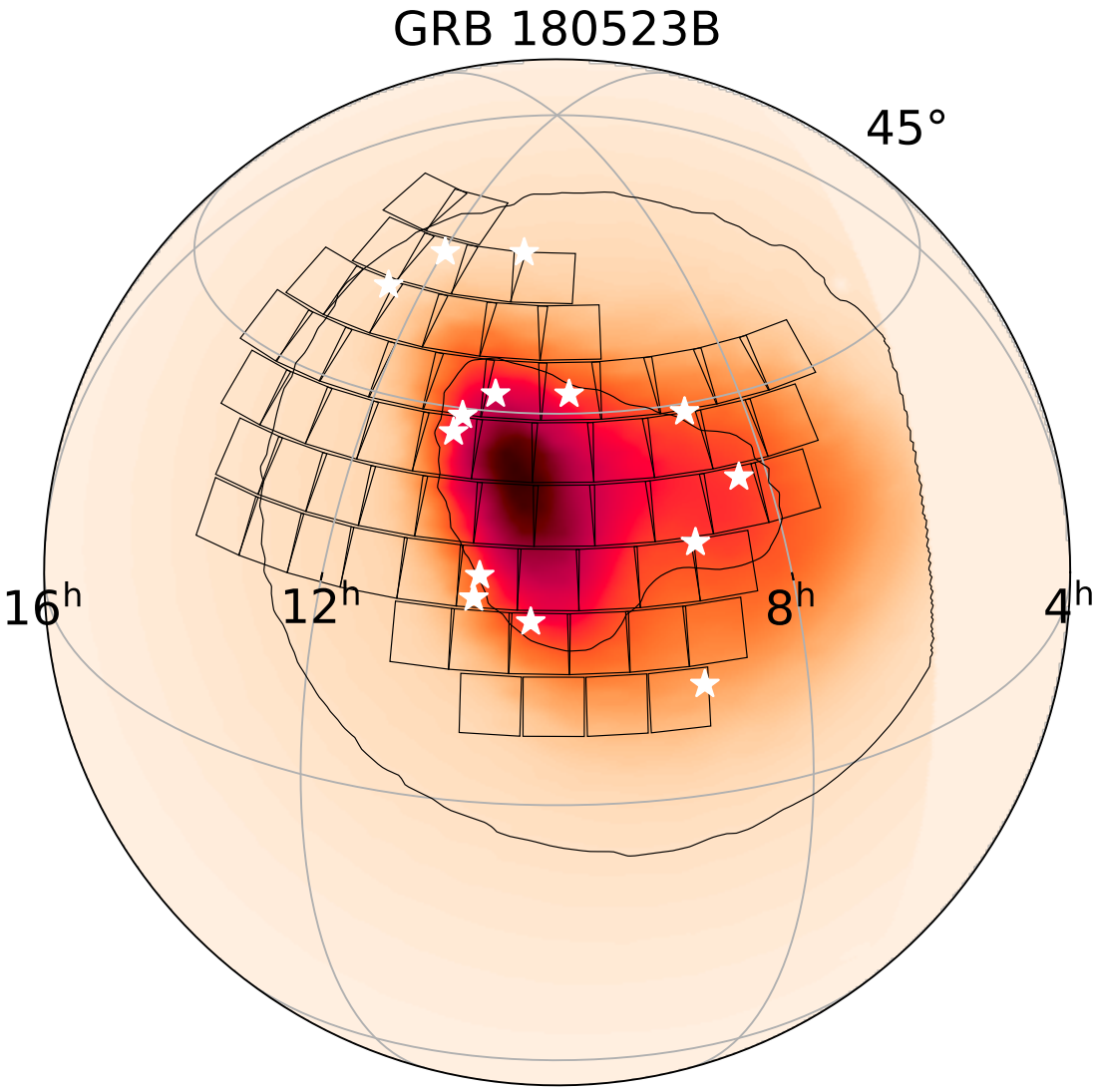

Figure 2.2: Coverage of the ZTF trigger on GRB 180523 and its *Fermi* GBM localization region. The ≈ 47 deg^2 ZTF tiles are shown as black quadrilaterals, and the 50% and 90% credible regions are shown as black contours and the sources discovered during the ZTF trigger as white stars (details in Section 2.5). The grid shows the Right Ascension in hours and the Declination in degrees.

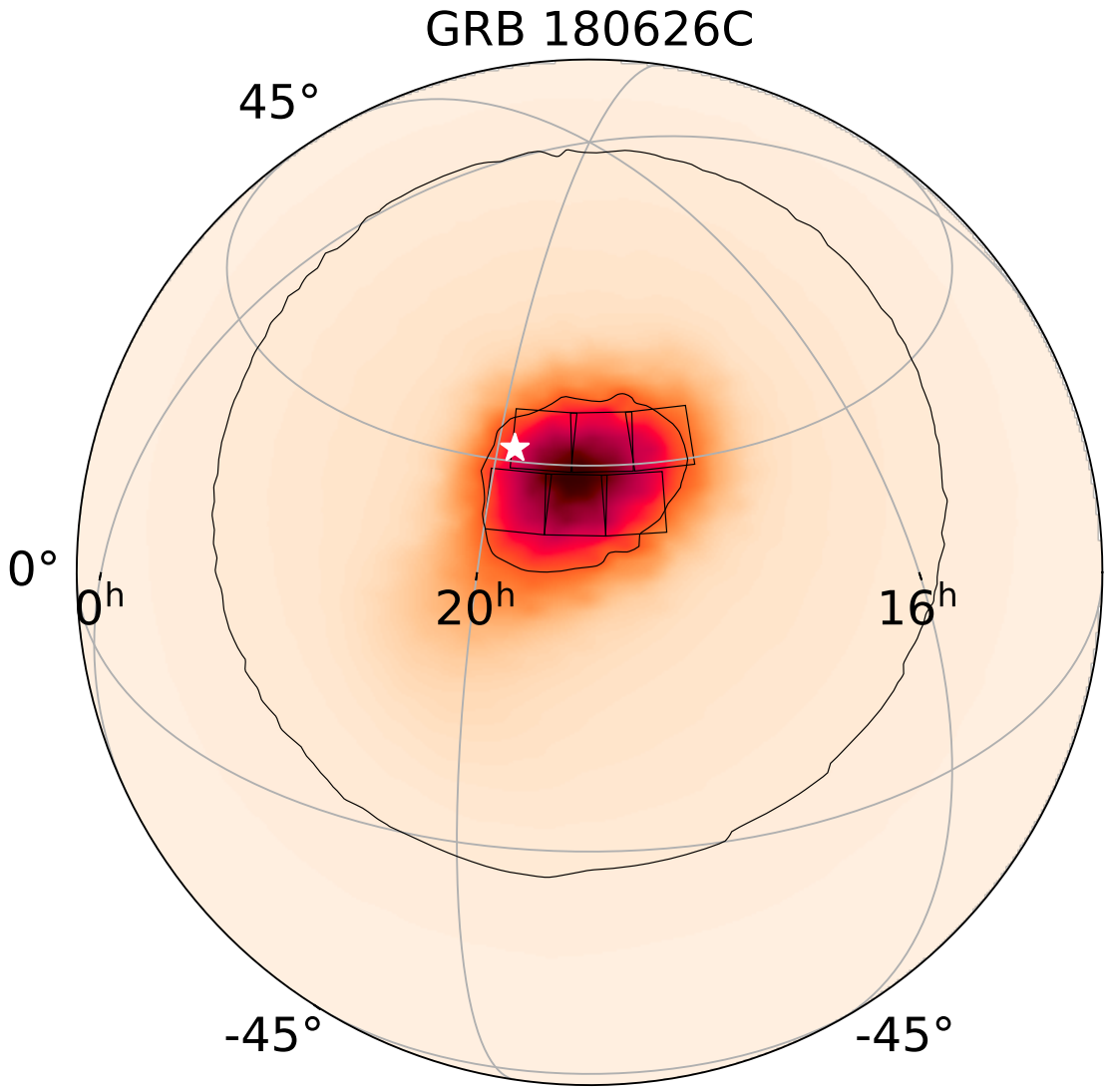

Figure 2.3: Coverage of the ZTF trigger on GRB 180626 and its *Fermi* GBM localization region. The ≈ 47 deg^2 ZTF tiles are shown as black quadrilaterals, and the 50% and 90% credible regions are shown as black contours and the sources discovered during the ZTF trigger as white stars (details in Section 2.5). The grid shows the Right Ascension in hours and the Declination in degrees.

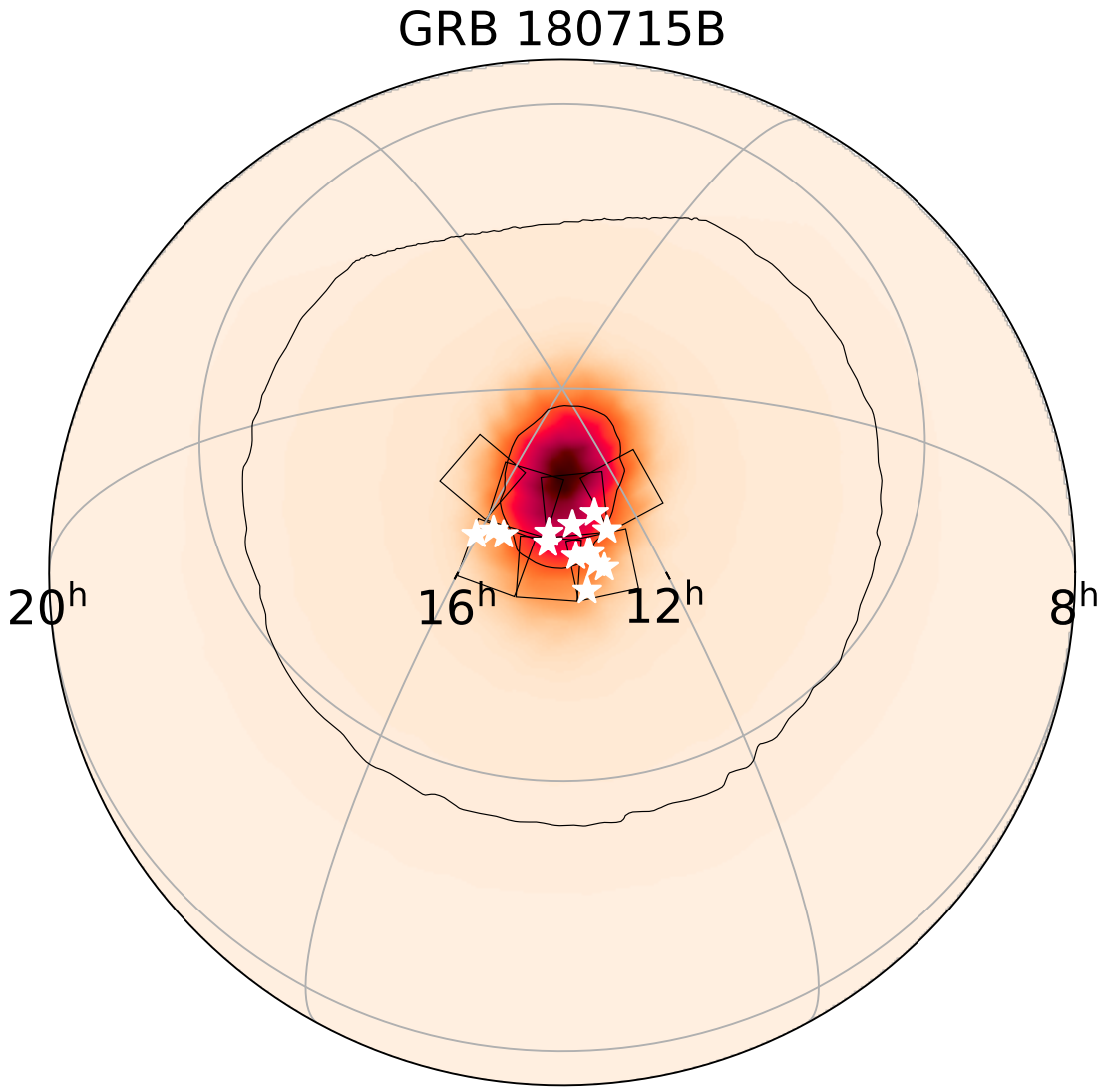

Figure 2.4: Coverage of the ZTF trigger on GRB 180715 and its *Fermi* GBM localization region. The ≈ 47 deg^2 ZTF tiles are shown as black quadrilaterals, and the 50% and 90% credible regions are shown as black contours and the sources discovered during the ZTF trigger as white stars (details in Section 2.5). The grid shows the Right Ascension in hours and the Declination in degrees.

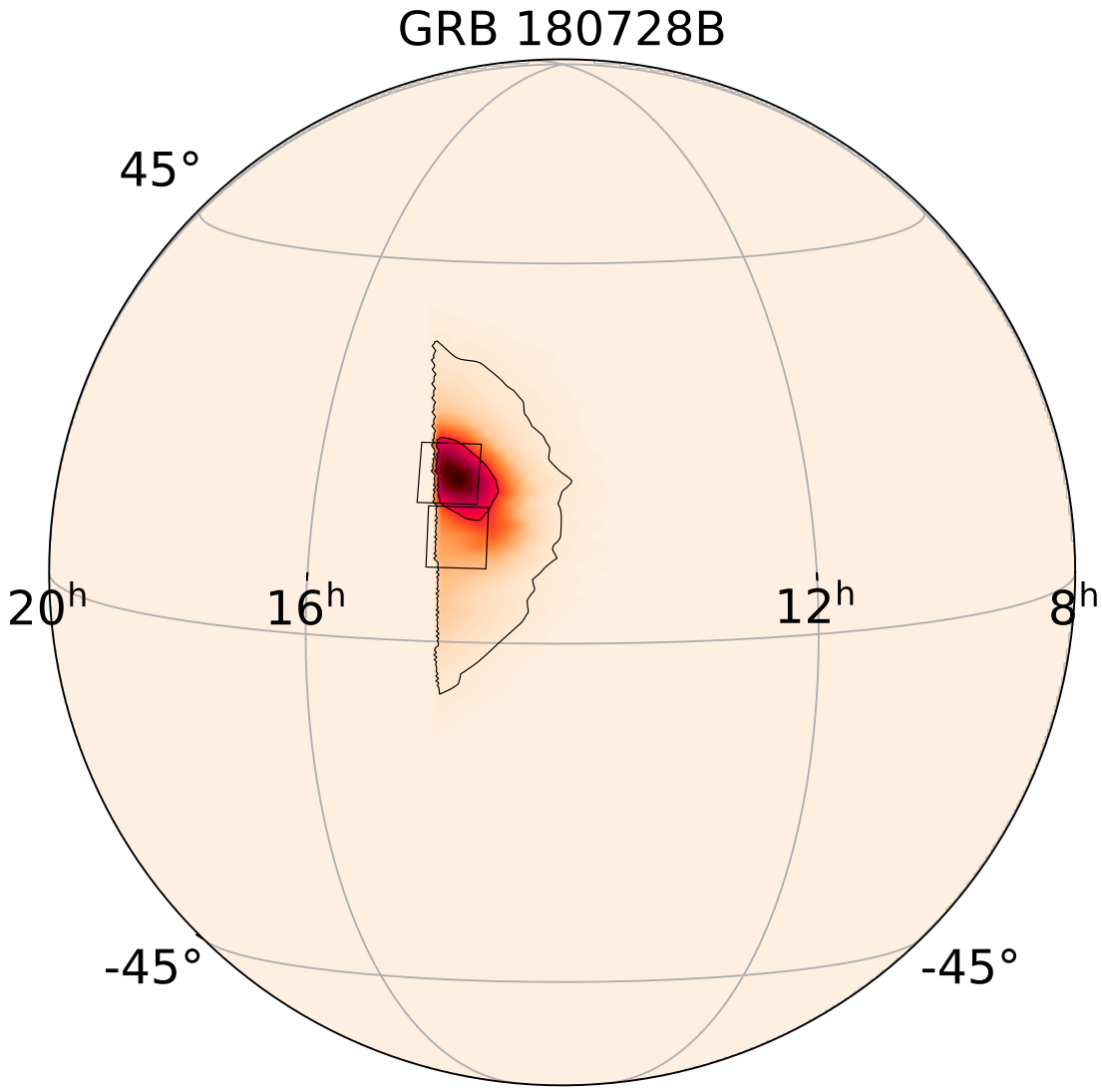

Figure 2.5: Coverage of the ZTF trigger on GRB 180728 and its *Fermi* GBM localization region. The $\approx$ 47 deg^2 ZTF tiles are shown as black quadrilaterals, and the 50% and 90% credible regions are shown as black contours and the sources discovered during the ZTF trigger as white stars (details in Section 2.5). The grid shows the Right Ascension in hours and the Declination in degrees.

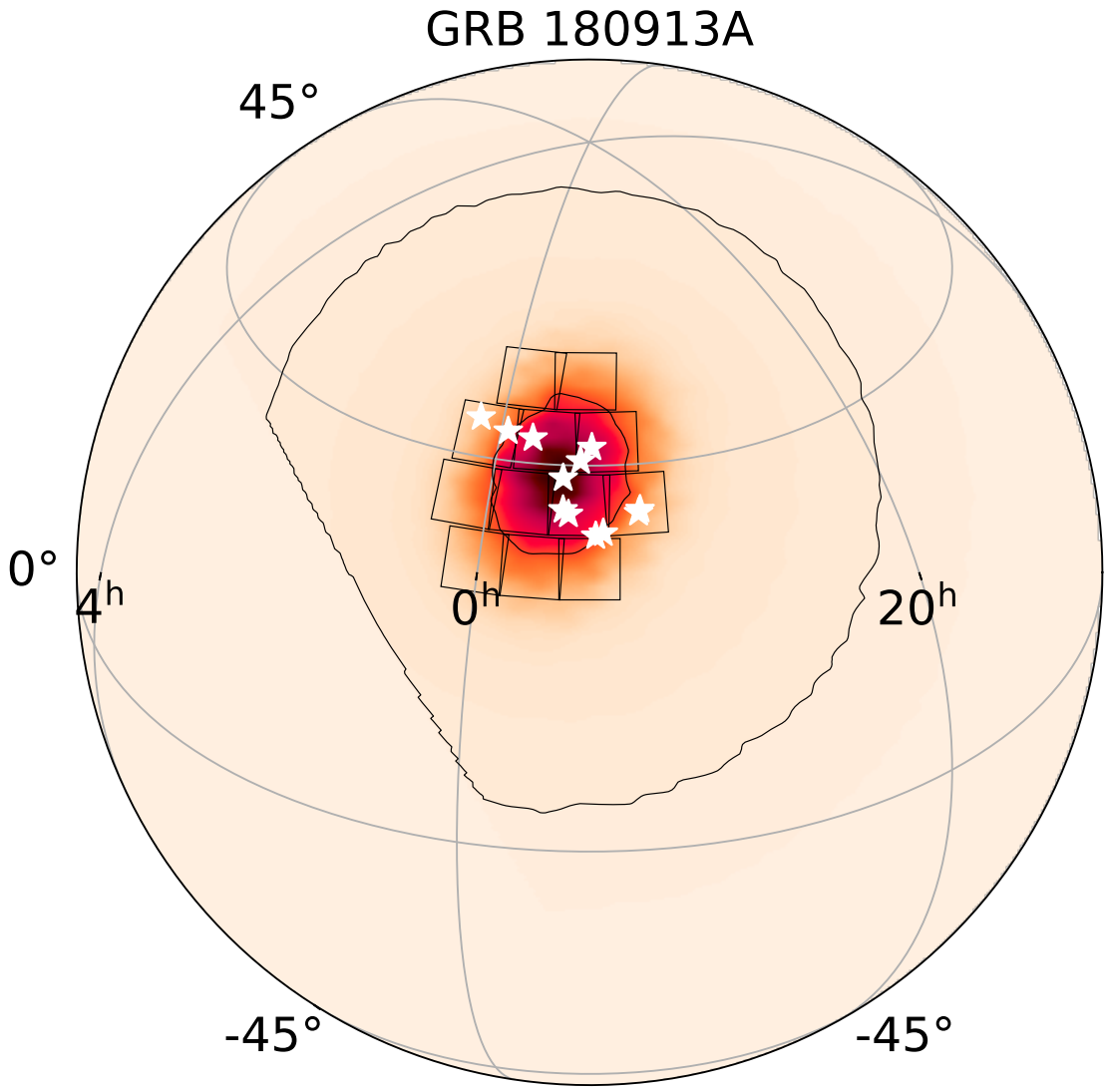

Figure 2.6: Coverage of the ZTF trigger on GRB 180913 and its *Fermi* GBM localization region. The $\approx$ 47 deg^2 ZTF tiles are shown as black quadrilaterals, and the 50% and 90% credible regions are shown as black contours and the sources discovered during the ZTF trigger as white stars (details in Section 2.5). The grid shows the Right Ascension in hours and the Declination in degrees.

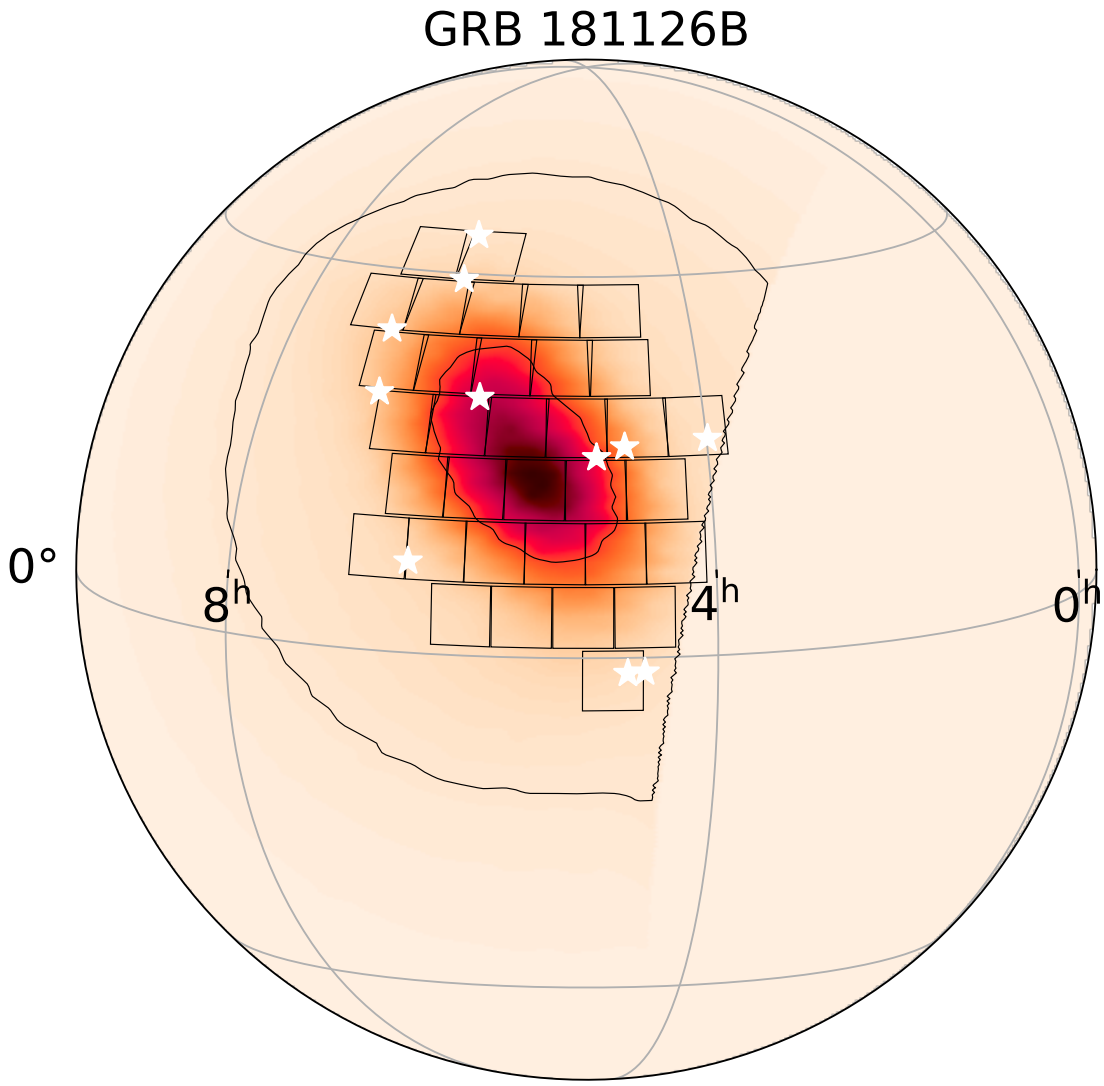

Figure 2.7: Coverage of the ZTF trigger on GRB 181126 and its *Fermi* GBM localization region. The ≈ 47 deg^2 ZTF tiles are shown as black quadrilaterals, and the 50% and 90% credible regions are shown as black contours and the sources discovered during the ZTF trigger as white stars (details in Section 2.5). The grid shows the Right Ascension in hours and the Declination in degrees.

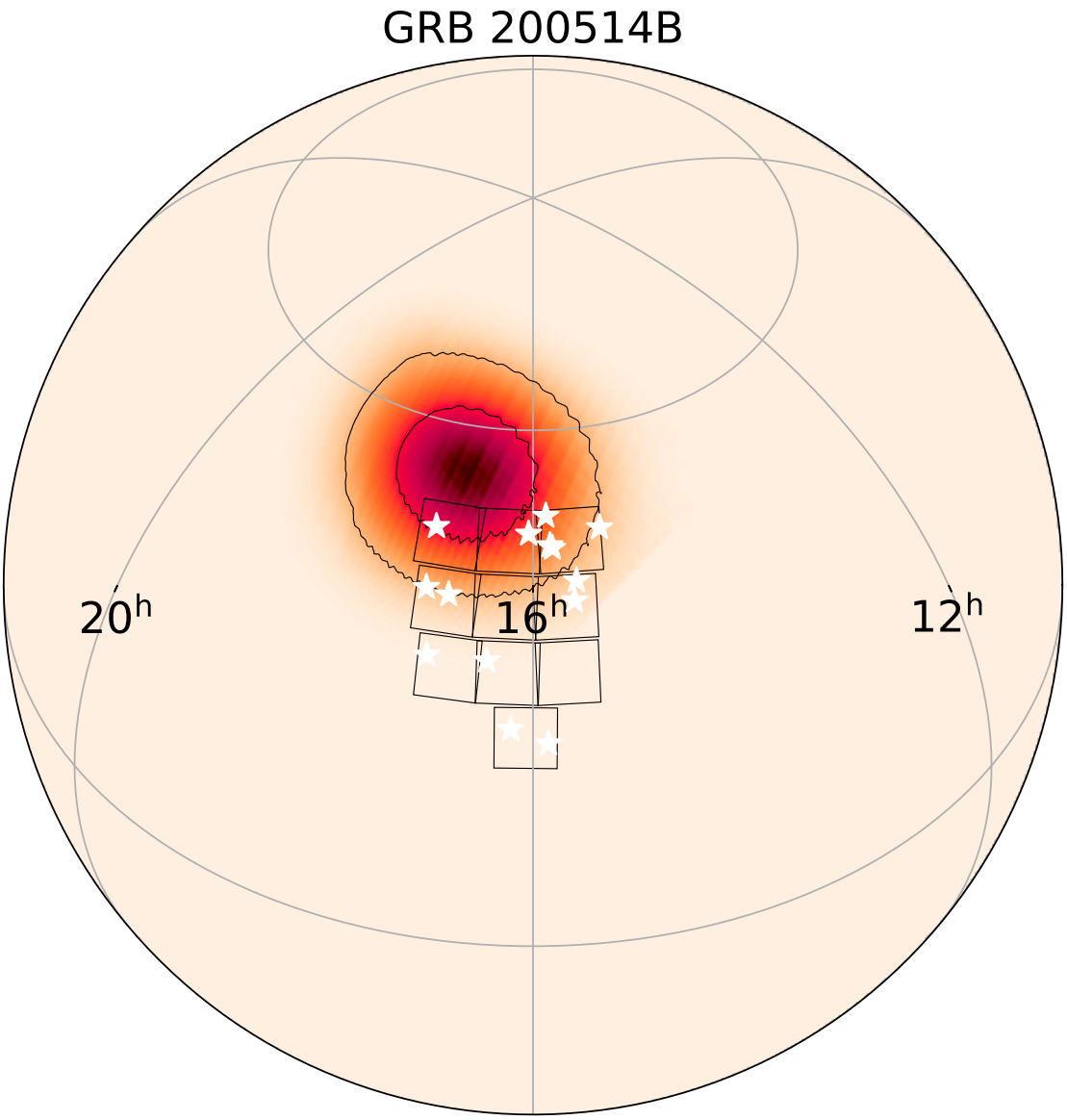

Figure 2.8: Coverage of the ZTF trigger on GRB 200514 and its *Fermi* GBM localization region. The ≈ 47 deg^2 ZTF tiles are shown as black quadrilaterals, and the 50% and 90% credible regions are shown as black contours and the sources discovered during the ZTF trigger as white stars (details in Section 2.5). Note that for GRB 200514, we tiled the preliminary region, which was offset from the final localization. The grid shows the Right Ascension in hours and the Declination in degrees.

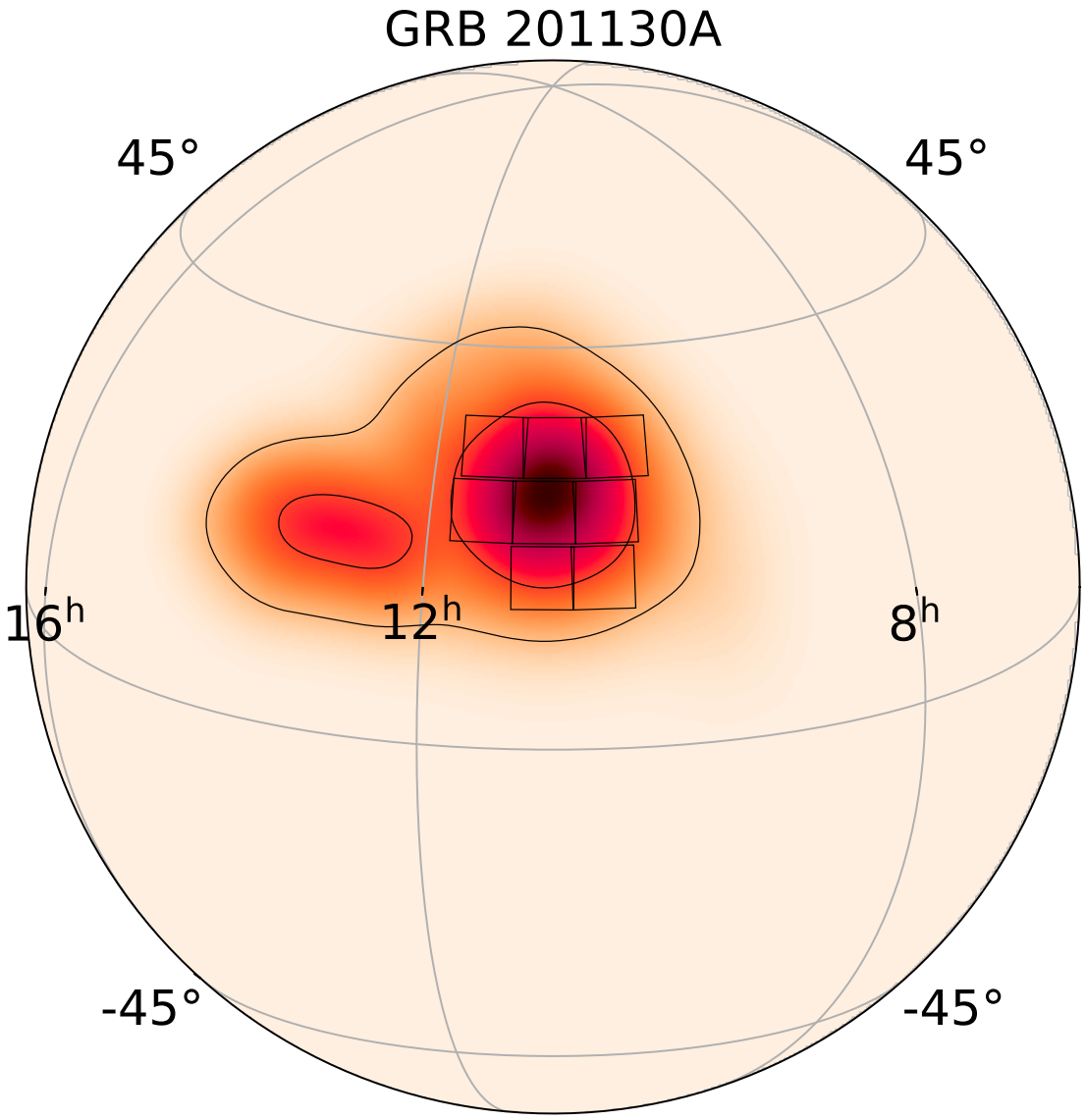

Figure 2.9: Coverage of the ZTF trigger on GRB 201130 and its *Fermi* GBM localization region. The ≈ 47 deg^2 ZTF tiles are shown as black quadrilaterals, and the 50% and 90% credible regions are shown as black contours and the sources discovered during the ZTF trigger as white stars (details in Section 2.5). The grid shows the Right Ascension in hours and the Declination in degrees.

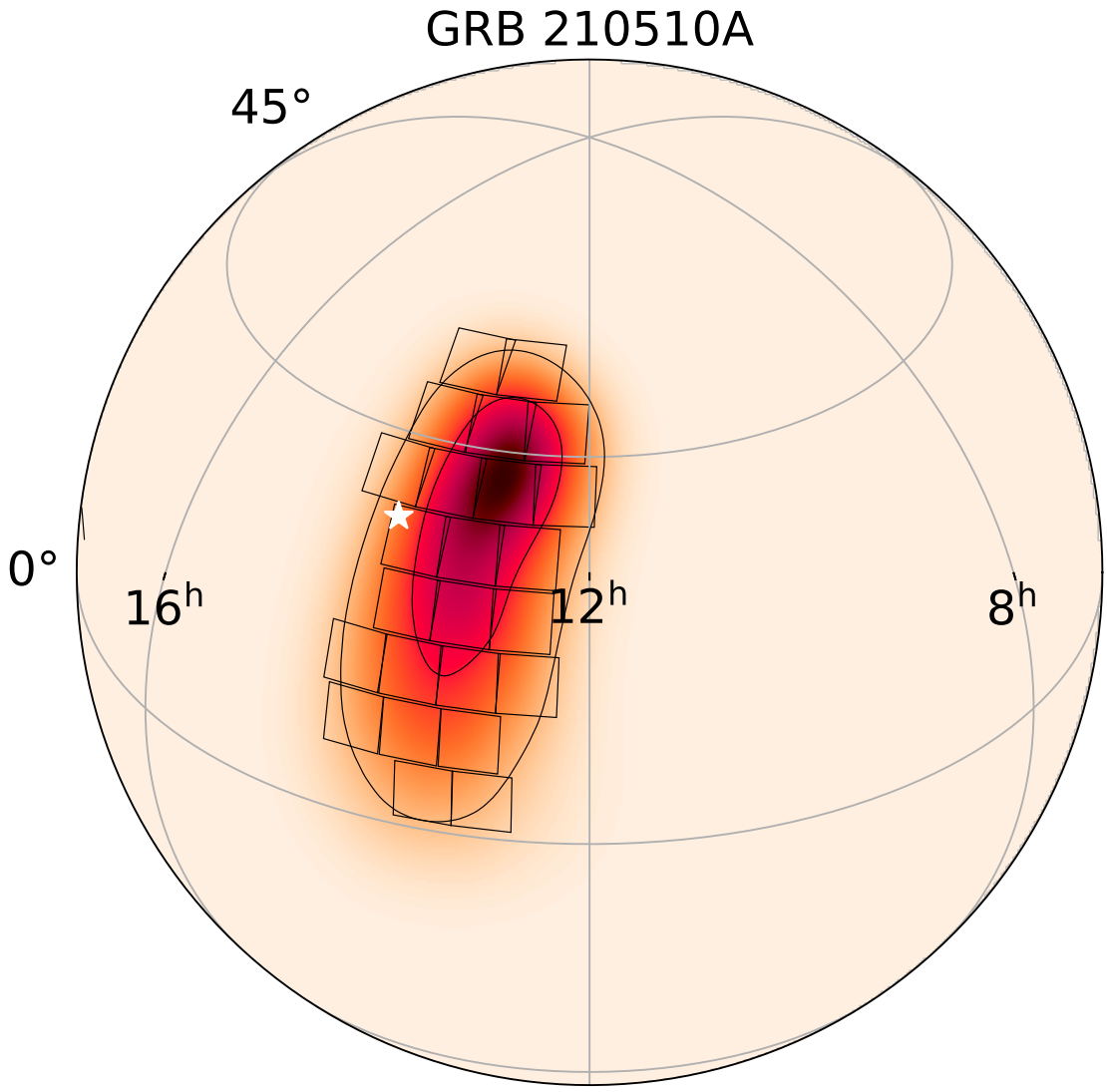

Figure 2.10: Coverage of the ZTF trigger and *Fermi* GBM localization region of GRB 210510, along the ≈ 47 deg^2 ZTF tiles (black quadrilaterals). The 50% and 90% credible regions are shown as black contours and the source discovered during the ZTF trigger as white star (details in Section 2.5). The grid shows the Right Ascension in hours and the Declination in degrees.

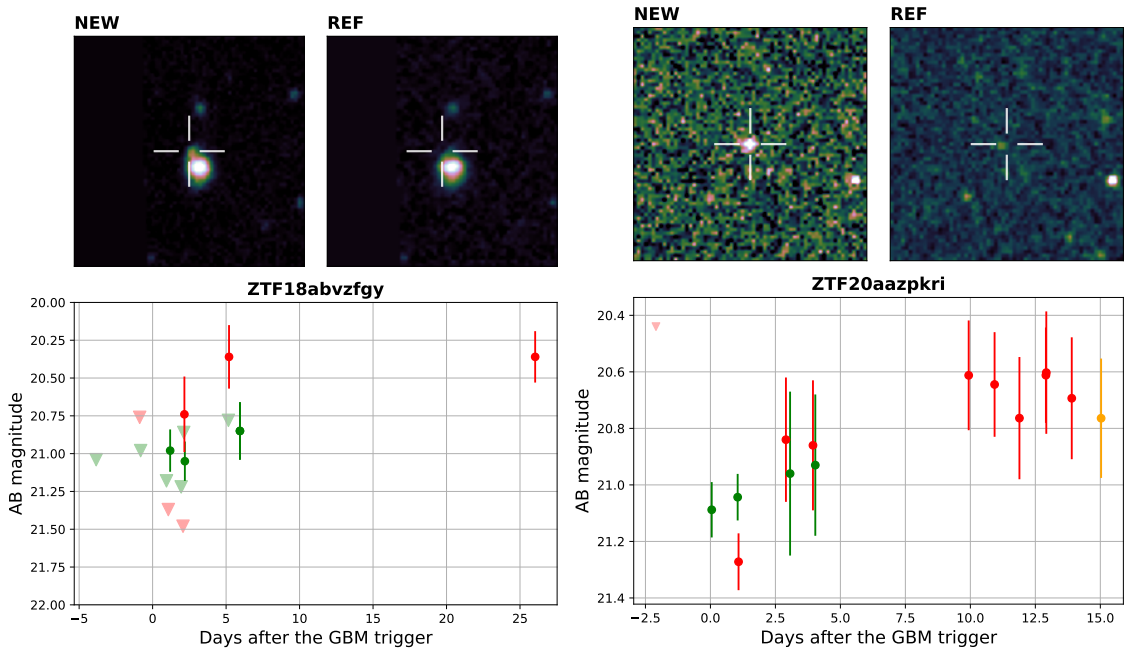

Figure 2.11: Examples of light-curves and cut-outs for candidates that passed our filtering criteria. Candidate ZTF18abvzfgy (candidate counterpart to GRB 180913A) in the left panel and ZTF20aazpkri (candidate counterpart to GRB 200514B) in the right panel. The observations in $g-$ and $r-$ band are plotted in green and red colors respectively. Filled circles represent ZTF detections, while the 5σ upper limits are shown as triangles in the light-curve. The top half of each panel shows the discovery image on the left and the reference image on the right. In the 0.7 sq. arcmin cutouts, north is up and east is to the left. A cross marks the location of the transient.

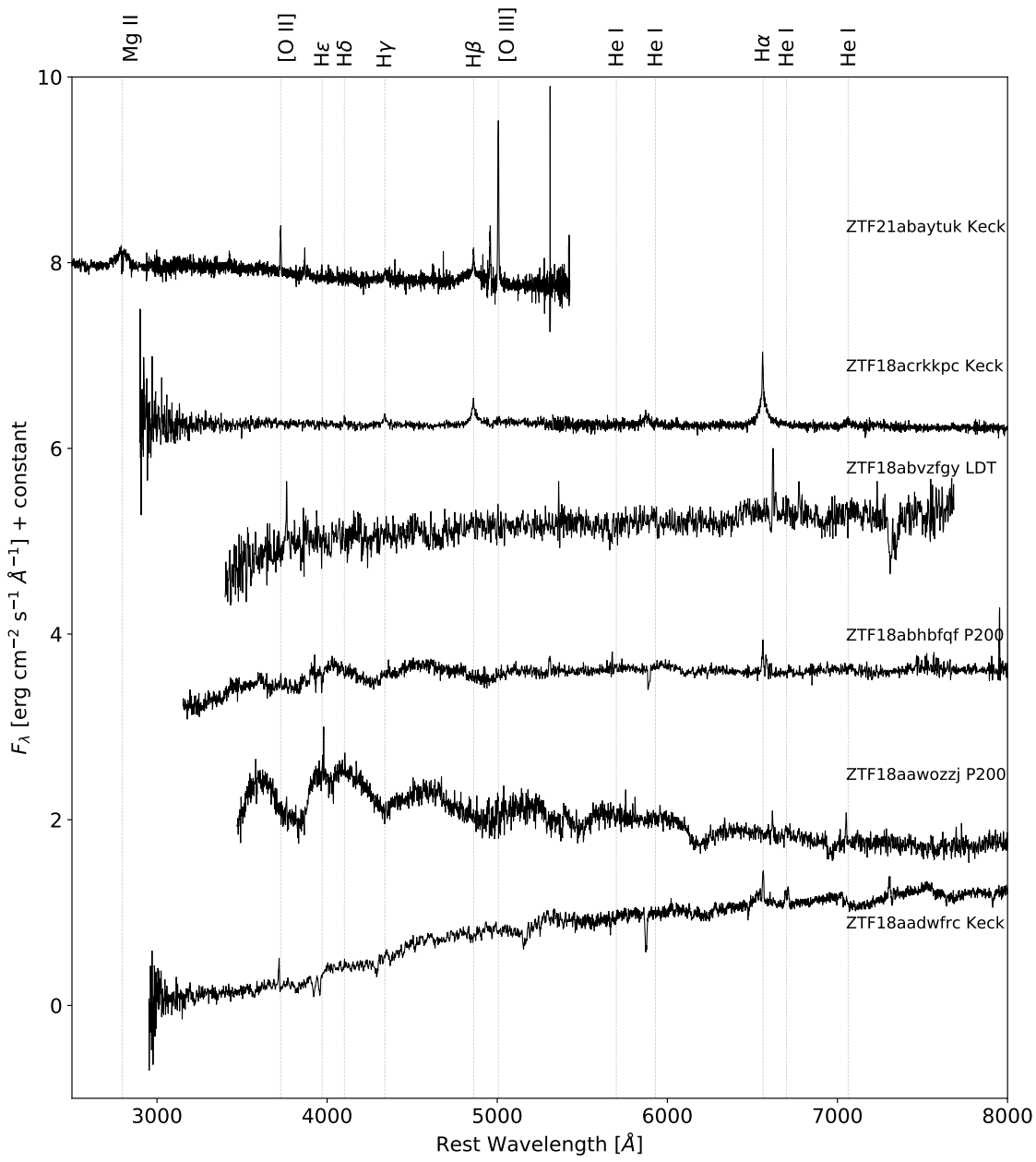

Figure 2.12: The spectra of some representative candidates. The spectrum of transient ZTF18aadwfrc was taken with the LRIS at the Keck Observatory and was classified as a SN Ia at $z = 0.04$. Similarly, the spectrum of ZTF18acrkkpc and ZTF21abaytuk come from Keck as well, and were classified as a SN II at $z = 0.061$ and as an AGN at $z = 0.89$ respectively. We used the DBSP at P200 to aqcuire spectra of ZTF18aawozzj and ZTF18abhbfqf, two SN Ia at redshift $z = 0.095$ and z= 0.11 respectively. Lastly, the spectrum of ZTF18abvzfgy was obtained with the DeVeny Spectrograph at the LDT, and using `dash`, we classified it as a SN Ic at $z = 0.04$. For reference, we show the Hydrogen, Helium, Magnesium, and some Oxygen lines as vertical lines.

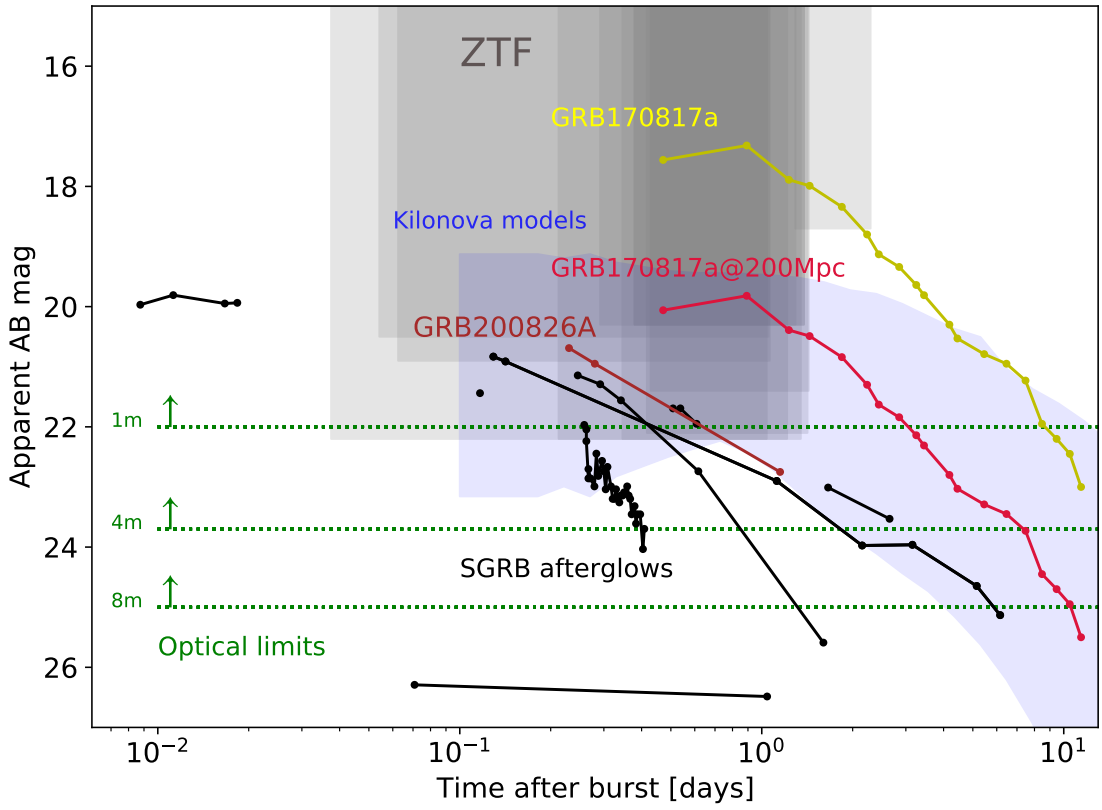

Figure 2.13: The light-curves (black) of the optical counterparts of SGRBs with known redshift listed in (Fong et al., 2015). The yellow light-curve is the GW170817 light-curve and the red line is the GW170817 light-curve scaled to a distance of 200 Mpc. Each of the ZTF search windows occupies a grey region, limited by the median limiting magnitude and the time window in which the search took place. The brown light-curve is the afterglow of GRB 200826A (Ahumada et al., 2021) and the blue shaded region represents the region that the KN models (Bulla, 2019; Dietrich et al., 2020) occupy when scaled to 200 Mpc. The green-dotted lines represent the typical optical limits of imagers mounted at different telescopes, while the size of the telescope is annotated as a label in the plot.

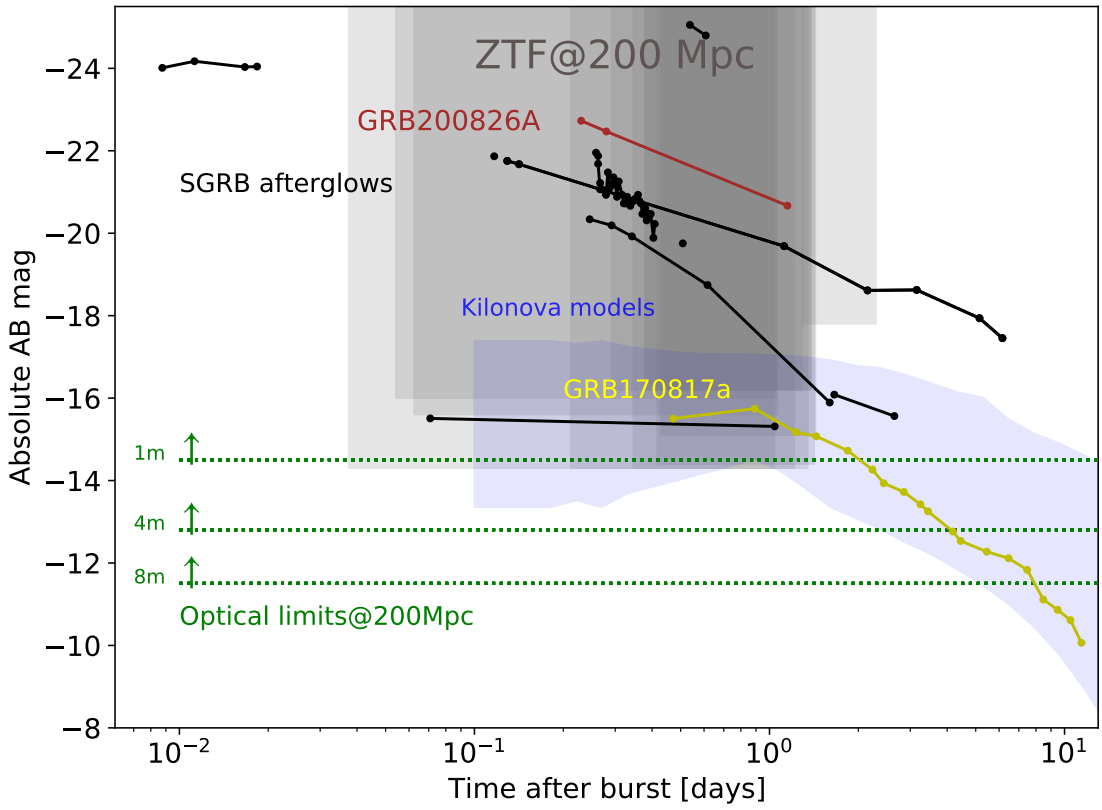

Figure 2.14: The absolute magnitude of the same data plotted in Fig. 2.13. We compare their absolute magnitudes to the ZTF magnitude limits, scaled to a fiducial distance of 200 Mpc. Similarly, the green-dotted lines show the optical limits of different facilities, ranging in size, at 200 Mpc.

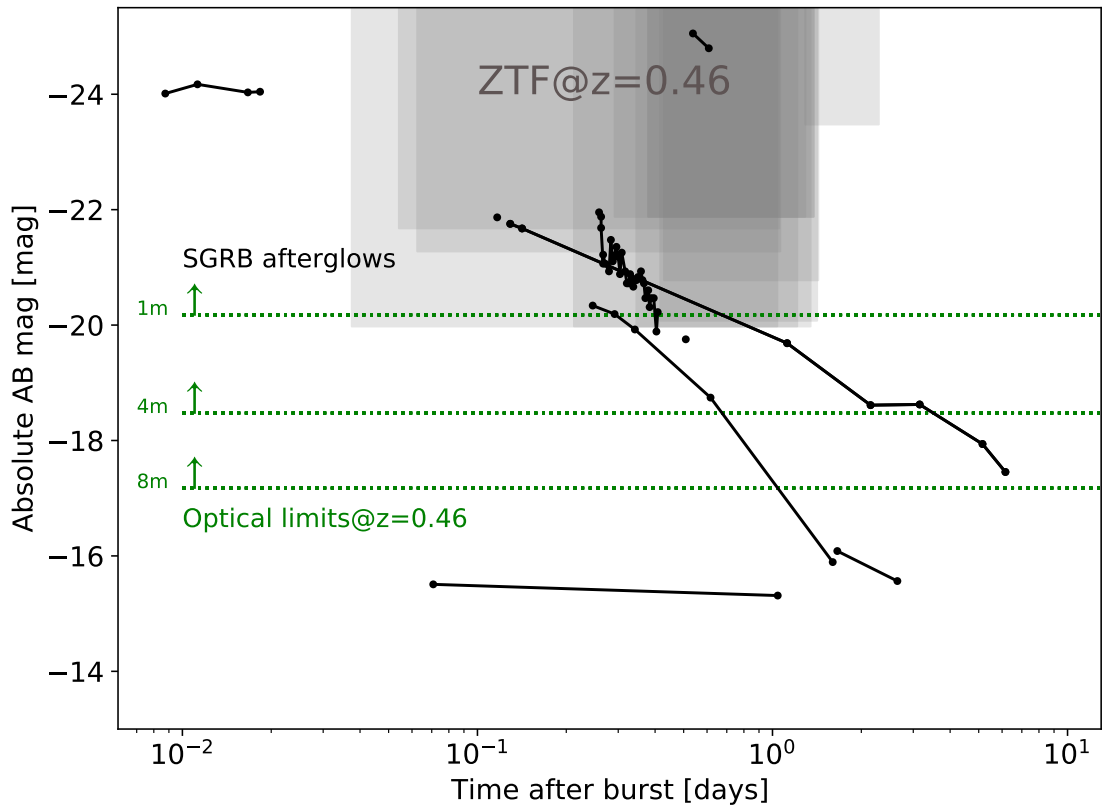

Figure 2.15: The absolute magnitude (black) of the optical counterparts of SGRBs with known redshift listed in Fong et al. (2015). Each of the ZTF search windows occupies a grey region, limited by the median limiting magnitude and the time window in which the search took place. The median limiting magnitudes are scaled to the median SGRB redshift of z=0.47. The green-dotted lines represent the typical optical limits of imagers mounted at different telescopes, while the size of the telescope is annotated as a label in the plot. These limits are also scaled to the median SGRB redshift of at $z = 0.47$.

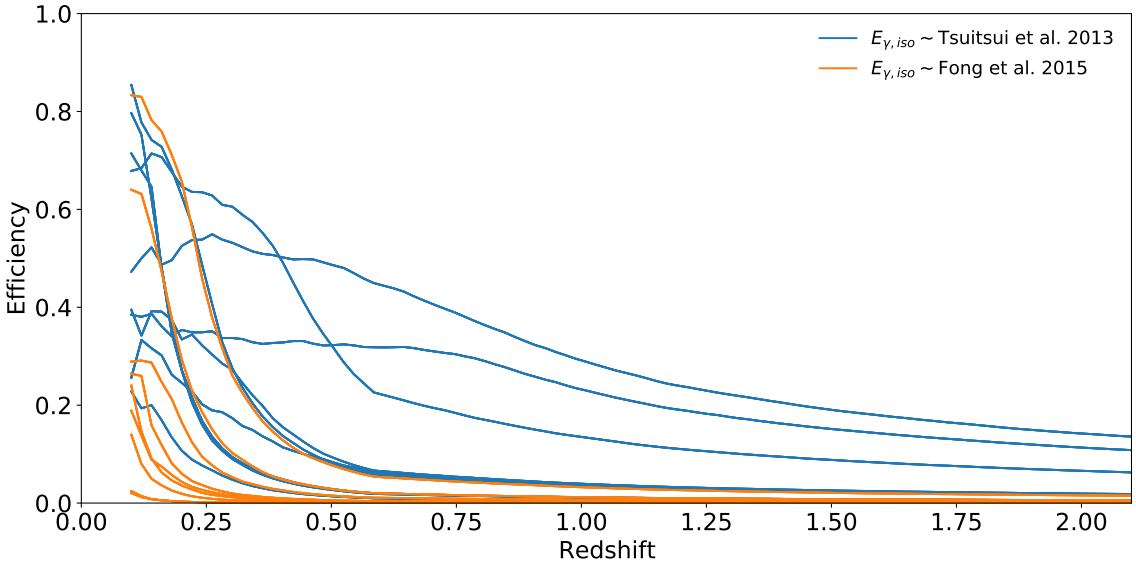

Figure 2.16: The individual efficiency for each SGRB trigger. The blue curves are based on the E_{iso} derived from the Band model E_p and Eq. 2.1, while the orange curves are the efficiencies assuming all GRBs have the same E_{iso} as the mean $E_{K,iso}$ from Fong et al. (2015).

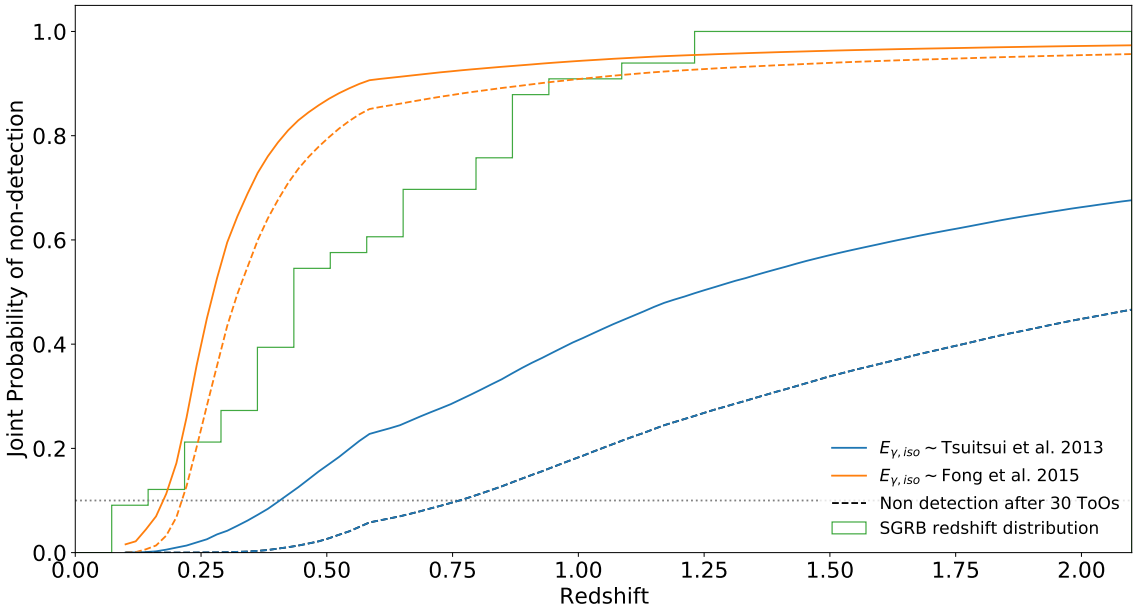

Figure 2.17: The solid lines represent the joint probability of non-detection using the 9 SGRB triggers with no optical counterparts. We adopt the same color coding as in Fig. 2.16, meaning blue for the E_{iso} as a function of E_p and orange for E_{iso} as the mean $E_{K,iso}$ from Fong et al. (2015). The dashed line represents the joint probability of non-detection after 30 ToOs, assuming an efficiency equal to the median efficiency of the ToOs presented. We show the cumulative redshift distribution for SGRBs as a green line. The grey dotted line shows the $CL = 0.9$ level, at which the joint probability of non detection is $1 - CL = 0.1$.

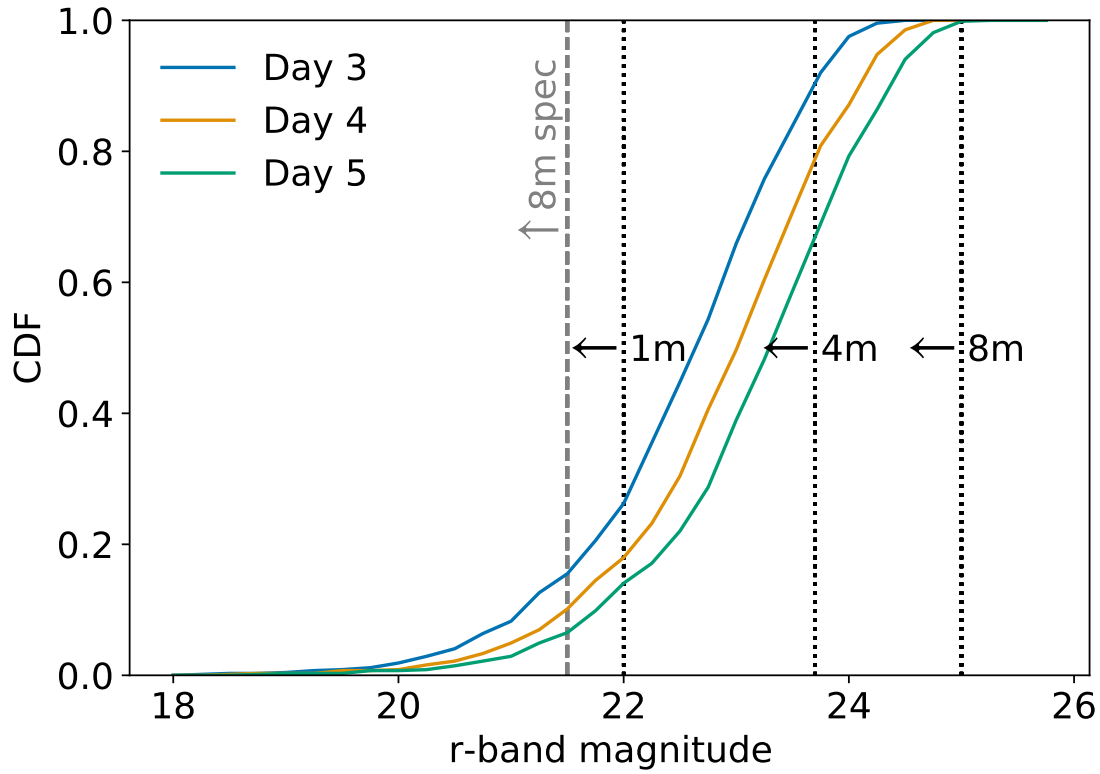

Figure 2.18: The magnitude cumulative distribution of the sources detected using `simsurvey` as a function of the days after the burst. This distribution contains all the sources detected up to z=2. The photometric and spectroscopic limits of different facilities are shown as dotted vertical lines.

GRB trigger	ZTF Name	RA	Dec	Discovery magnitude	Redshift	Rejection criteria
GRB 180523B	ZTF18aawozzj	12:31:09.02	+57:35:01.8	g = 20.20	(s) 0.095	SN Ia-91T P200
	ZTF18aawnbgg	10:40:54.05	+23:44:43.3	r = 19.80	(s) 0.135	SN Ia P200
	ZTF18aawmvbj	10:12:41.17	+21:24:55.5	r = 19.75	(s) 0.14	SN Ia P200
	ZTF18aawcwsx	10:40:33.46	+47:02:24.4	r = 19.84	(s) 0.09	SN Ia-91T P60
	ZTF18aawnbkw	10:38:47.66	+26:18:51.8	r = 19.91	(p) 0.31	slow SDSS
	ZTF18aawmqwo	09:52:06.90	+47:18:34.8	r = 19.98	(p) 0.04	slow SDSS
	ZTF18aawmkik	08:51:11.45	+13:13:16.7	r = 19.04	(p) 0.52	slow SDSS
	ZTF18aawnmlm	11:03:11.38	+42:07:29.9	r = 20.12	orphan	slow flat in 7 days
	ZTF18aauhzav	10:59:29.32	+44:10:02.7	r = 19.97	(s) 0.05	slow 2MASX
	ZTF18aavrhqs	11:58:09.57	+63:45:34.6	r = 19.99	orphan	slow
	ZTF18aawmwwk	10:35:26.51	+65:22:34.3	r = 19.99	(p) 0.18	slow SDSS
	ZTF18aawwbwm	08:16:44.98	+35:34:13.1	r = 19.79	(p) 0.15	slow SDSS
	ZTF18aawmjru	08:39:11.39	+44:01:53.6	r = 18.43	(p) 0.44	slow SDSS
	ZTF18aawmigr	08:48:01.76	+29:13:51.9	r = 19.63	(s) 0.1	slow 2MASX
GRB 180626C	ZTF18aauebur	19:48:49.10	+46:30:36.1	r = 18.85	stellar	CV multiple previous bursts
GRB 180715B	ZTF18aamwzlv	13:06:44.59	+68:59:52.9	r = 18.50	(s) 0.1	slow
	ZTF18abhbevp	14:21:00.83	+72:11:43.8	g = 20.63	–	slow
	ZTF18abhbpkm	16:02:36.78	+70:47:05.1	g = 21.24	–	slow
	ZTF18abhhjyd	13:02:32.07	+75:16:49.4	g = 20.43	–	AGN Milliquas match
	ZTF18abhbgan	15:43:18.86	+72:05:24.8	g = 21.22	orphan	slow
	ZTF18abhbfoi	13:24:34.01	+70:56:47.5	g = 21.12	(s)1.2	AGN Milliquas and PS1
	ZTF18abhbcjy	14:20:50.39	+73:25:40.5	g = 20.78	–	slow
	ZTF18abhaogg	13:42:45.47	+74:19:38.3	r = 20.38	orphan	slow
	ZTF18abhbamj	15:26:58.78	+72:02:17.8	r = 21.27	orphan	slow
	ZTF18abhawjn	13:31:27.33	+66:46:45.4	g = 20.69	(s) 0.4	AGN Milliquas
	ZTF18abharzk	13:41:09.05	+70:43:06.8	r = 21.30	–	slow
	ZTF18abhbckn	12:49:53.85	+73:02:00.5	r = 20.93	(s) 0.00541	slow CLU
	ZTF18abhbfqf	13:16:00.24	+69:37:24.1	r = 19.80	(s) 0.11	SN Ia-91T P200
	ZTF18aauhpyb	13:21:45.49	+70:55:59.8	g = 19.67	stellar	CV multiple bursts P60
GRB 180913A	ZTF18abvzgms	23:37:50.57	+47:53:21.2	g = 21.29	(p) 0.35	flat evolution SDSS
	ZTF18abwiios	23:12:14.06	+39:27:50.6	g = 22.04	–	flat evolution
	ZTF18abvzfgy	23:16:15.20	+43:31:59.3	g = 20.98	(s) 0.04	SN Ic LDT
	ZTF18abvzjwk	22:30:32.49	+39:50:14.6	g = 21.70	orphan	flat evolution
	ZTF18abvwhkl	23:05:44.17	+45:32:34.8	r = 21.44	–	flat evolution 3 points
	ZTF18abvucnv	22:31:31.96	+39:30:03.7	r = 21.15	stellar	Star flare
	ZTF18abwiitm	23:15:27.61	+39:57:10.5	g = 21.71	–	slow AGN WISE
	ZTF18abvubdm	22:58:28.45	+47:06:03.8	g = 21.01	–	slow evolution nice lc
	ZTF18abvzsld	00:15:57.12	+49:28:51.0	g = 21.50	Stellar	flat evolution
	ZTF18abwiivr	22:52:15.80	+37:22:29.4	g = 21.73	Stellar	slow evolution
	ZTF18abvzmtm	23:55:13.07	+48:21:37.8	g = 21.65	orphan	slow

Table 2.4: Follow-up table of the candidates identified for GRB 180523B (Coughlin et al., 2018c), GRB 180626C (Coughlin et al., 2018a), GRB 180715B (Cenko et al., 2018), and GRB 180913A (Coughlin et al., 2018b). The spectroscopic (s) or photometric (p) redshifts of the respective host galaxies are listed as well. The photometric slow evolution of some candidates was used as a rejection criteria when the object presents a variation on its magnitude smaller than 0.3 mag/day.

GRB trigger	ZTF Name	RA	Dec	Discovery magnitude	Redshift	Rejection criteria
GRB 181126B	ZTF18achtkfy	06:54:02.63	+37:04:28.6	g = 19.69	orphan	slow
	ZTF18achflqs	04:41:09.49	+23:53:24.9	r = 20.20	(p) 0.38	flat evolution SDSS
	ZTF18acrkcxa	04:55:02.52	+22:40:43.4	r = 20.85	Stellar	Flare Keck LRIS
	ZTF18acrkkpc	06:23:15.56	+10:19:22.6	r = 20.17	(s) 0.061	SN II Keck LRIS
	ZTF18aadwfrc	06:17:18.02	+50:29:03.3	r = 19.65	(s) 0.04	SN Ia-02cx Keck LRIS
	ZTF18acrfond	03:59:26.95	+24:35:20.4	r = 10.13	(s) 0.117	SN Ia Keck LRIS
	ZTF18acrfymv	06:18:01.18	+44:10:52.7	g = 20.82	(s) 0.072	SN Ic-BL Keck LRIS
	ZTF18acptgzz	04:33:32.45	-01:38:51.1	r = 19.56	(s) 0.096	SN Ia Keck LRIS
	ZTF18acbyrll	05:55:28.67	+29:28:20.3	r = 19.34	orphan	slow evolution
	ZTF18acrewzd	04:41:17.29	-01:46:07.5	g = 20.74	(s) 0.13	SN Ia Keck LRIS
GRB 200514B	ZTF20aazpphd	242.7149675	+27.1616870	r = 19.6		slow
	ZTF20aazppnv	238.1438691	+25.5764946	r = 21.1	(p) 0.17	slow
	ZTF20aazprjq	233.5213585	+43.3298714	r = 21.3	(p) 0.23	slow
	ZTF20aazptlp	229.007524	+48.774925	r = 21.5	(p) 0.40	slow
	ZTF20aazptnn	237.2967278	+47.271954	r = 21.6	(p) 0.26	slow
	ZTF20aazpnst	254.0989833	+34.4655542	r = 22.0	(p) 0.19	slow
	ZTF20aazpofi	236.929525	+46.9809542	r = 21.5	(p) 0.46	slow
	ZTF20aazplwp	2734.0167814	41.1672761	r = 21.6		slow
	ZTF20aazqlgx	2746.0908608	34.6259478	r = 22.3	(p) 0.35	slow
	ZTF20aazphye	2755.6577428	41.7013160	r = 21.6	(p) 0.26	slow
	ZTF20aazpnxd	2755.931646	48.3862806	r = 21.6		slow
	ZTF20aazpkri	2740.7324792	48.5554957	r = 21.3		slow
	ZTF20aazqndp	2737.8212032	50.4933039	r = 22.1	(s) 0.03	slow
	ZTF20aazqpps	2752.2388065	41.3097433	r = 21.6	(s) 0.2	slow
GRB 210510A	ZTF21abaytuk	13:48:49.89	+35:32:13.05	g = 21.76	(s) 0.8970	AGN Keck LRIS

Table 2.5: Follow-up table of the candidates identified for GRB 181126B (Ahumada et al., 2018), GRB 200514B (Ahumada et al., 2020; Reusch et al., 2020a), and GRB 210510A (Anand et al., 2021). The spectroscopic (s) or photometric (p) redshifts of the respective host galaxies are listed as well. The photometric slow evolution of some candidates was used as a rejection criteria when the object presents a variation on its magnitude smaller than 0.3 mag/day.

Chapter 3: The Discovery and confirmation of the shortest GRB from a collapsar

3.1 Abstract

Gamma-ray bursts (GRBs) are among the brightest and most energetic events in the universe. The duration and hardness distribution of GRBs has two clusters (Kouveliotou et al., 1993), now understood to reflect (at least) two different progenitors (Nakar, 2007). Short-hard GRBs (SGRBs; T_{90} <2 s) arise from compact binary mergers, while long-soft GRBs (LGRBs; T_{90} >2 s) have been attributed to the collapse of peculiar massive stars (collapsars) (Woosley & Bloom, 2006). The discovery of SN 1998bw/GRB 980425 (Galama et al., 1998) marked the first association of a LGRB with a collapsar and AT 2017gfo (Coulter et al., 2017)/GRB 170817A/GW170817 (Goldstein et al., 2017) marked the first association of a SGRB with a binary neutron star merger, producing also gravitational wave (GW). Here, we present the discovery of ZTF20abwysqy (AT 2020scz), a fast-fading optical transient in the *Fermi* Satellite and the InterPlanetary Network (IPN) localization regions of GRB 200826A; X-ray and radio emission further confirm that this is the afterglow. Follow-up imaging (at rest-frame 16.5 days) reveals excess emission above the afterglow that cannot be explained as an underlying kilonova, but is consistent with being the supernova. Despite the GRB duration being short (rest-

frame T_{90} of 0.65 s), our panchromatic follow-up data confirms a collapsar origin. GRB 200826A is the shortest LGRB found with an associated collapsar; it appears to sit on the brink between a successful and a failed collapsar. Our discovery is consistent with the hypothesis that most collapsars fail to produce ultra-relativistic jets.

3.2 The shortest GRB from a collapsar

On August 26, 2020, at 04:29:52 UT, the Gamma-ray Burst Monitor (GBM) on board the *Fermi* Gamma-ray Space Telescope detected GRB 200826A with duration (T_{90}) of 1.14 ± 0.13 seconds in the 50–300 keV energy range, In addition to *Fermi* (GBM trigger 620108997), GRB 200826A was detected by four other Interplanetary Network (IPN) instruments (see Methods).

The gamma-ray properties alone do not always yield an unambiguous classification. Some SGRBs show afterglow and host properties akin to LGRBs, e.g. Antonelli et al. 2009; some LGRBs show no evidence for collapsars to deep limits akin to SGRBs, e.g. Gal-Yam et al. 2006. Based solely on T_{90} (Bromberg et al., 2013), GRB 200826A has a SGRB probability of $65\%^{+12}_{-11}$. Also taking into consideration the E_{peak} parameter of a Comptonized model fit to the single spectrum over the duration of the burst (see Table 3.5), the probability that GRB 200826A is a SGRB increases to 74% (see Figure 3.1 and Methods). However, based on rest-frame energetics, GRB 200826A is not consistent with the SGRB population (right panel in Fig. 3.4).

Starting 4.2 hours after the GRB, we observed 180 sq. degrees of the *Fermi*-

GBM localization with the Zwicky Transient Facility (ZTF) (Bellm et al., 2019a) (see Fig. 3.2). At 17 hours after the GRB, IPN triangulated the source to a smaller region. ZTF20abwysqy was the only candidate that passed our alert filtering scheme and was also inside the IPN region (see Methods). We discovered ZTF20abwysqy at a brightness of $g = 20.86 \pm 0.04$ mag (AB system). The previous upper limit ($g > 21.3$ mag at 5σ) was 17.3 hours before the GRB, as part of the nominal all-sky survey mode (see Table 3.1). In addition to the spatial coincidence, ZTF20abwysqy was associated with a fading X-ray counterpart (D'Ai et al., 2020) and variable radio emission (Alexander et al., 2020), confirming ZTF20abwysqy as the afterglow of GRB 200826A (see Table 3.3 and Table 3.4).

ZTF20abwysqy was discovered in a galaxy with archival detections in Pan-STARRS 1 (PS1) (Chambers et al., 2016b) and Legacy Survey (LS) (Dey et al., 2019), at a LS photometric redshift of $z_p = 0.71 \pm 0.14$. The offset between the host galaxy's centroid and the transient is 0.18 ± 0.05 arcsec, corresponding to a physical distance of 2.09 ± 0.6 kpc. We acquired a Gran Telescopio Canarias (GTC) spectrum of the galaxy; we see strong [OII] and [OIII] lines at $z = 0.748$ (see Table 3.2 and Fig. 3.5). With both spectral and photometric spectral energy distribution (SED) fitting, we infer a stellar mass for the host galaxy of $\sim 10^{9.7}\ M_\odot$ (see Fig. 3.5, Fig. 3.6 and Table 3.6 in Sec. 3.3), which is near the distribution peak for LGRBs (Leibler & Berger, 2010), while below the median for SGRBs based on Fong et al. 2015.

We model the GRB afterglow using the standard synchrotron fireball model to constrain parameters related to the energy and geometry of the GRB central

engine (see Sec. 3.3). Electrons in the circumburst medium are accelerated by the shock wave and reach a power-law energy distribution characterized by the index p, $N(E) \propto E^{-p}$. This results in a SED described by a series of broken power laws, e.g. Sari et al. 1998 (See Figures 3.7 and 3.8). The associated isotropic kinetic energy of $E_{\rm K,iso} = 6.0^{+51.3}_{-4.4} \times 10^{52}$ erg lies in the top 5% of the $E_{K,iso}$ distribution for SGRBs (Fong et al., 2015), but within the 90% confidence range of the LGRB energy distribution (Shivvers & Berger, 2011) (see Sec. 3.3). Our data can only loosely constrain the circumburst density. The upper end of the distribution is consistent with the values found for the median circumburst densities (Panaitescu & Kumar, 2002) of LGRBs, while the lower end is more representative of SGRBs (Fong et al., 2015).

In the collapsar scenario, a high-velocity stripped-envelope supernova (SN) (SN Ic-BL) should follow the GRB detection (Woosley & Bloom, 2006). To test this scenario, we used the Gemini Multi-Object Spectrograph (GMOS-N; see Sec. 3.3) to acquire r- and i-band images of ZTF20abwysqy on three different epochs: $\sim$28, $\sim$45, and $\sim$80 days after the GRB trigger (epoch 1, 2 and 3 respectively). Using epoch 3 as the reference, we undertook image subtraction using two different subtraction algorithms (see Sec. 3.3 for details). On epoch 1, our Gemini observations show evidence of a transient with an i-band magnitude of 25.45$\pm$0.15 mag (with an i-band 5σ limit of 25.9 mag, see Table 3.1); there is no source in the r-band observations up to a 5σ limit of 25.4 mag (see Fig. 3.3). On epoch 2, we do not detect a source up to a 5σ limit of 25.5 mag in the i-band and 25.7 mag in the r-band. Thus, at a rest-frame time of $\sim$16 days, the foreground extinction-corrected absolute magnitude of

ZTF20abwysqy is $M_i = -18.0$ mag.

To understand the source of the i-band excess, we use Markov chain Monte Carlo (MCMC) and full forward modeling of all multi-band observations excluding the GMOS detection to compare three scenarios: an afterglow only, an afterglow plus a kilonova (KN), and an afterglow plus a SN. The KN model is based on a best-fit template to AT2017gfo (Dietrich et al., 2020) scaled by a compilation of SGRB-KN candidates (Gompertz et al., 2018); the collapsar model uses a SN1998bw template (Clocchiatti et al., 2011) with stretch and scale parameters drawn from a prior that is consistent with the historical GRB-SN sample (Cano et al., 2017). We dismiss the afterglow-only and afterglow-plus-KN models because they predict i-band flux at the time of the GMOS data point that is too faint by $1.6^{+1.8}_{-0.3}$ mag – inconsistent with the observations at the $\sim 5\sigma$ level (see Fig. 3.9 and Table 3.7).

We repeated the analysis of all three scenarios including the GMOS data point in order to do Bayesian model comparison. The Bayes factor between the afterglow-plus-KN and afterglow-only models is ~ 1, indicating that neither model is favored over the other. However, the Bayes factor between the afterglow-plus-SN and afterglow-only model is $10^{5.5}$, indicating that the afterglow-plus-SN model is strongly favored. Based on the compilation of Cano et al. 2017 of GRBs with associated SNe, GRB 200826A is the shortest LGRB found with an associated collapsar, with an observed T_{90} of 1.13 s and rest-frame T_{90} of 0.65 s (see Figure 3.1). The second shortest LGRB with a SN is GRB 040924, with a rest-frame T_{90} of 1.29 s (Cano et al., 2017).

In the conventional fireball model of a LGRB, the rest-frame duration of the

prompt emission, t_γ, is the difference between the duration of the activity of the central engine, t_e, and the time required to break out of the envelope, t_b (Sobacchi et al., 2017). The short duration of GRB 200826A suggests that $t_e \gtrsim t_b$, which might imply that its central engine is active only very briefly, or that the stellar envelope is unusually thick, as compared to other LGRBs, perhaps requiring a nonstandard progenitor (Zhang et al., 2021). Then it is natural to infer that there must be collapsars for which $t_e < t_b$ that fail to produce a fireball. For $t_e \lesssim t_b$, the jet may fail to clear a path for itself and remains cocooned within the exploding star, yet the cocoon itself may still produce a mildly relativistic shock breakout that manifests as a soft, quasi-thermal, low-luminosity GRB (llGRB) like GRB 980425/SN 1998bw or GRB 060218/SN2006aj (Nakar, 2015; Soderberg et al., 2006). For $t_e \ll t_b$, there may be no prompt emission at all.

GRB 200826A, then, may sit on the brink between a successful LGRB and a failed one. The sign of one continuous physical parameter, $t_e - t_b$, switches a collapsar-powered GRB discontinuously between two dominant emission mechanisms: internal shocks in a relativistic jet or mildly relativistic shock breakout at the surface of the exploding star. These two mechanisms correspond to two widely separated and disconnected regions in the hardness-duration-fluence phase space: the traditional border between SGRBs and LGRBs, and the exceptionally long and soft region occupied by llGRBs and X-ray flashes (XRFs). The local rate of LGRBs ($\sim 1\,\mathrm{Gpc^{-3}yr^{-1}}$) (Nakar, 2015) is 2 orders of magnitude lower than the rate of llGRBs ($300\,\mathrm{Gpc^{-3}yr^{-1}}$) (Nakar, 2015) and 3 orders of magnitude lower than the rate of SNe Ic-BL ($4500\,\mathrm{Gpc^{-3}yr^{-1}}$) (Graham & Schady, 2016). It is understood that

LGRBs, and to a lesser extent, llGRBs, are collimated and relativistically beamed, suppressing the detection of events in which the jet is pointed away from our line of sight. However, even allowing for a beaming correction to their rates of 100 for LGRBs and 1–10 for llGRBs (Nakar, 2015) (but no beaming correction for SNe), LGRBs still occur at a rate ($100\,\mathrm{Gpc^{-3}yr^{-1}}$) that is up to an order of magnitude lower than that of llGRBs (300-3000 $\mathrm{Gpc^{-3}yr^{-1}}$) or that of SNe Ic-BL, suggesting that the majority of the collapsars fail to produce an ultra-relativistic jet and instead drive a wide-angle or nearly isotropic and only mildly-relativistic cocoon.

Based on indirect evidence from the host, afterglow, and gamma-ray properties, it has been argued that as many as 84% of bursts detected by the *Neil Gehrels Swift Observatory* (Gehrels et al., 2004) (*Swift*) and 40% of the *Fermi* bursts that are nominally SGRBs ($T_{90} < 2\,\mathrm{s}$) are actually misclassified LGRBs (Piran et al., 2013). If this is correct, then one would expect many more short-duration GRBs with collapsars that are on the edge between success and failure of the jet. The discovery of GRB 200826A, an SGRB imposter, lends credence to this bold claim, and would suggest that the rates of such short-duration LGRBs is comparable to the rate of llGRBs, up to a few hundred $\mathrm{Gpc^{-3}yr^{-1}}$. Thus, our discovery upholds the hypothesis that most collapsars fail to produce jets.

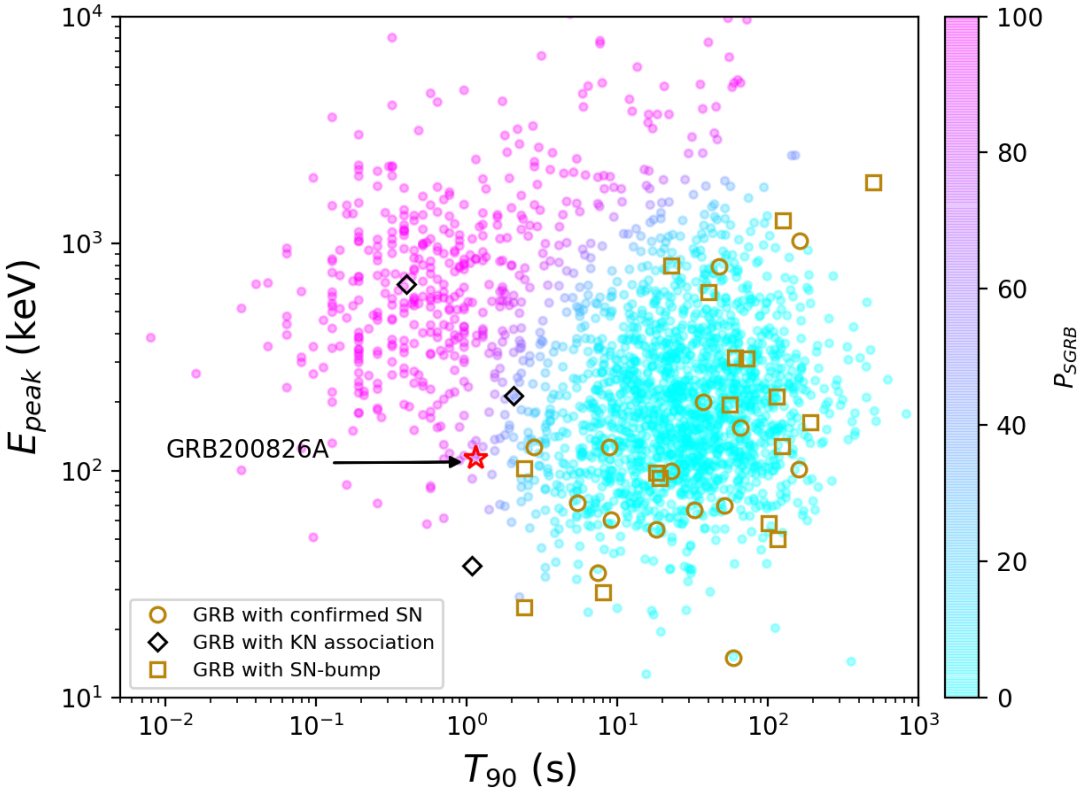

Figure 3.1: **Gamma-ray properties of GRB 200826A in context.** The peak energy based on a Comptonised fit, E_{peak} (keV), vs. the time-integrated, T_{90} (s), for 2310 *Fermi* GBM GRBs. The data are fit with two log-normal distributions for the two GRB classes. The color of the data points indicate the probability with magenta being 100% SGRB and cyan being 100% LGRB. GRB 200826A is surrounded by a red star with a SGRB probability of 74% (See Methods). Yellow squares show LGRBs with SN-bumps, yellow circles show LGRBs with spectroscopically confirmed SN (Cano et al., 2017), black diamonds show SGRBs with claimed KN excess (Gompertz et al., 2018).

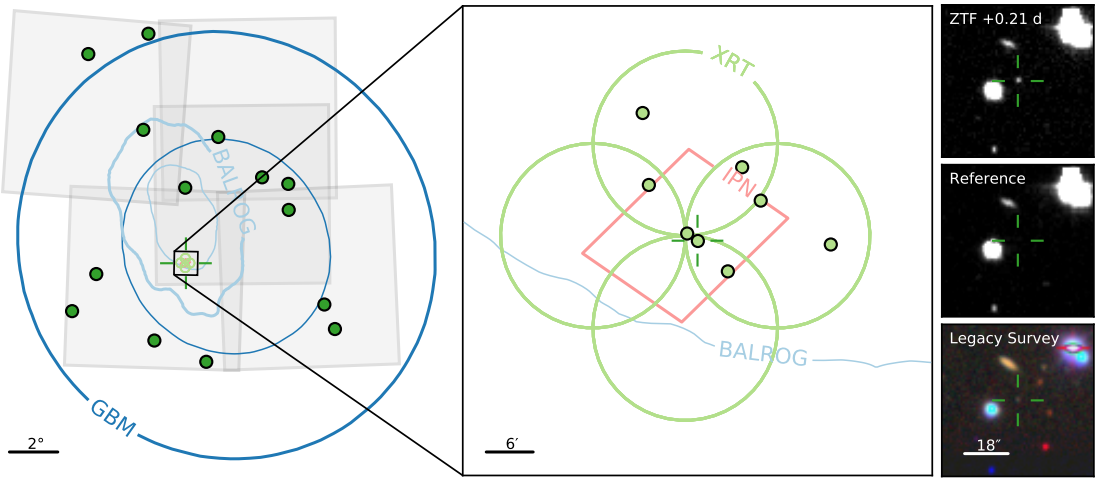

Figure 3.2: **Discovery of the afterglow of GRB 200826A.** It was found at the position $\alpha = 00^h27^m08.542^s$, $\delta = +34^h01^m38.327^s$ (J2000) with an uncertainty of 0.08." Contours in the left panel represent the *Fermi* GBM 90% (thick) and 50% (thin) credible regions from the official *Fermi* GBM localization (dark blue) and BALROG (light blue). The filled gray squares show the ZTF fields observed and the dark green dots are the positions of the ZTF Night 1 optical candidates. In the middle panel, 3σ IPN triangulation is shown in pink; the four fields of the four XRT tiled observations are shown as light green circles and the XRT candidates are light green dots. The position of the afterglow is marked by the dark green reticle. The right-hand panels are centered at the position of ZTF20abwysqy. The cutouts, from top to bottom, show the ZTF discovery image, the ZTF stacked reference image, and a false color image showing the host galaxy from Legacy Survey DR8. In the cutouts, North is up and East to the left.

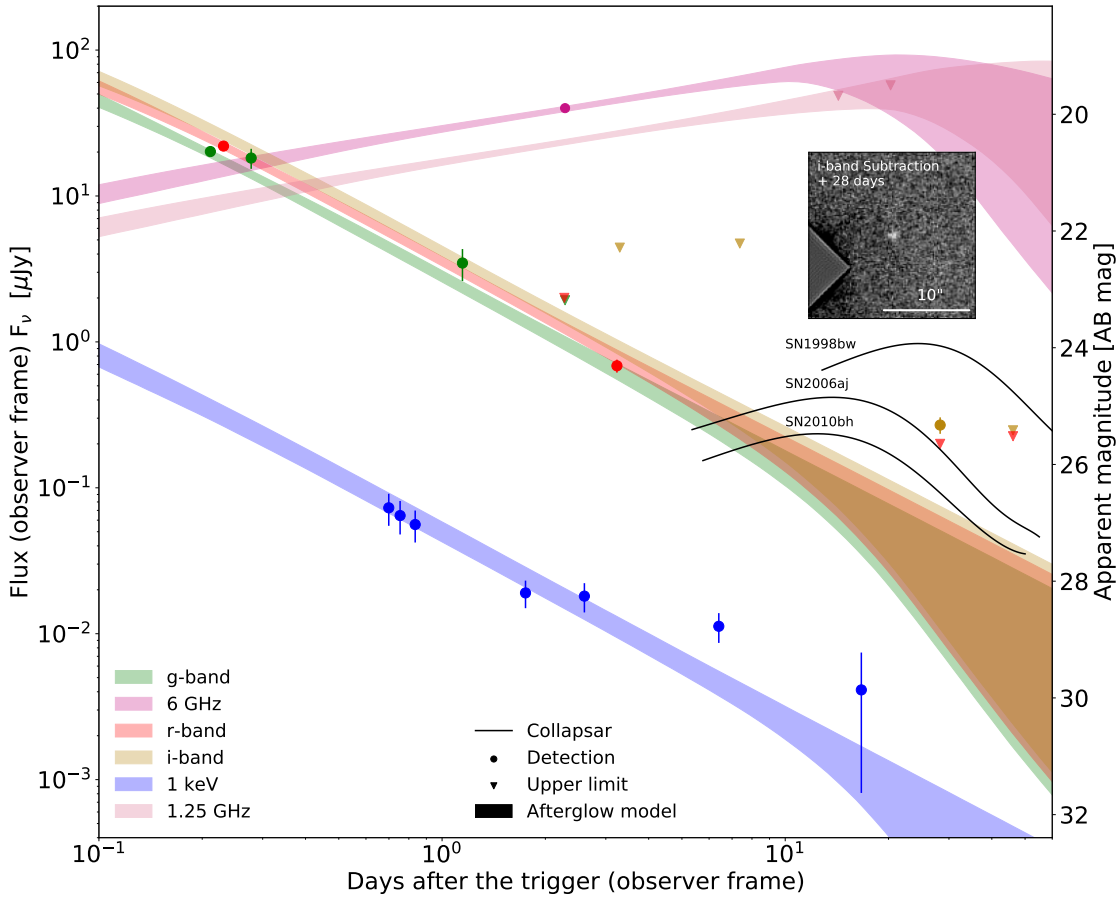

Figure 3.3: **Panchromatic afterglow and collapsar confirmation.** The available multiwavelength light curve data is over-plotted with the best fits (5th to 95th percentiles) from the `afterglowpy` modeling assuming an ISM-like environment. Detections are shown as circles with their respective error bars (1σ), and 5σ upper limits are shown as inverted triangles. The optical g-, r- and i- bands are shown in green, red and yellow, the XRT 1 keV data is shown in blue, the VLA in fuchsia (darker pink), while the GMRT data is presented in pink. We show the K-corrected light curves of three well-studied GRB-SNe (SN1998bw, one of the brightest; SN2006aj and SN2010bh, two of the faintest) with solid black lines. The Gemini GMOS-N i-band detection is shown at day 28.28, as a yellow circle, and is consistent with the collapsar population. We show a cutout of the i-band ZOGY subtraction, revealing our 25.45 mag detection with a ZOGY corrected score of 4.

3.3 Methods

3.3.0.1 Background

The traditional paradigm of classifying a GRB based only on its gamma-ray properties is debated (Bromberg et al., 2013; Zhang & Choi, 2008). Although the two types of progenitors broadly map to the time duration of the signals, there is no clear boundary in the bimodal distribution. Some SGRBs show afterglow and host properties akin to LGRBs, e.g. Antonelli et al. 2009; Levesque et al. 2010; some LGRBs show no evidence for collapsars to deep limits akin to SGRBs, e.g. Fynbo et al. 2006; Yang et al. 2015.

In the mid 2000s, SGRB-related breakthroughs triggered by the *Neil Gehrels Swift Observatory* (Gehrels et al., 2004) and HETE-II (Ricker & Vanderspek, 2003) included detections of SGRBs X-ray afterglows, identification of likely host galaxies (Gehrels et al., 2005), and the first SGRB optical afterglow (Hjorth et al., 2005; Villasenor et al., 2005). Yet, in the first decade of optical follow-up of *Swift* SGRBs, only about 30 optical/NIR afterglows were detected (Berger, 2014; Fong et al., 2015) and even fewer had associated redshifts. On 2017 August 17, the joint detection of the binary neutron star (BNS) merger (GW170817) in GWs with LIGO and Virgo (Abbott et al., 2017c), and in gamma-rays by *Fermi* GBM (Meegan et al., 2009) and INTEGRAL (Abbott et al., 2017b; Goldstein et al., 2017; Savchenko et al., 2017), unequivocally confirmed BNS mergers as at least one of the mechanisms that can produce a SGRB. The merger illuminated the entire electromagnetic spectrum (Abbott et al., 2017a) and the optical/NIR emission provided robust evidence of a

radioactively powered KN (Arcavi et al., 2017; Chornock et al., 2017; Cowperthwaite et al., 2017; Drout et al., 2017; Kasen et al., 2017; Kasliwal et al., 2017b; Pian et al., 2017; Smartt et al., 2017; Tanvir et al., 2017; Troja et al., 2017).

The bulk of our knowledge about SGRBs comes from the well-studied *Swift* SGRB afterglow sample; however, the low *Swift* local rate of SGRBs (Dichiara et al., 2020) has hampered the detection of a GW170817-like event. On the other hand, the *Fermi* GBM is arguably the most prolific engine of discovery for *compact binary mergers*, as it detects ≈ 1 SGRB each week, which is four times the rate of *Swift* (Sakamoto et al., 2011; von Kienlin et al., 2020), and comparable to the rate of the LIGO and Virgo detectors when in observing mode (≈ 1.5 per week during O3a (Abbott et al., 2020)). Unfortunately, there is a relative paucity of electromagnetic observations of *Fermi* GRBs and LIGO/Virgo GW events alike because it is challenging to pinpoint them within their positional uncertainties of tens to thousands of square degrees (Aasi et al., 2016; Abbott et al., 2018; Nissanke et al., 2011).

In order to better understand the phenomenology of GRBs and compact binary mergers, wide field of view (FOV) optical instruments have looked for *Fermi* GRBs and LIGO/Virgo GW counterparts. In 2013, the Palomar Transient Factory (PTF) (Law et al., 2009) used a $7\,\mathrm{deg}^2$ camera on the Palomar 48 inch Oschin telescope (P48) to discover the first optical afterglow of a GRB based *solely* on a *Fermi* GBM localization (Singer et al., 2013) and subsequently found afterglows of 7 other LGRBs (Singer et al., 2015). Now, the Zwicky Transient Facility (ZTF; Bellm et al. 2019a; Graham et al. 2019; Masci et al. 2019), a $47\,\mathrm{deg}^2$ camera mounted at

the P48 telescope, has enabled searches an order of magnitude faster in areal and volumetric survey speed and has been used to search the coarse error regions of *Fermi* GBM SGRBs (Coughlin et al., 2019c) and LIGO/Virgo events (Anand et al., 2021; Andreoni et al., 2019a; Coughlin et al., 2019d; Kasliwal et al., 2020b). Both PTF and ZTF have also discovered afterglow-like transients with optical, X-ray, and radio emission, but no gamma-ray counterpart (Cenko et al., 2013, 2015; Ho et al., 2020).

3.3.0.2 Gamma-ray detections

Fermi (GBM trigger 620108997) (Fermi GBM Team, 2020), and the IPN instruments – *AGILE* (Pittori et al., 2020), *INTEGRAL* (SPI-ACS), *Mars-Odyssey* (HEND), Konus-*Wind* (Ridnaia et al., 2020), and AstroSat (Gupta et al., 2020) detected the burst. The GBM localization calculated by the ground software (Connaughton et al., 2015; Goldstein et al., 2020) is RA = 4.7, Dec = 35.3 (J2000 degrees, equivalent to J2000 00h 18m, 35d 17') with a statistical uncertainty of 1.7 degrees (Fermi GBM Team, 2020). The BALROG localization is consistent with this (Burgess et al., 2016). The final GBM localization of the GRB was available a few minutes after the trigger, and it enclosed 339 (63) deg^2 within the 95% (50%) credible region.

The light curve shows a bright GRB featuring three distinct peaks in the 50–300 keV energy range, with with a signal-to-noise ratio (S/N) of ∼100 and a T_{90} duration of 1.14 ± 0.13 s. This GRB is within the top 36% in terms of fluence (in the 50–300 keV energy band as measured over T_{100}) from bursts recorded in the *Fermi*

GBM catalog (von Kienlin et al., 2020). Spectral analysis was performed using the RMFIT 4.4.2 light curve and spectral analysis software[1] in the interval of T_0 to T_0 +1.152 s encompassing the T_{90} start time and duration. The detector selection for the analysis consisted of the brightest NaI detectors with angle $< 60°$ (N6, N7, N8, N9, NB11) and BGO detector B1. NaI and BGO detector data from ∼8 keV to ∼900 keV and ∼300 keV to ∼40 MeV respectively was used for the analysis. The Band Model (Band et al., 1993), a standard model for GRB analysis (Gruber et al., 2014), provided best fit with parameters consistent with the initial analysis (Mangan et al., 2020), where $E_{peak} = 88.9 \pm 3.2$ keV, $\alpha = -0.26 \pm 0.07$, and $\beta = -2.4 \pm 0.1$. The peak flux in the 64 ms time (10 keV - 1 MeV), measured from T_0 +1.152 s, is 64.3 ± 2.1 ph cm^{-2} s^{-1}. The fluence over T_{90} (10 keV to 1 MeV) is $42.6 \pm 0.2 \times 10^{-7}$ erg cm^{-2} (the fit merit of the spectral fit is 1.09).

A time resolved spectral analysis was performed from T_0 to T_0 +1.152 s. The data was binned by S/N, with at least 20σ for the S/N in each bin. For 6 of the bins, the best-fit parameters of the Band Model are displayed in Table 3.5. The parameters for the Band model in the initial time interval were poorly constrained so a cutoff power law (Comptonised) model (Yu et al., 2016) was fitted to this interval. The Band Model was primarily used as this was the best constrained model for the time integrated analysis. The Castor C-stat statistic (Guiriec et al., 2010) was used for its robustness when dealing with low count statistics, while the background was modeled as a first order polynomial over all qualifying detectors, as discussed above,

[1]Available at the *Fermi* Science Support Center: `https://fermi.gsfc.nasa.gov/ssc/data/p7rep/analysis/rmfit/`

using TTE data products. Spectral evolution of the E_{peak} parameter is observed over the duration of the burst, and is found to exhibit hardness-intensity tracking behavior (Guiriec et al., 2010; Yu et al., 2016).

The distribution of GRB T_{90} durations demonstrates a bimodality that is best fit with double log-normal components. This suggests two distinct but overlapping progenitor probabilities, and by extension, classifications for short and long GRBs. Using only the T_{90}, and the parameters derived for the *Fermi* GBM distribution of bursts in Bromberg et al. 2013, we determine a SGRB probability of $64.94\%^{11.59}_{-11.30}$ for GRB 200826A.

According to BATSE (Kouveliotou et al., 1993), the overlap of GRB T_{90} duration distributions occurs at $\sim 2\,\mathrm{s}$. In the past, GRB hardness ratios, quantifiable for the majority of GRBs in the absence of location information, have been used as a measure for the spectral hardness. Hardness ratio is presented for the GBM catalogue events in von Kienlin et al. 2020, where the data shows an anti-correlation between hardness and duration; however, there is a large scatter in the data. We derive a T_{90} value of 4.2 s as the duration where an event has equal probability of being in the short or long class (von Kienlin et al., 2020) based on 2353 GRBs. We choose the E_{peak} parameter instead of hardness for separating LGRB and SGRB populations as it does not require set energy bands for a comparison to be made (Goldstein et al., 2010). In Figure 3.1 we presents a log-log plot of the T_{90} and E_{peak} parameter, for which we fit two log-normal distributions, one for each class, and the probability that an event is an SGRB is translated into a colour. From this analysis, the probability that GRB 200826A belongs to the short class is 74%.

GRB 200826A triggered Konus-*Wind* (KW) at $T_{0\mathrm{KW}} = 16195.106$ s UT (04:29:55.106). The propagation delay from Earth to *Wind* is 2.540 s for this GRB; correcting for this factor, the KW trigger time corresponds to the Earth-crossing time 16192.566 s UT (04:29:52.566). The burst light curve shows a multi-peaked pulse which starts at about $T_{0\mathrm{KW}} - 0.10$ s and has $T_{100} = 0.97$ s, $T_{90} = 0.67^{+0.13}_{-0.03}$ s, and $T_{50} = 0.28^{+0.04}_{-0.03}$ s measured in the 80–1300 keV band. Considering only the duration, the T_{90} and T_{50} of GRB 200826A are consistent with the short GRB population in the KW sample. The T_{90} and T_{50} durations at which a KW-detected GRB has an equal probability of being short- or long-duration are 2 s and 0.7 s, respectively (Svinkin et al., 2019). The spectral lag between the 20–80 keV and 80–330 keV 16 ms light curves is 30 ± 11 ms, consistent with the bulk of KW short GRBs (Svinkin et al., 2016).

During the burst, KW measured five spectra in the 20 keV–10 MeV band. The first four with 64 ms accumulation time cover the interval from $T_{0\mathrm{KW}}$ to $T_{0\mathrm{KW}} + 0.256$ s and the fifth, from $T_{0\mathrm{KW}} + 0.256$ s to $T_{0\mathrm{KW}} + 8.448$ s. The time-averaged spectrum of the burst (measured from $T_{0\mathrm{KW}}$ s to $T_{0\mathrm{KW}} + 8.448$ s) is best fit in the 20 keV–2 MeV range by the Band function with a low-energy photon index $\alpha = 1.26^{+1.91}_{-1.12}$, a high-energy photon index $\beta = -2.32^{+0.12}_{-0.15}$, and a spectrum peak energy $E_{peak} = 67^{+13}_{-11}$ keV (χ^2/d.o.f. = 50/59). The burst had a fluence of $4.60^{+0.71}_{-0.60} \times 10^{-6}$ erg cm^{-2}, and a 16-ms peak flux, measured from $T_{0\mathrm{KW}} + 0.544$ s, of $9.81^{+1.83}_{-1.64} \times 10^{-6}$ erg cm^{-2} s^{-1} (both in the 20 keV–10 MeV energy range). Using the spectroscopic redshift $z = 0.7481$ (Rothberg et al., 2020) we have estimated the following rest-frame parameters: the isotropic energy release E_{iso} is $7.17^{+1.11}_{-0.94} \times 10^{51}$ erg,

the peak luminosity L_{iso} is $2.67^{+0.50}_{-0.45} \times 10^{52}$ erg s^{-1}, and the rest-frame peak energy of the time-integrated spectrum, $E_{peak,z}$ is 117^{+23}_{-19} keV.

With these values, GRB 200826A is within the softest $\sim 1\%$ of KW short GRBs in terms of the observed $E_{peak,z}$ and is within the 1σ prediction band of both the 'Amati' and 'Yonetoku' relations based on 315 long/soft (Type II) GRBs with known z (Amati et al., 2002; Tsvetkova et al., 2021; Yonetoku et al., 2004). Furthermore, in the $E_{\rm iso}$-$E_{\rm peak,z}$ plane, GRB 200826A is inconsistent with the short-hard (Type I) GRB population (see Fig. 3.4). Thus, despite the short duration, the KW parameters of GRB 200826A imply that it belongs to the long/soft GRB population.

In addition to the IPN detections, the Cadmium Zinc Telluride Imager (CZTI (Bhalerao et al., 2017)) on board AstroSat also detected the burst. We reanalysed the data, combining data from all four quadrants to create 20–200 keV light curves with 0.05 s, 0.1 s and 0.2 s bins. All light curves show a single pulse, with hints of sub-structure in during the rise in the smaller time bins (see Fig. 3.4). We process the 0.05 s light curves with the CIFT pipeline (Sharma et al., 2020), which incorporates better data analysis as compared to the quick-look pipeline and produces more robust results. Our reanalysis yields a peak time of UT 04:29:52.95 - consistent with the *Fermi* peak. The new value of T_{90} is $0.94^{+0.72}_{-0.18}$ s, significantly shorter than the quick-look values reported in Gupta et al. 2020, but consistent with *Fermi* and Konus-*Wind*.

3.3.0.3 Optical

We ingested the GBM localization map into the GROWTH target-of-opportunity (ToO) marshal, an interactive tool design to plan and schedule ToO observations for ZTF (Coughlin et al., 2019c). The observation plan generated by the ToO marshal relies on `gwemopt` (Almualla et al., 2020; Coughlin et al., 2018, 2019a), a code that optimizes the telescope scheduling process for skymaps with a healpix format, like the *Fermi*-GBM maps. The `gwemopt` procedure involves slicing the skymap into predefined tiles of the size and shape of the ZTF field-of-view, determining which fields have the highest enclosed probability, and optimizing observations based on airmass and visibility windows. For this purpose, we used a modified version of the "greedy" algorithm described in Rana et al. 2017, implemented within `gwemopt`. The resulting optimized plan for the optical follow-up of GRB 200826A consisted of four primary ZTF fields and one secondary field[2]. The fields were observed in the r- and g-band for 300 s each, starting 4.9 hours after the GBM detection. The observing plan for the first night covered 186 deg^2, corresponding to 77% of the GBM region (see Fig. 3.2). Once the Konus-*Wind* data became available on ground at about 17:55 UT, the 288 arcmin^2 IPN error box was derived using Konus, GBM, and HEND data, which allowed the X-ray Telescope (XRT (Burrows et al., 2005)) on board *Swift* to initiate a ToO at about 20:45 UT. The IPN box was published later at about 21:30 UT (Hurley & et al., 2020).

Reference images of the fields are then subtracted from the ZTF ToO obser-

[2]The ZTF secondary fields are strategically located to cover the chip-gaps of the fields in the primary grid.

vations and any high significance difference ($>5\sigma$) generates an *alert* (Masci et al., 2019; Patterson et al., 2019) that contains relevant information about the transient. We queried the stream of alerts using three different tools: the GROWTH marshal (Kasliwal et al., 2019a), the Kowalski infrastructure (Duev et al., 2019)[3] and AMPEL (Nordin et al., 2019; Soumagnac & Ofek, 2018; Stein & Reusch, 2020; Stein et al., 2021)[4]. Our filtering scheme has been described in previous SGRB and GW searches (Coughlin et al., 2019c; Kasliwal et al., 2020b), but we summarize the main points here. We aim to identify sources that 1) are spatially coincident with the skymap, 2) are detected only after the GBM trigger, 3) are far from known bright sources, 4) are spatially distinct from Pan-STARRS 1 (PS1; Chambers et al. 2016b) stars (based on Tachibana & Miller 2018), 5) have at least two detections separated by at least 15 minutes to avoid moving objects, 6) have a real-bogus score (RB; Duev et al. 2019; Mahabal et al. 2019) greater than 0.15, and 7) showed an increase in their flux relative to the reference image. For each candidate passing these filters, we visually inspected the light curve, cross-matched with the PS1-DR2 catalog to check for previous activity, and cross-matched against the Wide-field Infrared Survey Explorer (WISE; Cutri et al. 2013) catalog to determine whether it was consistent with an active galactic nucleus (AGN) based on its position in the WISE color space (Assef et al., 2018; Stern et al., 2012; Wright et al., 2010). Additionally, we searched the Minor Planet Center (MPC) to ensure that our potential counterparts were not consistent with known solar system objects. Forced photometry (Yao et al., 2019)

[3] `https://github.com/dmitryduev/kowalski`
[4] `https://github.com/AmpelProject`

was performed using data from the 10 nights previous to the trigger, to remove young SNe from the sample. A final quality check was done by querying for alerts around each candidate, and rejecting transients that have multiple alerts within a radius of 15" as these alerts could suggest artifacts, ghosts, or slow-moving objects near the stationary points (Jedicke et al., 2016).

After the first night of observations 28195 alerts were generated in the region and 14 sources passed every stage of our filtering criteria (Sagues Carracedo et al., 2020). The SGRB afterglow, ZTF20abwysqy (Ahumada et al., 2020a), was not in our first selection as there was a ZTF alert 11" NE; however, it passed all the other filtering criteria. Two of the ZTF ToO fields triggered during the first night covered $> 99\%$ of the triangulated IPN region. However, none of the candidates reported in Sagues Carracedo et al. 2020 fell there. For our second night of observations, we scheduled 600 s observations in r- and g-band and queried the database.

3.3.0.4 Probability of Chance Coincidence

We roughly calculate the probability of chance coincidence (p) of this optical transient to be independent of GRB 200826A. For this we follow Stalder et al. 2017 and use Poissonian statistics to derive the probability for one or more events to be randomly coincident:

$$p = 1 - e^{-\lambda}$$

where λ is the product of three different values, $\lambda = \prod_{i=1}^{3} r_i$. For this study, we consider r_1 to be the time window between the last ZTF non-detection (0.72 days before the trigger time) and the time of the detection (0.21 days, see Table 3.1),

resulting in $r_1 = 0.93$ days. The parameter r_2 is the rate of *Fermi* GRBs, which from the latest GBM catalog (von Kienlin et al., 2020) gives ~ 0.65 bursts per day. Finally r_3 is the ratio between the total IPN area (288 arcmin^2) and the sky. This derivation gives a $p = 1.16 \times 10^{-6}$, and allows us to rule out a random association between the GRB and the afterglow at the 4.87σ level.

3.3.1 Follow-up

This section describes the panchromatic follow-up of the afterglow of GRB 200826A, along with the details on the facilities, instruments, and configurations used to acquire data. This data was later used to model the afterglow emission and test the KN and SN hypotheses. The summary of the follow-up results can be found in Tables 3.1, 3.3, and 3.4.

3.3.1.1 Optical/NIR

Here we present our optical and near infrared (NIR) follow-up results. In addition to our observations, MASTER (Lipunov et al., 2005) and Kitab follow-up with a clear filter (Belkin et al., 2020; Lipunov et al., 2020) led to upper limits of 18.3 mag and 20.4 mag respectively.

Las Cumbres Observatory. We performed follow-up of ZTF20abwysqy with the Spectral camera mounted at the 2-m Faulkes Telescope North (FTN), located at Haleakala Observatory. Starting on 2020-08-28 11:32:26 UT we acquired three sets of images with 300 s exposures each in g- and r-bands through the LCO observation portal[5]. Furthermore, we obtained a second (reference) epoch in g- and r-bands

[5] `https://observe.lco.global/`

on 2020-09-02 UT. Our images were reduced by an automatic subtraction pipeline. Our pipeline retrieves images from LCO, stacks them, extracts sources from the image using `Source Extractor` (Bertin & Arnouts, 1996) and performs photometric calibration of sources using the PS1 catalog. Then, the pipeline performs image subtraction using the High Order Transform of Psf ANd Template Subtraction code (HOTPANTS; Becker 2015) to subtract a PSF-scaled reference image aligned using `SCAMP` (Bertin, 2006). Our photometry measurements reported in g- and r-band were determined after host subtraction using the LCO reference images in the same filters acquired on 2020-09-05.

Hale Telescope. We obtained two epochs of dithered J-band imaging with the Wide Field Infrared Camera (WIRC; Wilson et al. 2003) on the Palomar Hale 200-in (P200) telescope on 2020-08-28 UT and on 2020-09-04 UT, spending an hour integrating on target during each epoch. We reduced the images using the image reduction pipeline described in De et al. 2020b. Images were aligned and stacked using `SWarp` (Bertin et al., 2002) and calibrated against the 2MASS catalog. Image subtraction between the two epochs was performed using the method described in De et al. 2020c to derive flux measurements and its uncertainty for the first epoch.

Gran Telescopio Canarias. The 10.4m Gran Telescopio Canarias (GTC) (+OSIRIS) obtained spectroscopic observations starting on August 30, 04:30 UT. Two 1200s exposures were gathered with the R1000B grism and one 1200s exposure was obtained with the R2500I grism, in order to cover the entire 3700–10000 Å range. The slit was placed covering the position of the potential host galaxy. Standard routines from the Image Reduction and Analysis Facility (IRAF) were used to

reduce the data.

Lowell Discovery Telescope. We used the Large Monolithic Imager (LMI (Massey et al., 2013)) mounted on the 4.3m Lowell Discovery Telescope (LDT) to observe the optical transient ZTF20abwysqy on three different nights: August 29, September 13, and September 19 (3.2, 18.1 and 24.2 days after the GRB trigger). Observations were conducted with an average airmass of 1.0 while the seeing varied from 1.1 arcsec for the first night to 1.4 arcsec and 1.6 arcsec for the second and third night, respectively. We took 8 exposures of 180 s in the r-band on August 29. Images were taken with different filters on September 13: 5 exposures of 180 s in u-band, 4 exposures of 180 s in g-band, 6 exposures of 180 s in i-band and 6 exposures of 180 s in z-band. Finally, 10 exposure of 150 s in the i-band and r-band were taken during the last night of observations on September 19. We used standard procedures to perform bias and flat-field correction. The astrometry was calibrated against the SDSS catalog (release DR16; Ahumada et al. 2020a) and frames were aligned using `SCAMP` and stacked with `SWarp`. After stacking the images, we extracted sources using `Source Extractor` and the magnitudes were calibrated against 45 PS1 stars in the field on average. We used HOTPANTS to perform image subtraction between the first and third epochs and found a source in the r-band at the location of ZTF20abwysky with a magnitude of 24.46±0.12 mag (see Table 3.1). We determine the magnitudes of the host galaxy using the second epoch of observations. To verify this result, we used the 80 days i-band GMOS-North (see description in the paragraph below) as a reference and the HOTPANTS subtraction shows a source with r-band magnitude of 24.76±0.23 mag, consistent with the result

using the LDT reference.

Gemini Observatory. We acquired images of the transient location on September 23, October 10, and November 7 corresponding to 28.28, 46.15 and 80.23 days after the GRB trigger respectively, which we denote as epoch 1, 2, and 3. We used GMOS-North, mounted on the Gemini North 8-meter telescope on Mauna Kea, under the approved Director's Discretionary Time (DDT) proposal DD-104 (P.I.: L. Singer). The host galaxy coordinates, in the Gemini images, are $\alpha = 00^d27^m08.5557^s$, $\delta = +34^d01^m38.634^s$.

The first set of observations (epoch 1) was scheduled to be closest in time to a SN1998bw-like peak without suffering from moon illumination. All three sets of observations consisted of 14 200 s r- and i-band exposures, with a position angle of 45° to avoid blooming from neighboring bright stars. The average airmass for the observations was $\sim$1.0 and the seeing was stable throughout the three epochs, at 0.7 arcsec, 0.5 arcsec, and 0.85 arcsec. The images were later reduced using DRAGONS[6] (Labrie et al., 2019), a Python-based data reduction platform provided by the Gemini Observatory.

We extracted sources using `Source Extractor` and determined a photometric zero point using 23 PS1 stars in the field. Using the ZOGY (Zackay et al., 2016) algorithm-based python pipeline, we performed image differencing on Gemini data. The pipeline makes use of `Source Extractor`, `PSFEx` (Bertin, 2011), `SWarp`, `SCAMP`, and `PyZOGY` (Guevel & Hosseinzadeh, 2017) to perform image subtraction. We took a 1300 pix × 1300 pix sized cutout for both the science and reference images, centered

[6] `https://dragons.readthedocs.io/`

at the ZTF20abzwysqy position in the image in order to achieve good subtraction quality, as the images were affected by background variation. Sources were extracted using `Source Extractor` from both science and reference images with a 5-σ detection threshold. The resulting catalogues were fed to `SCAMP`, which calculates and corrects for the astrometric errors in both science and reference catalogues with the help of a Gaia data release 2 catalogue (Gaia Collaboration et al., 2018) for the same field. Using `SWarp`, images are then re-sampled to subtract the background and the point-spread function (PSF) of the images. `Source Extractor`-generated weight maps were used as input to the `SWarp` to generate variances, which when added with the images' Poisson noise in quadrature, which results in the root mean square (rms) image. We select good sources from `Source Extractor` catalogues based on their S/N, full width at half-maximum (FWHM) and `Source Extractor` flag values. Sources which raised a `Source Extractor` flag were discarded. These sources were used to match the flux level of the images. We used `PSFEx` to extract the PSF model of the re-sampled images with the `Source Extractor` catalogue as input to `PSFEx`. The rms images, re-sampled images, PSF models and astrometric uncertainty are used as input to `PyZOGY`, which generate the difference image and a corrected score image as final products (Zackay et al., 2016). A source is detected with a ZOGY corrected score of 4 in the i-band, at the location of the transient. With ZOGY, we derive an i-band magnitude of 25.49$\pm$0.12 mag for epoch 1. No source is detected in the r-band of epoch 1 nor in any band in epoch 2.

We have confirmed the ZOGY-based results using an independent image subtraction pipeline, FPipe (Fremling et al., 2016), which is based on empirically mea-

suring the PSFs of the science and reference images and matching them using the common PSF method (CPM (Gal-Yam et al., 2008)). We detect the source with an i-band brightness of 25.45±15 mag in epoch 1. The results agree within uncertainties with the ZOGY-based subtractions. We do not detect the source in the r-band up to a 5-σ limit of $r > 25.6$ mag for epoch 1. No source is detected in either filter during epoch 2 up to a 5σ upper limit of $i > 25.4$ mag and $r > 25.5$ mag (Ahumada et al., 2020c) (see Figure 3.3).

Therefore, using two independent image subtraction pipelines, we confirm the detection of a source in the i-band, at the location of the transient.

3.3.1.2 UV/X-ray

Swift began observing the IPN localization region of GRB 200826A 0.7 days after the trigger. The last two observations were ∼4 ks and triggered as ToO observations. The XRT data was reduced by the online reduction pipeline [7] (Evans et al., 2007, 2009). As the hardness ratio remains constant within error bars, we assume a single absorbed power law spectrum, with a Galactic neutral hydrogen column (Willingale et al., 2013) of to $6.02 \times 10^{20}\mathrm{cm}^{-2}$. We convert the count rates (see Table 3.3) to flux density at an energy of 1 keV, using the parameters derived by the *Swift* pipeline: a photon index of $\Gamma_X = 1.5^{+0.7}_{-0.5}$, an intrinsic host absorption of $n_{H,int} = 6^{+32}_{-6} \times 10^{20}\mathrm{cm}^{-2}$, and an unabsorbed counts-to-flux conversion factor of 4.27×10^{-11} erg cm^{-2} ct^{-1}.

The first UV/Optical Telescope (UVOT) observations of ZTF20abwysqy was

[7] `https://www.swift.ac.uk/xrt_curves/00021028/`

∼1.6 days after the burst and the detection in the white filter was associated to the underlying galaxy (D'Ai et al., 2020).

3.3.1.3 Radio

For the afterglow modeling, we additionally use data reported by Alexander et al. 2020. They measure a flux density of ~ 40 μJy at a mean frequency of 6 GHz using the Karl G. Jansky Very Large Array (VLA), 2.28 days after the trigger. We observed GRB 200826A in band-5 (1050–1450 MHz) of the upgraded Giant Metrewave Radio Telescope (uGMRT (Gupta et al., 2017)) on 2020-09-09 15:41:30.5 UT and 2020-09-14 23:38:25.5 UT ($\sim$ 14.5 and $\sim$ 19.8 days after the burst respectively) under the approved DDT proposal ddtC147 (P.I.: Poonam Chandra). The data was recorded with the GMRT Wideband Backend (GWB) correlator with a bandwidth of 400 MHz divided in 2048 channels, with the central frequency of 1250 MHz. The total on-source time was ∼75 mins with overheads of ∼30 mins. 3C48 was used as the flux and bandpass calibrator and J0029+349 was used as the phase calibrator. We used standard data reduction procedures in Common Astronomy Software Applications (`CASA`) (McMullin et al., 2007) for analysing the data. The dead antennas were first flagged by manual inspection and the end channels were flagged due to low gain. The automatic flagging algorithms incorporated into the `CASA` task *flagdata* were used to remove most of the Radio Frequency Interference (RFI). Any remaining corrupted data were then flagged manually. The calibrated data was then imaged and self-calibrated to get the final image. The synthesized beam for the final image was ∼4 arcsec×2 arcsec. We found no evidence of radio emission at

the GRB position on both days. The 3σ upper limits were 48.6 μJy/beam for the observations taken on 2020-09-09 (Chandra et al., 2020) and 57.4 μJy/beam for the observations taken on 2020-09-14.

3.3.2 The Host Galaxy

Our GTC spectra of the host galaxy show strong [OII] and [OIII] features at $z = 0.748$, in agreement with a previous report based on data from the Large Binocular Telescope Observatory (LBTO) (Rothberg et al., 2020).

We modeled the GTC spectrum with the Penalized Pixel-Fitting (pPXF) (Cappellari, 2017) to infer the properties of the host galaxy's stellar populations, resulting in a fit with $\chi^2_\nu = 1.011$. The pPXF results confirmed the [OII] features at 3726Å and [OIII] lines at 4959Å and 5007Å, indicators of recent star-formation and young, hot stars. The stellar population age derived from the weighted ages of the templates is $1.514^{+3.83}_{-0.85}$ Gyr, with evidence for a younger $\sim$0.1 Gyr population (see Figure 3.5 and Table 3.6).

Additionally, we corrected the magnitudes of the host galaxy (see Table 3.2) using foreground extinction maps (Schlafly & Finkbeiner, 2011) and fed them to `Prospector` (Johnson et al., 2019), to model the SED of the host galaxy. `Prospector` uses `fsps` (Conroy & Gunn, 2010; Conroy et al., 2009) to generate multiple stellar populations, and fits the observed photometry to determine the formed mass of the galaxy, age, and intrinsic extinction among other parameters, using the WMAP9 cosmology (Hinshaw et al., 2013) internally. We fitted the photometry to a galaxy using the Chabrier (Chabrier, 2003) initial mass function (IMF), the Calzetti

(Calzetti et al., 2000) extinction curves for the dust around old stars, and a star formation history (SFH) with the form of $te^{-t/\tau}$. Our results using the nested sampling `dynesty` (Speagle, 2020) algorithm, gave a galactic stellar mass distribution of $M_{gal} = 4.64 \pm 1.67 \times 10^9\, M_\odot$, a mass-weighted galactic age of $t_{gal} = 1.08^{+1.28}_{-0.72}$ Gyr, a metallicity of $log(Z/Z_\odot) = -1.06^{+0.67}_{-0.48}$, a dust extinction of $A_V = 0.34^{+0.33}_{-0.22}$, and a star formation rate (SFR) of $4.01^{+41.87}_{-3.59}$ $M_\odot$ yr^{-1} (see the resulting SED in Fig. 3.5 and the posterior probability distributions for the free parameters in Fig. 3.6). We derived the SFR and weighted-mass age following similar studies on GRB host galaxies (Nugent et al., 2020; O'Connor et al., 2021; Paterson et al., 2020), and the stellar mass from the mass fraction derived with `Prospector`.

3.3.3 Modeling

For the modeling of the multiwavelength emission, all optical and NIR observations were from difference images and were corrected for foreground extinction (Schlafly & Finkbeiner, 2011).

3.3.3.1 The afterglow

In the standard synchrotron fireball model a power-law energy distribution characterized by the index p, $N(E) \propto E^{-p}$, results in a SED described by a series of broken power laws (Granot & Sari, 2002; Sari et al., 1998). The frequencies at which the broadband SED presents its breaks are the self-absorption frequency ν_a, the synchrotron frequency ν_m, and the cooling frequency ν_c.

The temporal decline of both the optical and X-ray data during the first four days can be described by a single power law model which suggests the jet-break

has not yet occurred. Our ZTF g-band observations are the most constraining in the optical therefore we use these to estimate the temporal decline rate $\alpha_{\rm o} = -1.05 \pm 0.13$. We use the 1 keV XRT data to find $\alpha_{\rm x} = -0.89 \pm 0.07$. The similar slopes between the optical and X-ray observations suggest the location of the cooling break frequency, ν_c, lies beyond X-ray frequencies. Therefore, we estimate the spectral index at $\sim$1 day between the X-ray and optical as $\beta_{\rm ox} = -0.67 \pm 0.02$.

We now use $\alpha_{\rm o}$ and α_x to estimate the power law index of the electron energy distribution, p, and to determine the circumburst density profile. In a constant density (ISM-like) medium $\alpha_{\rm ISM} = \frac{3(1-p)}{4}$ ($\nu < \nu_c$), which gives $p_{\rm o} = 2.44 \pm 0.17$ and $p_{\rm x} = 2.17 \pm 0.10$ (Zhang et al., 2006). In the wind-like scenario $\alpha_{\rm wind} = \frac{(1-3p)}{4}$, which gives $p_{\rm o} = 1.78 \pm 0.17$ and $p_{\rm x} = 1.50 \pm 0.10$. The optical to X-ray spectral index $\beta_{\rm ox}$ gives an estimate for p of 2.34 ± 0.04 ($\beta = \frac{1-p}{2}$). Theoretical studies of relativistic collisionless shocks predict $p \gtrsim 2$ and particularly $p \sim 2.2$ in the ultra-relativistic limit (Sironi et al., 2015). Given the low values of p for the wind-like scenario we choose to assume an ISM-like density profile and $p \sim 2.4$ throughout this work.

We note the possibility of a wind-like environment with $p < 2$ and a spectral break ν_c between the optical and X-rays. Such a scenario would not change the predicted optical and NIR emission and it would be unable to account for the late GMOS i-band detection without an additional component. However, this scenario may allow for a better fit of the afterglow X-ray evolution, which would decay at a rate shallower than the optical by $\Delta\alpha = 0.25$. We do not consider this scenario further because of the theoretically disfavored value of p.

3.3.3.2 Bayesian afterglow modeling

We now use Bayesian inference to analyze the X-ray, optical, NIR, and radio counterpart. We use two independent pipelines, one using Markov chain Monte Carlo (MCMC) based on the `EMCEE` Python package (Foreman-Mackey et al., 2013) and one using nested sampling based on `PyMultinest` (Buchner et al., 2014). The pipelines use different priors and implementations, but arrive at consistent results. Both utilize the `afterglowpy` python package (Ryan et al., 2020) to estimate the physical parameters of the multi-wavelength afterglow. `afterglowpy` is a public, open-source computational tool which models forward shock synchrotron emission from relativistic blast waves as a function of jet structure and viewing angle. Descriptions of the MCMC implementation may be found in Refs. (Cunningham et al., 2020; Troja et al., 2018) and the nested sampling implementation in Dietrich et al. 2020.

For this work we assume Gaussian statistics for the optical and radio data, while assuming Poissonian statistics (via the C-statistic; Cash 1979) for the X-ray data due to low detector counts. The `afterglowpy` model is parametrized by the isotropic kinetic energy, $E_{\rm K,iso}$; jet collimation angle, θ_c; viewing angle, θ_v; the circumburst constant density, n; the spectral slope of the electron distribution, p; the fraction of energy imparted to both the electrons, ϵ_e, and to the magnetic field, ϵ_B, by the shock. The redshift and luminosity distance of the source are held fixed.

Our modelling of the host indicates a small galaxy of stellar mass $\sim 5\times10^9 M_\odot$ with moderate extinction $A_V = 0.34^{+0.33}_{-0.22}$ (see §3.3.2 for details). In the MCMC

implementation, we incorporate a Small Magellanic Cloud-like host extinction correction with total-to-selective extinction $R_V = 2.93$ (Pei, 1992) implemented with the `dust-extinction` software package (Robitaille et al., 2013). We leave the color excess $E(B-V)$ as a free parameter, with a prior distribution computed from the A_V posterior found from modelling the host galaxy. This posterior is similar to the distribution of host extinction values observed in LGRBs with well-sampled multi-band photometry (Littlejohns et al., 2015; Schady, 2015; Zafar et al., 2018). The nested sampling implementation performs no extinction correction.

Using a top hat model for the jet structure, we perform a search over the parameter space by allowing all the parameters $E_{\rm K,iso}$, θ_c, θ_v, n, p, ϵ_e, ϵ_B, and $E(B-V)$ to vary with broad priors. We report only the MCMC results, although the nested sampling results are consistent. Given both the highly degenerate nature of the afterglow fitting and the low number of observations available, some of the parameters are not particularly constrained. One exception is the spectral slope of the electron distribution, for which we find $p = 2.4 \pm 0.04$, consistent with the analytical results. The uncertainty in the circumburst density, $n = 5.5^{+187.3}_{-5.4} \times 10^{-2}\,{\rm cm}^{-3}$, includes typical ranges for both SGRBs and LGRBs. We find very little reddening from the host, $E(B-V) = 2.5^{+4.8}_{-2.3} \times 10^{-2}$. The posterior probability distributions are shown in Fig. 3.8 and the parameter estimates are listed in 3.7.

3.3.3.3 Bayesian model selection

In addition to an afterglow-only model, we consider an afterglow plus a KN and an afterglow plus a SN.

Kilonova. We use SEDs simulated by the multi-dimensional Monte Carlo radiative transfer code `POSSIS` (Bulla, 2019). The simulations are performed over a grid of KN parameters: dynamical ejecta $M_{\rm ej}^{\rm dyn}$, disk wind ejecta $M_{\rm ej}^{\rm wind}$, opening angle Φ, and the observation angle $\Theta_{\rm obs}$ (see Dietrich et al. 2020 for details). We use Gaussian process regression (Coughlin et al., 2018, 2020a) to interpolate the model, enabling rapid parameter inference.

Supernova. The SN model starts with a bicubic spline in time and frequency, $L_\nu^{\rm SN}(t,\nu)$, that interpolates a K-corrected SN1998bw template (Clocchiatti et al., 2011). We apply to the template a scale factor, k, and a stretch factor, s, which are drawn from a bivariate normal distribution that is consistent with a historical sample of GRB-SNe (Cano et al., 2017; Klose et al., 2019). The model for the observed flux density is

$$F_\nu^{\rm SN}\left(t_{\rm obs},\nu_{\rm obs}\right) = \frac{(1+z)k}{4\pi {d_{\rm L}}^2} L_\nu^{\rm SN}\left(\frac{t_{\rm obs}}{(1+z)s},(1+z)\nu_{\rm obs}\right).$$

We perform Bayesian model selection to determine which model best explains the data. We used the nested sampling pipeline to calculate the Bayesian evidence for each of the three models. The Bayes factor, or the ratio of the evidences, between the afterglow-plus-KN model and the afterglow-only model is ~ 1, indicating that neither model is strongly favored over the other, because the KN contributes negligible flux compared to the afterglow at the time of the GMOS observation. The Bayes factor between the afterglow-plus-SN model and the afterglow-only model is $\sim 10^{5.5}$, strongly favoring the presence of a SN.

To better understand the source of discriminating power between models, we

carry out a posterior predictive check. Here, we sample the posterior while excluding the GMOS i-band data point and then predict its value using the rest of the data. The posterior predictive distribution of the AB magnitude for the GMOS i-band detection both with and without the inclusion of a SN contribution is shown in Fig. 3.9. The fit with the SN is consistent with the observation, while the fit without the SN is inconsistent at the $\sim 5\sigma$ level. Therefore, inclusion of the GMOS i-band data point requires a SN component, confirming a collapsar origin.

We compared our GMOS-N detection against extinction-corrected i-band fluxes of three GRB-KN candidates found in the literature (Kasliwal et al., 2017b); using photometry from GRB 130603B (Berger et al., 2013) and GRB 160821B (Kasliwal et al., 2017a; Troja et al., 2019), and the compiled light curve of AT2017gfo (Coulter et al., 2017; Villar et al., 2017), we correct to the redshift of GRB 200826A. We fit each light curve to the best-fit 2D model of GW170817 (Dietrich et al., 2020) from `POSSIS` using SNCosmo (Barbary et al., 2016) and extract the corresponding i-band magnitude at a rest-frame time of 16 days. At $z = 0.748$, both AT2017gfo and GRB 160821B would be at M≈ -10 mag, $\sim$8 mags fainter than our detection. GRB 130603B does not have enough late-time detections at the same phase for comparison.

Our detection of a source with an extinction-corrected absolute magnitude in the i-band with $M_i = -18.0$ is consistent with the population of collapsars associated with LGRBs. A typical SN Ic reaches its peak magnitude 10 to 20 days post-burst, at $M_B = -17.66 \pm 1.18$ mag (Richardson et al., 2014). Fig. 3.3 shows K-corrected light curves for three well-sampled GRB-SNe: SN1998bw, one of the

brightest; SN2006aj and SN2010bh, among the faintest.

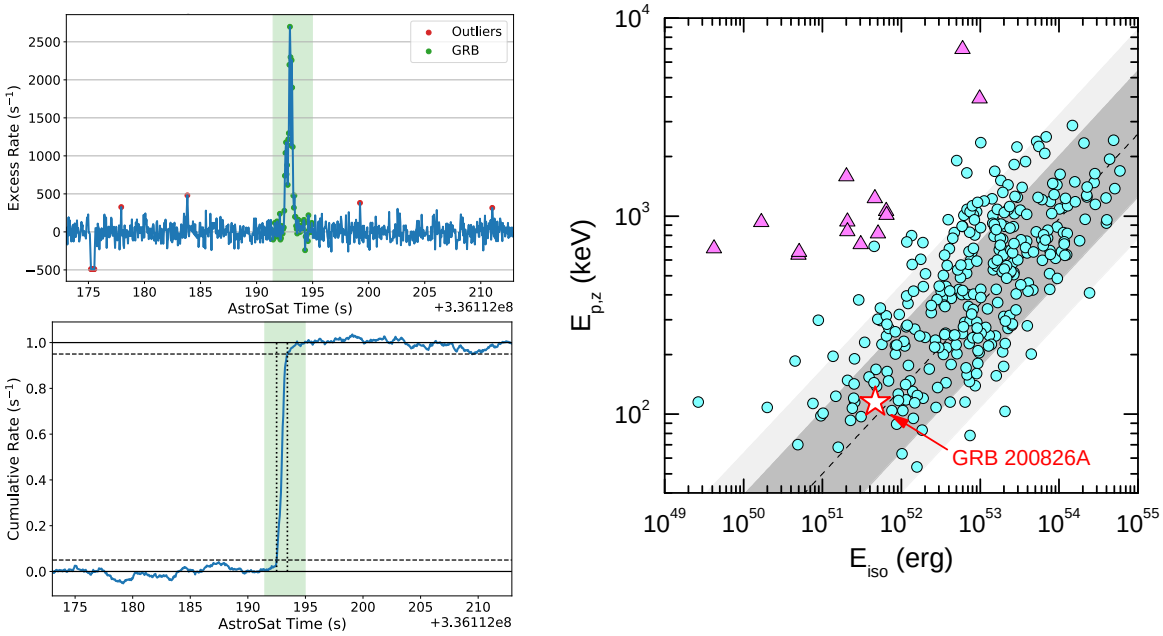

Figure 3.4: **The AstroSat and Konus-*Wind* gamma-ray detections.** (*left*) Upper panel: The de-trended light curve (blue) for GRB 200826A obtained from AstroSat CZTI data. We combined data from all four CZTI quadrants and binned it in 0.05 s bins. We fit and subtract a quadratic trend from the background to obtain zero-mean data. The shaded green region and corresponding green symbols denote a conservative GRB time span excluded from background trend estimation. Similarly red points denote outliers that are automatically flagged and rejected from the background estimate. Lower panel: A cumulative light curve (blue) obtained by summing the de-trended data, and normalised such that the median post-GRB value is 1.0. The dashed horizontal lines denote the 5% and 95% intensity levels. The corresponding vertical dotted black lines denote T_{05} and T_{95}, yielding T_{90} of $0.94^{+0.72}_{-0.18}$ s. (*right*) Rest-frame energetics of 331 Konus-*Wind* GRBs (SGRB: triangles, LGRB: circles) with known redshift in the $E_{\rm iso}$—$E_{\rm peak,z}$ plane, with $E_{\rm peak,z}$ the rest frame $E_{\rm peak}$. The hardness-intensity ('Amati') relation for LGRBs is plotted with its 68% and 90% prediction intervals (dark and light gray regions, respectively). GRB 200826A, as a red star, appears not to be consistent with the SGRB population.

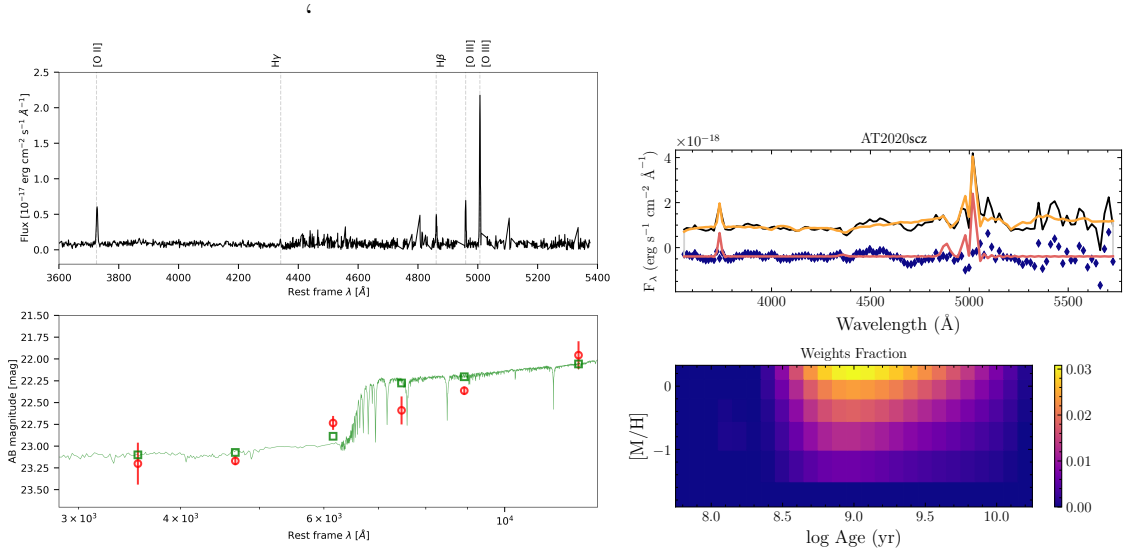

Figure 3.5: **The Host Galaxy.** (*left*) In the upper panel, we show the GTC spectrum of the host galaxy and the lines used to determine a redshift of 0.748. In the bottom panel, the photometry of the host galaxy (*ugrizJ*, see Table 3.2) in the AB system is presented in red circles. The SED model and photometry from `Prospector` are shown in green. (*right*) The pPXF host galaxy model results described in Sec. 3.3.2. (top) The integrated spectrum (black) overlaid with the best-fit spectrum (orange), which sums the contributions of stars and gas in the modeled galaxy. The red spectrum shows the gas contribution to the spectrum, and the blue diamonds show the residuals to the fit. The gas is offset by 1.59e-18 erg s^{-1} cm^{-2}. (bottom) The pPXF weights (color bar) of the different stellar population templates used to construct the best-fit galaxy.

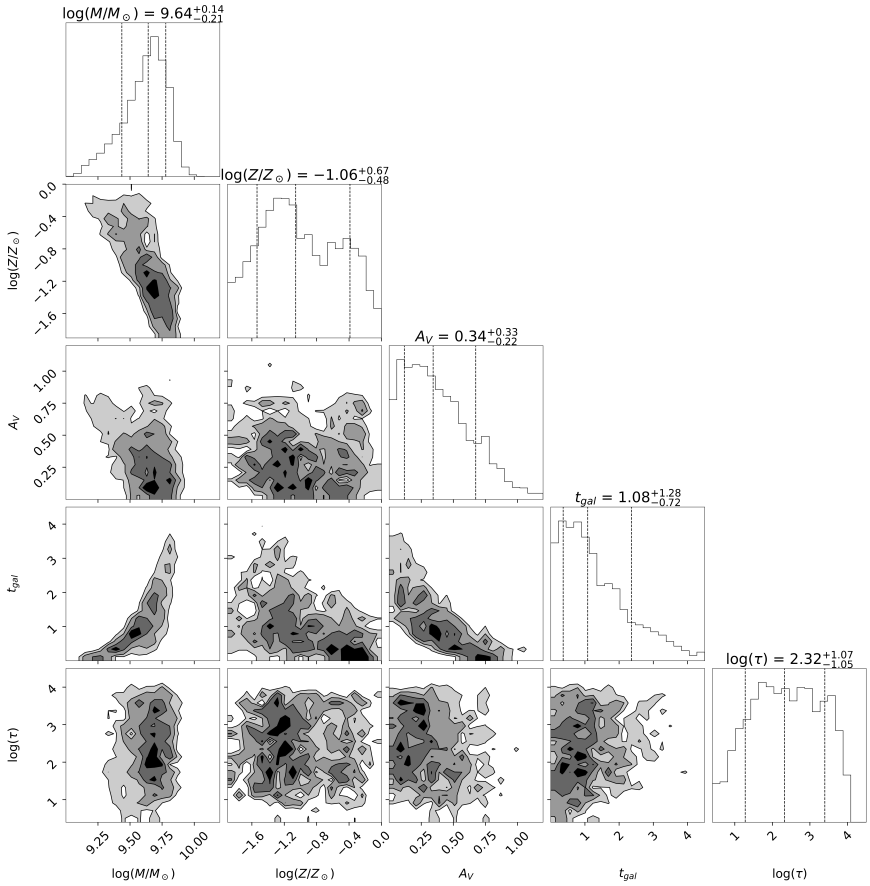

Figure 3.6: **Posterior distribution of the `Prospector` parameters.** The covariances and posterior probability distributions of: the log of the host galactic stellar mass in units of $M_\odot$, the log of the metallicity (Z) of the host galaxy in units of $Z_\odot$, the dust extinction in the V-band (A_V) in mags, the mass-weighted galactic age (t_{gal}) in Gyr, and the log of the e-folding time for the SFH (τ) in Gyr. The contours show the 1σ to the 4σ levels of the distributions, while the dotted lines in the histograms indicate the 14, 50, and 84 percentiles of the distributions.

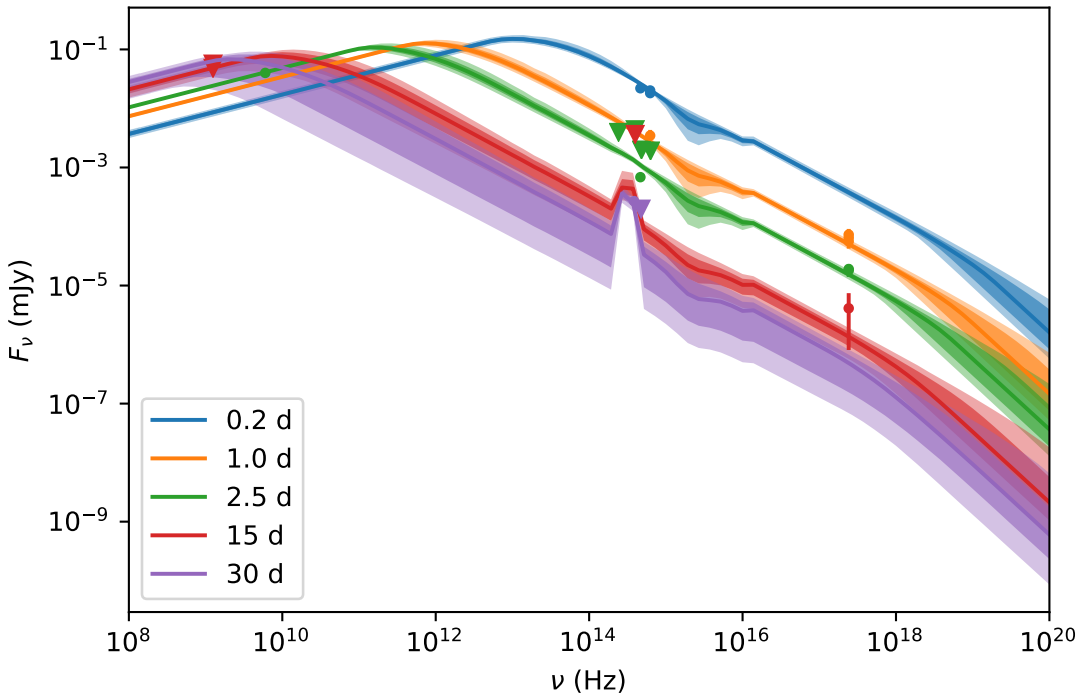

Figure 3.7: **SED sequence of the afterglow.** The SED of our model compared to observations at five epochs. Multiwavelenght data are shown as circles along their uncerntainties (1σ), while the 5σ upper-limits are shown as triangles. The shaded regions correspond to the 5th to 95th percentiles of the best fitting model. The cooling frequency ν_c is located at frequencies higher than 1 keV (i.e. $\nu_c > 2.4 \times 10^{17}$ Hz). The glitches at optical $\nu \sim 10^{16}$ Hz are the edge of validity of our dust extinction model. The SN makes a large contribution at late times. See the observations in Table 3.1, 3.3, and 3.4.

This work was supported by the GROWTH (Global Relay of Observatories Watching Transients Happen) project funded by the National Science Foundation under PIRE Grant No 1545949. GROWTH is a collaborative project among California Institute of Technology (USA), University of Maryland College Park (USA), University of Wisconsin Milwaukee (USA), Texas Tech University (USA), San Diego State University (USA), University of Washington (USA), Los Alamos National Laboratory (USA), Tokyo Institute of Technology (Japan), National Central University (Taiwan), Indian Institute of Astrophysics (India), Indian Institute of Technology

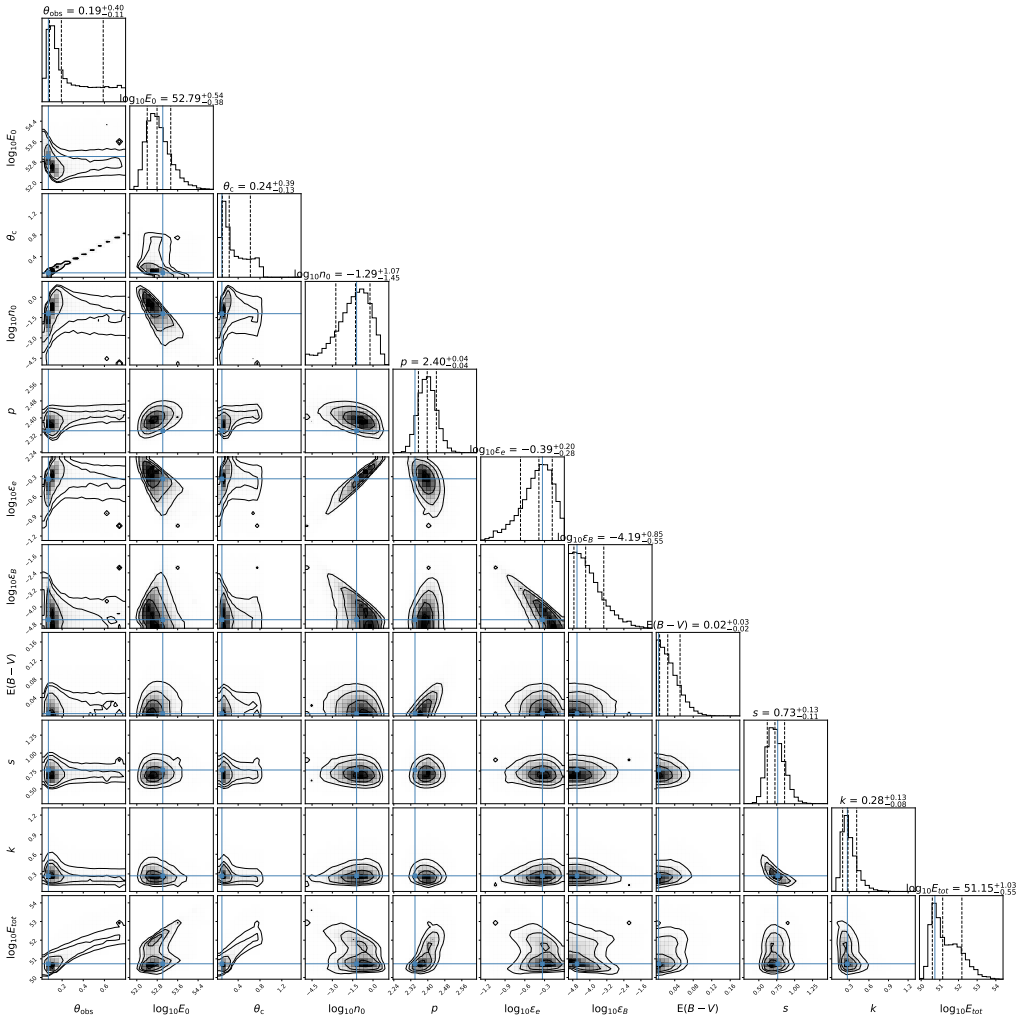

Figure 3.8: **Posterior distribution for the `afterglowpy` fit.** The covariances and posterior probability distributions of the parameters for the top hat jet afterglow with 1998bw-like SN model described in §3.3.3. The afterglow parameters are the viewing angle $\theta_{\rm obs}$ (rad), on-axis isotropic kinetic energy E_0 (erg), opening angle θ_c (rad), circumburst number density n_0 ($\rm cm^{-3}$), electron spectral index p, fraction of energy in accelerated electrons ϵ_e, and fraction of energy in magnetic field ϵ_B. We assume an SMC-like extinction curve with variable $E(B-V)$. The SN model is a 1998bw template with variable stretch s and scale k. The total beaming-corrected kinetic energy in the jet $E_{\rm tot}$ (erg), computed from the afterglow parameters, is also reported. The histograms denote the 14, 50, and 84 percentiles of the distributions, with blue lines marking the solution with maximum posterior probability density.

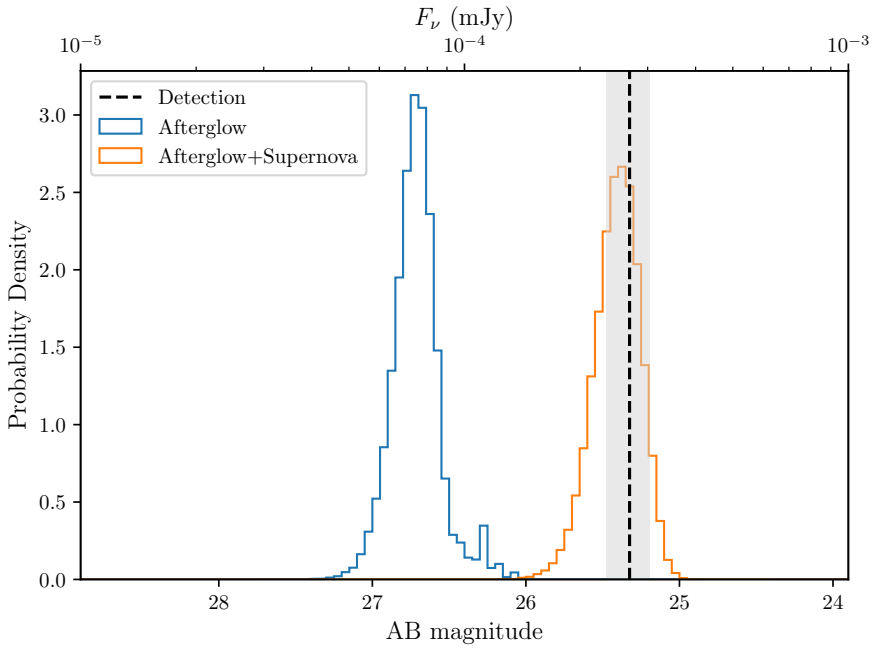

Figure 3.9: **Posterior predictive plot for the GMOS i-band detection.** The posterior of the AB magnitude estimated at the time of the i-band data point ($\sim$ 28 days after the trigger) using afterglow only (blue) and afterglow-and-SN (orange) light curves are shown. The dashed black line shows the magnitude of the transient at $\sim$ 28 days, an the grey area its 1σ uncertainty.

Julian day	δt	**Instrument**	**Filter**	**AB magnitude**	σ_{mag}	**5σ Limiting magnitude**	**A$_\nu$**
2459085.8814	-1.81	P48+ZTF	g	–	–	21.50	0.21
2459085.9678	-1.72	P48+ZTF	r	–	–	21.46	0.15
2459086.9011	-0.79	P48+ZTF	r	–	–	21.33	0.15
2459086.9696	-0.72	P48+ZTF	g	–	–	21.31	0.21
2459087.8986	0.21	P48+ZTF	g	20.86	0.04	22.50	0.21
2459087.9181	0.23	P48+ZTF	r	20.69	0.05	22.27	0.15
2459087.9651	0.28	P48+ZTF	g	20.95	0.16	21.23	0.21
2459088.8340	1.15	P48+ZTF	g	22.75	0.26	22.53	0.21
2459088.9038	1.22	P48+ZTF	r	–	–	21.30	0.15
2459088.9761	1.29	P48+ZTF	g	–	–	21.2	0.21
2459089.6256	1.93	P200+WIRC	J	–	–	21.8	0.06
2459089.9585	2.27	FNT+LCO	r	–	–	23.30	0.15
2459089.9698	2.28	FNT+LCO	g	–	–	23.41	0.21
2459090.9200	3.23	LDT+LMI	r	24.46	0.12	26.37	0.15
2459115.9675	28.28	Gemini+GMOS	i	25.45	0.15	25.9	0.11
2459115.9675	28.28	Gemini+GMOS	r	–	–	25.4	0.15
2459133.8039	46.11	Gemini+GMOS	i	–	–	25.5	0.11
2459133.8039	46.11	Gemini+GMOS	r	–	–	25.7	0.15

Table 3.1: **Afterglow panchromatic observations.** Observations of the GRB 200826A afterglow and SN. GRB 200826A was triggered at Julian day 2459087.6874. The δt column shows the days from the trigger date.

Julian day	δt	Instrument	Filter	Host AB magnitude	σ_{mag}	A_ν
2459089.62569	9.73	P200+WIRC	J	21.11*	0.16	0.05
2459105.80457	18.11	LMI+LDT	u	23.45	0.24	0.28
2459105.80457	18.11	LMI+LDT	g	23.36	0.05	0.22
2459105.80457	18.11	LMI+LDT	r	22.86	0.18	0.15
2459105.80457	18.11	LMI+LDT	i	22.66	0.16	0.11
2459105.80457	18.11	LMI+LDT	z	22.13	0.05	0.09

Table 3.2: **Host galaxy panchromatic data.** Observations of the host galaxy of GRB 200826A. The δt column shows the days from the trigger. *Magnitudes are in the Vega system.

Julian day	δt	Instrument	Energy range	Count rate [s^{-1}]
2459088.386616	0.70	XRT	0.3–10 keV	$2.16^{0.53}_{-0.53} \times 10^{-2}$
2459088.441940	0.75	XRT	0.3–10 keV	$1.91^{0.49}_{-0.49} \times 10^{-2}$
2459088.522328	0.83	XRT	0.3–10 keV	$1.66^{0.41}_{-0.41} \times 10^{-2}$
2459089.437860	1.75	XRT	0.3–10 keV	$5.64^{1.21}_{-1.21} \times 10^{-3}$
2459090.285972	2.60	XRT	0.3–10 keV	$5.36^{1.22}_{-1.22} \times 10^{-3}$
2459094.090850	6.40	XRT	0.3–10 keV	$3.33^{0.77}_{-0.77} \times 10^{-3}$
2459104.352156	16.66	XRT	0.3–10 keV	$1.22^{0.98}_{-0.67} \times 10^{-3}$

Table 3.3: **Afterglow X-ray detections.** X-ray observations of GRB 200826A. The δt column shows the days from the trigger.

Julian day	δt	Instrument	Frequency	Flux [erg cm^{-2} s^{-1}]
2459089.967407	2.28	VLA	6 GHz	40 **
2459102.153825	14.46	GMRT	1.256 GHz	< 48.6
2459107.485017	19.79	GMRT	1.256 GHz	< 57.4

Table 3.4: **Radio data.** Radio observations of GRB 200826A. The δt column shows the days from the trigger. ** VLA data from Alexander et al. 2020.

Time Bins (s)	Model	Amplitude	E_{peak} [keV]	α	β	Photon Flux [ph s^{-1} cm^{-2}]	Photon Fluence [ph cm^{-2}]	Energy Flux [erg s^{-1} cm^{-2}]	Energy Fluence [erg cm^{-2}]	Fit Merit
0.000-0.180	Comp	0.3±0.04	114.8±6.0	-0.6±0.1	-	32.2±0.9	5.8±0.2	$3.1\pm0.2\times10^{-6}$	$0.6\pm0.02\times10^{-6}$	1.1
0.180-0.318	Band	4.2 ± 2.3	61.3±0.5	0.5±0.3	-2.7±0.1	41.5±1.1	11.5±0.2	$3.7\pm0.2\times10^{-6}$	$1.2\pm0.2\times10^{-6}$	0.9
0.318-0.414	Band	0.6 ± 0.1	141.9±10.3	-0.5±0.1	-3.0±0.4	61.5±1.5	17.4±0.2	$7.8\pm0.4\times10^{-6}$	$1.9\pm0.3\times10^{-6}$	0.9
0.414-0.506	Band	0.7 ± 0.1	145.4±13.5	-0.3±0.1	-2.3±0.2	61.4±1.5	23.0±0.1	$9.6\pm0.4\times10^{-6}$	$2.8\pm0.4\times10^{-6}$	1.0
0.506-0.607	Band	1.2±0.4	99.6±7.4	-0.04±0.2	-2.5±0.2	56.4±1.4	28.8±0.1	$6.9\pm0.3\times10^{-6}$	$3.5\pm0.3\times10^{-6}$	0.9
0.607-0.747	Band	0.9±0.2	95.3±5.3	-0.2±0.1	-3.3±0.4	41.7±1.1	34.6±0.2	$4.2\pm0.2\times10^{-6}$	$4.1\pm0.3\times10^{-6}$	0.9
0.747-1.152	Band	0.6±0.5	41.2±3.9	-0.3±0.4	-2.7±0.2	15.0±0.5	40.7±0.2	$0.9\pm0.1\times10^{-6}$	$4.5\pm0.3\times10^{-6}$	1.1

Table 3.5: **Parameters of the *Fermi*-GBM fit.** Fitting parameter of the *Fermi*-GBM gamma-ray spectrum of GRB 200826A.

Line $\mathring{A}$	F_ν $10^{-17}\,\mathrm{erg\,s^{-1}\,cm^{-2}}$
$[OII]_{3726}$	1.268 ± 0.37
$[OII]_{3729}$	2.522 ± 0.37
$[OIII]_{5007}$	8.21 ± 3.5

Table 3.6: **Host galaxy emission line fluxes.** Fluxes derived with pPXF for the lines detected in the GTC spectrum of the host galaxy.

Parameter	Unit	Value
θ_v	[rad]	$0.20^{+0.53}_{-0.15}$
$E_{\rm K,iso}$	[erg]	$6.0^{+51.3}_{-4.4} \times 10^{52}$
θ_c	[rad]	$0.24^{+0.53}_{-0.17}$
n	[cm^{-3}]	$5.5^{+187.3}_{-5.4} \times 10^{-2}$
p		$2.40^{+0.07}_{-0.07}$
ϵ_e		$0.42^{+0.40}_{-0.28}$
ϵ_B		$6.4^{+197.4}_{-5.2} \times 10^{-5}$
$E(B-V)$		$2.5^{+4.8}_{-2.3} \times 10^{-2}$
stretch s		$0.73^{+0.23}_{-0.16}$
scale k		$0.28^{+0.25}_{-0.12}$
$E_{\rm k}$	[erg]	$1.4^{+54.8}_{-1.2} \times 10^{51}$

Table 3.7: **Afterglow properties.** Posterior `afterglowpy` fit model parameters with an SMC extinction curve, a SN1998bw template and including the final Gemini+GMOS detection. Uncertainties are quoted at 90%. $E_{\rm k}$ is the beamed corrected kinetic energy. See §3.3.3 for more details.

Bombay (India), Weizmann Institute of Science (Israel), The Oskar Klein Centre at Stockholm University (Sweden), Humboldt University (Germany), Liverpool John Moores University (UK) and University of Sydney (Australia).

Based on observations obtained with the Samuel Oschin Telescope 48-inch and the 60-inch Telescope at the Palomar Observatory as part of the Zwicky Transient Facility project. ZTF is supported by the National Science Foundation under Grant No. AST-1440341 and a collaboration including Caltech, IPAC, the Weizmann Institute for Science, the Oskar Klein Center at Stockholm University, the University of Maryland, the University of Washington (UW), Deutsches Elektronen-Synchrotron and Humboldt University, Los Alamos National Laboratories, the TANGO Consortium of Taiwan, the University of Wisconsin at Milwaukee, and Lawrence Berkeley National Laboratories. Operations are conducted by Caltech Optical Observatories, IPAC, and UW. The work is partly based on the observations made with the Gran Telescopio Canarias (GTC), installed in the Spanish Observatorio del Roque de los

Muchachos of the Instituto de Astrofisica de Canarias, in the island of La Palma.

The material is based upon work supported by NASA under award number 80GSFC17M0002.

The ZTF forced-photometry service was funded under the Heising-Simons Foundation grant #12540303 (PI: Graham).

Analysis was performed on the YORP cluster administered by the Center for Theory and Computation, part of the Department of Astronomy at the University of Maryland.

Resources supporting this work were provided by the NASA High-End Computing (HEC) Program through the NASA Advanced Supercomputing (NAS) Division at Ames Research Center.

These results also made use of Lowell Observatory's Lowell Discovery Telescope (LDT), formerly the Discovery Channel Telescope. Lowell operates the LDT in partnership with Boston University, Northern Arizona University, the University of Maryland, and the University of Toledo. Partial support of the LDT was provided by Discovery Communications. LMI was built by Lowell Observatory using funds from the National Science Foundation (AST-1005313).

Part of this research was carried out at the Jet Propulsion Laboratory, California Institute of Technology, under a contract with the National Aeronautics and Space Administration.

Chapter 4: Gravitational-waves optical follow-up

This chapter of the thesis aims to summarize the Zwicky Transient Facility (ZTF)/Global Relay of Observatories Watching Transients Happen (GROWTH) follow-up campaign of gravitational wave (GW) events circulated by the the LIGO-Virgo Collaboration during their third observing run (O3). All the data and analysis related to the GW events had been published (Andreoni et al., 2019a; Andreoni et al., 2020; Coughlin et al., 2019d; Goldstein et al., 2019; Kasliwal et al., 2020b), and even though I have not led any of the articles, I played a major role in these searches. Throughout this chapter I will focus on my contributions and describe the overall observing plan, along with a report on the spectroscopic and photometric follow-up, focused on the facilities I led the observations and data reduction, i.e. KPED, Las Cumbres Observatory Global Telescope (LCOGT) and the Gemini observatory. As a part of this chapter I will reanalyze the observational constraints derived for each of the triggers, and conclude with remarks on the future campaigns.

4.0.1 Introduction

The joint discovery of GWs (Abbott et al., 2017b) and electromagnetic (EM) radiation (Abbott et al., 2017c) from the binary neutron star (BNS) merger GW170817 was a watershed moment for astrophysics, heralding a new era of multi-messenger

astronomy, as it allowed for the study of the long searched kilonova (KN) (Alexander et al., 2017; Chornock et al., 2017; Cowperthwaite et al., 2017; Drout et al., 2017; Evans et al., 2017; Haggard et al., 2017; Hallinan et al., 2017; Kasliwal et al., 2017b; Kilpatrick et al., 2017; Margutti et al., 2017; McCully et al., 2017; Nicholl et al., 2017; Pian et al., 2017; Shappee et al., 2017; Smartt et al., 2017; Troja et al., 2017; Utsumi et al., 2017). The discovery of the optical counterpart of a GW had tremendous implications and touched upon several fields, such as the measurement of the equation of state (EOS) of neutron stars (Abbott et al., 2018; Bauswein et al., 2013; Bauswein et al., 2017; Coughlin et al., 2018b; Radice et al., 2018), the formation of heavy elements (Abbott et al., 2017e; Just et al., 2015; Roberts et al., 2017; Rosswog et al., 2017; Wu et al., 2016), and the expansion rate of the universe (Abbott et al., 2017d).

Due to the prominent success of GW170817/GRB 170817A/AT2017gfo, we have used ZTF (Bellm et al., 2019a; Dekany et al., 2020; Graham et al., 2019; Masci et al., 2019) on the Palomar 48 inch telescope to observed both SGRBs from the *Fermi* Gamma-ray Burst Monitor (Ahumada et al., 2022; Cenko et al., 2018; Coughlin et al., 2018a; Coughlin et al., 2018a,b) and GW events from LIGO. We take advantage of the wide field of view (FOV) and high cadance of ZTF to search for the afterglow emission associated with the highly relativistic jet powered by the short gamma-ray burst (GRB), and the optical/near infrared (NIR) KN emission, powered by the radioactive decay of r-process elements (Kasen et al., 2017; Lattimer & Schramm, 1974; Li & Paczynski, 1998; Metzger et al., 2010; Roberts et al., 2011; Rosswog, 2015).

The third observing run (O3) by the network of gravitational-wave (GW) detectors with Advanced LIGO (Aasi et al, 2015) and Advanced Virgo (Acernese et al, 2015) began in April 2019. This detector network scored more than 70 binary black holes during O3 (The LIGO Scientific Collaboration et al., 2021b). The current discovery rate builds on the success of the first few observing runs, which yielded 10 binary black hole detections (Abbott et al., 2019).

There are many survey systems participating in the searches for GW counterparts. Amongst many others, the Dark Energy Camera (DECam; Flaugher et al. 2015), the Gravitational-wave Optical Transient Observer (GOTO; O'Brien 2018), the Panoramic Survey Telescope and Rapid Response System (Pan-STARRS; Chambers et al. 2016a; Kaiser et al. 2010), the All-Sky Automated Survey for Supernovae (ASAS-SN; Shappee et al. 2014) and Asteroid Terrestrial-impact Last Alert System (ATLAS; Tonry et al. 2018) all have performed observations of events during the third observing run. ZTF provides a competitive addition to these systems, given its depth ($m_{\rm AB} \sim 20.6$ in 30 s), wide field of view (FOV ≈ 47 deg^2 per exposure), and average cadence of ~ 3 days over the entire accessible sky. In particular, the cadence is important for establishing candidate history when performing target of opportunity (ToO) observations. The SGRB program, which has covered localization regions spanning thousands of square degrees (Ahumada et al., 2022; Coughlin et al., 2019c), demonstrated that ZTF is capable of detecting GW170817-like sources out to the Advanced LIGO/Virgo detection horizon at about $\sim$200 Mpc (Abbott et al., 2018).

Our team used ZTF to trigger target-of-opportunity (ToO) observations on 13

the LIGO-Virgo Collaboration (LVC) events that had at least one neutron star (NS) involved, as it it more likely to show an optical counterpart. Additionally, we took advantage of the ZTF systematic coverage of the accessible Northern Sky to look for candidates in the "serendipitously" covered GW skymaps. In fact, the serendipitous coverage contributed with more than 30% of the region for 7 of the 13 ZTF triggers. The latency of the observations ranged between 11 s (thanks to the serendipitous coverage) to 13.7 hr.

All the observations were originally planned based on the BAYESTAR skymaps, as these are available seconds after the trigger. However, the LALInference skymaps are more accurate (Veitch et al., 2015), thus the analysis presented in the GROWTH series of papers relies on the later. This induces differences in the coverage enclosed by our observations.

Similar to the short gamma-ray burst (SGRB) observations, the triggering of target-of-opportunity observations requires a pause in the ongoing observations and the scheduling of the corresponding fields in the skymap. The observing plan is derived using `gwemopt`, a code that optimizes the synoptic search of a compact binary coalescence (CBC) for a given skymap. These observations are planned through the GROWTH TOO marshal[1], an interface designed to ingest Gamma-ray Coordinates Network (GCN) circulars and determine the best strategy.

Due to the coarse size of the regions, the number of alerts increased significantly, compared to the SGRB triggers. The method we used to rule out candidates is the same as the one described in previous works (Ahumada et al., 2021; Coughlin

[1] `https://github.com/growth-astro/growth-too-marshal`

et al., 2019c), since the object we expect to see is the same. The most important consideration in this case was to use the correct and most updated skymap available. Due to the large volume of candidates we had to monitor, we took advantage of multiple 1-m telescopes in our GROWTH network, as well as other facilities in which we had time allocated. The photometric results were used to determine the decay rate of the candidates, and helped rule out a number of them.

In this chapter I will focus on my contributions to these searches, which are broadly the vetting strategy (described in Sec. 4.1), and the follow up and monitoring of candidates. I describe the search for the first neutron star merger in O3 (see also Coughlin et al. 2019b) in Sec. 4.2, and the searches for NSBH mergers in Sec. 4.3 (see also Anand et al. 2021). In Section 4.4 I describe summarize the rest of the ZTF searches on LVC events and contextualize the limits using the expected emission of a KN based on current models. The description, light-curves, and observational details can be found in Appendix A.

4.1 The vetting strategy across the board

A ZTF transient alert is defined as a 5σ change in brightness in the image relative to the reference epoch. For ZTF, all transient alerts flagged for follow-up required at least two detections separated by 15 minutes in order to remove asteroids and other transient objects. We used the Pan-STARRS1 point source catalog (PS1 PSC; Tachibana & Miller 2018) to remove candidates located less than 2 arcsec from likely point sources (i.e., stars). Full details on the PS1 PSC can be found in Tachibana & Miller (2018); briefly, the authors build a machine learning model that

determines the relative likelihood that a PS1 source is a point source or extended based on PS1 colors and shape measurements. The model is trained using sources observed with the *Hubble Space Telescope*, achieving an overall accuracy of ∼94%, and classifying $\sim 1.5 \times 10^9$ total sources.

We also used a real-bogus (RB) classifier to remove common image subtraction artifacts (Mahabal et al., 2019). This method consists of a random forest classifier trained with real objects and artifacts from ZTF images, separating objects with an accuracy of ∼89%. In order to capture the majority of real events, the threshold was set to $RB > 0.25$. In addition, the transients must have brightened relative to the reference image, leading to a positive residual after the image subtraction. Furthermore, the program excluded all objects within 20 arcsec of $m_{\rm AB} < 15$ stars to avoid artifacts from blooming, thus excluding $\sim 2-5\%$ of the imaged region, which depends significantly on stellar density. These estimates rely on the assumption that the sky fraction excluded around $m_{\rm AB} < 15$ stars, within a few circular regions of 1 deg^2 in the skymap that we checked, is representative of the overall sky fraction excluded from the entire imaged region. The final step involved constraining the search to events that have no historical detections prior to three days before the trigger. A summary in the bullet points below:

- Positive Subtraction: The object must have brightened relative to the reference image.

- Astrophysical: The object must have a real bogus (rb) score > 0.25 or a deep learning (drb) score > 0.8 (Duev et al., 2019; Mahabal et al., 2019) for it to

be considered astrophysical.

- Not Stellar: The object must be >2 arcsec away from a catalogued point source in the Pan-STARRS Point Source Catalog (Tachibana & Miller, 2018).

- Far from a bright source: The object must be at least 20 arcsec away from a bright ($m_{AB} < 15$ mag) star to avoid blooming artifacts.

- Not moving: The object must have at least two detections separated by at least 15 minutes to reject asteroids (moves <4 arcsec hr^{-1})

- No previous history: The object must not have any historical detections in the ZTF alert stream prior to the GW merger time.

While the GROWTH marshal queried all fields triggered as part of the Target of Opportunity search, the `Kowalski` queries searched for candidates in both serendipitous and triggered data within the 95% contour of the latest skymap that was available.

If a transient was consistent with the nucleus of a galaxy and if the mid-infrared colors based on the Wide-field Infrared Survey Explorer catalog (WISE; Wright et al. 2010) of the host galaxy were consistent with Active Galactic Nuclei (AGN), the candidate was deemed unrelated (Wright et al., 2010).

All viable candidates were promptly announced to the worldwide community via GCN circulars and many teams (not only GROWTH) triggered follow-up observations for many of our candidates[2]. Using the GROWTH marshal system, we

[2]The GROWTH collaboration posted 82 GCNs during O3. An additional 151 GCNs refer to follow-up of ZTF objects by other teams.

prioritized and triggered follow-up of candidates that exhibited rapid photometric evolution (faster than 0.3 mag day^{-1}) or showed red colors or were close to a host galaxy with a redshift consistent with the GW distance constraint.

4.1.1 Follow-up

The GROWTH team obtained follow-up with the following facilities to characterize the photometric and/or spectroscopic evolution: the Liverpool Telescope (LT; Steele et al. 2004), the Lowell Discovery Telescope (LDT[3], formerly known as the Discovery Channel Telescope), the Las Cumbres Observatory (LCO; Brown et al. 2013), the Apache Point Observatory (APO; Huehnerhoff et al. 2016), the Kitt Peak EMCCD Demonstrator (KPED; Coughlin et al. 2019e), the Lulin One-meter Telescope (LOT; Huang et al. 2005), the GROWTH-India telescope (GIT[4]; Kumar et al. 2022), the Palomar 60-inch telescope (P60; Cenko et al. 2006), the Palomar 200-inch Hale Telescope[5] (P200), the Keck Observatory[6], the Gemini Observatory[7], the Southern African Large Telescope[8] (SALT), the Himalayan Chandra Telescope[9] (HCT), the Robert Stobie Spectrograph (RSS; Smith et al. 2006) on the Southern African Large Telescope (SALT), and the Gran Telescopio Canarias[10] (GTC). Figures 4.4, 4.5, 4.6, 4.11, 4.12, 4.13, A.1, and A.2 illustrate examples of follow-up by the GROWTH team on some ZTF candidates. The specific instrument configura-

[3] https://lowell.edu/research/research-facilities/4-3-meter-ldt/
[4] https://sites.google.com/view/growthindia/
[5] https://www.astro.caltech.edu/palomar/about/telescopes/hale.html
[6] http://www.keckobservatory.org/
[7] http://www.gemini.edu/
[8] https://www.salt.ac.za/
[9] https://www.iiap.res.in/?q=telescope_iao
[10] http://www.gtc.iac.es/gtc/gtc.php

tions and data reduction methods are described in the Appendix A, particularly in Sec. A.1.

The follow-up observations include both photometric and spectroscopic data. Moreover, the association of a candidate with a GW trigger was rejected if its properties fell into one or more of the categories described below:

1. Inconsistent spectroscopic classification: We ruled out candidates that could be spectroscopically classified as supernovae (SNe), AGN, cataclysmic variables (CVs) and other flare stars. We used `SNID` (Blondin & Tonry, 2007) and `dash` (Muthukrishna et al., 2019) to classify the SNe and AGN found in our searches. CVs and variable stars often showed hydrogen features at zero redshift.

2. Inconsistent distance: We ruled out candidates whose spectroscopic redshift was not consistent with the GW distance within 2-σ. We cross-matched the transient positions with the Census of the Local Universe (CLU; Cook et al. 2019) galaxy catalog and the NASA Extragalactic Database (NED) to look up host redshifts where available. We also cross-matched the candidates against the Photometric Redshifts Legacy Survey (PRLS; Zhou et al. 2021) catalog and report the photometric redshifts when the spectroscopic redshift is unavailable.

3. Slow photometric evolution: As kilonovae are expected to evolve faster than SNe, we ruled out candidates that evolved slower than 0.3 mag day^{-1}. We used `ForcePhot`[11] (Yao et al., 2019), a forced photometry package, to examine the

[11] `https://github.com/yaoyuhan/ForcePhotZTF`

transient lightcurves. To quantify the evolution of a given transient, we define the parameter $\alpha_f = \Delta m/\Delta t$ [mag/day], where f corresponds to the filter used to determine the variation in magnitude (Δm) over time (Δt). A positive α indicates a fading source, while a negative α describes a rising source. The baseline (Δt) is defined to be the number of days it takes an object to rise from its discovery to its peak magnitude ($\alpha < 0$) or the amount of days it takes the transient to fade from peak to undetectable by ZTF ($\alpha > 0$). We used a minimum time baseline of 3 days to compute slopes.

4. Outside of the latest LALInference map: The majority of the candidates were selected and announced via GCN based on the promptly available BAYESTAR map (Singer & Price, 2016). When the LALInference map was made available, if a candidate was outside the 90% probability contour, we rejected it.

5. Artifacts: Most of the ZTF ghosts and artifacts are well known (Bellm et al., 2019a; Masci et al., 2019) [12] and masked automatically. Additionally, we take further precautions by ignoring transients close to bright stars in our initial vetting. However, for example, our extensive analysis revealed a subtle gain mismatch in the reference images that posed as a faint and fast transient (see discussion related to ZTF19aassfws in the Appendix §A.2). All references for ToOs were re-built after this artifact was identified.

6. Asteroids: Sometimes slow moving asteroids, especially near stationary points, can mimic a fast fading transient (Jedicke et al., 2016). For these objects,

[12] `http://nesssi.cacr.caltech.edu/ZTF/Web/Ghosts.html`

either a more careful inspection of the centroids or movement in follow-up imaging served as the reason for rejection.

7. Previous activity: Candidates were rejected if they showed previous detections prior to the GW merger time in other surveys, e.g., Catalina Real Time Survey (CRTS; Djorgovski et al. 2011), Palomar Transient Factory (PTF; Law et al. 2009), intermediate Palomar Transient Factory (iPTF; Cao et al. 2016; Masci et al. 2017), PS1 (Tachibana & Miller, 2018).

4.2 The BNS merger in O3

The first BNS detection of O3, LIGO/Virgo S190425z, was a single detector event discovered by the Advanced LIGO-Livingston detector, with Virgo also observing at the time (Singer et al., 2019a). Occurring at 2019-04-25 08:18:05 UTC, the estimated false alarm rate was 1 in 70,000 years, with a high likelihood of being a binary neutron star. The first reported BAYESTAR skymap provided an extremely coarse localization, resulting from the low signal-to-noise ratio in Advanced Virgo; it spanned $\sim$10,000 deg^2, which is nearly a "pi of the sky." The updated LALInference skymap (Singer et al., 2019b), released at 2019-04-26 15:32:37 UTC, reduced the localization region requiring coverage by $\approx$25% to $\sim$7500 deg^2. The all-sky averaged distance to the source is 156 ± 41 Mpc.

In this section, we describe an $\sim$8000 square degree search for the KN counterpart to a single-detector GW event. Our campaign emphasizes the key role played by large FOV telescopes like ZTF, as well as the associated follow-up systems. We demonstrate that our strategy for tiling the sky, vetting candidates, and pursuing

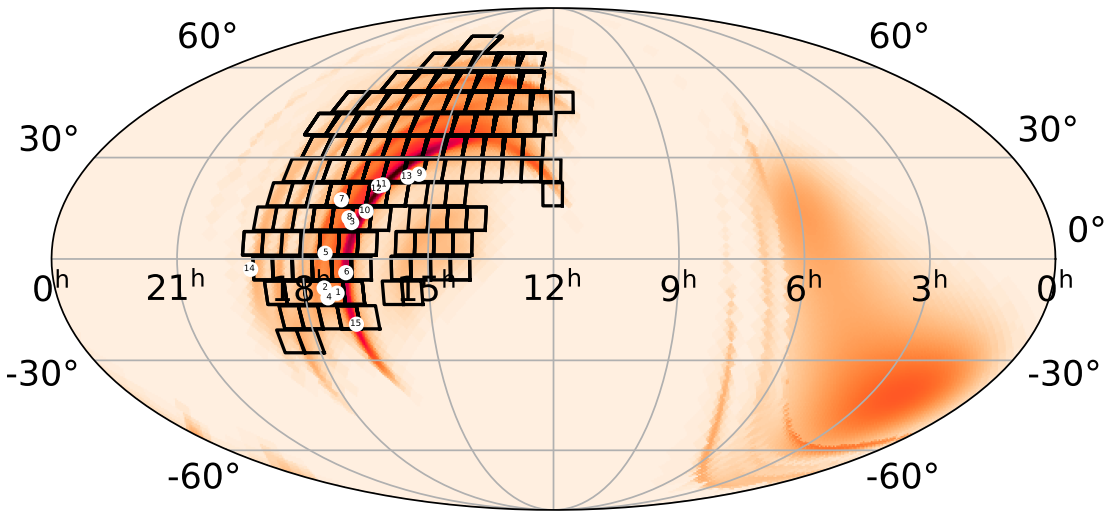

Figure 4.1: Coverage of S190425z. We show the $\approx$ 47 deg^2 ZTF tiles on the 90% probability region of the initial BAYESTAR skymap, along with the identified transients highlighted in Table 4.3. For the ZTF observations, the numbering scheme is 1: ZTF19aarykkb, 2: ZTF19aarzaod, 3: ZTF19aasckwd, 4: ZTF19aasfogv, 5: ZTF19aasejil, 6: ZTF19aaryxjf, 7: ZTF19aascxux, 8: ZTF19aasdajo, 9: ZTF19aasbamy, 10: ZTF19aasckkq, 11: ZTF19aarycuy, 12: ZTF19aasbphu, 13: ZTF19aasbaui, 14: ZTF19aarxxwb, 15: ZTF19aashlts.

follow-up is robust, and capable of promptly reducing 338,646 transient alerts from ZTF to a handful of interesting candidates for follow-up.

4.2.1 Observing Plan

Because S190425z came during Palomar night-time (2019-04-25 08:18:05 UTC), it occurred concurrently with ongoing survey observations by both ZTF and Palomar Gattini-IR. Within the 90% localization, approximately 44% of the original BAYESTAR map was observable from Palomar over the whole night, corresponding to $\approx$ 5000 deg^2. The GW event was automatically ingested into the GROWTH ToO marshal, a database we specifically designed to perform target-of-opportunity follow-up of events localized to large sky-error regions, including GW, neutrino, and gamma-ray burst events (Coughlin et al., 2019c). Amongst several other features,

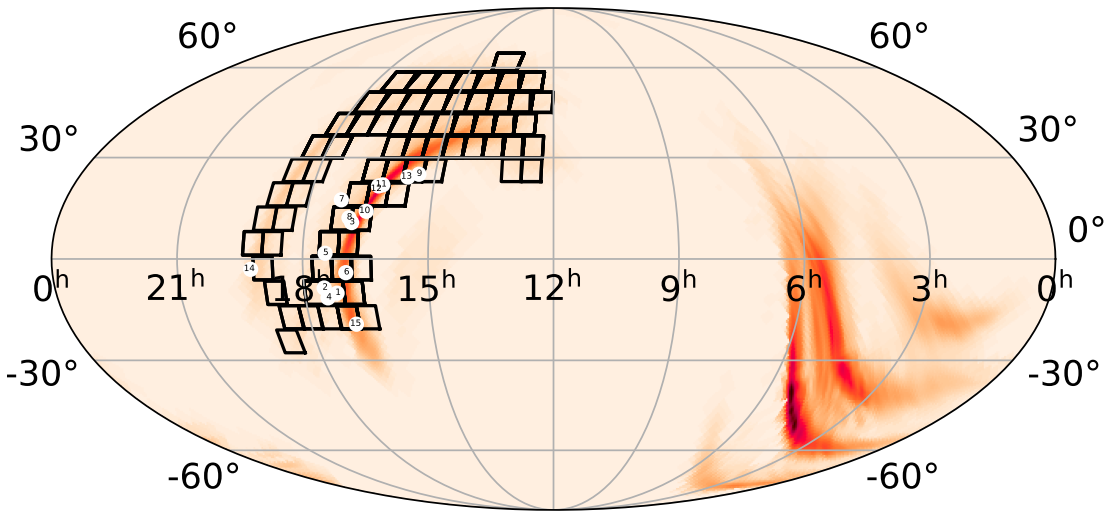

Figure 4.2: Coverage of S190425z. Similar to Fig. 4.1, the ZTF fields are shown as black rectangles, over the 90% probability region of the LALInference map.

the ToO marshal allows us to directly trigger the telescope queue for certain facilities to which GROWTH has access, namely ZTF, Palomar Gattini-IR, DECam, Kitt Peak EMCCD Demonstrator (KPED) on the Kitt Peak 84 inch telescope (Coughlin et al., 2019b), the Lulin One-meter Telescope (LOT) in Taiwan and the GROWTH-India telescope[13]. We provide a brief description of each instrument in Table 4.1.

[13]https://sites.google.com/view/growthindia/

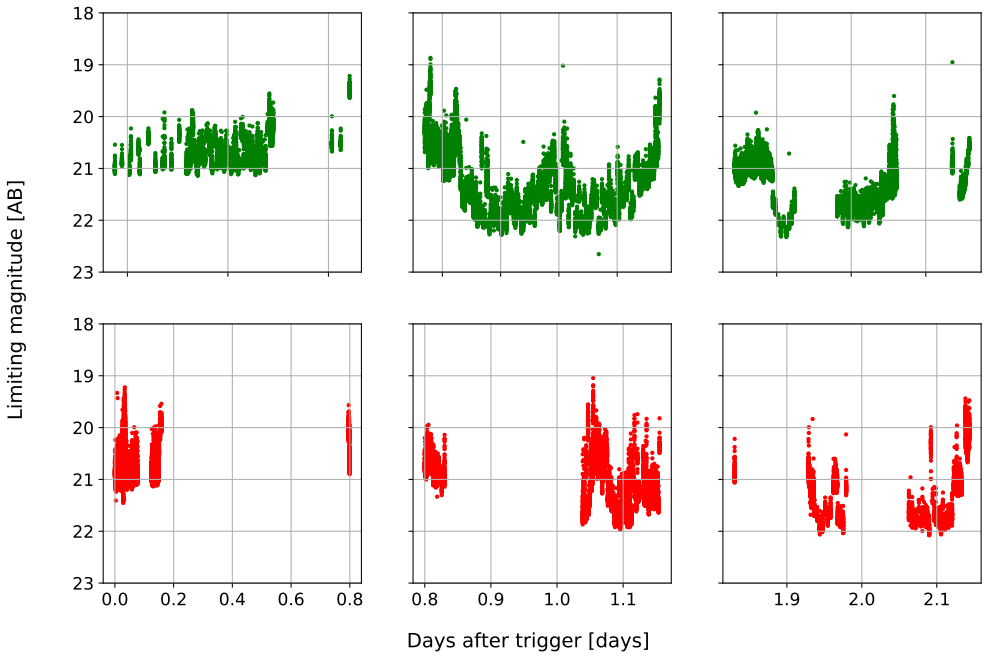

Figure 4.3: The ZTF limiting magnitude as a function of time for S190425z. The left, middle, and right panels corresponding to observations on the first, second, and third nights. The red and green circles correspond to the r- and g-band limits from ZTF respectively.

Triggering ToO observations for synoptic surveys, such as the ZTF, interrupts ongoing observations and redirects them to observe only certain fields, as indicated by an observation plan. The observing plan generated by the ToO marshal is based on `gwemopt` (Coughlin et al., 2018, 2019a), a code that optimizes the process of scheduling telescopes to follow gravitational waves. `gwemopt` manages both synoptic and galaxy-targeted search strategies; we use the former for observations with some of our facilities, Palomar Gattini-IR, GROWTH-India and ZTF, and the latter for scheduling observations with KPED. The ZTF coverage is shown in Figure 4.1 and the limiting magnitudes as a function of time in Figure 4.3.

Name	FOV	Pixel Scale	Aperture	Filters
ZTF	47 $\deg^2$	$1.0''$	48 in	g,r,i
Palomar Gattini-IR	25 $\deg^2$	$8.7''$	30 cm	J
GROWTH-India	0.5 $\deg^2$	$0.67''$	70 cm	u,g,r,i,z
LOT	$13.2' \times 13.2'$	$0.39''$	1 m	g,r,i
KPED	$4.4' \times 4.4'$	$0.26''$	2.1 m	g,r,U,B,V,I

Table 4.1: Telescope specifications, including name, field of view, pixel scale, telescope aperture, and available filters.

4.2.2 ZTF strategy

Serendipitously, after the BNS merger time and before the GW alert was distributed, ZTF had already observed 1920 $\deg^2$ of the sky in the r-band, corresponding to $\sim 19\%$ of the initial BAYESTAR map and $\sim 12\%$ of the LALInference map. This overlap between ongoing survey observations and the LIGO-Livingston-only localization is unsurprising as both of the Advanced LIGO interferometers have maximum sensitivity in the sky overhead in North America (Finn & Chernoff, 1993; Kasliwal & Nissanke, 2014).

ZTF triggered ToO observations lasting three hours starting at 2019-04-25 09:19:07.161 UT, one hour after the trigger time. On night 1, our observing strategy involved a sequence of g-r-g band exposure blocks; each exposure was 30 s, with a typical depth of 20.4 mag, which is the normal duration of exposures during ZTF survey operation. The g-r-g sequence is the baseline observing strategy for GW follow-up with ZTF as it is specifically designed to capture the inter- and intra-night color evolution of GW170817-like KNe and to distinguish them from supernovae (Kilpatrick et al., 2017; Shappee et al., 2017). Due to the size of the localization, we obtained a g-r sequence, requiring references for each scheduled field. In addition,

we required a 30 minute gap between observations in g and r to avoid asteroids. Accounting for the loss in probability due to chip gaps and the processing success, ZTF covered 3250 deg^2, corresponding to about 36% of the initial BAYESTAR and 19% of the LALInference maps on night 1.

Motivated by the increase in available observation time ($\sim$5 more hours than the first night), we modified our strategy on night 2 by taking longer integrations of 90 s each, corresponding to an average depth of 21.0 mag. We obtained one epoch in each of g- and r-band, corresponding to about 46% probability in the initial BAYESTAR or 21% of the LALInference maps.

After our observations on both nights were complete, a new LALInference skymap was released at 2019-04-26 14:51:42 UT (Ligo Scientific Collaboration & VIRGO Collaboration, 2019). The LALInference runs reduced the skymap to $\sim$7500 deg^2 and shifted more of the probability to two lobes near the sun and in the Southern hemisphere (see Figure 4.2). In summary, ZTF covered about 8000 deg^2 within the 99% integrated probability region within its two nights of observations. This corresponds to 46% of the probability in the original BAYESTAR skymap and 21% of the probability in the LALInference skymap. Our observations with ZTF over the two nights covered a 5 σ median depth of $m_{\rm AB} = 21.0$ in r-band and $m_{\rm AB} = 20.9$ in g-band.

4.2.3 Galaxy Targeted Follow-up

In addition to the synoptic surveys for counterparts, a subset of the available systems performed galaxy-targeted follow-up. This strategy was used by a number

of teams to observe GW170817 (Arcavi et al., 2017; Coulter et al., 2017; Valenti et al., 2017). The galaxy-targeted follow-up program relies on the Census of the Local Universe (CLU) catalog (Cook et al., 2017); it is complete to 85% in star-formation and 70% in stellar mass at 200 Mpc. The sky area coverage of galaxies is $\approx 1\,\%$ within these local volumes (Cook et al., 2017). This makes targeted galaxy pointing tractable for small FOV telescopes (see Arcavi et al. (2017) or Golkhou et al. (2018) for example). Of the galaxies within the volume, our work prioritizes them for follow-up as follows.

The GROWTH ToO marshal uses an algorithm modified from LCO's galaxy-targeted follow-up of GW events (Arcavi et al., 2017), which uses a combination of a galaxy's location in the GW localization region (including the distance), $S_{\rm loc}$, the galaxy's absolute B-band luminosity, $S_{\rm lum}$, and the likelihood of detecting a counterpart at the galaxy's distance $S_{\rm det}$. We define $S_{\rm det}$ as a prioritization of a transient's potential brightness, taking a fiducial limiting magnitude, $m_{\rm lim}$, for the exposures of $m_{\rm AB} = 22$, and convert it to a limiting apparent luminosity $L_{\rm lim}$. We also compute the luminosity for a potential transient with an absolute magnitude between -12 and -17, using wide bounds to be robust against differences in intrinsic brightness. Then, $S_{\rm det}$ becomes $S_{\rm det} = \frac{L_{\rm KNmax} - L_{\rm KNmin}}{L_{\rm KNmax} - L_{\rm lim}}$, that we limit to be between 0.01 and 1. Our final metric is therefore $S = S_{\rm loc} \times S_{\rm lum} \times S_{\rm det}$.

Beginning 4 hrs after the event, LOT observed 85 galaxies in the initial 90% localization (Tan et al., 2019a,b). LOT used 180 s exposures in R-band with seeing varying between 1.5-2.5 arcsec. Using comparisons to Pan-STARRS images, these exposures yielded a typical $5\,\sigma$ limiting magnitude of $m_{\rm AB} = 20$. Similarly, KPED

started the galaxy targeted follow-up 1.9 hours after the merger and continued until the first ZTF candidates came online. KPED imaged 10 galaxies in the r-band filter for 300 seconds, finding no visible transients up to $r = 20.8$ (Ahumada et al., 2019a). 300 s is the fiducial time chosen for KPED to potentially reach limiting magnitudes of $m_{\rm AB} = 22$, useful for both the transient discovery and follow-up (Coughlin et al., 2019b).

4.2.4 Candidates

Following the alert filtering scheme descrbe in 4.1, we were able to reduce the number of ZTF alerts from 50802 to 28 for the first night and from 287844 to 234 relevant candidates for the second night. A more detailed breakdown on the number of alerts that successfully met the criteria at each filtering step can be found in Table 4.2.

Filtering criteria	# of Alerts on April-25	# of Alerts on April-26
ToO alerts	50,802	287,844
Positive subtraction	33,139	182,095
Real	19,990	118,446
Not stellar	10,546	61,583
Far from a bright source	10,045	58,881
Not moving	990	5,815
No previous history	**28**	**234**

Table 4.2: Filtering results for both ZTF nights. The quantities represent the number of alerts that passed a particular step in the filter. Each step is run over the remaining alerts from the previous stage. The criteria are described in Section 4.1 and the total number of relevant candidates is highlighted. In particular, "Real" indicates a real-bogus score greater than 0.25, and "not moving" indicates that are there more than 2 detections separated by at least 30 minutes.

The candidates that passed these criteria were filtered and displayed by the GROWTH marshal (Kasliwal et al., 2019a), a database used to display historical lightcurves (including upper limits) for each object that also performs cross-matches with external catalogs. We subjected each of the remaining candidates to a thorough human vetting process to determine whether the transient could be a viable counterpart to S190425z. Through this vetting process, we removed candidates whose coordinates were outside the 90% contour in the GW localization, and candidates that had archival detections in the Pan-STARRS1 Data Release 2 (Flewelling, 2018). We flagged Active Galactic Nuclei (AGN) based on the WISE colors (Wright et al., 2010) for each transient and its offset from the nucleus of the galaxy. Furthermore, we prioritized candidates whose photometric/spectroscopic redshift was consistent with the GW distance estimate, and whose extinction-corrected lightcurve exhibited rapid color evolution initially. For the most promising candidates in our vetted list, we performed forced photometry at the position of the source to ensure there were no historical detections with ZTF.

Our first night of observations yielded only two such candidates that passed both the automatic filtering and human vetting processes. These two candidates were ZTF19aarykkb and ZTF19aarzaod. The second night of observations allowed us to identify additional candidates detected on the first night that were consistent with the new skymap, thereby increasing our candidate list from two to 13 from the first night to the second. We describe the most promising of these 15 candidates in more detail in Sec. 4.2.5.

To double-check that we did not miss any candidates, we used `Kowalski`[14], an open-source system used internally at Caltech (primarily) to archive and access ZTF's alerts and light curves (Duev et al., 2019). Specifically, we used `Kowalski`'s web-based GUI called the ZTF Alert Lab (ZAL), with which users can efficiently query, search and preview alerts. Our results were consistent with the results above. To triple-check that we did not miss any candidates, we also carried out an additional automatic search of the AMPEL alert archive (Nordin et al., 2019) for transients that might have escaped. No additional candidates from either night were found.

No viable counterparts were identified in this search.

4.2.5 Follow-up of ZTF candidates

The 15 sources that were identified from ZTF observations are shown in Table 4.3 and on Figures 4.7 and 4.8. See follow-up facilities in Sec. 4.1.1 and Sec. A.1.1.

A total of 5 objects were classified using spectroscopy (Buckley et al., 2019; Nicholl et al., 2019; Perley et al., 2019a) and we tracked the color evolution of 15 objects using photometry for about 7 days on average. A KN is expected to show a rapid evolution in magnitude (Metzger, 2017); GW170817 faded $\Delta r \sim 1$ mag per day over the first 3 days and by $\Delta r \sim 4.2$ mags total around day 10. Thus, we can use photometric lightcurves to determine whether a transient is consistent with the expected evolution for a KN. Some photometrically monitored transients showed evolution that was too slow ($\Delta r \sim 0.1$ mag per day) to be consistent with

[14] `https://github.com/dmitryduev/kowalski`

GW170817 or kilonova model predictions. Many other candidates highlighted in Kasliwal et al. 2019 were observed with GROWTH facilities, however, they were later excluded by the updated LALInference skymap. In addition to these sources, we reported objects in Kasliwal et al. 2019 with ZTF detections before the event time to the community in order to limit the number of false positives identified by other surveys that may not have recently imaged those areas of the sky.

We now provide a broad summary of the most promising candidates ruled out by spectroscopy, as examples of the follow-up performed by the GROWTH facilities when vetting candidates. In particular, we highlight the lightcurves of ZTF19aarykkb, ZTF19aarzaod, ZTF19aasckkq, and ZTF19aasckwd in the top left, top right, lower left and lower right panels respectively in Figure 4.4 and discuss them briefly below. The associated spectra are shown in the top panel of Figure 4.6; the spectrum of ZTF19aasckwd is not shown as we only have a spectrum of the galaxy host. We used the value of $H_0 = 67.4\,\mathrm{km\ s^{-1}\ Mpc^{-1}}$ (Aghanim et al., 2018) to calculate absolute magnitudes.

ZTF19aarykkb: We first detected the transient ZTF19aarykkb 2.13 hours after the merger and highlighted it in the first ZTF GCN (Kasliwal et al., 2019). ZTF19aarykkb is 12.1 arcsec offset from the host galaxy, which is at a redshift of $z = 0.024$, corresponding to a luminosity distance of 106 Mpc. The absolute magnitude of the discovery is $g = -15.9$, broadly consistent with GW170817 and KNe predictions. We ran forced photometry in archival ZTF images of the region, finding no variability at the coordinates before the merger. The last upper limit at this location

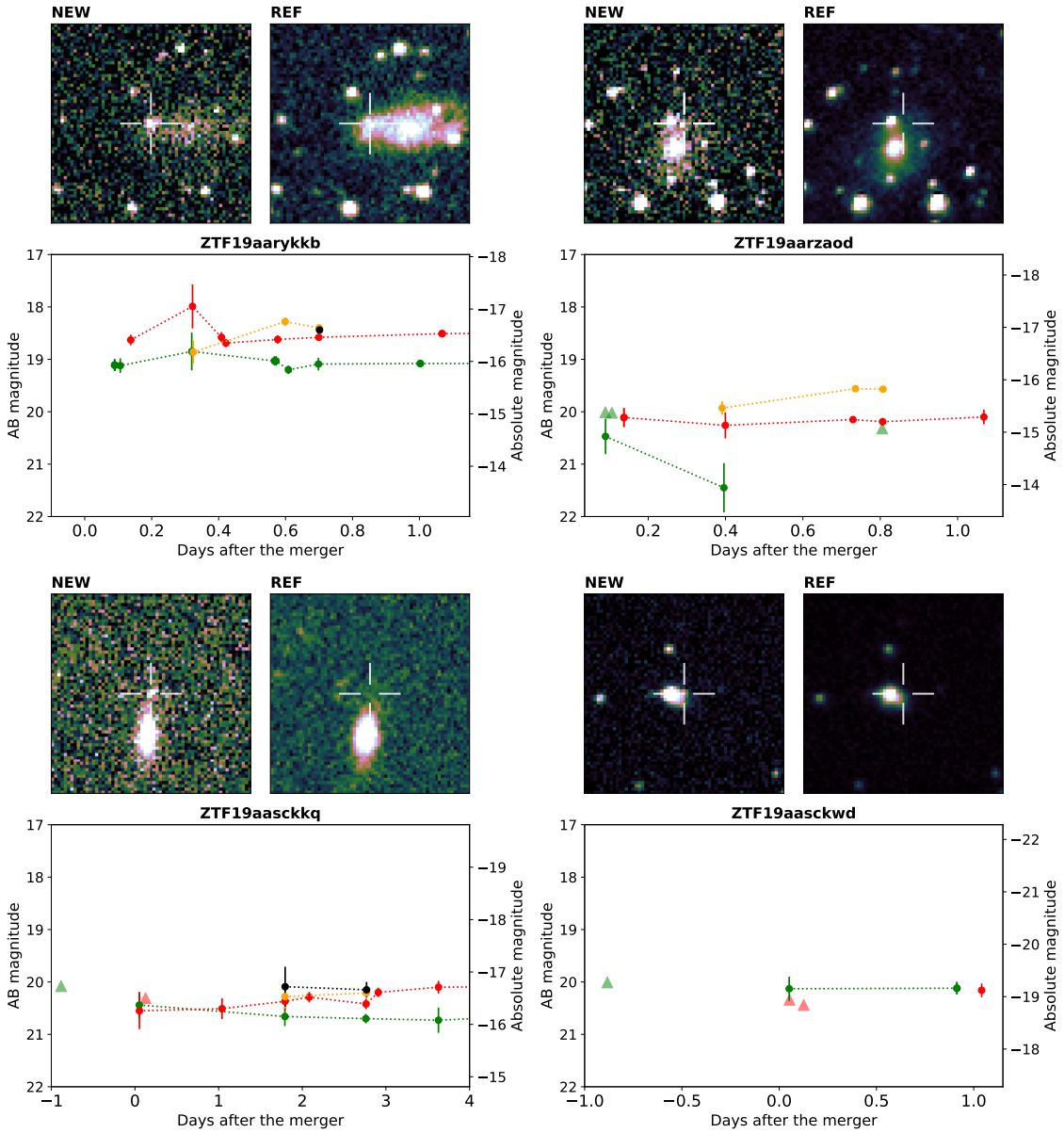

Figure 4.4: Lightcurves and r-band cutouts for the ZTF candidates discussed in Section 4.2.5. The lightcurves are constructed with data acquired with GROWTH facilities: for ZTF19aarykkb, the data is from ZTF, LOT, GIT and LT, for ZTF19aarzaod, ZTF, LOT and LT, for ZTF19aasckkq, ZTF, KPED and LT and for ZTF19aasckwd, ZTF and KPED. We used colors to represent each band in the lightcurves: green for g-band, red for r-band, yellow for i-band and black for z-band. While triangles in the lightcurve represent upper limits, filled circles are the magnitudes of the object. For each transient, the cutout on the left corresponds to the ZTF discovery image and the right cutout corresponds to the ZTF reference image of the host. A cross marks the location of the transient in the reference image. The cutouts are 0.7 sq. arcmin with north being up and east to the left.

was 5.8 days before the LVC alert in g-band ($m_{\rm AB} > 18.74$ in g-band). Due to its distance and discovery mag, several facilities followed-up this source (Burke et al., 2019; Chang et al., 2019b; Dichiara et al., 2019; Morihana et al., 2019a; Nicholl et al., 2019; Perley et al., 2019a; Rhodes et al., 2019) The LOT group in Taiwan imaged the object 6 hours after the transient set in Palomar (Tan et al., 2019b); later that day, the LT continued the monitoring. This object was imaged 18 times within the first 26 hours after the merger. The first spectrum for this object came from the Himalayan Chandra Telescope (HCT) about 10.67 hours after the trigger (Pavana et al., 2019), showing a strong Hα line at a redshift of $z = 0.024$. This was confirmed 8 hours later by the LT team with the Spectrograph for the Rapid Acquisition of Transients (SPRAT) (Piascik et al., 2014), who classified it as a young SN Type II (Perley et al., 2019a), based on the characteristic P-Cygni profile in the LT spectrum. An additional spectrum was taken about 10 hours later with the DeVeny spectrograph mounted on the 4.3 m DCT (Dichiara et al., 2019), showing similar strong Hα, furthermore confirming the SN classification (see Figure 4.6).

ZTF19aarzaod: ZTF19aarzaod was first detected by ZTF 2.15 hrs after the merger (Kasliwal et al., 2019) with its last upper limit ($m_{\rm AB} > 20.01$ in g-band) 6 days prior the merger. Forced photometry did not show previous history of variability at the transient location. The redshift of the host galaxy is $z = 0.028$, putting the transient at a distance of 128.7 Mpc. The transient is offset by 8.2 arcsec from the host galaxy and its absolute magnitude at discovery was $r = -15.3$, also consistent with a GW170817-like KN. ZTF19aarzaod was extensively followed-up with various

observatories (Buckley et al., 2019; Castro-Tirado et al., 2019; Hiramatsu et al., 2019; Izzo et al., 2019b; Morihana et al., 2019a; Nicholl et al., 2019; Rhodes et al., 2019; Wiersema et al., 2019) and was imaged 13 times during the first day. Spectroscopic observations of ZTF19aarzaod were taken with RSS mounted on SALT on UT 2019-04-26.0 under a special gravitational-wave follow-up program 2018-2-GWE-002 and reduced with a custom pipeline based on PyRAF routines and the PySALT package (Crawford et al., 2010). The spectrum covered a wavelength range of 470-760 nm with a spectral resolution of R = 400. The spectrum shows broad Hα emission along with some He I features (see Fig. 4.6) classifying it as a type II supernova at $z = 0.028$ (Buckley et al., 2019).

ZTF19aasckkq: The transient ZTF19aasckkq (Anand et al., 2019b) was first detected by ZTF 1.23 hrs after the merger. It is offset from the host galaxy by 10.1 arcsec, and its last upper limit ($m_{\rm AB} > 20.1$ in g-band) was the night before the merger. We ran forced photometry at the location of the transient, finding no activity before the merger. The discovery absolute mag is $r = -16.3$, similar to GW170817 at peak. ZTF19aasckkq was followed-up 18 hours after the last ZTF detection by LT and KPED (Ahumada et al., 2019b). This transient was imaged 16 times for a period of 3.8 days by a variety of observing groups (Ahumada et al., 2019b,c; Perley et al., 2019b). Nicholl et al. 2019 first classified ZTF19aasckkq as a Type IIb SN at $z \sim 0.05$, consistent with the galaxy redshift (Hosseinzadeh et al., 2019). In Figure 4.6, we highlight the presence of He I, Hα and Hβ absorption features in the first spectrum we acquired with P200+DBSP, confirming its clas-

sification as a SN IIb at a redshift of $z = 0.0528$. The source was still bright at $r = 19.8$, 14 days after S190425z.

ZTF19aasckwd: ZTF19aasckwd was detected 1.23 hrs after the merger about 4.2 arcsec from its host galaxy (Anand et al., 2019b). Its last upper limit ($m_{\rm AB} > 20.1$ in g-band) was the night before the trigger. The forced photometry search did not show activity prior to the merger. This transient was imaged 5 times during the first 24 hrs and it was classified as a SN Ia by Nicholl et al. (2019) at a redshift of $z = 0.145$ (Hosseinzadeh et al., 2019). The absolute magnitude at discovery was $r = -19.2$, a few magnitudes brighter than what is expected from a KN.

4.2.6 Follow-up of non-ZTF candidates

Here, we report on the follow-up triggered by the GROWTH team of a number of transients discovered by other facilities to be consistent with the LALInference skymap. We queried the GROWTH follow-up marshal at the positions of the most promising transients announced in order to determine whether 1) the transient had historical detections with ZTF, or 2) our concurrent photometry of the object also supported the KN hypothesis. Additionally, we used LT, GROWTH-India Telescope, and DECam to obtain photometry of the candidates that were not detected with ZTF because they were either fainter than the ZTF average upper limits or inaccessible due to their sky location. Table 4.4 summarizes the most relevant non-GROWTH objects followed-up by the GROWTH collaboration, and we briefly discuss them below.

***Swift*'s Ultraviolet/Optical Telescope (UVOT) candidate:** We followed up photometrically the *Swift*/UVOT candidate (Breeveld et al., 2019), discovered at RA=17:02:19.2, Dec=−12:29:08.2 in u-band with $m_{\rm Vega} = 17.7 \pm 0.2$. The transient was within a few hundred arcseconds of two galaxies within the localization volume. After its initial detection with Swift, several other facilities (Andreoni et al., 2019b; Arcavi et al., 2019; Breeveld et al., 2019; Chang et al., 2019a; De et al., 2019; Hu et al., 2019a; Im et al., 2019; Kann et al., 2019; Kong et al., 2019; Morihana et al., 2019b; Shappee et al., 2019; Tanvir et al., 2019; Troja et al., 2019; Waratkar et al., 2019), including ZTF and Palomar Gattini-IR, reported non-detections or pre-discovery upper limits that indicated the transient might be rapidly fading in the ultraviolet. Palmese et al. 2019 reported an object offset by < 1 arcsec from the position of the reported UVOT candidate after visually inspecting archival DECam optical images. Using the GROWTH-DECam program, Bloom et al. 2019 detected a source consistent with the coordinates reported by Palmese et al. 2019, but no transient at the coordinates reported by Swift (Kong et al., 2019) (see Table 4.4). The slight trailing observed in images of the original UVOT source (which introduced uncertainty in the astrometry) strongly hinted at the physical association between the transient and the offset source. The colors of the associated source ($r - z = 1.53$ and $g - r > 0.97$) are consistent with those of a M2-dwarf (West et al., 2011). For this reason, a likely explanation for the observed ultraviolet transient is that it was a galactic M2-dwarf flare (Bloom et al., 2019; Lipunov et al., 2019a), unassociated with the GW event. The photometry of the UVOT candidate is shown with a SDSS spectra of a M2-dwarf in Figure 4.5.

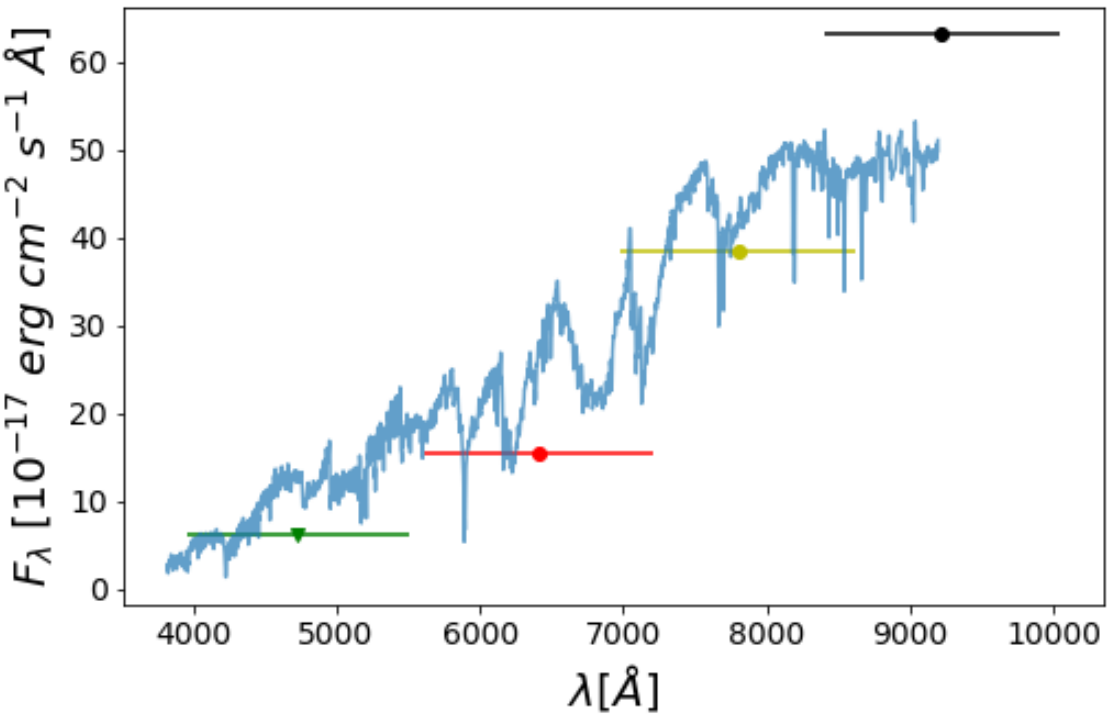

Figure 4.5: The DECam (g, r, i and z-band) fluxes of the UVOT candidate discussed on Section 4.2.6 are over-plotted on the spectra of an SDSS M2-dwarf.

AT2019ebq/PS19qp We also obtained spectroscopy of AT2019ebq/PS19qp (Smith et al., 2019b) with the Near-Infrared Echellete Spectrometer (NIRES) on Keck II. This candidate was initially claimed to be exceptional in that its optical spectrum taken with the Gran Telescopio Canarias (GTC) contained broad absorption features "unlike normal supernovae;" therefore Jonker et al. (2019) highlighted it as a promising KN candidate. Our NIR spectrum taken $\sim$ 1.5 days after the trigger, however, exhibited broad P Cygni SN-like features of He I that indicated that the transient was a Type Ib/c SN (Jencson et al., 2019), ruling out its association with S190425z (see bottom panel of Fig. 4.6). Several other facilities that also followed up this source helped verify its classification (Carini et al., 2019; Dimitriadis et al., 2019; Jencson et al., 2019; Lipunov et al., 2019b; McCully et al., 2019; Morokuma

et al., 2019; Schady et al., 2019).

7 additional PS1 candidates (out of the 20 transients reported by Smith et al. (2019b)) were ruled out based on previous ZTF detections (Andreoni et al. 2019a; see Table 4.4).

Marginal ATLAS candidates Additionally, we acquired a short sequence (40 seconds each in *gri* filters) of imaging at the locations of all five of the marginal ATLAS transients reported by McBrien et al. (2019) using IO:O on the 2 m Liverpool Telescope (Perley & Copperwheat, 2019b). No significant source was detected at the location of any of them (to typical depths of 22 mag; see Table 4.4). Combined with the fact that none of these transients had a detectable host galaxy, this suggests these transients were likely to be spurious or perhaps short-timescale flares from faint stars.

4.3 The NSBH mergers in O3

BNS, as well as neutron star - black hole (NSBH) mergers, were long predicted to produce UV/optical/near-IR emission known as KNe, which arise from the radioactive decay of r-process elements (Kasen et al., 2017; Lattimer & Schramm, 1974; Li & Paczynski, 1998; Metzger et al., 2010; Roberts et al., 2011; Rosswog, 2015). These counterparts to GW events are interesting for a variety of reasons, including their use in measuring the expansion rate of the universe (Abbott et al., 2017d; Coughlin et al., 2020b; Hotokezaka et al., 2019), placing constraints on the equation of state (EOS) of neutron stars (Abbott et al., 2017b; Bauswein et al., 2013;

Candidate	Coordinates (RA, Dec)	Discov. Mag.	Classification	Spec. facilities	Phot. evol.	Redshift/Host
ZTF19aarykkb	17:13:21.95 −09:57:52.1	r = 18.63	SNII z=0.024	HCT, LT, DCT	...	0.024 (s)
ZTF19aarzaod	17:31:09.96 −08:27:02.6	r = 20.11	SNIIn z=0.028	SALT	...	0.028 (s)
ZTF19aasckwd	16:52:39.45 +10:36:08.3	r = 20.15	SN Ia z=0.145	SOAR	...	0.15 (s)
ZTF19aasckkq	16:33:39.14 +13:54:36.7	g = 20.86	SN IIb z=0.052	P200, SOAR	...	0.053 (s)
ZTF19aasbphu	16:22:19.95 +21:24:29.5	r = 19.71	Nuclear*	...	0.11	0.0971 (p)
ZTF19aaryxjf	16:58:22.87 −03:59:05.1	g = 19.95	SN*	...	-0.014	0.07791 (s)
ZTF19aarxxwb	19:14:46.40 −03:00:27.0	g = 18.89	SN*	...	0.12	hostless
ZTF19aasdajo	16:57:25.21 +11:59:46.0	g = 20.7	SN*	...	0.045	0.292 (p)
ZTF19aasbamy	15:25:03.76 +24:55:39.3	g = 20.66	SN*	...	0.01	0.201 (p)
ZTF19aarycuy	16:16:19.97 +21:44:27.4	r = 20.07	SN*	...	0.02	0.127 (p)
ZTF19aasbaui	15:40:59.91 +24:04:53.8	g = 20.49	SN*	...	0.01	0.04 (s)
ZTF19aasejil	17:27:46.99 +01:39:13.4	g = 20.53	SN*	...	0.01	0.199 (p)
ZTF19aascxux	17:13:10.39 +17:17:37.9	g = 20.56	SN*	...	0.06	0.165 (p)
ZTF19aashlts	16:52:45.01 −19:05:38.9	r = 19.95	SN*	...	0.03	hostless
ZTF19aasfogv	17:27:22.32 −11:20:01.9	g = 20.53	SN*	...	0.01	hostless

Table 4.3: Follow-up table for the 15 most interesting ZTF candidates from Kasliwal et al. (2019) and Anand et al. (2019b). The sources with a star (*) have photometric evolution (in units of mag/day) inconsistent with the evolution of a KN (Section 4.2.5). Spectra obtained with SOAR (Nicholl et al., 2019) were critical in classifying ZTF19aasckwd and ZTF19aasckkq while spectra from SALT (Buckley et al., 2019) allowed the classification of ZTF19aarzaod. GROWTH teams acquired spectra of ZTF19aarykkb with HCT, LT, and DCT (Dichiara et al., 2019; Pavana et al., 2019; Perley et al., 2019a) and also provided useful photometric data towards the classification of these transients (Ahumada et al., 2019a,b; Bhalerao et al., 2019; Perley et al., 2019b; Tan et al., 2019b). We monitored the transients on average for 7 days. The redshift, spectroscopic (s) or photometric, (p) of the host galaxy is also listed.

Candidate	Coordinates (RA, Dec)	Discovery Mag.	GROWTH follow-up	upper limits
UVOT	17:02:19.21 −12:29:08.2	u=17.74	GIT, LOT, DECAM	DECam g > 24.0
...	...	...	...	DECam r > 24.0
...	...	...	...	DECam i > 23.7
...	...	...	...	DECam z > 23.1
AT2019ebq-PS19qp	17:01:18.33 −07:00:10.4	i= 20.40	Keck spectrum SN Ib/c	...
Gaia19bpt	14:09:41.88 +55:29:28.1	o = 18.49	ZTF19aarioci (4.12)	...
AT2019ebu-PS19pp	14:19:49.43 +33:00:21.7	i = 20.77	ZTF19aasbgll (2.10)	r=20.60
AT2019ebw-PS19pq	15:02:17.02 +31:14:51.6	i = 20.92	ZTF19aasazok (11.95)	g=20.91
AT2019ecc-PS19pw	15:26:29.53 +31:39:47.5	i = 20.10	ZTF19aapwgpg (17.96)	r=20.14
AT2019eck-PS19qe	15:44:24.53 +32:41:11.0	i = 20.81	ZTF19aapfrrw (24.97)	g=20.13
AT2019ecl-PS19qg	15:48:11.85 +29:12:07.1	i = 20.51	ZTF19aasgwnp (25.89)	g=21.02
AT2019ebr-PS19qj	16:35:26.48 +22:21:36.4	i = 19.79	ZTF18aaoxrvr (25.86)	g=20.83
AT2019ebo-PS19qn	16:54:54.71 +04:51:31.5	i = 20.02	ZTF19aarpgau (9.87)	g=20.40
AT2019eao-ATLAS19hyo	13:01:18.63 +52:09:02.1	o = 19.36	LT	g > 22.1
AT2019ebn-ATLAS19hwh	13:54:47.42 +44:46:27.3	o = 19.07	LT	g > 22.1
AT2019ebm-ATLAS19hwn	12:59:58.58 +29:14:30.7	o = 19.42	LT	g > 22.3
AT2019ebl-ATLAS19hyx	14:32:31.53 +55:45:00.1	o = 19.28	LT	g > 22.3
AT2019dzv-ATLAS19hxm	14:01:45.02 +46:12:56.1	o = 19.23	LT	g > 22.2

Table 4.4: GROWTH follow-up table for candidates reported by other surveys. GROWTH-India, LOT, and DECam-GROWTH follow-up of the Swift/UVOT candidate discovered by Breeveld et al. (2019) helped confirm its classification as a likely M-dwarf flare (Andreoni et al., 2019b; Arcavi et al., 2019; Bloom et al., 2019; Breeveld et al., 2019; Chang et al., 2019a; De et al., 2019; Hu et al., 2019a; Im et al., 2019; Kann et al., 2019; Kong et al., 2019; Lipunov et al., 2019a; Morihana et al., 2019b; Palmese et al., 2019; Shappee et al., 2019; Tanvir et al., 2019; Troja et al., 2019; Waratkar et al., 2019). Our initial Keck spectrum of another promising candidate, AT2019ebq/PS19qp (Smith et al., 2019b) showed it was a Type II SN (Jencson et al., 2019). Several of the PS1 candidates reported by Smith et al. (2019b), as well as Gaia19bpt (Kostrzewa-Rutkowska et al., 2019) were found to have previous detections with ZTF (Andreoni & Bellm, 2019; Coughlin et al., 2019a). For these sources, we list the number of days before S190425z that they were detected in parentheses. LT provided constraining upper limits of some reported ATLAS candidates (McBrien et al., 2019; Perley & Copperwheat, 2019b).

Bauswein et al., 2017; Coughlin et al., 2018b; Radice et al., 2018), and probing the formation of heavy elements (Abbott et al., 2017e; Just et al., 2015; Kasliwal et al., 2019b; Roberts et al., 2017; Rosswog et al., 2017; Watson et al., 2019; Wu et al., 2016).

LIGO/Virgo S200105ae (LIGO Scientific Collaboration & Virgo Collaboration, 2020a), a candidate NSBH event which occurred at 2020-01-05 16:24:26.057 UTC, was discovered by the Advanced LIGO-Livingston detector, with Virgo also observing at the time. The event was initially reported as having 97% terrestrial probability, with a false alarm rate (FAR) of 24 per year, and therefore not generally of interest for follow-up. However, the LIGO and Virgo Collaborations reported that the significance was likely grossly underestimated as a single-instrument event, and the presence of chirp-like structure in the spectrograms gave confidence in it being a real event (LIGO Scientific Collaboration & Virgo Collaboration, 2020a,b). Unlike other NSBH events, this trigger initially had $p_{\mathrm{remnant}} > 0\%$; this parameter indicates the probability of whether there is remnant matter outside of the merger that could generate an electromagnetic transient counterpart (Chatterjee et al., 2019a; Foucart et al., 2018). Similar to GW190425 (The LIGO Scientific Collaboration and the Virgo Collaboration, 2020), as a single detector event, the 90% credible region spans $7720\,\mathrm{deg}^2$, with an all-sky averaged distance to the source of $265 \pm 81\,\mathrm{Mpc}$. After our observations on the three following nights were complete (see Section 4.3.1), a new LALInference skymap was released (LIGO Scientific Collaboration & Virgo Collaboration, 2020c). The LALInference map slightly reduced the 90% area to $7373\,\mathrm{deg}^2$ (while making the 50% area larger), modified the all-sky

averaged distance to the source to 283 ± 74 Mpc, and shifted more of the probability to be uniform across the lobes (including the one near the sun, which was at ~ 19 hr in RA and $\sim -22°$ in declination at the time of the trigger, see Figure 4.7). Further parameter estimation maintained that the merger was likely to have contained a neutron star ($> 98\%$ probability) but significantly reduced the estimated remnant probability ($p_{\rm remnant} < 1\%$).

LIGO/Virgo S200115j (LIGO Scientific Collaboration & Virgo Collaboration, 2020d), a candidate NSBH event which occurred at 2020-01-15 04:23:09.742 UTC, was discovered by the two Advanced LIGO interferometers and the Advanced Virgo interferometer. This event was classified as a "MassGap" event, with HasNS $> 99\%$, indicating that one component's mass fell into the range between 3 and 5 solar masses, and the other component was a neutron star, respectively. Although S200115j initially had a non-zero terrestrial probability, its revised classification reflected that the trigger was astrophysical (MassGap $> 99\%$), with a FAR of 1 per 1513 years. As a three-detector localized event, the skymap was better-constrained than for S200105ae, spanning 908 deg^2 (at 90% confidence). Additionally, it contained two disjointed lobes, one in each hemisphere, and had a median distance of 331 ± 97 Mpc. Considering all of these factors, along with the remnant probability $p_{\rm remnant} = 8.7\%$, we chose to trigger our program for ZTF follow-up and obtained ToO observations. Nearly three days later, an updated LALInference skymap reduced the 90% credible region to 765 deg^2 and shifted most of the probability to the southern-most tip of the lower lobe (LIGO Scientific Collaboration & Virgo Collaboration, 2020e), see Figure 4.8. The median distance was only slightly modified to

340 ± 79 Mpc. This update also distinguished S200115j from other NSBH candidates as an exceptional event for electromagnetic follow-up, with a $p_{\rm remnant} > 99\%$ (LIGO Scientific Collaboration & Virgo Collaboration, 2020e).

In addition to follow-up efforts from facilities that are part of the GROWTH network, a number of other teams actively contributed to the search for transient counterparts to both S200105ae and S200115j. In the case of S200105ae, the MASTER-Net team (Lipunov et al., 2010) covered an area corresponding to $\sim 51\%$ of the probability (Lipunov et al., 2020a), and observations made by the FRAM, TAROT, and GRANDMA collaborations collectively resulted in 9% coverage (Turpin et al., 2020) of the initial BAYESTAR map (LIGO Scientific Collaboration & Virgo Collaboration, 2020a) after a 27 hr delay. S200115j was also followed up by the MASTER-Net team, as well as the SVOM Multi-Messenger Astronomy and GWAC teams, achieving 61% (Lipunov et al., 2020b) and 67% (Han et al., 2020) coverage of the BAYESTAR map respectively; additionally, the GOTO collaboration covered 60% of the initial BAYESTAR map (Steeghs et al., 2020), and the FRAM, TAROT, and GRANDMA teams cumulatively covered 13% of the LALInference sky localization area (Noysena et al., 2020) beginning less than 30 min post-merger.

In this section, we describe a triggered $\sim 3000\,{\rm deg}^2$ search for a KN counterpart to S200105ae, and a largely serendipitous $1100\,{\rm deg}^2$ search for a counterpart to S200115j. We delineate our observing plan in Section 4.3.1, and the candidates and associated follow-up in Section 4.3.3.

4.3.1 Observing Plan

S200105ae was detected by LIGO and Virgo during the morning Palomar time on 2020-01-05 UT (LIGO Scientific Collaboration & Virgo Collaboration, 2020a). Because it was originally identified as having a FAR above the threshold for automated public release, the skymap was not released until the following day. On 2020-01-06, beginning at 02:21:59 UT (hereafter night 1), only $\sim 2\,\%$ of the localization was covered serendipitously by ZTF routine survey operations, which have 30 s observations, emphasizing that the delay in the skymap may have been a critical loss to the chances of detection for any fast fading counterparts.

On 2020-01-07 UT (night 2) following the belated publication of the alert by LIGO and Virgo, we adopted a survey strategy of g- and r-band exposure blocks with 180 s exposures for ZTF. The length of the exposures was chosen to balance both the depth required for a relatively distant event and the sky area requiring coverage. We used `gwemopt` (Coughlin et al., 2018, 2019a), a codebase designed to optimize telescope scheduling for GW follow-up, to schedule the observations. The schedule is designed such that fields have reference images available to facilitate image subtraction, as well as a 30 minute gap between the observations in $g-$ and $r-$ bands to identify and remove moving objects. These observations were submitted from the GROWTH ToO marshal (Coughlin et al., 2019c), which we use to ingest alerts and plan observations.

We split the schedule into two blocks of right ascension due to the significantly displaced lobes in the skymap (see Figure 4.7), with observations lasting three hours

per block. We additionally utilized the "filter balancing" feature (Almualla et al., 2020), which optimizes for the number of fields that have observations scheduled in all requested filters, and employed the greedy-slew algorithm (Rana et al., 2019) for conducting our search. The ability to split the skymap in right ascension and the use of filter balancing was novel for these observations, and served to help address the previous difficulty with multi-lobed skymaps to make it possible to observe all filters requested for the scheduled fields. Previously, maps of this type created conflicts between the rising/setting times of the lobes, as well as the separation in time between each of the epochs. This problem impacts the transient filtering process as well, for example, resulting in a number of transients failing to satisfy the criteria of 15 minutes between consecutive detections to reject asteroids. With the implementation of these features, both g- and r-band epochs were successfully scheduled for almost all fields.

Due to poor weather conditions at Palomar, the limiting magnitudes in the first block of night 2 were shallower than expected at a $5\,\sigma$ median depth of $m_{\rm AB} = 19.5$ in g- and r-bands (see Figure 4.9), and the second block originally scheduled for the same night was subsequently cancelled because of this (Anand et al., 2020a). Combining the serendipitous and ToO observations, we covered 2200 deg^2, corresponding to about 44% of the initial BAYESTAR and 35% of the final LALInference maps on night 2. We adopted a similar strategy on night 3 (2020-01-08 UT), and improved weather led to deeper limits, with a $5\,\sigma$ median depth of $m_{\rm AB} = 20.2$ in g- and r-bands (Stein et al., 2020). Combining the serendipitous and ToO observations, we covered 2100 deg^2 on night 3, corresponding to about 18% of the initial

BAYESTAR and 23% of the LALInference maps. In total, over the 3 nights, we covered 3300 deg^2, corresponding to about 52% of the initial BAYESTAR and 48% of the LALInference maps.

The skymap for S200115j was released during Palomar nighttime on 2020-01-15 UT; we triggered ToO observations with ZTF and were on-sky within minutes. We employed the greedy-slew algorithm, same as for S200105ae, taking 300 s exposures in g- and r-bands (Anand et al., 2020b). Because the fields were rapidly setting by the time the skymap arrived, we were only able to cover 36% of the skymap in our ToO observations on that night. Poor weather and seeing conditions prevented us from triggering the following night (2020-01-16 UT). The subsequently released LALInference skymap shifted the innermost probability contour to the Southern lobe (LIGO Scientific Collaboration & Virgo Collaboration, 2020e), which was largely inaccessible to ZTF. While we were unable to obtain further triggered observations due to poor weather, our total serendipitous and triggered coverage within three days of the merger was 1100 deg^2, corresponding to about 52% probability of the initial BAYESTAR map and 50% probability of the final LALInference map.

4.3.2 Observational details

4.3.2.1 Photometric Observations

The ZTF observations used to discover potential candidates were primarily obtained with proprietary ToO program time, however the public ZTF data (Bellm et al., 2019a) provided with candidates as well. The nominal exposure time for the ZTF public survey is 30 s while for the ToO program varies from 120-300 s

depending on the available time and sky area requiring coverage. Our first source of photometry comes from the ZTF alert production pipeline (Masci et al., 2019), however for the purposes of this paper we have performed forced photometry (Yao et al., 2019) on the candidates and reported these values.

For photometric follow-up we used telescopes that are part of the Las Cumbres Observatory (LCO) network and the Kitt Peak EMCCD Demonstrator (KPED; Coughlin et al. 2019b). The LCO observations were scheduled using the LCO Observation Portal[15], an online platform designed to coordinate observations. Our imaging plans changed case by case, however our standard requests involved 3 sets of 300 s in g- and r- band in the 1-m telescopes. For fainter sources we requested 300 s of g- and r- band in the 2-m telescopes. The reduced images available from the Observation Portal were later stacked and sources were extracted with the SourceExtractor package (Bertin & Arnouts, 1996). The magnitudes were calibrated against Pan-STARRS1 (Chambers et al., 2016a) sources in the field. For transients separated < 8 arcsec from their hosts, we aligned a cutout of the transient with a Pan-STARRS1 template using SCAMP (Berti, 2006) and performed image subtraction with the High Order Transform of Psf ANd Template Subtraction (HOTPANTS) code (Becker, 2015), an enhanced version of the method derived by Alard 2000. Photometry for these candidates comes from an analogous analysis on the residual images. Furthermore, images obtained with the Liverpool telescope (LT; Steele et al. (2004)) were reduced, calibrated and analyzed in a similar fashion.

For KPED data, our standard procedure is to stack an hour worth of r-band

[15] `https://observe.lco.global/`

data and reduce the stacked images following to standard bias and flat field calibrations. The photometry is obtained following the same methods as for the LCO data.

The photometric data obtained with the Gemini Multi-Object Spectrographs (GMOS-N; Hook et al. 2004) mounted on the Gemini-North 8-meter telescope on Mauna Kea was split in four 200 s g-band images later combined and reduced with DRAGONS [16], a Python-base data reduction platform provided by the Gemini Observatory. The data were later calibrated using the methods described for LCO.

Additionally, we scheduled photometric observations with the Spectral Energy Distribution Machine (SEDM) on the Palomar 60-inch telescope Blagorodnova et al. (2018) automatically through the GROWTH marshal. We acquired g-, r-, and i-band imaging with the Rainbow Camera on SEDM in 300 s exposures. SEDM employs a python-based pipeline that performs standard photometric reduction techniques and uses an adaptation of `FPipe` (Fremling Automated Pipeline; described in detail in Fremling et al. 2016) for difference imaging. Data are automatically uploaded to the GROWTH marshal after having been reduced and calibrated.

We obtained near-infrared photometry using the Wide-field Infrared Camera (WIRC; Wilson et al. 2003) on the Palomar 200-inch telescope. The data were reduced using a custom data reduction pipeline described in De et al. (2020b), and involved dark subtraction followed by flat-fielding using sky-flats. The images were then stacked using Swarp (Bertin et al., 2002) and photometric calibration was performed against the 2MASS point source catalog (Skrutskie et al., 2006). Reported

[16] `https://dragons.readthedocs.io/en/stable/`

magnitudes were derived by performing aperture photometry at the location of the transient using an aperture matched to the seeing at the time of observation, including an aperture correction to infinite radius.

The photometry presented in the light-curves on this paper was corrected for galactic extinction using dust maps from Schlafly & Finkbeiner 2011.

4.3.2.2 Spectroscopic Observations

For the candidate dataset described in Sec. 4.3.3, we obtained two main sets of spectroscopic data, using the Gran Telescopio Canarias (GTC) and Palomar observatory. We obtained optical spectra of one set of candidates with the 10.4-meter GTC telescope (equipped with OSIRIS). Observations made use of the R1000B and R500R grisms, using typically a slit of width 1.2 arcsec. Data reduction was performed using standard routines from the Image Reduction and Analysis Facility (IRAF).

For the second set of candidates, we acquired most of our spectra with the Integral Field Unit (IFU) on SEDM, a robotic spectrograph on the Palomar 60-inch telescope (Blagorodnova et al., 2018). We scheduled spectroscopic observations for our brighter ($m_{AB} < 19$) and higher priority targets using a tool on the GROWTH marshal that directly adds the target to the SEDM queue. For each science target, the SEDM robot obtains an acquisition image, solves the astrometry and then sets the target at the center of the integral field unit field of view. At the end of exposure, the automated pysedm pipeline is run (Rigault et al., 2019). It first extracts the IFU spaxel tracers into a x,y,λ cube accounting for instrument flexures; the target

spectrum is then extracted from the cube using a 3D PSF model which accounts for atmospheric differential refractions. The spectrum is finally flux calibrated using the most recent standard star observation of the night, with the telluric absorption lines scaled for the target's airmass. See Rigault et al. (2019) for more details on the reduction pipeline. The final extracted spectra are then uploaded to the marshal; we use the SNID software (Blondin & Tonry, 2007) to classify our transients.

Using the Double Spectrograph (DBSP) on the Palomar 200-inch telescope we obtained one transient and one host galaxy spectrum during our classical observing run on 2020-01-18 UT. For the setup configuration, we use 1.0 arcsec and 1.5 arcsec slitmasks, a D55 dichroic, a B grating of 600/4000 and R grating of 316/7500. Data were reduced using a custom PyRAF DBSP reduction pipeline (Bellm & Sesar, 2016)[17].

4.3.3 Candidates

We will use the criteria mentioned in Sec. 4.1 in the following subsections to group and rule out candidates. The redshifts presented in this section come either from the spectra of the transient, z_s, or from the Photometric Redshifts for the Legacy Surveys (PRLS) catalogue (Zhou et al., 2021), which is based on Data Release 8 of DESI Legacy Imaging Surveys (Dey et al., 2019), z_p.

4.3.3.1 S200105ae candidates

In this subsection, we provide brief descriptions of candidates identified within the skymap of S200105ae. Due to the poor seeing conditions and moon brightness,

[17]https://github.com/ebellm/pyraf-dbsp

there were no candidates that passed all of the criteria after the second night of observations. After the third night of observations of S200105ae, we identified 5 candidates within the skymap (Stein et al., 2020), shown in Table 4.5 and on Figure 4.7. In addition, we later identified and reported other additional candidate counterparts (Ahumada et al., 2020b). A late-time query (>1 month after the mergers) yielded two further candidates of interest, ZTF20aafsnux and ZTF20aaegqfp, that were not already reported via Gamma-ray burst Coordinates Network (GCN).

All the transients are displayed in Table 4.6; here we briefly describe each set, and show examples of light curves and cutouts for the most well-sampled, slowly photometrically evolving ones in Figure 4.10. For the candidates with spectroscopic redshifts, we compare their distance calculated assuming Planck15 cosmological parameters (Ade et al., 2016) to get the LIGO $\pm 1\sigma$ distance uncertainty.

Spectroscopic Classification

For this set of spectra, we quote the photometric phase at which the spectrum was taken when the photometry is well-sampled. In all other cases, we derive the spectroscopic phase of the transient using SNID (Blondin & Tonry, 2007) unless otherwise specified. Most of the spectroscopic classifications were determined using SNID.

ZTF20aaertpj - The first r- and g-band detections of this transient 3 days after the merger showed a red color $g-r=0.4$ mag; it rapidly brightened 1 mag to reach $g=18.9$ after 7 days. The Gran Telescopio Canarias (GTC) classified it as a Type Ib SN ($z_s=0.026$) on January 10th (Castro-Tirado et al., 2020) a few days before the ZTF lightcurve reached maximum light, implying an absolute magnitude

of -15.9. This supernova is closer than the -1σ LIGO distance.

ZTF20aaervoa - This object was found 3 days after the merger at 20.74 in g band with a red color ($g - r = 0.66$ mag). This field was last observed 1.6 days before the merger. It showed a flat evolution over the first few days. Spectroscopic follow-up with GTC on January 10th classified it as a SN Type IIP ($z_s = 0.046$), ~ 3 days after maximum (Valeev et al., 2020) using SNID templates. This implied an absolute magnitude of -16.4 mag in r band. Its redshift is marginally consistent with the LIGO distance uncertainty, though it fell outside the 95% confidence level of the LALInference skymap.

ZTF20aaervyn - Its first detection was in the g band ($g = 20.62$), 3 days after the merger, which first showed a red color ($g - r = 0.3$ mag). This field was last visited 3 hours before the LVC alert. It was classified by GTC on Janunary 11th as a Type Ia SN, with $z_s = 0.1146$ (Valeev et al., 2020), much farther than $+1\sigma$ LIGO distance. The spectroscopic phase corresponds to $\gtrsim 1$ week before the lightcurve reached maximum light.

ZTF20aaerxsd - Similarly, this region was visited 3 hours before the LVC alert and this candidate was first detected 3 days after the merger at $g = 20.27$ and showed a red color of $g - r = 0.37$ mag. The next couple of detections showed a quickly evolving transient, brightening ~ 0.35 mag/day. GTC spectroscopically classified it as a SN Type Ia ($z_s = 0.0533$) on January 10th (Valeev et al., 2020); concurrent photometry with ZTF indicates that the spectrum was taken > 12 days before maximum.

ZTF20aaerqbx - This transient was first detected in g-band at $g = 19.46$ 3

days after the merger. It faded 0.5 mag over the first 8 days and was classified by GTC on January 11th as a Type IIP SN ($z_s = 0.098$) at 5 days before maximum, using SNID (Castro-Tirado et al., 2020). Its redshift places it outside of the LIGO volume.

ZTF20aafanxk - This candidate was detected at $r = 18.52$, 6 days after the merger with galactic latitude $< 15°$ and offset by 7 arcsec from a possible host (Ahumada et al., 2020b); it faded 0.3 mag in the r-band the first 10 days and a spectrum taken with the P60 SEDM spectrograph revealed its classification to be a SN Ia at $z_s = 0.103$, too far to be consistent with the LIGO distance.

ZTF20aafujqk - Offset by 2.26 arcsec from the center of a large spiral galaxy host (Ahumada et al., 2020b), ZTF20aafujqk was detected in r-band during serendipitous observations 10 days after the merger, and later followed up with SEDM photometry in g- and i- bands, which showed a steadily declining lightcurve. SEDM spectroscopy showed that it was also a SN Ia at $z_s = 0.06$, consistent with LIGO distance uncertainties.

(Slow) Photometric Evolution

As mentioned above, we deem candidates to be slowly evolving by checking whether their rise or decay rate is faster than our photometric cut of $< |0.3|$ mag/day. We justify this cut based on the evolution rates of KNe from NSBH mergers, which shows that over a baseline of $\gtrsim$1 week, nearly all KN model lightcurves evolve faster than this cut in both g- and r-bands.

ZTF20aafduvt - The field where this transient lies was observed 12 hours before the LVC alert, and it was detected six days after the merger in r- and g-

bands (Ahumada et al., 2020b), offset from a possible host at $z_p = 0.21 \pm 0.02$ by 51kpc, this candidate faded 0.1 mag in the g-band during the first 9 days after the discovery. The photometric redshift places this transient at an absolute magnitude of M = -21.

ZTF20aaflndh - With its last non-detection 12 hours before the GW alert, ZTF20aaflndh was first detected 10 days after the merger. This source is located 0.8 arcsec from the center of an apparently small galaxy (Ahumada et al., 2020b) and evolved photometrically to resemble a Type Ia SN light curve; it faded in the r-band by 0.17 mag in 17 days. Furthermore, the photo-z of the host galaxy is z_p = 0.091 ± 0.023 which puts the transient at an absolute magnitude of M = -19.06, consistent with a Type Ia SN.

ZTF20aaexpwt - This candidate was first detected one week post-merger, and was one of several hostless candidates identified in a low galactic latitude ($b_{gal} < 15°$) field (Ahumada et al., 2020b). The last non-detection was 5 hours before the LVC alert. Its evolution over the next seven days was 0.12 mag/day in the r-band, marked by a declining lightcurve.

ZTF20aafukgx - Offset from a potential bright host by 3.85 arcsec, at low galactic latitude (Ahumada et al., 2020b), this candidate was detected at r = 18.4 ten days after the merger but remained flat within error-bars over the next ten days of observations.

ZTF20aagijez - First detected 11 days post-merger, this candidate, offset 3.15 arcsec from the nucleus of a star-forming galaxy at z_s = 0.061 (Ahumada et al., 2020b), exhibited a flat lightcurve for more than 10 days and it was still detectable

after 40 days; it photometrically resembles a SN light curve. The spectroscopic host redshift implies an absolute magnitude of M = -17.6. The last visit to the field where this transient lies was 3.6 hours before the GW alert.

ZTF20aagiiik - This field was last visited 2 days before the LVC alert. We identified ZTF20aagiiik as a candidate of interest due to its rapid rise in r-band after being detected 11 days after the merger; it is offset by 5.79 arcsec from a potential spiral galaxy host (Ahumada et al., 2020b). However, it only faded 0.4 mag in 12 days. Additionally, at the redshift of the potential host galaxy ($z_s = 0.13$, separated by 5.25 arcsec) the absolute magnitude (M = -19.24) is consistent with a Type Ia SN.

ZTF20aafdxkf - Detected just three days after the merger, this hostless candidate exhibited a rise in r-band over the first three days (Ahumada et al., 2020b), but its declining g-band photometry showed it to be too slow to be a KN. It only faded 0.5 mag in the g-band during the first 14 days. The last non-detection was 12 hours before the LVC alert.

ZTF20aagiipi - Offset by 27 kpc from a potential faint host at $z_p = 0.388 \pm 0.016$, this candidate seemed to be rising when it was detected in the first 11 days after merger. Supplemented with SEDM photometry, its lightcurve closely resembles that of a typical Type Ia supernova, which at the redshift of the host would peak at M = -21.6. This field was last observed 3.6 hrs before the LVC alert.

ZTF20aafsnux - A hostless candidate, ZTF20aafsnux appeared to be declining gradually based on its first two g-band detections two and nine days after the merger. Close monitoring revealed that the source was fluctuating between $g \sim$ 19.0–20.0

over a period of 17 days. This region was last visited 3 hours before the GW alert.

ZTF20aafksha - This last non-detection for this transient was 1.2 days before the GW alert. We discovered this candidate nine days after the merger, offset by 7.92 arcsec from a possible spiral galaxy host at $z_s = 0.167$ at $g = 20.06$ (Ahumada et al., 2020b), corresponding to an absolute magnitude of about -19.6. The steadily declining lightcurve post-peak in both g-band and r-band, 0.7 mag in g-band during the first 19 days, and the bright absolute magnitude, suggests that the candidate is a SN Ia.

ZTF20aaertil - This candidate was first detected three days after the merger; it was located 0.2 arcsec from the nucleus of a faint galaxy host and appeared to be rising in g-band (Ahumada et al., 2020b). Our spectrum of the host galaxy with DBSP on Jan 18th demonstrated that the galaxy, at $z_s = 0.093$, was outside the one-sigma distance uncertainty for S200105ae; furthermore, in 40 days, it faded only 0.5 mag in the r-band. The absolute magnitude at this host redshift is M = -18.5. The last non-detection in this field was 3 hours before the LVC alert.

ZTF20aagjemb - First detected 3 days after merger, this nuclear candidate rose by one magnitude over the course of 5 days in g-band (Ahumada et al., 2020b). After tracking its evolution over 20 days time, the lightcurve seems to exhibits a SN-like rise and decline. It presents a slowly-evolving lightcurve, only fading 0.1 mag in the r-band during the twenty days. The transient is located in a host with a z_p = 0.21 $\pm$ 0.06, separated by 6 kpc, implying an absolute magnitude M = -19.24. The last non-detection in this region was 3 hours before the LVC alert.

ZTF20aafefxe - This candidate's two detections in r-band suggest fading be-

havior, but subsequently the source has not been detected by the nominal survey observations (Ahumada et al., 2020b). The last non-detection in this region was 5 hours before the LVC alert. The first detection was 9 days after the merger, and there may be a faint host separated by 41 kpc from the transient with $z_p = 0.09 \pm 0.05$, indicating a luminosity of M = -17.2. Forced photometry revealed that it had only evolved 0.16 mags in 11 days in the g-band, placing it clearly into the category of slow evolvers.

ZTF20aafaoki - The last non-detection in this region was 12 hours before the LVC alert. This candidate had two r-band detections at 19.2 mag, but had faded below 21.4 mag just 5 days later (Ahumada et al., 2020b). Our images taken with KPED do not show any transient or background source up to $g > 19.55$ mag 6 days after the discovery. Similarly, our LCO follow-up observations showed that 8 days after the discovery, the transient is not detected and there is no visible source at the corresponding coordinate up to $g > 20.25$ mag and $r > 21.6$ mag. Our last LCO observations, obtained 72 days after the discovery, show no transient up to $g > 22.10$ mag. However, after running forced photometry at the transient position, we find a detection 14 days after the initial discovery at $r = 21.2$ mag, implying re-brightening of the transient after the non-detection upper limits, or very slow evolution.

Stellar Variables

ZTF20aafexle - This particular region was observed serendipitously 1 hour before the LVC alert. After its initial detection 8 days after the merger, it brightened by nearly one magnitude over four days but returned to its original brightness after

5 days (Ahumada et al., 2020b). We posit that it may be stellar due to the PS1 detections at the source position. Additionally, its evolution over the first 10 days after the discovery is only 0.3 mag in the r-band.

ZTF20aaevbzl - This region was last observed 3 hours before the LVC alert. ZTF20aaevbzl was detected six days after the merger (Ahumada et al., 2020b), this candidate was selected for its atypical rapid decline in its lightcurve in r- and g-bands. This hostless transient faded 1.1 mag in 5 days in the g-band. We obtained a spectrum of ZTF20aaevbzl with P200+DBSP, whose Hα feature at $z_s = 0$ amidst a blue, mostly featureless spectrum indicates that it is a galactic cataclysmic variable. Further follow-up with SEDM and LCO showed that the transient was consistently fading at 0.18 magnitudes per day in the g- band.

Slow-moving asteroids

ZTF20aaegqfp - We detected this hostless candidate a day after the merger in r band. The last non-detection of this transient was 5 hours before the GW alert. Our pipelines identified it as a fast-evolving transient due to its rise by more than 0.5 mag over the course of the night; subsequently, it was not detected in any our serendipitous observations. We find non-physical upper limits interspersed with detections, suggesting that the photometry for this transient may not be reliable. Using the Kowalski infrastructure, we queried for alerts in the vicinity of the transient (around 25 arcsec) and found 13 alerts, the oldest of which was $\sim$ 4 days before the trigger, which showed a moving object across the field alerts (see Figure 4.11).

4.3.3.2 S200115j candidates

In this subsection, we provide brief descriptions of candidates identified within the skymap of S200115j. Most of our candidates were identified during the serendipitous coverage of the map. Some of our transients were discovered within ZTF Uniform Depth Survey (ZUDS) a dedicated survey for catching high-redshift SNe by acquiring and stacking images to achieve greater depth compared to the nominal survey. Intrinsically faint transients ($m_{AB} \sim -16$) discovered in these fields are more likely to be at redshifts consistent with the distance of this event (340 ± 79 Mpc).

The relevant candidates circulated by the GROWTH collaboration (Anand et al., 2020b) were found on the first night of observations. Weather issues affected systematic follow-up in the following days; nevertheless, a later deeper search led to more candidates found to be temporally and spatially consistent, which we report here. Additionally, candidates from Evans et al. 2020 were cross-matched with the ZTF database in order to temporally constrain the transients. Only S200115j_X136 (Evans et al., 2020) had an optical counterpart we could identify, ZTF20aafapey, with a flaring AGN (Andreoni et al., 2020).

Every candidate that was found in the region of interest is listed in Table 4.7.

Spectroscopic Classification

ZTF20aafqpum - This transient is located at the edge of a host galaxy at $z_p = 0.12 \pm 0.03$ (Anand et al., 2020b). The region was last observed 1 hour before the LVC trigger and the transient. Follow-up with the Liverpool telescope in r-

and i-bands showed this candidate to be red, with $g - r \sim 0.5$ mag. This transient was then spectroscopically classified by ePESSTO+ as a SN Ia 91-bg, at $z_s = 0.09$ (Schulze et al., 2020), placing it at an absolute magnitude of M = -17.3.

(Slow) Photometric Evolution

ZTF20aahenrt - This candidate, detected during our serendipitous search 3 days after the merger, is separated from a galaxy host by 8.8 kpc at $z_p = 0.16 \pm 0.04$, giving it an absolute magnitude of M = -15.6. We monitored the transient after its initial rise in g-band, but over 12 days the candidate lightcurve exhibits very flat evolution, rising by 0.14 mag in 7 days. We highlight it in Figure 4.10 as an example of a very slowly evolving transient identified in our searches. This field was serendipitously observed 30 min before the LVC alert.

ZTF20aagjqxg - We selected this hostless candidate during our scanning due to its faint g-band detection at $g = 20.65$ and subsequent rise three days after the initial detection two hours after the merger; its detection 11 days later in the r-band suggests that it was rising or reddening at a rate of < 0.1 mag/day. This field was last observed 3.5 days before the LVC alert.

ZTF20aahakkp - This hostless transient was first detected eight days after the merger in $g = 15.67$ and $r = 16.01$. The last non- detection of this transient was 20 hours before the issue of the LVC alert. While the transient seems to be rapidly fading over the course of a day from $r = 16.26$ to $r = 17.9$, this detection is likely affected by poor weather and bad seeing on that day (seeing > 4 arcsec). 20 days later, the lightcurve is near the original detection magnitude, and exhibits a slow fade since then.

ZTF20aafqulk - This region was last observed 1 hour before the issue of the GW alert. This source was detected 2.5 hours after the merger in g-band and 43 minutes later in r-band, with a blue color (g-r = 0.2). The candidate is offset by 0.3 arcsec from a potential host galaxy at a photometric redshift of $z_p = 0.27 \pm 0.04$ (Anand et al., 2020b). Our P60+SEDM spectrum does not offer a clear classification, but we detect a source in our LCO images 5 days after its discovery with $r = 20.16 \pm 0.1$. When running forced photometry, we find a detection in the r-band 89 days before the trigger, definitively ruling out its association with the GW event. Furthermore, the lightcurve appears nearly flat in the r-band over the course of 10 days.

Slow-moving asteroids

Solar System asteroids located in the proximity of the stationary points located at $\sim 60^\circ$ from opposition and low ecliptic latitude (Green, 1985) have slow, $\lesssim 1$ arcsec/h sky motions (Jedicke et al., 2016).

ZTF20aafqvyc - This was first detected as a hostless candidate 2.5 hours after the merger in g-band, followed by a detection in r-band just 49 minutes later (Anand et al., 2020b). Due to the transient being faint at $g = 20.39$, with a $g - r$ color of 0.34 mag, we pursued follow-up with P200+WIRC on 2020-01-18 with NIR non-detections down to $J > 21.5$ and $K_s > 20.9$ (De et al., 2020a) and LCO on 2020-01-19 with optical non-detections down to $g > 22.6$ mag, $r > 21.8$ mag and $i > 20.9$ (Ahumada et al., 2020b). Follow-up reported with AZT-33IK telescope of Sayan observatory (Mondy) revealed non-detections just 13 hours and one day after the merger, down to upper limits of 21.6 and 22.1 in the r-band, suggesting that the

source could be fast-fading, if astrophysical (Mazaeva et al., 2020). Finally, we conducted follow-up with Gemini GMOS-N, detecting no source down to an upper limit of $g > 24.5$ mag (Ahumada et al., 2020). Based on the puzzling non-detections, we investigated the possibilities that it could be an artifact or that it was a moving object. Close inspection of the images taken with the Liverpool Telescope, 12.9 hours after the merger in g- and r-bands clearly demonstrated that the object had shifted position in the image with a slow angular rate of motion consistent with being an asteroid with an opposition-centric location of $\pm 60^{\circ}$ near the evening sky stationary point.

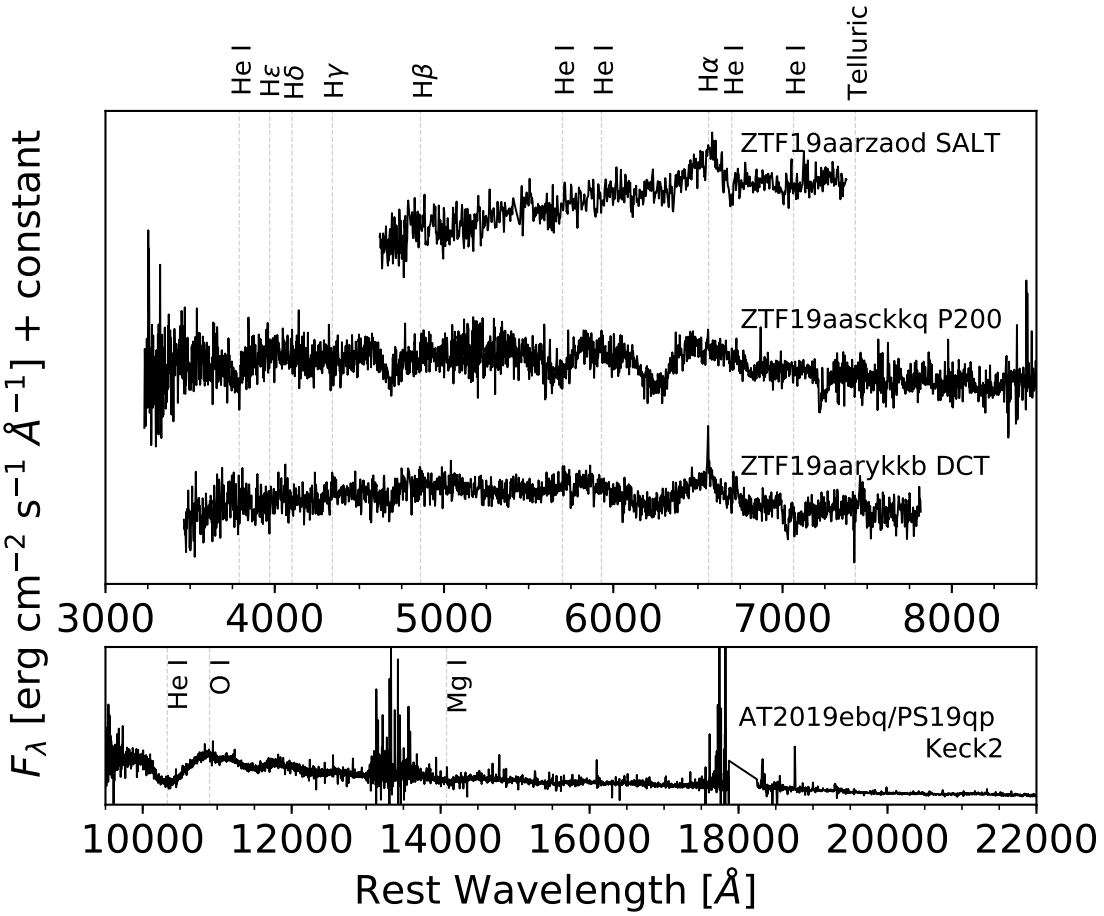

Figure 4.6: Spectra of all the candidates for which spectroscopic data were taken. The transient name and instrument used to obtain the spectrum are noted on the right hand side of the plot. We show the spectrum for AT2019ebq/PS19qp in its own panel given the different wavelengths covered from the other transients. The dotted gray lines show the characteristic features in each spectrum that helped with its classification. These four transients were all classified as core-collapse SNe. The classification and phase for each transient is as follows: ZTF19aasckkq - SN IIb, 7 days; ZTF19aarykkb - SN II, 1 day (Dichiara et al., 2019); ZTF19aarzaod - SN II, 0 days (Buckley et al., 2019); AT2019ebq/PS19qp - SN Ib/c, 1 day (Jencson et al., 2019).

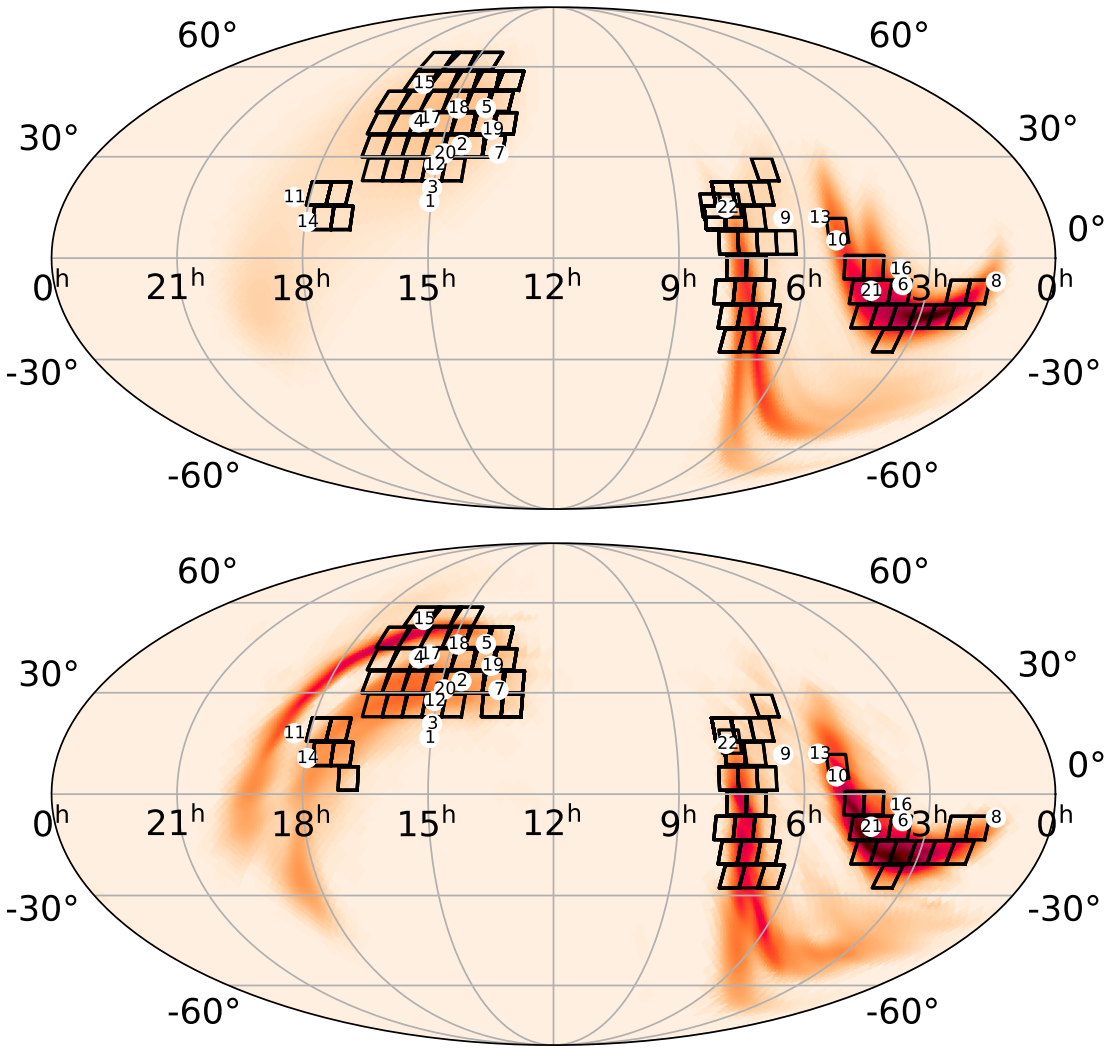

Figure 4.7: Coverage of S200105ae, showing the tiles on the 90% probability region of the initial BAYESTAR (top) and final LALInference (bottom) skymaps. The mapping of candidates to numbers is 1: ZTF20aaervoa, 2: ZTF20aaertpj, 3: ZTF20aaervyn, 4: ZTF20aaerqbx, 5: ZTF20aaerxsd, 6: ZTF20aafduvt, 7: ZTF20aaevbzl, 8: ZTF20aaflndh, 9: ZTF20aaexpwt, 10: ZTF20aafaoki, 11: ZTF20aafukgx, 12: ZTF20aagijez, 13: ZTF20aafanxk, 14: ZTF20aafujqk, 15: ZTF20aagiiik, 16: ZTF20aafdxkf, 17: ZTF20aagiipi, 18: ZTF20aagjemb, 19: ZTF20fksha, 20: ZTF20aaertil, 21: ZTF20fexle and 22: ZTF20fefxe.

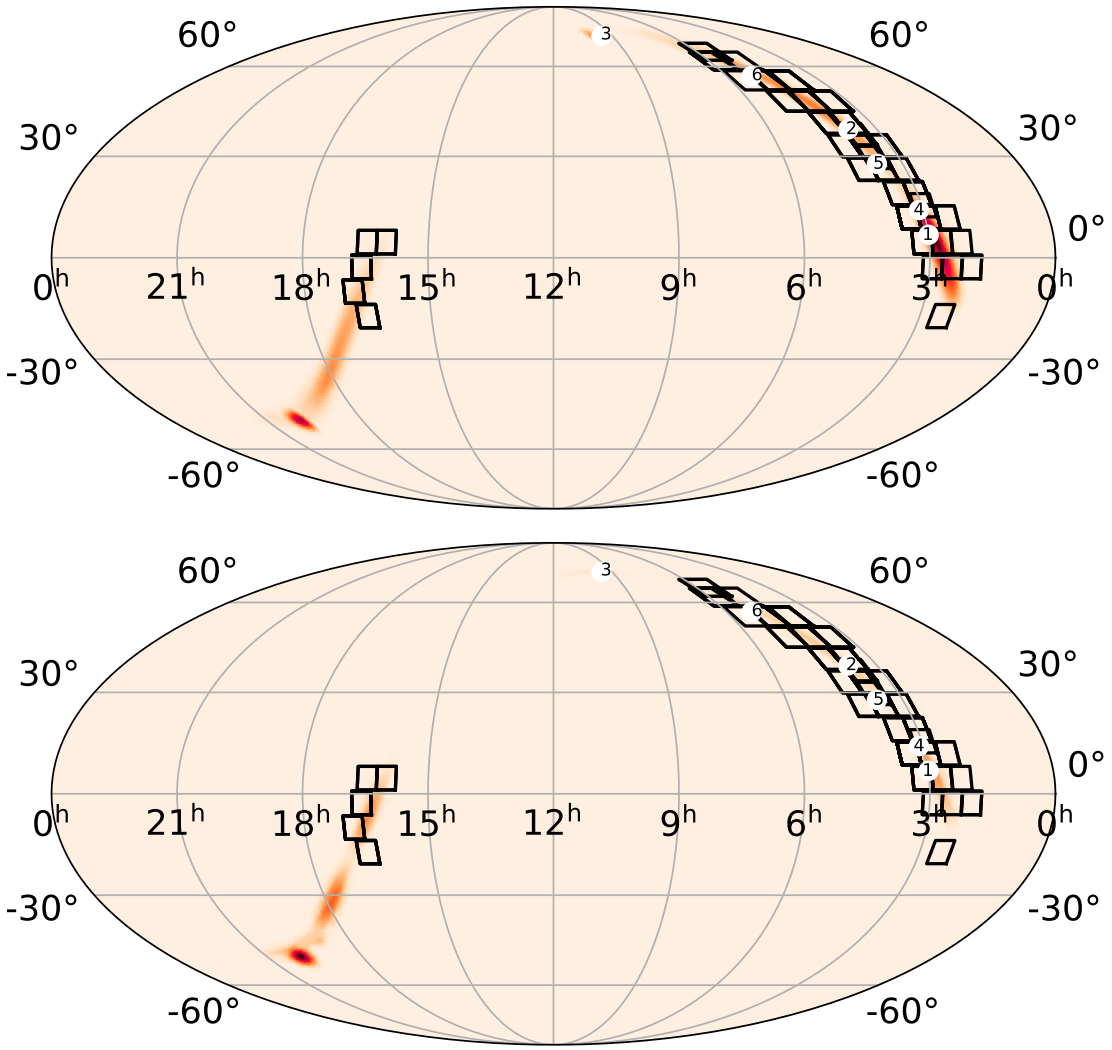

Figure 4.8: Same as Fig.4.7, for S200115j. The mapping of candidates to numbers is 1: ZTF20aagjqxg, 2: ZTF20aafqvyc, 3: ZTF20aahenrt, 4: ZTF20aafqpum, 5: ZTF20aafqulk, and 6: ZTF20aahakkp. We note that we include candidates up to and including the 95% probability region, and therefore some are outside of the fields we plot here.

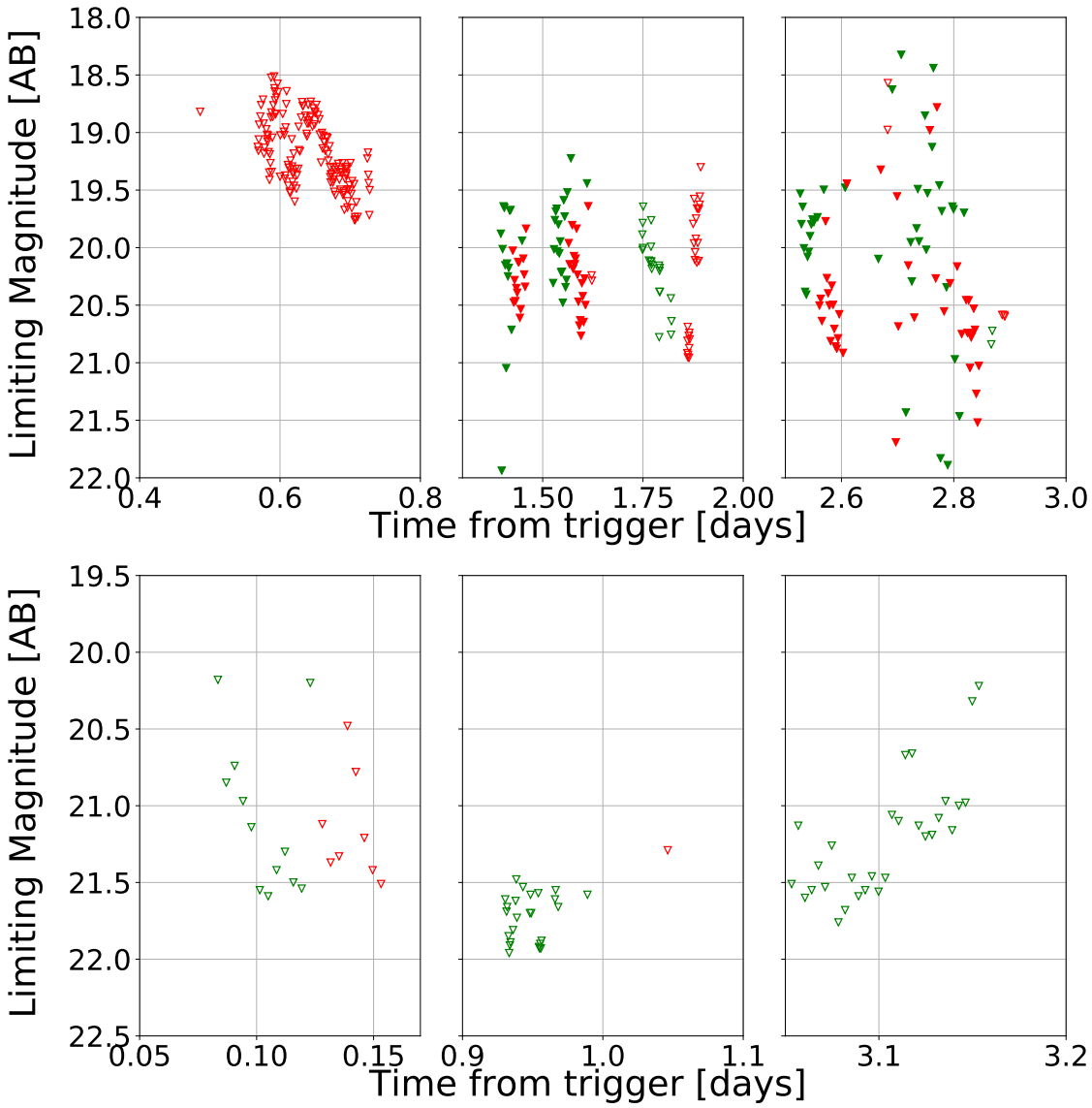

Figure 4.9: Limiting magnitude as a function of time for S200105ae (top) and S200115j (bottom), with the left, middle, and right panels corresponding to observations on the first, second, and third nights for S200105ae and first, second, and fourth nights for S200115j. The red and green triangles correspond to the r- and g-band limits, with open triangles serendipitous observations and closed ToO observations. The large differences in limiting magnitude from observation to observation are due to poor weather.

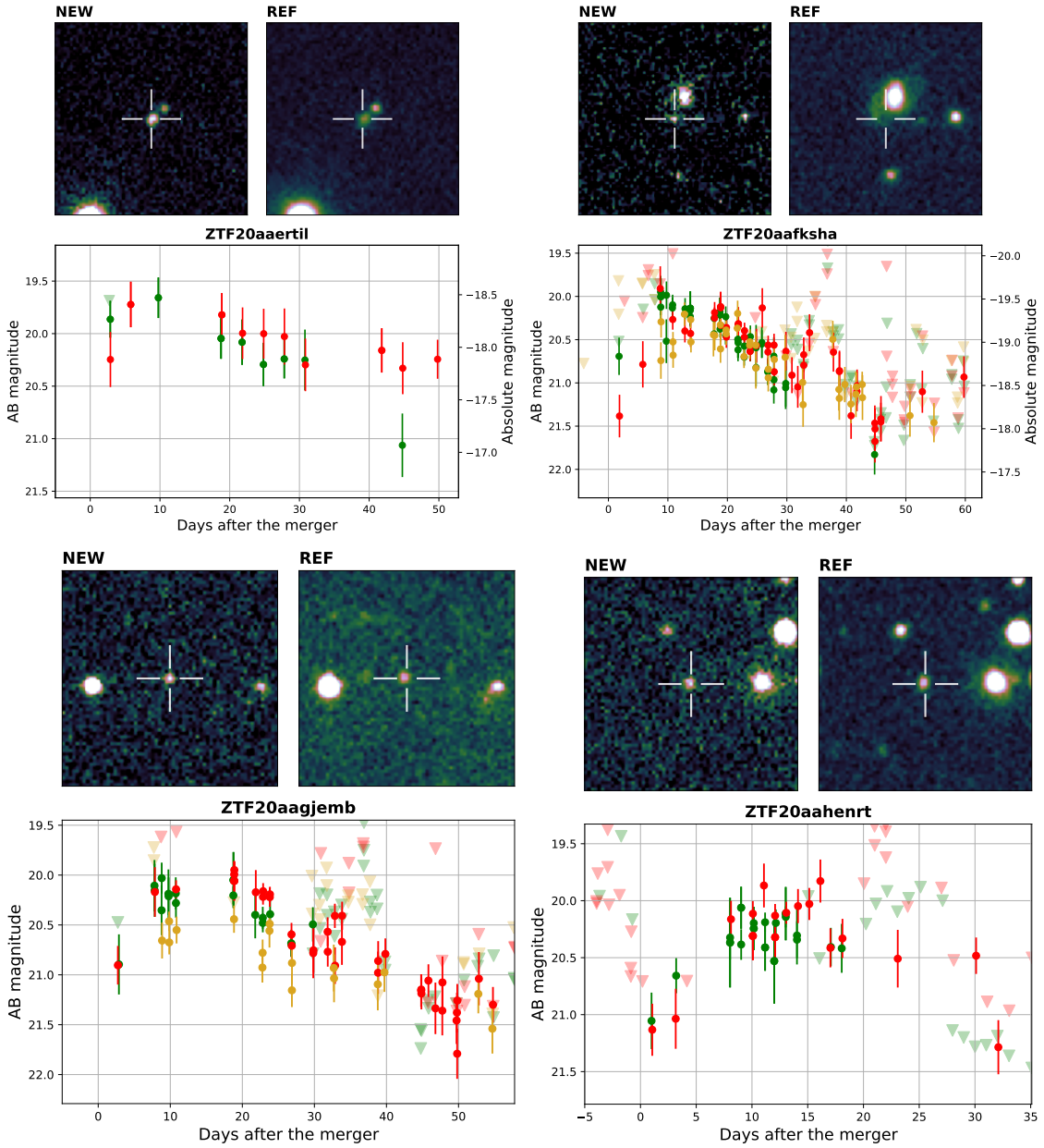

Figure 4.10: Lightcurves and r-band cutouts for a subset of the most well-sampled lightcurves for ZTF candidates ruled out photometrically, discussed in Section 4.3.3. Colors were used to represent the different bands: green, red and yellow for g-, r- and i- bands. The triangles in the lightcurve represent upper limits and filled circles are the detected magnitudes of the object. On each panel, the left cutout is the ZTF discovery image and the right one is the corresponding ZTF reference image. The transient is marked with a cross and the size of the cutouts is 0.7 sq. arcmin with north being up and east to the left.

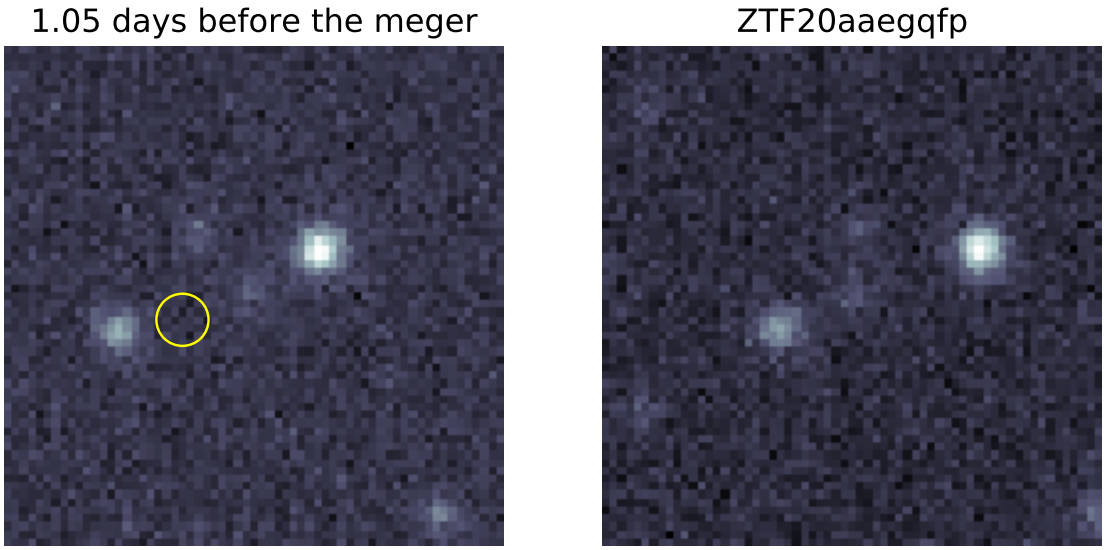

Figure 4.11: ZTF r-band cutouts of the slow moving asteroid ZTF20aaegqfp. The left panel is centered in a transient discovered a day before the trigger and 7.3 arcsec from our candidate ZTF20aaegqfp. The yellow circle in the left panel shows the coordinates of ZTF20aaegqfp. The right cutout is centered on the candidate ZTF20aaegqfp. The cutouts are 0.7 sq. arcmin and north and east are up and to the left respectively.

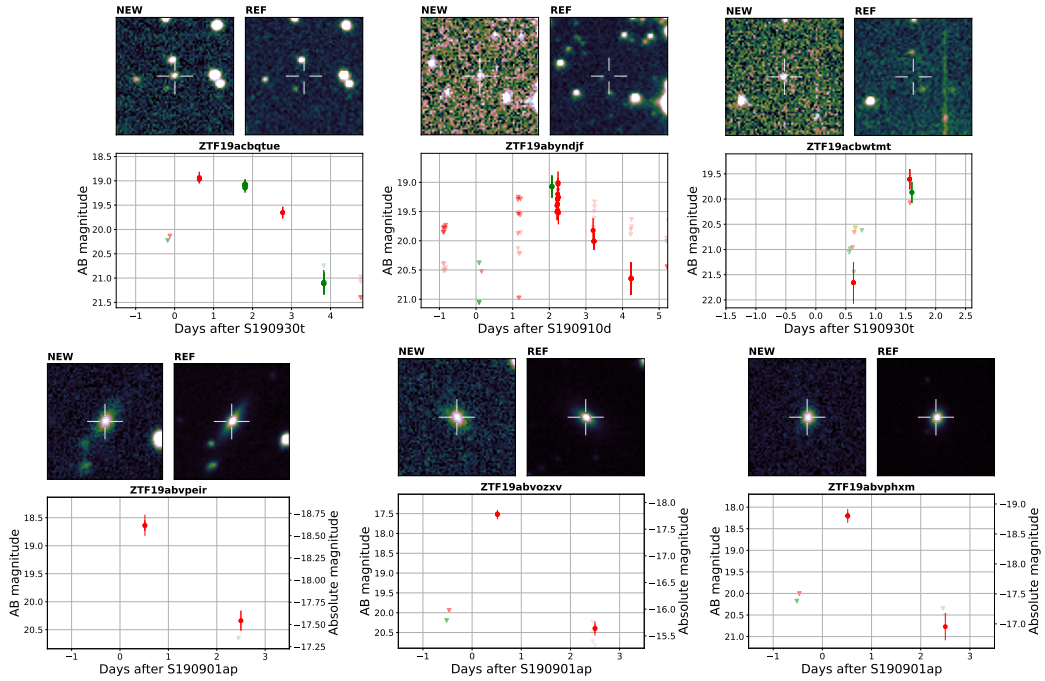

Figure 4.12: Collage of candidate counterparts found in deeper offline searches. Each candidate in the top row has two or more ZTF alerts: ZTF19acbqtue was ruled out as we found a quiescent stellar source with GMOS-N; ZTF19abyndjf does not have a galaxy in its vicinity and ZTF19acbwtmt had archival activity in PS1 DR2. Each candidate in the bottom row had only one ZTF alert but was flagged as interesting after performing forced photometry. These three candidates are nuclear transients that are ruled out as their absolute magnitudes are brighter than what is expected for kilonovae.

Name	RA	Dec	TNS	Discov. Mag.	Classification	Spec. facilities	Spec. Redshift
ZTF20aaervoa	15:02:38.38	16:28:21.5	AT2020pp*	$g = 20.63 \pm 0.30$	SN IIp	GTC	0.046
ZTF20aaertpj	14:27:52.03	33:34:09.7	AT2020pv*	$g = 19.88 \pm 0.16$	SN Ib	GTC	0.026
ZTF20aaervyn	15:01:27.45	20:37:23.5	AT2020pq*	$g = 20.62 \pm 0.26$	SN Ia	GTC	0.112
ZTF20aaerqbx	15:49:26.29	40:49:55.0	AT2020ps*	$g = 19.46 \pm 0.15$	SN IIp	GTC	0.098
ZTF20aaerxsd	14:00:54.27	45:28:21.8	AT2020py	$g = 20.27 \pm 0.23$	SN Ia	GTC	0.055
ZTF20aafanxk	05:35:36.05	11:46:15.3	AT2020adk	$r = 18.52 \pm 0.25$	SN Ia	P60+SEDM	0.133
ZTF20aafujqk	17:57:00.42	10:32:20.3	AT2020adg	$r = 18.17 \pm 0.10$	SN Ia	P60+SEDM	0.074
ZTF20aafqpum	03:06:07.50	13:54:48.4	SN2020yo	$g = 19.76 \pm 0.20$	SN Ia 91-bg	ePESSTO	0.09
ZTF20aaevbzl	13:26:41	30:52:31	AT2020adf	$i = 19.31 \pm 0.24$	CV	P200+DBSP	0.0

Table 4.5: Follow-up table for all spectroscopically classified transients. Spectra obtained with GTC were used to classify all 5 transients (Castro-Tirado et al., 2020; Valeev et al., 2020). Other spectra were obtained with ePESSTO, P60+SEDM, and P200+DBSP. The spectroscopic redshifts are listed as well. The objects with a star (*) were first reported to TNS by ALeRCE. Discovery magnitudes reported are extinction-corrected.

4.4 The O3 GW events

The previous sections (Sec. 4.2 and 4.3) showcase the modus operandi that the ZTF multi-messenger decided to take to search for optical counterparts to GWs. These examples portrait both the observing and vetting strategy that we took to search for over a dozen mergers that had a high probability of having a NS in the merger (either BNS or NSBH) and that the ZTF coverage within 24 hours from the merger could be $> 30\%$ of the initial BAYESTAR (Singer & Price, 2016) map. Although there were a total of 15 GW events with a NS involved, we only used ZTF to observe 13 localization regions. The events S190510g and S190924h were not followed-up as their localizations were too far south and too close to the moon, respectively. The nature of the ZTF survey allows for serendipitous coverage of the localization regions, as the survey systematically covers the northern night sky. For some of the GW events, the region was already being observed at the time of the event trigger. For a few events, this serendipitous coverage contributes to more than 30% of the localization map. This systematic and serendipitous coverage

Name	RA	Dec	TNS	Discov. Mag.	Host/Redshift	rejection criteria
ZTF20aafduvt	03:36:29	-7:49:35	AT2020ado	$g = 19.57 \pm 0.29$	0.25 ± 0.02 (p)	slow
ZTF20aaflndh	1:22:38	-6:49:34	AT2020xz	$g = 19.11 \pm 0.11$	0.091 ± 0.023 (p)	slow
ZTF20aaexpwt	06:26:01	11:33:39	AT2020adi	$r = 16.95 \pm 0.17$	-	slow
ZTF20aafukgx	18:23:21	17:49:32	AT2020adj	$r = 18.40 \pm 0.15$	-	slow
ZTF20aagijez	15:04:13	27:29:04	AT2020adm	$r = 19.67 \pm 0.3$	0.061 (s)	slow
ZTF20aagiiik	16:19:10	53:45:38	AT2020abl*	$g = 19.76 \pm 0.22$	0.13 (s)	slow
ZTF20aafdxkf	03:42:07	-3:11:39	AT2020ads	$r = 20.02 \pm 0.25$	-	slow
ZTF20aagiipi	15:33:25	42:02:37	AT2020adl	$g = 20.10 \pm 0.32$	0.39 ± 0.02 (p)	slow
ZTF20aafsnux	14:36:01	55:11:49	AT2020dzu	$g = 19.67 \pm 0.22$	-	slow
ZTF20aagjemb	14:51:26	45:20:41	AT2020adh	$r = 20.90 \pm 0.02$	0.21 ± 0.06 (p)	slow
ZTF20aafksha	13:43:54	38:25:14	AT2020adr	$g = 20.06 \pm 0.26$	0.167 (s)	slow
ZTF20aaertil	14:52:26	31:01:19	AT2020pu*	$g = 19.86 \pm 0.18$	0.093 (s)	slow
ZTF20aafexle	04:20:31	-9:30:28	AT2020adn	$r = 19.67 \pm 0.30$	0.18 ± 0.02 (p)	stellar
ZTF20aafefxe	07:47:24	14:42:24	AT2020adt	$g = 21.0 \pm 0.18$	0.09 ± 0.05 (p)	slow
ZTF20aafaoki	05:13:14	05:09:56	AT2020adq	$r = 19.21 \pm 0.28$	-	slow
ZTF20aaegqfp	07:49:02	12:29:26	AT2020dzt	$r = 19.37 \pm 0.27$	-	asteroid

Table 4.6: Follow-up table of the candidates identified for S200105ae, reported in Ahumada et al. (2020b). The ZTF objects with a star (*) in the TNS column were first reported to TNS by ALeRCE. The spectroscopic (s) or photometric (p) redshifts of the respective host galaxies are listed as well. As a reference, the redshift range at the distance of the event is z=0.045 to z=0.077. We use the same rejection criteria described in more detail in section 4.3.3 here, as follows: slow photometric evolution (slow), hostless, stellar, and slow moving asteroid (asteroid).

Name	RA	Dec	TNS	Discov. Mag.	Host/Redshift	rejection criteria
ZTF20aagjqxg	02:59:39	06:41:11	AT2020aeo	$g = 20.65 \pm 0.26$	-	slow
ZTF20aahenrt	09:32:53	72:23:06	AT2020axb	$g = 20.55 \pm 0.29$	0.16 ± 0.04 (p)	slow
ZTF20aahakkp	05:07:55	56:27:50	AT2020bbk	$g = 15.67 \pm 0.08$	-	slow
ZTF20aafqulk	03:39:45	27:44:05	AT2020yp	$g = 20.74 \pm 0.21$	-	stellar
ZTF20aafqvyc	03:47:58	38:26:32	AT2020yq	$r = 20.39 \pm 0.19$	-	asteroid

Table 4.7: Follow-up table of the candidates identified for S200115j, reported in Anand et al. (2020b). As a reference, the redshift range at the distance of the event spans from z=0.056 to z=0.089.

was supplemented with a ToO strategy, that allows to search for fainter sources and avoid unrelated sections of the sky in order to maximize coverage of the error regions associated to GW events. A summary of the triggers, classifications, and coverages can be found in Table 4.8. Not all the GW triggers were confirmed in the offline analysis presented in the GWTC-2 / 2.1 / 3 catalog papers (Abbott et al., 2021; The LIGO Scientific Collaboration et al., 2021a,b). We point out in Table 4.8 the triggers that the LVC confirmed as GW events with the 'GW' prefix, while the inconclusive events are presented with an 'S' as a prefix.

The selection and vetting of the candidates followed the guidelines listed in Sec. 4.1, and a compilation of the candidates of each trigger can be found in Sec. A.2 in the Appendix A. Moreover, the relevant quantities for the entirety of the search show that more than 2 million alerts were detected within 3 days of these 13 mergers, and only 2199 sources passed our filtering scheme (see Table 4.9). This translates to a reduction of $\sim 0.1\%$ of the original number of alerts. Out of these 2199 candidates, only 127 showed some sort of interesting features, such as a fast decay, being close to a host galaxy compatible with the sky localization. These candidates were circulated over GCN and we show the follow-up photometry and spectroscopy of a subset of them in Fig. 4.13.

Name	FAR (P_t)	Localization	Distance	Class	P_1	P_2	Time Lag	Depth	E(B−V)
GW190425	1 per 69000 yrs (1%)	7461 deg^2	156 ± 41 Mpc	BNS	24.13% (45.92%)	23.90% (44.62%)	0.003 hr	21.5	0.03
GW190426	1 per 1.6 yrs (58%)	1131 deg^2	377 ± 100 Mpc	NSBH	52.33% (59.69%)	51.57% (57.40%)	13.06 hr	21.5	0.34
GW190814	1 per 10^{25} yrs (1%)	23 deg^2	267 ± 52 Mpc	NSBH	88.57 % (87.00%)	78.37% (70.60%)	0.00 hr	21.0	0.02
S190901ap	1 per 4.5 yrs (14%)	14753 deg^2	241 ± 79 Mpc	BNS	56.94% (50.67%)	49.39% (42.76%)	3.61 hr	21.0	0.03
S190910d	1 per 8.5 yrs (2%)	2482 deg^2	632 ± 186 Mpc	NSBH	32.99%(42.50%)	31.17% (39.64%)	1.51 hr	20.3	0.04
S190910h	1 per 0.9 yrs (39%)	24264 deg^2	230 ± 88 Mpc	BNS	33.26% (42.95%)	28.92% (38.44%)	0.015 hr	20.4	0.08
S190923y	1 per 0.67 yrs (32%)	2107 deg^2	438 ± 133 Mpc	NSBH	NA (38.99%)	NA (19.22%)	13.73 hr	20.1	0.09
S190930t	1 per 2.0 yrs (26%)	24220 deg^2	108 ± 38 Mpc	NSBH	NA (50.63%)	NA (43.42%)	11.91 hr	21.1	0.05
S191205ah	1 per 2.5 yrs (7%)	6378 deg^2	385 ± 164 Mpc	NSBH	NA (5.68%)	NA (4.85%)	10.66 hr	17.9	0.04
S191213g	1 per 0.89 yrs (23%)	4480 deg^2	201 ± 81 Mpc	BNS	27.50% (0.80%)	25.10% (0.09%)	0.013 hr	20.4	0.30
S200105ae	NA (97%)	7373 deg^2	283 ± 74 Mpc	NSBH	52.39% (56.40%)	43.99% (47.96%)	9.96 hr	20.2	0.05
GW200115	1 per 1513 yrs (1%)	765 deg^2	340 ± 79 Mpc	NSBH	22.21% (34.92%)	15.76% (18.17%)	0.24 hr	20.8	0.13
S200213t	1 per 1.8 yrs (37%)	2326 deg^2	201 ± 80 Mpc	BNS	72.17% (79.29%)	70.48% (76.08%)	0.40 hr	21.2	0.19

Table 4.8: Summary of ZTF follow-up of 13 gravitational wave triggers in O3. We list the GW False Alarm Rate (FAR) and in parantheses, the probability that the event is terrestrial (P_t). We list the total size of the GW localization region, the GW median distance and the most probable GW classification. We report the integrated probability within the 90% contour of the LALinference skymap, covered by triggered and serendipitous ZTF searches during the first three days after merger observed at least once (P_1), and probability observed at least twice (P_2). In parentheses, we include the coverage based on the BAYESTAR skymap. For some alerts, only BAYESTAR skymaps were made available. All estimates correct for chip gaps and processing failures. We also report the time lag between merger time and start of ZTF observations (hours), the median depth (AB mag), and the median line-of-sight extinction. Modified from Kasliwal et al. (2020b).

Stage	Number
ZTF alerts within 3 days of merger	2,116,846
ZTF alerts that pass our filtering criteria	2,199
Candidates circulated via GC	127
Candidates Not ruled out with spectroscopy	70
Candidates not immediately ruled out with photometry	14
Candidates not ruled out after detailed inspection	0
Kilonovae	0

Table 4.9: Our candidate vetting and follow-up strategy for all the relevant events during O3.

4.4.1 ZTF limits

Under the assumption that the LVC events are astrophysical events, and that these are accompanied by a kilonova, we can use our limits and depths to compare to kilonova models. Since the outcome of a KN depends on several factors intrinsic to the merger, such as the ejecta mass, the ejecta velocity, the lanthanide fraction, the viewing angle, or the remnant lifetime, we compare the ZTF limits to a grid of KN models from Kasen et al. 2017. This comparison is shown in Fig. 4.14, where the ZTF windows are grey rectangles in the light-curve space. When taking GW170817 as our benchmark, it is clear that even the shallowest ZTF search (r $\sim$ 17.9 mag) would have been able to detect it.

It is more evident in the bottom panel of Fig. 4.14, which has the ZTF searches scaled to the main distances limits, and shows the limits as absolute magnitudes for each event. The main difference with the GW170817 case, is that the median distance to an O3 event was of 267 Mpc, while GW170817 occurred at 40 Mpc. At this distance, a GW170817-like event would peak at 21.4 mag in the r-band, making it virtually impossible to be detected with ZTF.

4.4.2 Conclusions

In this chapter I have compiled the efforts in which I have been involved during the third LIGO observing run. Particularly, part of Sec. 4.2 has been published in Coughlin et al. 2019b, parts of Sec. 4.3 have been published in Anand et al. 2021, and parts of the Appendix A have been published in Kasliwal et al. 2020b. My contribution to these searches was the design of a filtering strategy to vet candidates, the implementation of the observing strategies and the photometric and spectroscopic follow-up of multiple candidates.

During these campaign we have scanned more than 10,000 $\deg^2$ looking for the optical counterpart of BNS and NSBH merger, as well as MassGap events. We have proven possible large scale searches triggering Target of Opportunity observations with large field of view optical telescopes, effectively reducing the number of viable candidates to less than 0.01% of the original amount of alerts detected in the first place. This number was reduced after human vetting, and around a dozen candidates were intensively followed up with other facilities.

The rapid follow-up of transients showed to be essential to quickly narrow down the list of transients derived from wide field searches. Particularly, photometric monitoring helped us ruled out close to 55% of the transients mainly based on the inconsistent evolution of their brightness, compared to KN and afterglow models. Close to 45% of the candidates were spectroscopically classified as a different kind of object, thanks to the effort of the global community. A more challenging kind of contaminant appeared to be the slow moving asteroids, since they have an

unpredictable behavior and candidates showed rapid fading. Further analysis on the alert stream has been implemented as part of the metric and now it is possible to flag these objects.

Based on the ZTF limits (see Fig. 4.14), an event like GW170817 could have been detected up to $\sim$ 200 Mpc. However, the median distance for the events followed up during O3 was of 267 Mpc, making it very challenging for a GW170817-like event to be discovered with ZTF. This poses a major barrier in the multi-messenger astronomy side as usually the areas enclosed a median of 2482 deg^2, making virtually impossible a galaxy targeted search. The issue related to grater distances could be tackled with longer exposures, or with surveys with deeper limits (i.e. Rubin). As KN evolve differently in the NIR, future facilities such as WINTER or DREAMS (both wide field robotic telescopes in the NIR) could help bridge the gap between large error regions and optical and NIR searches.

Multiple sources faded past the ZTF limits after a day or two, hidering the continuous monitoring. The problem was s olved by using a network of small telescopes around the globe, available to observe these transients and go to deeper limits than ZTF. Wide-field surveys are an incredible discovery machine, the problem is that due to the fast fading nature of the KN and afterglows, these discoveries rapidly reach their limits. Robotic telescopes, like Las Cumbres Observatory (LCO), Kitt Peak Electron multiplying CCD Demonstrator (KPED), and the robotic Palomar 60 inch telescope (P60), allowed to keep track of the evolution of these transients and help ruling them out. Future telescopes joining the network would bring more resources to observe more candidates and, possibly, to a greater depth.

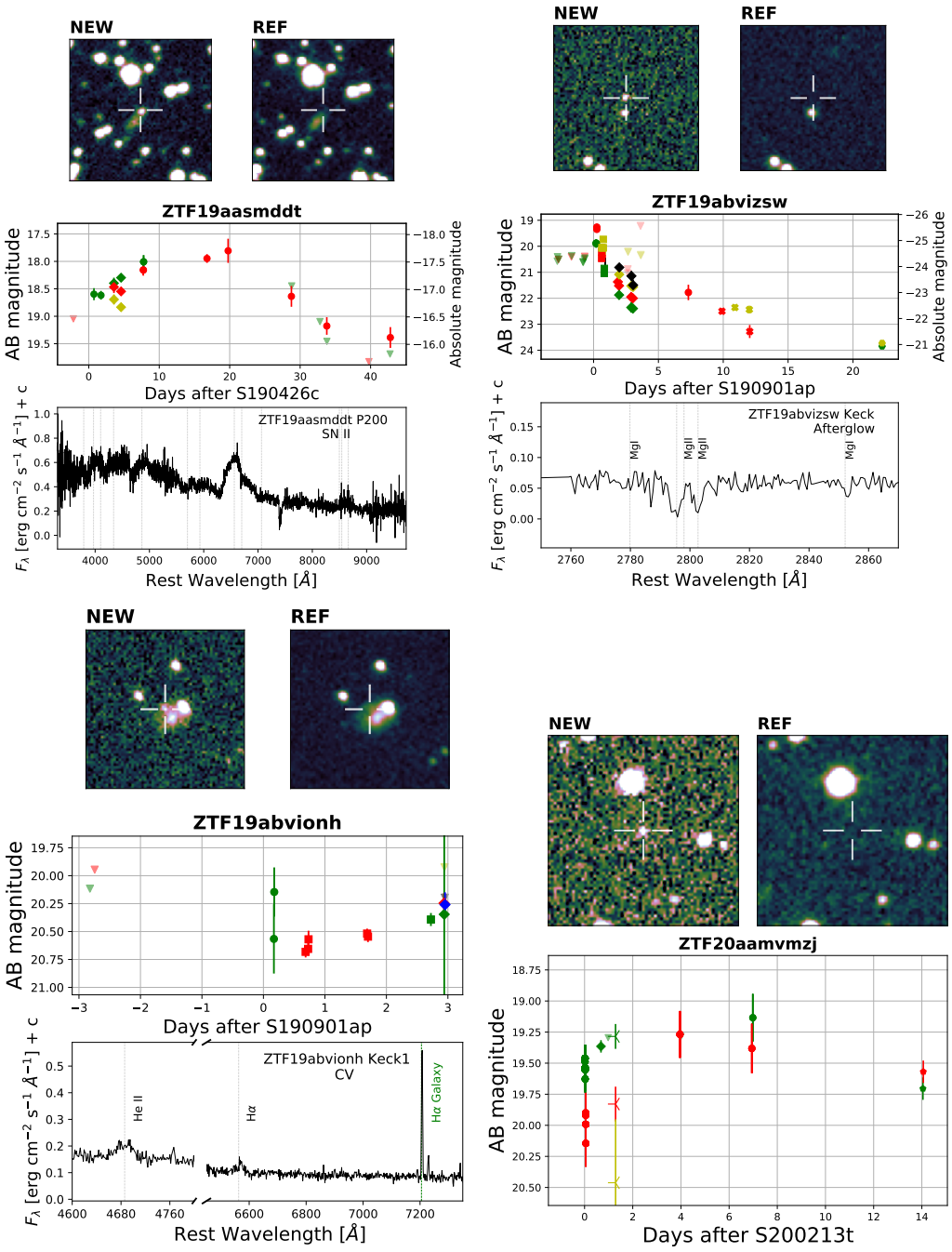

Figure 4.13: Collage of candidate counterparts found during real-time searches. We show a 7 arcsec $\times$ 7 arcsec region with North Up and East Left for the discovery (NEW) and reference (REF) images. We also show the light-curve of the candidate, where the u-, g-, r-, i- and z-band data are shown in blue, green, red, yellow and black respectively. ZTF data are presented with filled circles, while data from LT, GIT, Keck, WHT and LCO are presented as filled diamonds, squares, elongated diamonds, x-shapes and pentagons respectively. Absolute magnitude is shown for the candidates with a known redshift and upper limits are shown as inverted triangles. We also display the spectra of the transient where available and mark the Hydrogen and Helium lines for ZTF19aasmddt (SN II), the H and He II features of ZTF19abvionh (CV), and the Mg I and Mg II lines for ZTF19abvizsw (long GRB afterglow).

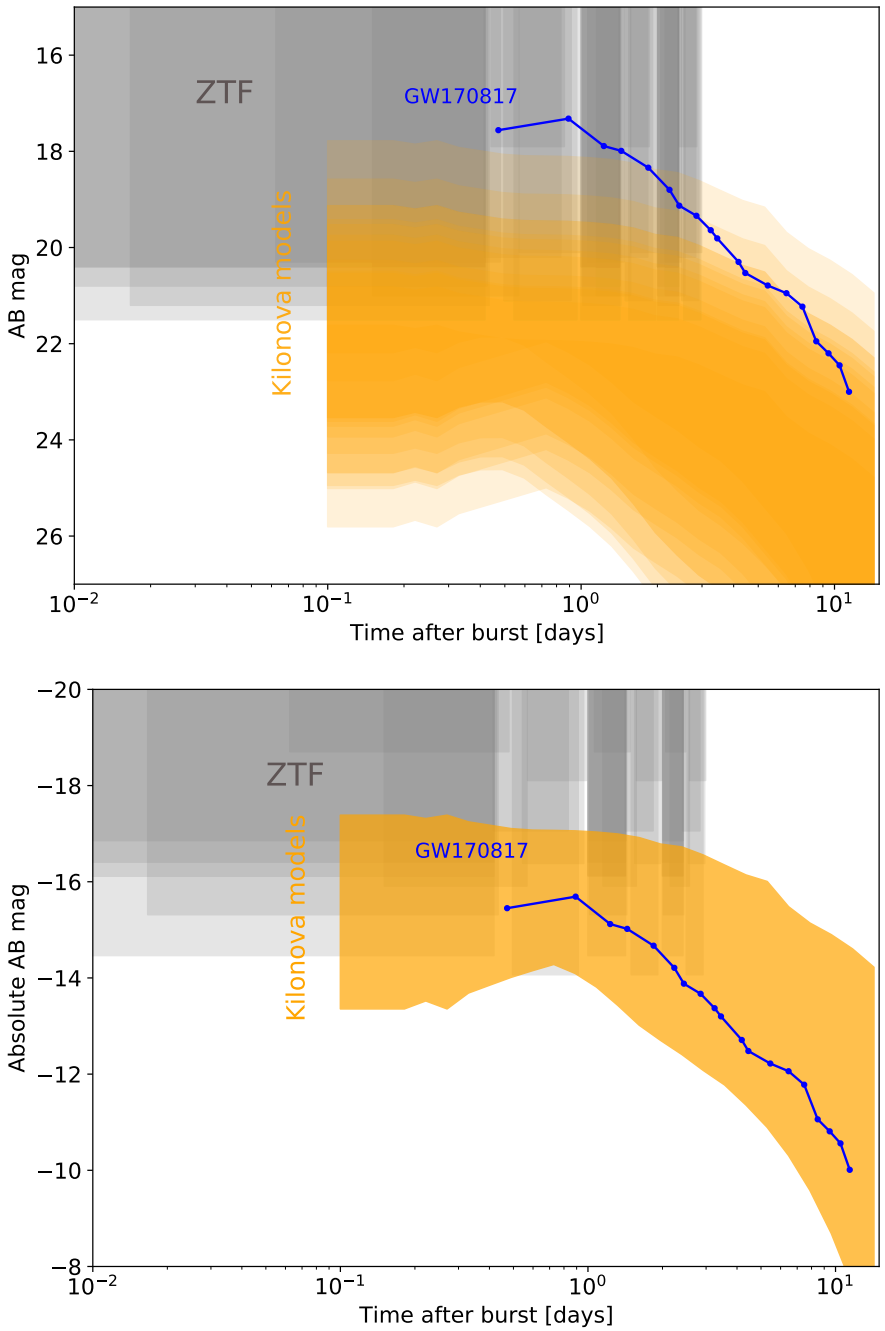

Figure 4.14: (Top) The ZTF search windows (grey) for all the 13 GW follow-ups, with a set of KN models from Kasen et al. 2017 scaled to the mean GW distance of each trigger (orange). In this case, due to the difference in distance for each trigger, KN models range between 18 and 26 mag. We additionally show the light-curve of the optical counterpart to GW170817. (Bottom) The same ZTF windows in the light-curve space, now scaled to the mean distance of each trigger (grey). The absolute magnitude of the Kasen et al. 2017 KN models (orange) and optical counterpart to GW170817 (blue).

Chapter 5: Towards future detections of Kilonovae: from alerts to science

5.1 Introduction

Multi-messenger sources of astrophysical transients are changing the face of time-domain astronomy. Recently, the detection of GW170817, its short gamma-ray burst (SGRB), its afterglow, and the optical/infrared kilonova (KN) counterpart, AT2017gfo, introduced the world to the scientific potential of discovering counterparts to gravitational waves (GWs) detections such as those made by the interferometers Advanced LIGO and Advanced Virgo. The discovery of GW170817 (Alexander et al., 2017; Chornock et al., 2017; Cowperthwaite et al., 2017; Drout et al., 2017; Evans et al., 2017; Haggard et al., 2017; Hallinan et al., 2017; Kasliwal et al., 2017b; Kilpatrick et al., 2017; Margutti et al., 2017) as a multi-messenger source marked a watershed moment in astrophysics, with prospects to strongly constrain both the neutron star equation of state (Abbott et al., 2017b; Bauswein et al., 2013) and the Hubble Constant (Abbott et al., 2017d), amongst many other science cases (Abbott et al., 2017e; Just et al., 2015; Roberts et al., 2017; Rosswog et al., 2017; Wu et al., 2016). This event additionally cemented the conection between GWs, SGRBs and KNe.

Previous SGRB detections have claimed optical and NIR excesses that could

be explained by KN emission (Tanvir et al., 2013; Troja et al., 2019). Thus, SGRBs present another way to find compact binary mergers. These short bursts have been detected at a rate of 10 and 40 per year, by the GRB instruments on board of the Neil Gehrels *Swift* Observatory (Gehrels et al., 2004) and the *Fermi* satellite respectively (von Kienlin et al., 2020). However, the optical counterparts for these bursts have proven to be elusive, mainly because the localization of *Fermi* SGRBs typically spans hundreds of square degrees (Ahumada et al., 2022; Mong et al., 2021). Similarly, the follow up of BNS and NSBH mergers detected by the the LIGO-Virgo Collaboration (LVC) has not been fruitful as the areas covered by the GW maps are similarly large (Andreoni et al., 2019a; Andreoni et al., 2020; Coughlin et al., 2019d; Goldstein et al., 2019; Kasliwal et al., 2020b). In fact, most of the knowledge about compact merger host galaxies and their environment comes from the localization of a few dozen of *Swift* SGRBs (Fong et al., 2015; Fong et al., 2022; Nugent et al., 2022; O'Connor et al., 2022), mainly based on the X-ray afterglow localization of the afterglow.

Besides instrumental limitations, the lack of detections can be mainly explained by the fast fading nature of both KNe and afterglows, and the low local rate of compact binary mergers (Dichiara et al., 2020). To illustrate this, a GW170817-like event occurring at 200 Mpc would be of magnitude ~ 20.5 in the r-band. This is comparable to the limiting magnitude of wide field of view surveys like the Zwicky Transient Facility (ZTF) (Bellm et al., 2019a) ($m_r \sim 21$ mag). Furthermore, multiple models predict a rapid decrease in the optical flux of the KN (Bulla, 2019; Dietrich et al., 2020; Kasen et al., 2017), which would make a GW170817-like coun-

terpart < 22 mag after 2 days.

Another approach to find compact binary mergers is to search for the KN signatures in current (and future) optical wide-field surveys like ZTF (Graham et al., 2019; Masci et al., 2019), the Panoramic Survey Telescope and Rapid Response System (Pan-STARRS; Tonry et al. 2012), the Asteroid Terrestrial-impact Last Alert System (ATLAS; Tonry et al. 2018), the Dark Energy Camera (DECam; Flaugher et al. 2015), the enhanced Public ESO Spectroscopic Survey for Transient Objects (ePESSTO; Smartt et al. 2015), the Global Rapid Advanced Network Devoted to Multi-messenger Addicts (GRANDMA; Antier et al. 2020), the Gravitational wave Optical Transient Observer (GOTO; Gompertz et al. 2020), and the Vera C. Rubin Observatory's Legacy Survey of Space and Time (LSST; Ivezic et al. 2008). The combination of wide field of view (FOV) and high cadence has already enabled the discovery of interesting fast transients, such as orphan GRB afterglows (Cenko et al., 2013; Ho et al., 2020; Ho et al., 2018), fast blue optical transients (FBOTs) (Ho et al., 2021; Perley et al., 2018), and even a jetted tidal disruption event (TDE) (Andreoni et al. submitted). Even though no KN emission has been detected, these avenues have been able to constrain the KN rates (Andreoni et al., 2020b; Andreoni et al., 2021) independently from GWs or GRBs triggers.

Particularly, ZTF approaches time domain astronomy (TDA) by nightly imaging the sky, to later perform image subtraction using reference templates (Masci et al., 2019). The fields are previously defined as they are part of a set of grids that tessellate the sky using the FOV of the camera. An *alert* is created for each flux residual greater than 5σ, and it stores information related to the source, such as its cur-

rent magnitude and the distance to the closest source in the Pan-STARRS 1 (PS1) catalog (Tachibana & Miller, 2018). In addition, the region is cross-matched and any previous alerts within 1.5 arcsec of the detection are appended to the history of the newly created alert. ZTF generates $\sim 10^5$ alerts per night, and these are publicly distributed to alert brokers. These alerts are publicly accessible and stored at Infrared Processing and Analysis Center (IPAC), thus the entire history of the transient is available by querying the IPAC database.

One of the projects that uses the ZTF stream of data to search for KN candidates is the ZTF REaltime Search and Triggering (ZTFReST) code (Andreoni et al., 2021). ZTFReST queries photometric data to identify fast fading transients that could be counterparts to neutron star mergers (kilonovae or GRBs afterglows), and allows for the automatic follow-up scheduling on robotic telescopes. This framework has developed an alert filtering scheme similar to Ahumada et al. 2022, and it has already identified at least seven confirmed afterglows. Their early discovery allowed for multi-wavelength follow-up observation and early classification.

Multiple works have characterized and evaluated the detectability of KN with Rubin (Andreoni et al., 2022a; Bellm et al., 2022), proposing different cadences or advocating for targets of opportunity (ToOs). The combination of a 9.6 deg^2 camera mounted on a 8.4 m telescope allow Rubin to reach depths of 25 mag and 24.7 mag in the g- and r-band respectively. Compared to ZTF, Rubin is expected to produce 10-100 times more alerts than ZTF (i.e. $10^5 - 10^6$ per night), which will translate into a much larger sample to characterize and sift through. Previous works have shown that depending on the cadence, between 10-100 KN will be discovered

with Rubin during the 10-year duration of the survey (Cowperthwaite et al., 2019). This chapter aims to fill the gap between the alerts and the discovery of a KN, by simulating KN alert packages along with other fast fading transients and applying filtering strategies to quantify the number of contaminant sources that will pollute the Rubin sample. Our approach is based on previous multi-messenger searches (see Ahumada et al. 2022; Anand et al. 2021; Coughlin et al. 2019b; Kasliwal et al. 2020b) and it will allow to prepare for future photometric and spectroscopic follow-up in terms of scale and resources, as we can determine the physical features (i.e. discovery or peak magnitude) of the KNe as well as the sources that will significantly contaminate the KN candidate sample.

This Chapter is organized as follows: in Sec. 5.2 we describe our simulated universe, as well as the transients included in it, the cadence chosen for the Rubin observations, and the details on the alert packages. In Sec. 5.3 we provide specifics for the construction of the filtering scheme. We present our results and discussion in Sec. 5.4, and our conclusions and future work in Sec. 5.5.

5.2 Simulated universe

Previous works have addressed the kilonovae detectability problem in large area surveys like the Legacy Survey of Space and Time (LSST) and ZTF (Andreoni et al., 2022a; Bellm et al., 2022; Sagués Carracedo et al., 2020). These works have made use of toolkits, such as `simsurvey` (Feindt et al., 2019) or the LSST metrics analysis framework [1] (MAF; Jones et al. 2015), which allow for the injection of tran-

[1] `https://github.com/LSST-nonproject/sims_maf_contrib/blob/master/mafContrib/kneMetrics.py`

sients directly into the simulated cadence and the direct comparison to the limiting magnitude of the corresponding fields (Sagués Carracedo et al., 2020). In this work we tackle this problem in a different way: we have simulated Rubin observations, and we have created a database populated with alerts derived for different classes of transients. The alerts are the expected nightly product of Rubin and they are part of the current ZTF nightly products. In ZTF, an alert is produced after a 5σ flux variation is detected, and it records information about the source that can be later used to discriminate and sift for interesting sources. The ZTF alerts have a particular *schema* (i.e. the structure and keywords to access the database[2]). It is expected that the Rubin alert schema will not deviate from the ZTF one.

The database we have created contains transients of different classes, such as KN, GRBs, TDEs, SNe Ia, and SN II shock break-out (SBO). We do not include variable stars, asteroids, active galactic nuclei (AGN), or Cataclysmic Variables (CVs). This *sandbox* aims to represents a truthful set of sources, taking into consideration the limitations of the survey at the detection level, as well as the rates and physical properties of the simulated transients. To produce a realistic simulation, we have estimated the number of transients that will fall in the observable horizon of a survey by taking the median limiting magnitude of the survey m_{lim}, and the characteristic absolute magnitude of a transient M. With these two quantities, we proceed to calculate the corresponding distance modulus $\mu_h = m_{lim} - M$, and derive a horizon distance in parsecs, d_h, for each transient class, using $\mu_h = 5\ log_{10}(d_h) + 5$.

Combining the maximum distance that a survey could detect a source of a

[2] `https://zwickytransientfacility.github.io/ztf-avro-alert/schema.html`

given class, d_h, and the available rates found in the literature, it is possible to estimate the number of transients that would fall within a survey's horizon. Once the number of sources is determined, we randomly retrieve a distance d_t and proceed to create alerts using the distance-scaled light-curve model for each specific class. Additionally, each alert is randomly assigned a set of coordinates (RA, Dec), and a start Julian Day (JD). Using the coordinates, and following the ZTF *schema*, we cross-match with Pan-STARRS and annotate in the alert package information about the environment of the transient: the distance to the three nearest sources, their star/galaxy scores and their magnitudes. Furthermore, using the JD and coordinates, we query the Minor Planet Center and annotate in the alert package any ephemerides or coincidences with solar system objects.

To create a light-curve for any given transient, we start randomizing the initial JD (`jdstarthist`) and creating a history of visits based on a given cadence. For this work we chose a cadence that observes the transient twice a night in the r-band and once in the g-band. Each visit was separated by 4 hours. Using the schedule of visits we take a transient model (described in Sec. 5.2.1) and calculate the magnitude at which the transient would be observed. Some models are generated with the `nmma` package, a framework that allows the rapid and user-friendly generation of a multi-wavelength grid of magnitudes for different transients such as KNe, GRBs, and SNe (for more information of the package please refer to Pang et al. 2022). For the transients that are not available in the `nmma` package we use ZTF light-curves as templates,scaling and interpolating the magnitudes as needed.

Once the light-curve is generated, we construct the alerts comparing randomly

picked limiting magnitudes, m_{lim}, to the model magnitudes, m_{mod}, in the synthetic light-curve. We draw m_{lim} from a skew gaussian distribution peaking at 24.7 mag, which corresponds to the expected Rubin limiting magnitude (see Fig. 5.1). We populate the alert packages with the model magnitude if $m_{lim} > m_{mod}$, otherwise we store only m_{lim}. The final product is a set of alerts for each transient, containing the distance-scaled magnitude or the limiting magnitude of the visit. The number of alerts per each class is a function of their intrinsic rate, although we factor that $\sim 1/3$ of the sky is observed by Rubin.

5.2.1 Models and rates

Kilonovae The `nmma` package has a few different models to generate KNe. For example, the Metzger 2017 model uses a 1D radiation transfer approach to generate a light-curve (see parameters in Table 5.1), while the POlarization Spectral Synthesis In Supernovae (POSSIS) simulates the KN spectral energy distribution (SED) using a multi-dimensional Monte Carlo radiative transfer code (Bulla, 2019).

Kilonovae rates are poorly constrained, and for this work we adopt the rates derived in Andreoni et al. 2021, where the conclusion is that a maximum of 900 Gpc^{-3} yr^{-1} should be expected. Additionally, the luminosity function of KN is vaguely constrained, thus we adopt the AT2017gfo peak absolute magnitude as a proxy to calculate the horizon distance d_h. For $M = -16.5$ mag, the horizon distance is of $d_h = 1.25$ Gpc and the number of KNe expected in this volume is 2507, considering that only $\sim 1/3$ of the sky is accessible to the survey (see Table 5.3).

KN parameter	Unit	Value
D_L	Mpc	46.48
β	-	3.69
$log_{10}(\kappa)$	cm^2 g^{-1}	1.66
KN$_{ts}$	days	0.18
Y_e	-	0.1
$log_{10}(v_{ej})$	c	-0.43
$log_{10}(M_{ej})$	$M_\odot$	-1.41

Table 5.1: The KN parameters fed to `nmma` that were used used in to create simulated light-curves for KN. The luminosity distance, D_L, is needed to generate the model, as well as the inverse mass ratio, β, the opacity of the material, κ, the time shift between the merger and the KN ligh-curve beginning, KN$_{ts}$, electron fraction, Y_e, and the velocity and mass of the ejecta, v_{ej} and M_{ej} respectively.

GRBs For the GRB models `nmma` makes use of the `afterglowpy` Python module, which provides numerical models to calculate synthetic light-curves and spectra of GRB afterglows. We use the top hat jet type, and set the standard afterglow properties to the mean values found in the literature: the viewing angle to a random value between 0.05 and 0.34 rad, the electron energy distribution index p to 2.4, as well as the fraction of shock energy imparted to electrons, ϵ_E to 0.1, and to the magnetic field, ϵ_B to 0.0001. Depending on the population of burst simulated (i.e. long or short), we adjust the values of the isotropic-equivalent energy E_0 and the circumburst density n_0.

The empirical rate of long GRBs is ~ 1 Gpc^{-3} yr^{-1} (Nakar, 2015). We do not correct this number by the beaming factor associated to these events, as we are interested in the population that can be observed by gamma-ray telescopes. These rates give a total of 5559 GRBs during a year of observations with Rubin, using an absolute magnitude of $M = -22$ mag. The mean E_0 for the long GRB population is of 10^{53} ergs, and the mean n_0 is of 0.1 cm^{-3}.

GRB parameter	Unit	Value
D_L	cm	1.36e26
θ_v	rad	0.05 - 0.34
θ_c	rad	0.05
θ_w	rad	0.4
E_0	erg	10^{53}
n_0	cm^{-3}	0.1
p	-	2.4
ϵ_e	-	0.1
ϵ_B	-	10^{-4}

Table 5.2: The GRB parameters fed to `nmma` and `afterglowpy` that were used to create simulated light-curves for the GRBs. The luminosity distance , D_L, is needed to generate the model, as well as the viewing angle, θ_v, the half-opening angle, θ_c, the outer truncation angle, θ_w, the isotropic-equivalent energy, E_0, the circumburst density, n_0, the electron energy distribution index, p, and the fraction of energy imparted to both the electrons, ϵ_e, and to the magnetic field, ϵ_B, by the shock.

Tidal Disruption Events

For the TDE models, we adopted a different strategy: we used as a template the TDE found in 2018, ZTF18abxftqm/AT2018hco (Hammerstein et al., 2022), and we interpolated its light-curve linearly to construct the TDE model.

We adopted the rates stated in Kremer et al. (2021), for which 200 Gpc^{-3} yr^{-1} give a total of 17620 TDEs distributed into a horizon distance caped by the peak absolute magnitude $M = -19$ mag.

Jetted Tidal Disruption Events

This particular set of TDEs occur when the accretion onto the supermassive black holes produces an ultra-relativistic jet. The detection rate is close to one a decade, with the last one being AT2022cmc (Andreoni et al., 2022b). We used the light-curve of this transient as a template, as it was discovered by ZTFReST (Andreoni et al., 2021). The specifics of AT2022cmc will be available in Andreoni et al. submitted. From this work, it was determined that the rate of these events is

of 0.02 Gpc^{-3} yr^{-1}, and that their absolute magnitude is of $\sim$ -22 mag.

SN Ia

For the SN Ia light-curve we used the template of a SN Ia found by ZTF, ZTF21abyjydm. We chose this transient as it has one of the longest and best sampled SN Ia light-curves in ZTF. Following Perley et al. (2020), the rate of SN Ia of 2.4×10^4 Gpc^{-3} yr^{-1} yields a total of 5.3×10^5 SN Ia when assuming an absolute magnitude of $M = -18$.

SN II shock break out

For the SN II shock break out (SBO) light-curve we used ZTF22aafrjnw as a the template. Found with the ZTFReST in April 18th 2022, this rapid transient faded 2 mag in 4.5 days. Originally considered a KN candidate, after the fourth day it started to show a rise in the g-, r-, and i-band. It was spectroscopically classified as a SN IIb (Chu et al., 2022), and the rapid decline was produced by the radiation of shock heated material as it expanded and cooled (Piro et al., 2021).

Based on the Sravan et al. (2019), only $\sim$4% of the core collapse supernovae are of the type IIb, leaving a rate of 5 Gpc^{-3} yr^{-1}. Assuming an absolute magitude of $M = -19$ mag for these transients, it yields a total of 1754 transients in our simulated universe.

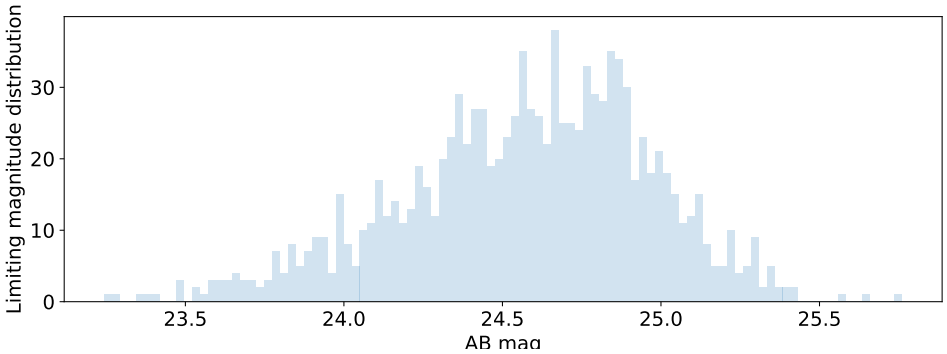

Figure 5.1: A histogram of the limiting magnitudes used for the simulations. A skewed Gaussian distribution was chosen as it better approaches the realistic case.

5.3 Filtering alerts

Currently, the ZTF *avro* packages are being analyzed by different alert brokers, such as Fink, Mars, Fritz, and others, to adjust and prepare for Rubin. For this work, we have focused on generating alert packages that follow the ZTF structure (i.e. the ZTF *avro* schema). Our alerts are packed into a `json` and stored in a MongoDB database [3][4] for public access. There, different pipelines can be tested through `MongoDB Compass`[5] and their results can be exported as `json` files for further analysis.

An alert will pass our filtering strategy if it is > 20 arcsec from a < 15 mag Pan-STARRS star, it does not crossmatch with a known point source from the Pan-STARRS catalog, and it has at least 2 detections separated by 15 minutes. Usually for these searches we additionally require a positive subtraction and a real-bogus score that marks the sources as real, but we do not use these cuts as the sources are simulated.

[3]Main page: `https://www.mongodb.com/`
[4]Cluster: mongodb+srv://alert_digger:WhereIsTheKN@cluster0.s0ada.mongodb.net/test
[5]`https://www.mongodb.com/es/products/compass`

For the sources with more than one detection, $n_{det} > 1$, we calculate the fading rate of each band, by taking the ratio $\alpha = \Delta m/\Delta t$ [mag/day], between the detections. We select as fast fading all the sources that have at least one epoch for which $\alpha > 0.4$ mag/day. The results for our filtering strategy are shown in Table 5.3.

5.4 The detections: results and discussion

Due to the way in which the alerts were generated, each transient has a different light-curve. We quantify in absolute terms how many of the generated sources (1) did not pass the filter, (2) passed the filter, and (3) the fast decline is detectable (see Table 5.3).

The only transients that show a significant fraction of sources that do not pass the filter are GRBs and KNe. The occurs mainly because these transients fade too quickly, beyond the limiting magnitudes of the simulated survey, and do not have more than one alert associated to them (i.e. $n_{det} \leq 1$). In fact, around 20% of each class only has one detection in the database. We show these results for each class in Fig. 5.2, 5.3, 5.4, 5.5, 5.6 , 5.7.

Future filters should consider the magnitude limit during the selection criteria and not solely the number of detections, as fast transients can fade beyond the limits between two survey visits. A transient could then still be interesting if the fading rate between the first detection and the next upper limit implies a significant fading rate. This approach could help treat these sources separately, instead of discarding them from the selection because they did not have a second detection. This should

not dramatically increase the number of contaminants, as only GRBs and KNs were severely affected by this issue.

For both SNe Ia and TDEs, the fast fading criteria (i.e. $\alpha > 0.4$) reduced the number of sources that end up as viable candidates to 0% of the initial number of transients. The filter is effectively leaving out these two classes, as none of the KN candidates were a TDE or a SNe Ia (see Fig. 5.4 and Fig. 5.6). On the other side, close to 20% of the SN IIb SBO (see Fig. 5.7) and the jetted TDEs passed our filtering criteria and contaminate our sample of KN candidates.

In Fig. 5.8 we show the breakdown of the transients that pass our criteria, separated per class. Due to the rapid evolution and the low intrinsic luminosity of the KN, they only make up $\sim$ 5% of the final selection. With over 60% of the candidates being GRB afterglows, this is the class that contaminates our sample the most. From Ahumada et al. 2022, we note that the range of magnitudes that the afterglows span starts around 21 mag, a few magnitudes brighter than the Rubin nominal limit. Our filtering criteria seems to open a window to the detection of more of these afterglows, as they are usually found at magnitudes $>$ 19 mag and their average fading rate $\alpha \sim$1 mag/day made these discoveries particularly hard. Since jetted TDEs show a much faster evolution than regular TDEs, it is not surprising that over 20% of them make it to the final set of candidates, although because of their low rates, they represent $\sim$ 2% of the total number of final candidates. Finally, over 20% of the SNe IIb SBO fade faster than our threshold (i.e. 0.4 mag/day). These sources make up $\sim$30% of the number of KN candidates. Even in this very simplistic simulated universe, more than 4000 sources were considered as candidates.

This translate to ~ 11 candidates per night, each with only 5% chances of being the real KN.

In Fig. 5.9 we show a histogram including all the detected magnitudes of sources that are selected as candidates. We exclude SNe Ia and TDEs as they do not make it to the final set. We note that although the KNe detected are few, the magnitude distribution shows that most of them will be spectroscopically accessible to 8 meter-class ground based telescopes. The histogram shows all the detections in the simulation for each type of transient, and the KN distribution peaks at a brighter magnitude ($m_{KN} \sim 22$ mag) than GRBs ($m_{GRB} \sim 24$ mag). This suggests that the KNe found using the filtering described in Sec. 5.2 will be in the brighter side of the distribution, possibly since the fainter ones will not have enough data points to show a fast decay and make it into the final data set.

Transient class	Rate [$\mathrm{Gpc^{-3}\ yr^{-1}}$]	Generated	$n_{det} > 1$	Passed Filter	Fast Fading detected
KN	900	9982	7748	5864	199
GRB	1	22129	17149	13581	2434
TDE	200	70145	69881	69881	0
jetted TDE	0.02	443	371	370	91
SN Ia	24000	2114358	2106429	2106429	0
SNII BO	5	6981	6954	6928	1474

Table 5.3: The filtering scheme summary showing the rate, the number of generated sources, the number of sources observed at least once by Rubin (i.e. $n_{det} > 1$, based on our cadence and m_{lim}), the number of sources that pass our filter, and the number of sources for which a fast fading ($\Delta m/\Delta t > 0.4$ mag/day) is detected.

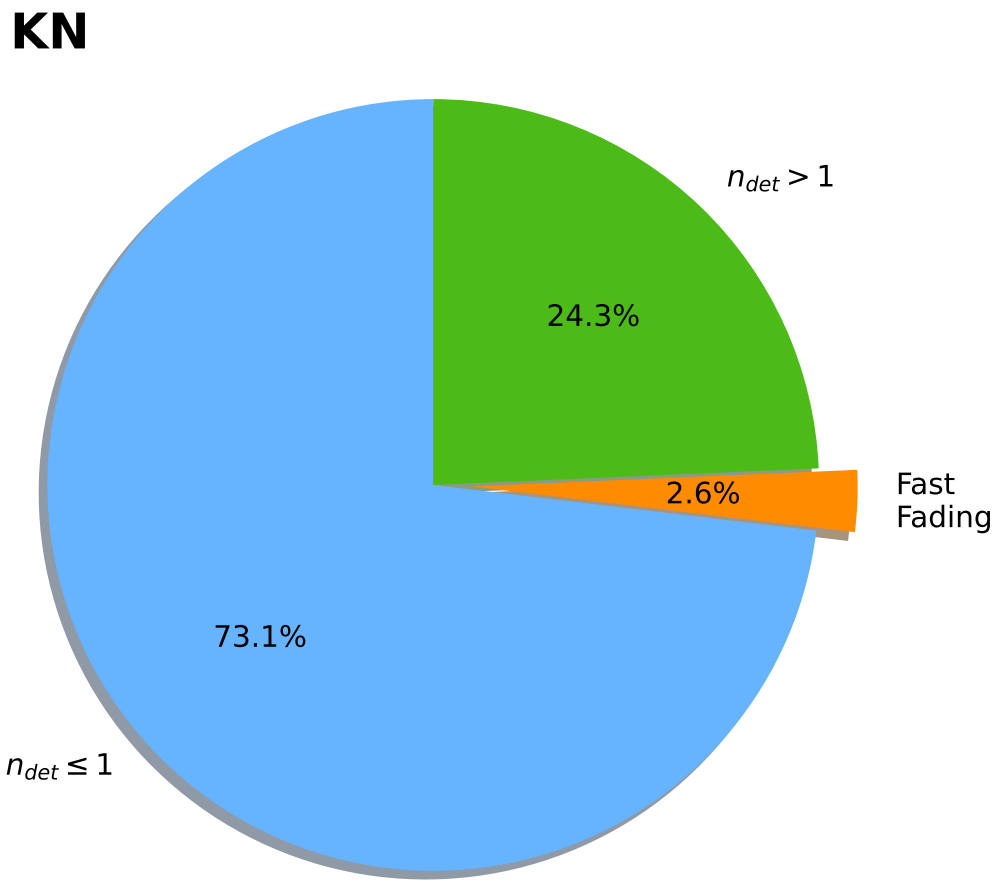

Figure 5.2: The distribution of the KNe found at different stages of the filter described in Sec. 5.3. The blue region represents the percentage of transients that had only one alert in the simulated Rubin archive. The orange region shows the percentage of sources which passed the filter, where the main discriminator was having at least two detections separated by at least 15 min. The green region shows the percentage of sources for which a fast decline ($\delta m/\Delta t > 0.4$ mag/day) can be measured using the alerts in the simulated universe.

5.5 Conclusion and Future work

We have created a database that recreates a year of Rubin observations. We have populated this simulated *sandbox* with alert packages, each containing a light-

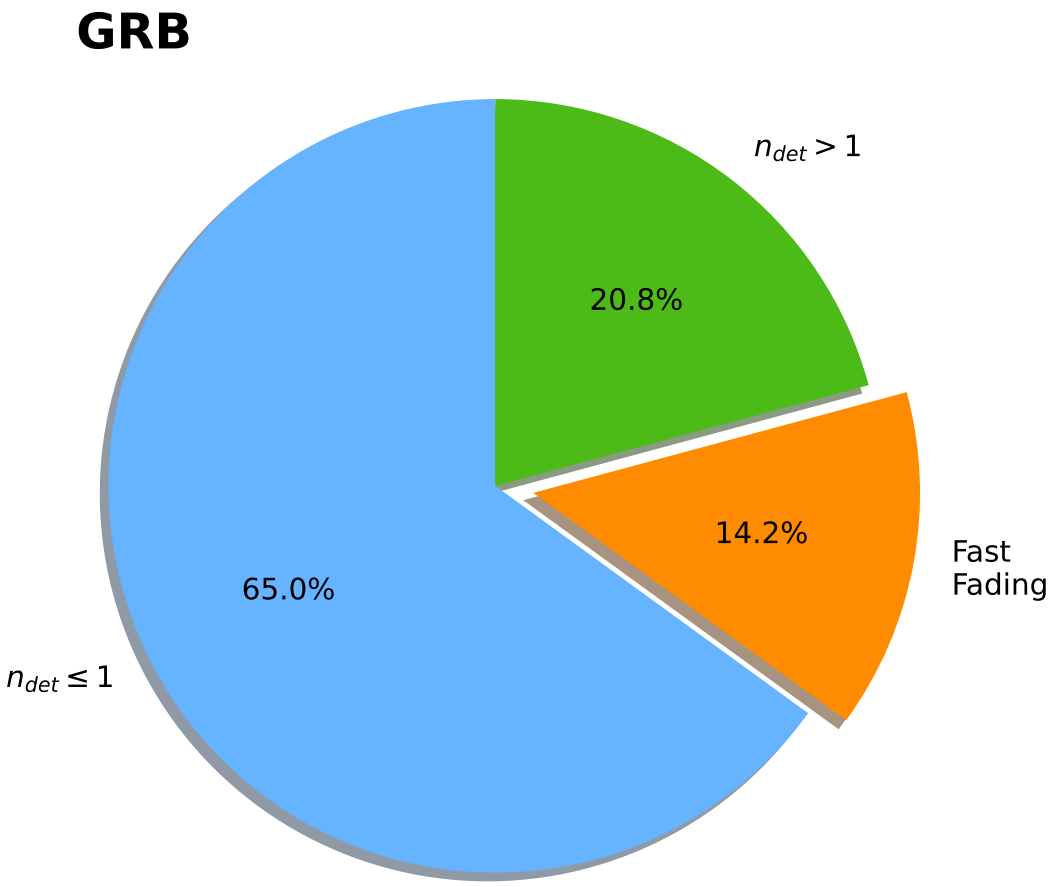

Figure 5.3: The distribution of the GRBs found at different stages of the filter described in Sec. 5.3.

curve of a transient, along with other meaningful parameters. Our database is publicly available, accessible through `MongoDB Compass`, and populated with KNe, GRB afterglows, TDEs (including jetted TDEs), SN Ia, and SN IIb SBO. We query our database in order to quantify the number of contaminants that will appear during routine serendipitous searches for KNe.

Our filtering strategy is able to retrieve only 3% of the KNe generated in

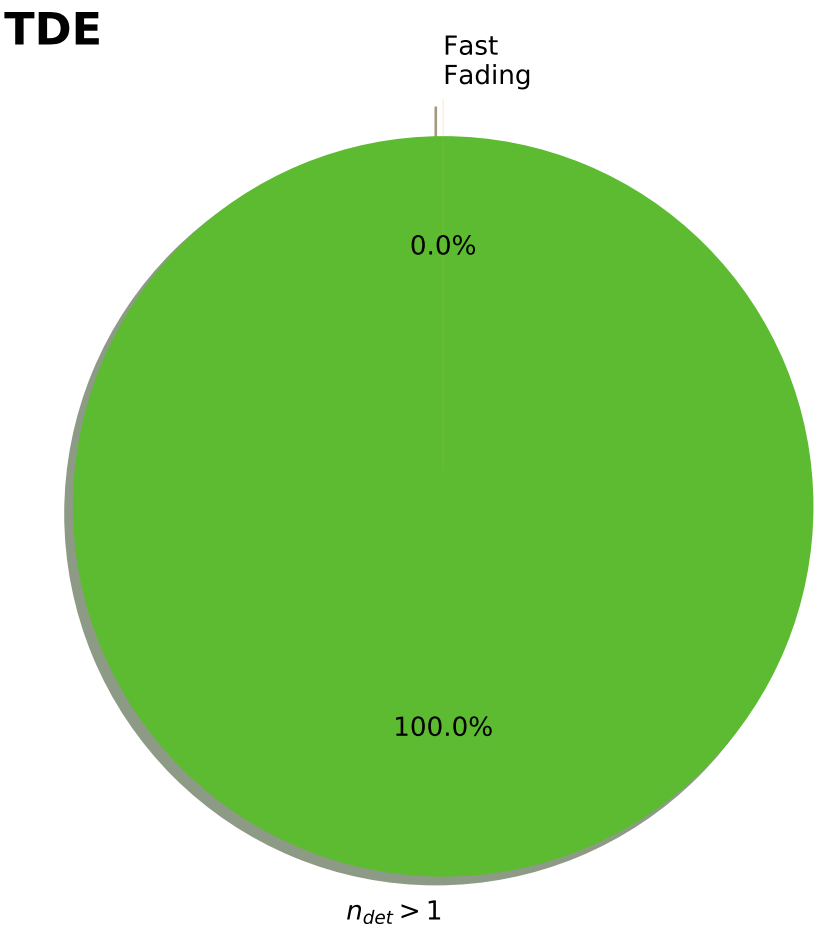

Figure 5.4: The distribution of the TDEs found at different stages of the filter described in Sec. 5.3. The color code description is the same as in Fig. 5.2, no blue area is shown as all sources passed our filter, and there is no orange region since their decay was not fast enough.

the first place, which translate in 5% of the transients that pass all of our filtering scheme. The main contaminants are GRBs afterglows and SN IIb SBO, making up to ∼92% of the transients in the final sample, mainly because of the large volume that Rubin will probe. Out of the ∼4000 sources retrieved, only ∼200 were true KNe. This translates into potentially ∼10 candidates per night that will require

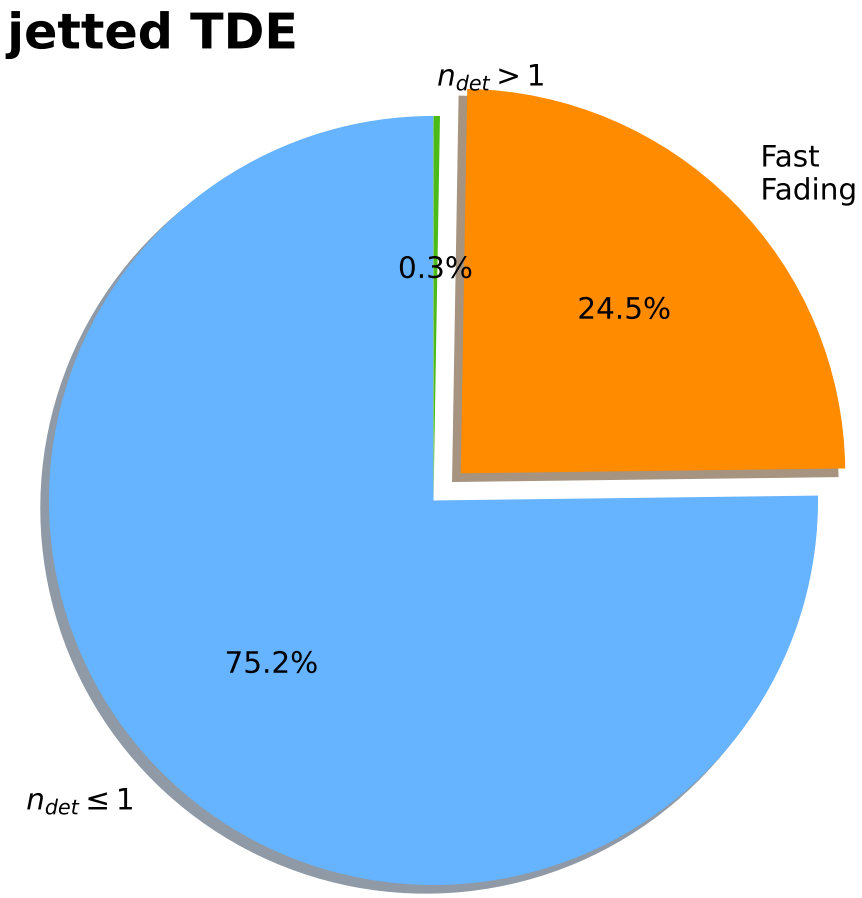

Figure 5.5: The distribution of the jetted TDEs found at different stages of the filter described in Sec. 5.3. The color code description is the same as in Fig. 5.2.

further observations.

Future works should address how to reduce the number of contaminants in the sample, simulating panchromatic light-curves for all the classes of transients. Features like the color evolution, the offset to a host galaxy, or the redshift of the potential host can help separate them from the KNe. Another unexplored side is the effect that multiple near infrared (NIR) wide field surveys will have on the

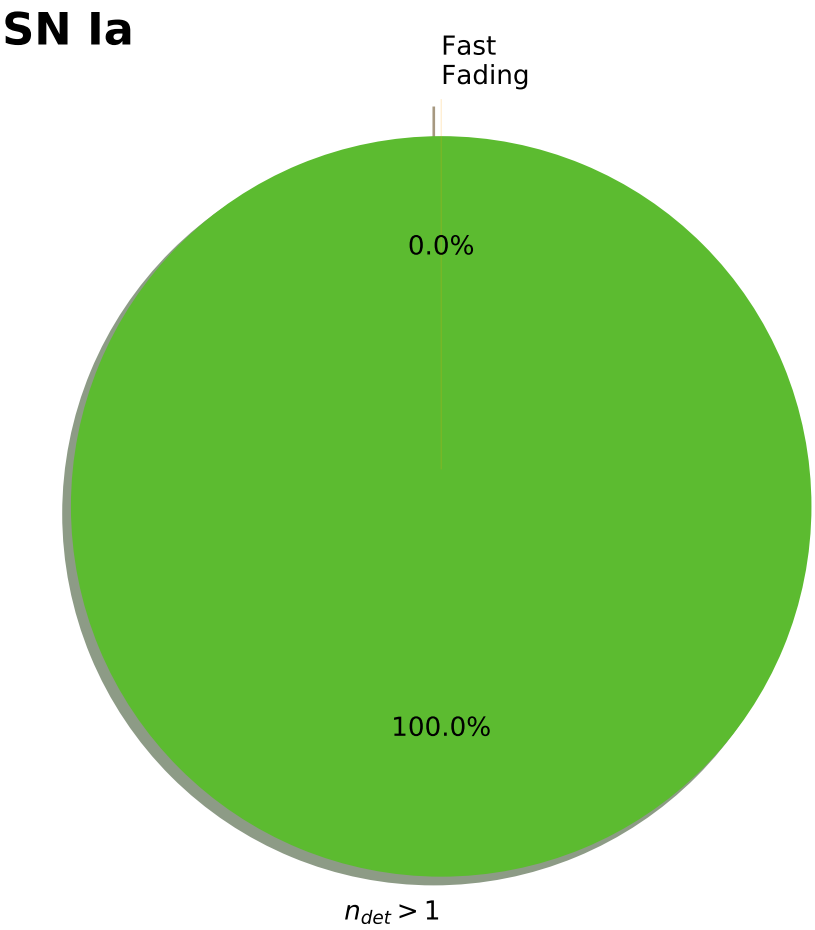

Figure 5.6: The distribution of the SNe Ia found at different stages of the filter described in Sec. 5.3. The color code description is the same as in Fig. 5.2, although no blue area is shown as all sources passed our filter, and there is no orange region since their decay was not fast enough.

filtering strategies. Potential cross-matching with the Wide-Field Infrared Transient Explorer (WINTER) and the Dynamic REd All-sky Monitoring Survey (DREAMS) could help separate KNe from other sources, as the NIR emission of KNe is expected to last longer and be more prominent than of GRB afterglows.

This work targets serendipitous searches based on observations performed

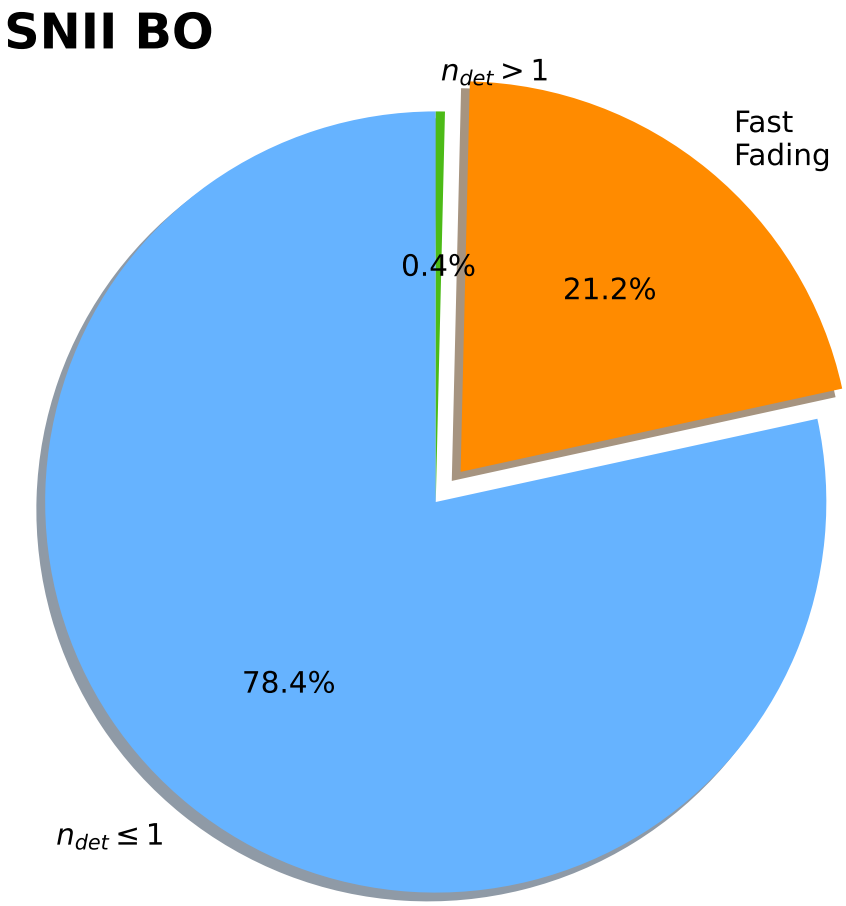

Figure 5.7: The distribution of the jetted SN II SBO found at different stages of the filter described in Sec. 5.3. The color code description is the same as in Fig. 5.2.

within routine survey observations. Future work is planned to address the effects of triggered ToO observation, which use timing and/or localization information from other wavelengths or messengers.

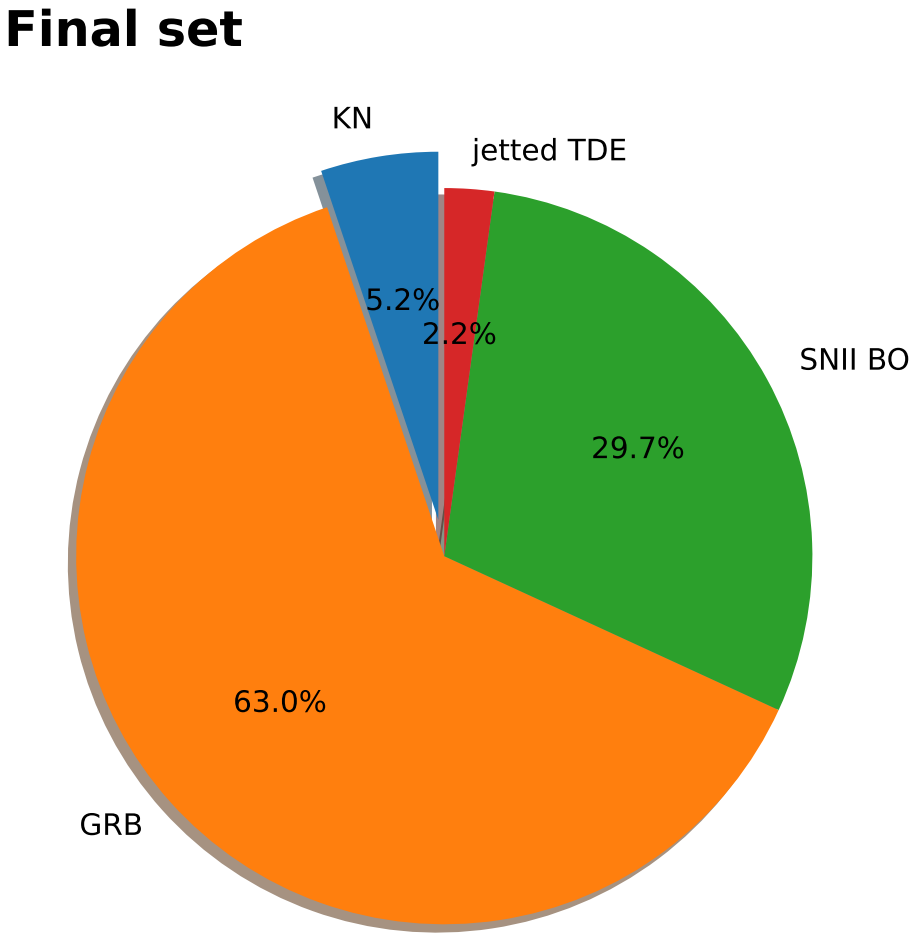

Figure 5.8: The distribution of candidates separated per class. The KN represent only 5% of the sources that passed our criteria, mainly because of the large number of TDEs and SNe generated within the LSST volume.

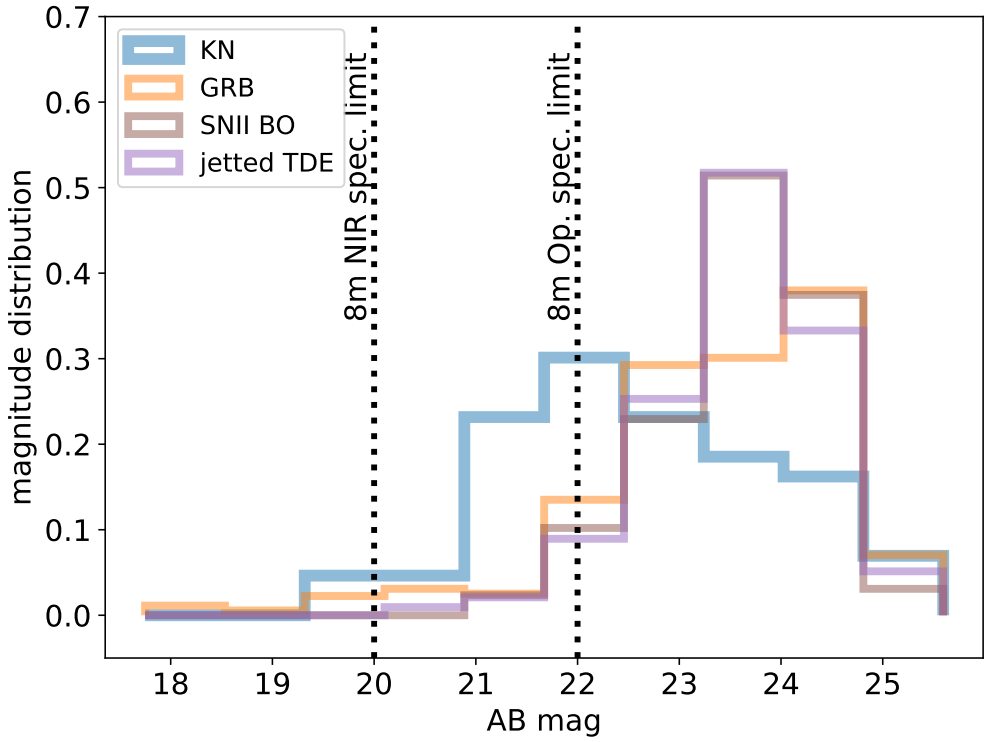

Figure 5.9: The magnitude distribution of the all the detections showed for each class. This histogram contains all the magnitudes, not just the magnitude at first detection.

Chapter 6: Conclusions and future work

6.1 Summary

The main objective of this thesis was to capture the essence of a compact binary merger and showcase it as a detailed portrait. This entailed an exploration over the multiple aspects that are associated to a merger of this class, diving into multi-messenger astronomy waters. To paint this portrait, I have used the colors provided by the Zwicky Transient Facility (mainly the g- and r-band), as well as the rest of the electromagnetic spectra (from gamma-rays to radio) to better understand and explore the nature of these mergers.

In Chapter 2, I show the systematic search for the optical counterpart of short gamma-rays using Zwicky Transient Facility (ZTF). These have been associated to compact binary mergers in the past, however only a few dozens have optical counterparts. Our triggers were based on *Fermi* SGRBs, and after following up 10 of them, we did not find a viable optical counterpart. During this process, we were able to develop a target-of-opportunity (ToO) strategy that considers both the observing plan, as well as the development of a filtering scheme capable of reducing the number of relevant sources to less than 0.03% of the initial number. Due to the fast fading nature of these transients, a rapid photometric and spectroscopic follow-up was shown to be essential. Close to 60 transients were followed-up and

ruled out as potential optical counterparts to these events. This search allowed us to set limits based on the energy associated to the GRBs. For this campaign we probe the close by universe up to a redshift of $z = 0.2$ - 0.4 depending on the energy model assumed.

During the SGRB campaign we found the optical afterglow of GRB 200826A, and I describe it in Chapter 3. This 1.1 sec duration event was found in close proximity to a galaxy, which allowed us to put a redshift to the source. Further analysis of the gamma-ray properties of the burst showed an ambiguity in the classification of the progenitor of the burst. Originally thought to come from a compact binary merger, this GRB lay in the LGRB locus of the GRB parameter space. The transient was 2.09 ± 0.6 kpc from a host galaxy with a stellar mass of $M_{gal} = \sim 10^{9.7}\ M_{\odot}$, and a star formation rate (SFR) of $4.01^{+41.87}_{-3.59}\ M_{\odot}\ \mathrm{yr}^{-1}$. From the afterglow analysis, we derived a kinetic energy of $E_{\mathrm{K,iso}} = 6.0^{+51.3}_{-4.4} \times 10^{52}$ erg and a circumburst density of $n = 5.5^{+187.3}_{-5.4} \times 10^{-2}\ \mathrm{cm}^{-3}$. Neither of these analyses revealed with certainty the true nature of the progenitor of GRB 200826A. For that reason we re-imaged the field, unveiling a rising source in the i-band. We tried fitting this photometric excess using afterglow and kilonova models, but the light-curve bump could not be explained by either of these models, nor a combination of them. However, the SN IcBL models in addition to the afterglow models were consistent with the i-band detection. The discovery of the shortest GRB powered by a collapsar supports the general idea that most collapsars fail to produce ultra-relativistic jets.

In Chapter 4, I return to the compact binary merger portrait, taking a multi-messenger approach. In this chapter I describe the ZTF searches for the optical

counterpart to LVC GW events. The third LIGO observing run started in April 2019, and was prematurely ended due to the COVID-19 pandemic. However, with ZTF we were able to follow up 13 events, which had a median distance of 267 Mpc and a median 90% localization region of 2482 deg^2. ZTF is currently among the few facilities capable of taking over this endeavor, as its 47 deg^2 camera can reach $\sim$ 21 mag in a 300 sec exposure. I use the search of the first BNS merger detected in O3 as well as the first two NSBH mergers to illustrate our observing strategy, and the selection and vetting of candidates. The filtering scheme I built allowed for the reduction of alerts to less than 0.1% of the original number and through a thorough follow-up of all these candidates, we were able to confidently say that none of them was associated to a compact binary merger. The chapter concludes that even though a GW170817-like event could have been detected up to 200 Mpc, most of the events occurred at greater distances and spanned much larger areas compared to GW170817, making the searches extremely challenging.

Finally, Chapter 5 focuses on the future possibility of serendipitously finding the KN optical emission using the Rubin Observatory. Multiple searches for the KN emission have been carried out using ZTF, although all have come empty handed. The Rubin observatory will probe a much larger volume, as it is designed to reach magnitudes of $g \sim 25.0$ and $r \sim 24.7$ on a single exposure. Thus it is expected to detect 10-100 KNe during the 10 year survey. This chapter investigated the efficiency of an alert filter that is based mainly on the decay rate $\alpha = \Delta m/\Delta t$ of the sources. Our simulations show that the main contaminant will be GRB afterglows and SN IIb shock break out, making up to 90% of the transients that passed our filters. In

fact, only 5% of the sources that pass our filter are KNe, as most of them do not pass the initial threshold of having more than one detection in the simulated database. We conclude suggesting new strategies that could improve both the detection of KNe and the reduction of contaminants.

6.2 Future Work

6.2.1 The GRB prospects

Before the discovery of GRB 200826A, a few works (Bromberg et al., 2013; Zhang et al., 2009)) suggested that the GRB classification based solely on the T_{90} distribution was not completely accurate, nor the association with a progenitor (i.e. collapsar or merger) inferred from this classification. It was expected that some short-duration GRBs would have collapsar features and, vice versa, some long-duration GRBs would show compact binary merger characteristics. In fact, a few very puzzling GRBs found in the past (i.e. GRB 060614; Gal-Yam et al. 2006, and GRB 090426; Antonelli et al. 2009) have challenged this classification. Furthermore, GRB 200826A was the first short-duration GRB to unequivocally show collapsar features. Recently, the observations of the GRB 211211A, a burst detected by Swift lasting ~ 43 sec was associated to a binary compact merger (Gompertz et al., 2022; Rastinejad et al., 2022; Yang et al., 2022) due to a lack of SN emission, but more importantly, because its NIR excess was compatible with a KN.

If not the duration of the GRB emission, what other gamma-ray features could isolate the different population of bursts? What percentage of short burst are related to collapsing massive stars? And inversely, how many long GRBs have

compact binaries as progenitors?

Furthermore, new phenomena have been observed to produce GRBs, increasing the diversity of progenitors. However, what other sources are yet to be associated to GRBs? Are these related to other transient events? Have we exhausted the search for other sources that could produce a GRB?

To answer most of this questions, a larger sample of bursts needs to be accurately localized. Future high energy missions, like the Space Variable Objects Monitor (SVOM), will allow for a larger coverage and more precise localization of the events. Although the wide-field optical search of these objects will still be required, more GRB missions will allow for the triangulation of the signal and reduce considerably the error regions associated to the GRB events.

6.2.2 The fourth LIGO/Virgo observing run

The LVC fourth observing run (O4) is expected to start in March 2023. Due to the differences in sensitivity between the LIGO and Virgo interferometers, it is expected that the size of the error regions during O4 will be comparable to the events in O3. Additional improvements in the sensitivity will allow for detections at larger distances as well, thus a revised strategy on the triggering criteria is needed for future wide-field optical follow-up.

To tackle these problems we are planning on using ZTF and the new incoming generation of wide-field NIR instruments. The second phase contemplates a compilation of deeper reference images, allowing for searches up to 2 mag deeper than the current survey. Additionally, new ZTF searches using the i-band will also

be possible. This, in conjunction with new wide-field infrared surveys, such as the Wide-Field Infrared Transient Explorer (WINTER) in California, or the Dynamic REd All-sky Monitoring Survey (DREAMS) in Australia, will open a redder window to the kilonova phase space, probing mergers with higher lanthanide fractions. As explored in Kasliwal et al. 2020b, even future non detections can help constrain even more the luminosity function of the KN, as long as the coverage is over 50% of the error region.

6.2.3 The Rubin observatory

The Rubin observatory will revolutionize time domain astronomy. The plan for the 10-year Legacy Survey of Space and Time (LSST) is to observe the southern night sky systematically in multiple filters at depths of $u \sim 23.9$, $g \sim 25.0$, $r \sim 24.7$, $i \sim 24.0$, $z \sim 23.3$ and $y \sim 22.1$. Comparatively, this means more bands and close to 3 magnitudes deeper than ZTF. The LSST currently faces multiple technical and scientific challenges, one them is the manage of million of variable sources that are predicted to be observed per night.

Similarly to ZTF, LSST will deliver **alert** packages that will be accessible to the community through brokers. Even in the absence of a GW alert or a SGRB trigger it is still possible to retrieve KN candidates by mining the ZTF or Rubin stream of data. Strategies similar to one presented in Chapter 5 could serendipitously discover orphan afterglows or KN.

During the search of fast-fading transients many rare, though unrelated events usually appear in the sample. These sources are *interesting in their own right*, and

it is important to characterize them, as synoptic surveys have done in the past (Cenko et al., 2013; Ho et al., 2020; Perley et al., 2018). More importantly, Rubin will allow to explore the multi-messenger aspect of bright fast-evolving transients. For example, the Swift discovered GRB 190829A showed an unexpected behavior in the TeV energy range that has challenged the common afterglow emission scenarios (H. E. S. S. Collaboration et al., 2021). The rapid detection of bright transients (potentially afterglows) and the coordination with Cherenkov telescopes like Major Atmospheric Gamma Imaging Cherenkov Telescopes (MAGIC), High Energy Stereoscopic System (HESS), and Cherenkov Telescope Array (CTA) can help unveil different mechanisms in the TeV energy range.

Furthermore, the implementation of a ToO strategy for Rubin will likely enhance the detection during O5 as LVC sensitivities will reach much larger distances and the associated kilonovae will be only detectable during a short period of time with 8 m class telescopes.

There is hope in the future to find brighter colors and paint a clearer portrait of multi-messenger events, including compact binary mergers.

Appendix A: Gravitational-waves optical follow-up

This appendix shows a summary of the candidates found during the Zwicky Transient Facility (ZTF) follow-up campaign of gravitational wave (GW) events found in the third LIGO/Virgo observing run (O3). I divide this appendix in Sec. A.1, with the technical details of all the instruments and facilities used during the campaign, and Sec. A.2 with an in-depth description of each of the candidates. This appendix is shown in Kasliwal et al. 2020b, and I contributed with candidate selection and analysis, their photometric monitoring, and the majority of the writing of this section.

A.1 Observing and data reduction details for follow-up observations

A.1.1 Photometric Follow-Up

We used the 1-m and 2-m telescopes available at the LCO global network to follow-up sources discovered with ZTF. The images were taken with the Sinistro and Spectral cameras (Brown et al., 2013) at the 1- and 2-m respectively, and were scheduled through the LCO Observation Portal[1]. The exposure time varied depending on the brightness of the object, yet our requests would normally involve 3 sets of 300s in g- and r- band. After stacking the reduced images, we extract sources using the Source Extractor package (Bertin & Arnouts, 2010) and we cali-

[1] `https://observe.lco.global/`

brated magnitudes against Pan-STARRS1 (Chambers et al., 2016a) objects in the vicinity. For nuclear transients located < 8 arcsec from their potential host, we use the High Order Transform of Psf ANd Template Subtraction code (HOTPANTS; Becker 2015) to subtract a PSF scaled Pan-STARRS1 template previously aligned using SCAMP (Bertin, 2006). The photometry for the nuclear candidates follows the same procedure described before, but in the residual image.

The images obtained with LT were acquired using the IO:O camera with the Sloan griz filterset. They were reduced using the automated pipeline, which performs the bias subtraction, trimming of the overscan regions, and flat fielding. The image subtraction takes place once a PS1 template is aligned, and the final data comes from the analysis of the subtracted image.

We used the Electronic Multiplier CCD camera at KPED to take hour long exposures in the r-band to follow-up candidates. After stacking the images and following standard reduction techniques, we calibrate the extracted sources using PS1 sources in the field. When the candidate has a host galaxy, we perform image subtraction as described for LCO.

We obtained data with the Gemini Multi-Object Spectrograph (GMOS-N; Allington-Smith et al. 2002; Gimeno et al. 2016; Hook et al. 2004) mounted on the Gemini-North 8-meter telescope on Mauna Kea. Data was analyzed after stacking four 200s exposures in the g- and i-bands. The reductions were performed using the python package DRAGONS [2] provided by the Gemini Observatory. We used PS1 sources in the field to calibrate the data.

[2] `https://dragons.readthedocs.io/en/stable/`

We used LOT at the Lulin Observatory in Taiwan to follow up candidates discovered with ZTF. The standard observations involved 240 sec in g'-, r'-, and i'-band. The reduction followed standard methods and the sources were calibrated against the PS1 catalogue. No further image subtraction was applied to the images acquired with LOT.

We used 0.7m robotic GROWTH-India Telescope (GIT) equipped with a 4096×4108 pixel back-illuminated Andor camera for LVC event followup during O3. GIT is situated at the IAO (Hanle, Ladakh). We used both tiled and targeted modes for the followup for different GW triggers. Tiled observations typically comprise a series of a series of 600 sec exposures in the SDSS r′ filter. Targeted observations were conducted with varying exposure times in SDSS u′, g′, r′, i′ filters. All data were downloaded in real time and processed with the automated GIT pipeline. Zero points for photometry were calculated using the PanSTARRS catalogue (Flewelling, 2018), downloaded from Vizier. PSF photometry was performed with PSFEx (Bertin, 2011). For sources with significant host background, we performed image subtraction with `pyzogy` (Guevel & Hosseinzadeh, 2017), based on the ZOGY algorithm (Zackay et al., 2016).

Additionally, we obtained photometric data with the Spectral Energy Distribution Machine (SEDM; Blagorodnova et al. 2018; Rigault et al. 2019) on the Palomar 60-inch telescope. The processing is automated, and can be triggered from the GROWTH Marshal. Standard requests involved g-, r-, and i- band imaging with the Rainbow Camera on SEDM in 300s exposures. The data is later reduced using a python-based pipeline that applies standard reduction techniques and applies a

customized version of `FPipe` (Fremling Automated Pipeline; Fremling et al. 2016) for image subtraction.

We used the imaging capabilities of the Optical System for Imaging and low-Intermediate-Resolution Integrated Spectroscopy (OSIRIS) (Cepa et al., 2005) camera at the GTC to obtain 60 sec exposures in the r-band. Standard reduction techniques were applied to the data and we used PS1 sources to calibrate the flux.

We obtained follow-up imaging of candidates with the Wafer Scale Imager for Prime (WASP) and the Wide-field Infrared Camera (WIRC; Wilson et al. 2003), both on the Palomar 200-inch telescope. For WASP data, a python based pipeline applied standard optical reduction techniques (as described in De et al. 2020b), and the photometric calibration was obtained against PS1 sources in the field. The WIRC data was treated similarly using the same pipeline, but it was additionally stacked using Swarp (Bertin et al., 2002) while the calibration was done using 2MASS point source catalog (Skrutskie et al., 2006).

We obtained imaging of one candidate using the Low Resolution Imaging Spectrometer (LRIS; Oke et al. 1995) mounted at the Keck I telescope. Our data was taken in the g- and i-bands reaching $m_{AB} \approx 24$. The data was reduced following standard methods.

We used the Large Monolithic Imager (LMI; Massey et al. 2013) on the 4.3m LDT at Happy Jack, AZ to follow-up ZTF disoveries. Observations were conducted with SDSS-r filter for 90 seconds each and the data was reduced using the photopipe[3] pipeline. The magnitudes were calibrated against the SDSS catalog or the GAIA

[3] `https://github.com/maxperry/photometrypipeline`

catalog (Ahumada et al., 2020a), using the conversion scheme provided in GAIA documentation[4].

We used the Ultraviolet/Optical Telescope (UVOT; Roming et al. 2005) mounted on the *Neil Gehrels Swift Observatory* (hereafter referred to as *Swift*; Gehrels et al. 2004) to follow-up interesting sources and track down their UV evolution. Target of opportunity observations were scheduled in the v-, b-, u-, w1-, m2- and w2- bands for an average of 320 sec per exposure. We used the products of the *Swift* pipeline to determine the magnitudes [5].

We observed candidate counterparts of S200213t using the Astrophysical Research Consortium Telescope Imaging Camera (ARCTIC; Huehnerhoff et al. 2016) on the Apache Point Observatory 3.5m. We obtained dithered 120-second exposures binned 2x2 in the u-, g-, r-, i- and z- bands. Images were bias-corrected, flat-fielded, and combined using standard IRAF packages (noao, imred, and ccdred). Source Extractor (Bertin & Arnouts, 2010) was used to find and photometer point sources in the images using PSF photometry, and a photometric calibration to PanSTARRS field stars was performed (without filter corrections).

All photometry presented in the light-curves and tables on this paper are corrected for galactic extinction using dust maps from Schlafly & Finkbeiner 2011.

We observed the field of ZTF 19aassfws with the Karl G. Jansky Very Large Array (VLA) in its B configuration on 2019 May 10, starting at 07:19:15 UT, and on 2019 June 4, starting at 08:20:32 UT. Our observations were carried out at a

[4]https://gea.esac.esa.int/archive/documentation/GDR2/Data_processing/chap_cu5pho/sec_cu5pho_calibr/ssec_cu5pho_PhotTransf.html

[5]https://swift.gsfc.nasa.gov/quicklook/

nominal central frequency of 3 GHz. We used 3C286 as our bandpass and absolute flux calibrator and J1927+6117 as our complex gain calibrator. Data were calibrated using the standard VLA automated calibration pipeline available in the Common Astronomy Software Applications (CASA) package. We then inspected the data for further flagging, and imaged interactively using the CLEAN algorithm. The image RMS was $\approx 5.2\,\mu$Jy for the first epoch, and $\approx 4.6\,\mu$Jy for the second epoch. Within a circular region centred on the optical position of ZTF19aassfws and of radius $\approx 2.1''$ (comparable to the nominal half-power beam width of the VLA at 3 GHz and for B configuration) we find no significant radio emission. Thus, we set upper-limits on the corresponding 3 GHz flux density of $\lesssim 16\,\mu$Jy and $\lesssim 14\,\mu$Jy, respectively for the first and second epochs.

A.1.2 Spectroscopic Follow-Up

Using the GROWTH Marshal, we regularly triggered the Liverpool Telescope Spectrograph for the Rapid Acquisition of Transients (SPRAT; Piascik et al. 2014). SPRAT uses a 1.8" slit, which provides a resolution of R=350 at the center of the spectrum. The data were reduced using the automated pipeline which removes low level instrumental signatures and then performs source extraction, sky subtraction, wavelength calibration and flux calibration.

We observed a number of transient candidates during classical observing runs with the Palomar 200in Double Spectrograph during O3. For the setup configuration, we used 1.0 arcsec, 1.5 arcsec, and 2 arcsec slitmasks, a D55 dichroic, a blue grating of 600/4000 and red grating of 316/7500. Using a custom PyRAF DBSP

reduction pipeline (Bellm & Sesar, 2016)[6], we reduced our data.

We obtained several optical spectra with the 10.4-meter GTC telescope (equipped with OSIRIS). We used the R1000B and R500R grisms for our observations, using typically a slit of width 1.2 arcsec. We used standard routines from the Image Reduction and Analysis Facility (IRAF) to perform our data reduction.

ZTF19aarykkb was observed using the DeVeny spectrograph mounted on the 4.3m Lowell Discovery Telescope (formerly, Discovery Channel Telescope). We obtained 22.5 min exposures at an average airmass of 1.5. We used the DV2 grating (300g/mm, 4000 Åblaze) for this observation. Our spectra cover a wavelength range of approximately 3,600–8,000 Å.

In addition we obtained a spectrum of ZTF20aarzaod with SALT (Buckley et al., 2003), using the Robert Stobie Spectrograph (RSS; Burgh et al. 2003), covering a wavelength range of 470-760 nm with a spectral resolution of R = 400. We triggered a special GW follow up program 2018-2-GWE-002 and reduced the data with a custom pipeline based on PyRAF routines and the PySALT package (Crawford et al., 2010).

Low-resolution spectra using the 2m HCT were obtained using the HFOSC instrument. ZTF19aarykkb was observed using grisms Gr7 (3500–7800 Å) and Gr8 (5200-9000 Å), while AT2019wxt was observed using Gr7. The spectra were bias subtracted, cosmic rays removed and the one-dimensional spectra extracted using the optimal extraction method. Wavelength calibration was effected using the arc lamp spectra FeAr (Gr7) and FeNe (Gr8). Instrumental response curves gener-

[6]https://github.com/ebellm/pyraf-dbsp

ated using spectrophotometric standards observed during the same night were used to calibrate the spectra onto a relative flux scale. The flux calibrated spectra of ZTF19aarykkb from the two grisms were combined to a single spectrum covering the wavelength range 4000–9000 Å.

We obtained spectroscopy with the GMOS-N, mounted on the Gemini-North 8-meter telescope on Mauna Kea by combining six 450 second exposures on the R400 and B600 grating respectively. We used the GMOS long-slit capability and reduced the data following standard PyRAF techniques.

We obtained near-infrared spectroscopy of candidates using NIRES on the Keck-II telescope. The data were acquired using standard ABBA dither patterns on the target source, followed by observations of an A0 telluric standard star close to the science target. The spectral traces were extracted using the `spextool` package (Cushing et al., 2004) for both the science target and standard star. The final spectra presented here were stacked from all the individual dithers, followed by flux calibration and telluric correction using the `xtellcor` package (Vacca et al., 2003).

We obtained spectra using the LRIS on the Keck I telescope. The 600/4000 grism was used on the blue side and the 600/7500 grating was used on the red side, providing wavelength coverage between 3139–5642 Å (blue) and 6236–9516 Å (red). The exposure time was 600 s on both sides. The spectrum was reduced using LPipe (Perley, 2019) with BD+28 as a flux calibrator. The red and blue relative flux are scaled by matching synthetic photometry to colors inferred from photometry of the transient.

A.2 Detailed Candidate Descriptions

Here we provide descriptions of each candidate identified within the skymap of each event followed up with ZTF. We discuss each object announced via GCN. For candidates with a redshift, we note whether it is spectroscopic [s] or photometric [p]. Some candidates were classified as a part of coordinated spectroscopic follow-up with the Bright Transient Survey (BTS; Fremling et al. 2019) and the ZTF Census of the Local Universe experiment (De et al., 2020c).

A.2.1 GW190425

For candidates identified within the skymap of GW190425, see Coughlin et al. (2019c). Two candidate counterparts of GW190425z, ZTF19aarykkb and ZTF19aarzoad, were observed with the Arcminute Microkelvin Imager (AMI) Large Array at 15GHz on 2019 April 26 (Rhodes et al., 2019). No radio emission was found to be associated with any of these candidates.

A.2.2 S190426c

We summarize the candidate counterparts to S190426c in Table A.1 and follow-up photometry in Table A.10. Next, we discuss why we conclude that each one is unrelated.

A.2.2.1 Spectroscopically Classified

ZTF19aasmftm/AT2019sne - The rising lightcurve of ZTF19aasmftm suggested it could be a young and faint object, with a galaxy host of $m_{AB} = 21.2$ mag in PS1, so we highlighted it in Perley et al. (2019d). A few days later, GTC spec-

troscopy of this event (Hu et al., 2019b) classified it as a pre-maximum SN Ia in the outskirts of its host galaxy at z[s] = 0.156.

ZTF19aaslzjf/AT2019snh - Another candidate discovered during our second night of observations, ZTF19aaslzjf, was at low galactic latitude and seemed to be located in a nearby host galaxy. A spectrum from GTC (Hu et al., 2019b) both confirmed that this source was nearby (at z[s] = 0.086) and that it was a SN Ia located in the outskirts of the galaxy host.

ZTF19aasmddt/SN2019fht - We highlighted this transient because its photometric redshift was consistent with the LVC distance estimate, and the lightcurve exhibited a rapid rise (Perley et al., 2019d). However the GTC spectrum taken shortly afterwards revealed that this transient was a young SN II pre-peak in the outskirts of its galaxy, at z[s] = 0.028.

ZTF19aaslszp/AT2019anj - Another candidate whose photo-z was consistent with the LVC distance estimate, ZTF19aaslszp, appeared to be relatively bright and red with a color of $g - r = 0.89$ mag. Subsequent ZTF and LT photometry revealed that the source appeared to have flaring behavior in the lightcurve. Our P200+DBSP spectrum classified the source as an AGN at z[s] = 0.084 as it shows broad Hydrogen lines.

A.2.2.2 Slow Photometric Evolution

ZTF19aaslzfk/AT2019snd - We identified this candidate during our initial search of the imaged region within the BAYESTAR localization of S190426c (Coughlin et al., 2019). Though the candidate had WISE detections in all four filters, its

WISE colors did not definitively place this transient into the AGN class. Continued photometric monitoring of this candidate revealed its slow evolution ($\alpha_g = -0.02$) ruling out its association with S190426c.

ZTF19aaslvwn/AT2019snf - We reported ZTF19aaslvwn in Perley et al. (2019d) as a lower priority transient, with initially slow photometric evolution at low galactic latitude (b $<$ 15 deg). After monitoring the transient over a period of $\sim$ 12 days, the photometry had only risen by 0.4 mag, indicating that it could not be a kilonova and was likely a CV.

ZTF19aasmdir/AT2019sng - ZTF19aasmdir, also reported in Perley et al. (2019d) was a nuclear transient at a low galactic latitude, with WISE colors consistent with an AGN within 1 arcsec of the transient. Several days of monitoring yielded a lightcurve that was far more consistent with a flaring AGN than with a KN, with a rate of evolution $\alpha_r < 0.01$.

ZTF19aaslolf/AT2019snn - This nuclear candidate was at a low priority in our follow-up list due to its high photometric redshift (z[p] = 0.42) and that its WISE colors placed it within the AGN locus. Though we could not spectroscopically confirm this, the slowly evolving 'flaring' lightcurve ($\alpha_r < 0.01$) and archival PS1 detections points to the AGN nature of this candidate.

ZTF19aaslphi/AT2019sno - ZTF19aaslphi had a photometric redshift that was also nominally inconsistent with the LVC distance. However, we identified it as a candidate of interest due to its relatively quick rise of $\sim$ 0.75 mag over the course of 4 days in g-band. Its later-time lightcurve exhibited a plateau, and thus we consider its evolution too slow to be associated with a GW event.

ZTF19aaslpds/AT2019snq - This candidate, at low galactic latitudes, had multiple detections in r- and g- filters; but as it only evolved by 0.04 mag over a day of monitoring and subsequently was not detected, we ruled it out as a potential counterpart to S190426c.

ZTF19aaslozu/AT2019snr - We included this candidate initially due to its rapid rise and g-r color of 0.3 mag (Perley et al., 2019d). Though ZTF19aaslozu did not clearly fall into the AGN locus, its detections in all four WISE filters, archival detections with PS1, and slow evolution point to it being a strong AGN candidate.

ZTF19aasshpf/AT2019snt - A lower priority candidate on our list discovered at r = 21.59 mag in the outskirts of a faint red galaxy. ZTF19aasshpf exhibited a flat evolution (0.06 mag) over a period of 27 days, thus ruling out its association to S190426c.

ZTF19aasmzqf - We could likewise rule out the possibility of ZTF19aasmzqf being a kilonova due to its slow evolution of 0.3 mags over 28 days, despite its initial red color g - r = 0.22 mag.

A.2.2.3 Stellar

ZTF19aasmekb/AT2019snl - ZTF19aasmekb, located at low galactic latitude (b = -8.64 deg), appeared to be hostless and exhibited a rapid fade initially; its later time lightcurve is photometrically consistent with a CV and its slow evolution ($\alpha_g = 0.24$) is inconsistent with a kilonova origin.

A.2.2.4 Artifacts

ZTF19aassfws/AT2019fuc - We highlighted ZTF19aassfws as a candidate of potential interest because its photometric redshift fell within the LIGO distance uncertainty (Perley et al., 2019d). We also obtained radio follow-up using the VLA and AMI under the Jansky VLA mapping of Gravitational Waves as Afterglows in Radio (JAGWAR; Mooley et al. 2018) and we did not detect any radio emission. However, upon careful inspection of the reference image, we identified a very subtle gain mismatch across the image. Comparing the initial photometry of the transient with the level of the gain mismatch provided a clear indication that our candidate was not astrophysical, but an artifact. This gain mismatch problem has since been fixed by re-building the references.

A.2.3 GW190814

No candidates were identified in the ZTF follow-up of the small localization of GW190814.

A.2.4 S190901ap

We summarize the candidate counterparts to S190901ap in Table A.2 and follow-up photometry in Table A.11. Next, we discuss why we conclude that each one is unrelated.

A.2.4.1 Spectroscopically Classified

ZTF19abvizsw/AT2019pim - We discovered a red transient ($g-r \approx 0.5$) that appeared to be hostless and fast evolving. We had observed the location of this

transient every night for the month leading up to 2019-09-01, with no previous detections, therefore indicating strongly that this object was a new transient. Grawita spectroscopic observations about 10 hours later seemed to suggest that the object was a galactic K- or M-dwarf (Salsamo et al., 2019), but our subsequent LRIS spectroscopic followup yielded a featureless continuum with Mg II, Mg I, and Fe II lines at z[s] = 1.26 (Burdge et al., 2019). Thus, we posited that the object could be a flaring AGN or a GRB afterglow. Observations with SVOM-GWAC-F60A (Wei et al., 2019) and LT (Perley et al., 2019c) indicated that the lightcurve was rapidly decaying, suggesting that the transient was likely an orphan GRB afterglow. More than 10 other GCNs contained reported followups of this transient; the collated evidence posed the coherent picture that we had, remarkably, detected an untriggered long GRB afterglow in temporal and spatial coincidence with the skymap of S190901ap. This candidate will be discussed in more detail in Perley et al. in prep.

ZTF19abvixoy/AT2019pin - We detected this transient with an upper limit from the day before the merger, though it appeared to have a faint counterpart in PS1. GRAWITA spectroscopic observations classified this transient as a CV, due to its blue continuum, and weak Hα emission surrounded by broad absorption troughs (Salmaso et al., 2019).

ZTF19abvionh/AT2019pip - The photometric redshift of the putative host of this transient initially made it an interesting candidate for association with S190901ap, even though its first two detections were separated by a short baseline of 7 minutes. About 15 hours later, spectroscopic observations with the Hobby-Eberly observatory suggested that the host galaxy GALEXASC J165500.03+140301.3 was

located at a distance of ∼450 Mpc (Rosell et al., 2019); our LRIS spectrum, showing a hot blue continuum and host galaxy lines at z[s] = 0.0985 confirmed this conclusion, placing the transient outside of the GW distance errorbar by 2.5σ. Upon close inspection of spectra, we find Hα and He II at zero redshift, suggesting that the transient is a foreground CV and the background host galaxy is unrelated.

ZTF19abwvals/AT2019pni - Another transient detected via the `AMPEL` alert archive, ZTF19abwvals, appeared to be red (g-r ∼0.5) and had a photometric redshift of 0.13, slightly higher than the GW distance, also with upper limits in the g-band the previous day (Stein et al., 2019). SNID template matching to the spectra taken with the ALFOSC spectrograph on the Nordic Optical Telescope revealed that ZTF19abwvals was a normal SN Ia, about 4-6 days post-peak (Izzo et al., 2019a).

A.2.4.2 Slow Photometric Evolution

ZTF19abwsmmd/AT2019pnc - Further searches of the data with the `AMPEL` pipeline yielded two additional candidates, including ZTF19abwsmmd (Stein et al., 2019). This candidate exhibited a blue color (g-r∼0.25) and had non-detections in the g-band to 20.64 mag a day before the merger. ZTF survey operations monitored it over a period of about 35 days; the lightcurve exhibited a change of only 0.2 mags decline over that baseline, therefore we deemed it too slow to be associated with the GW event.

ZTF19abvislp/AT2019pnx - We performed a second search of the `AMPEL` alert archive in which we identified this transient, detected on the first night of observations. ZTF19abvislp was interesting due to its rising lightcurve and host SDSS

galaxy being at a redshift of 0.1, on the upper end of the LIGO distance range. Instead of using our spectroscopic resources, we chose to monitor the transient photometrically, and its evolution over nearly 30 days proved to be too slow ($\alpha_r = 0.05$) to be a KN.

ZTF19abxdvcs/AT2019qev - We also discovered ZTF19abxdvcs during a second `AMPEL` archive search, and highlighted it due to its photometric redshift (z $\sim$0.118) and the fact that it had risen by more than 0.65 mags over the course of three days, with its first detection on the first night. Though we did not report this candidate via GCN, our continued photometric monitoring with ZTF demonstrated that the transient was evolving with $\alpha_g = 0.03$, and its lightcurve resembled that of a supernova, so we could confidently reject it.

A.2.5 S190910d

We summarize the candidate counterparts to S190910d in Table A.3 and follow-up photometry in Table A.12. Next, we discuss why we conclude that each one is unrelated.

A.2.5.1 Spectroscopically Classified

ZTF19abyfhov/AT2019pvu - We identified this candidate during our follow-up campaign for S190910d with no available photometric redshifts due to cross-matches at its sky position (Anand et al., 2019a). Castro-Tirado et al. 2019 observed it with the 10.4m GTC telescope equipped with OSIRIS in La Palma, Spain, about 16 hours after initial detection, and derived an r-band magnitude of 20.33 mag for the transient. The best match to their spectrum indicated that the candidate was a SN

Ia at z[s] = 0.133 ± 0.001. Another spectrum taken with the ACAM instrument on the William Herschel Telesope in Roque de los Muchachos Observatory in La Palma confirmed the classification (Cannizzaro et al., 2019).

ZTF19abyfhaq/AT2019pvv - Similarly, we detected ZTF19abyfhaq with little other information than the r-band magnitude of its initial detection at 20.3 mag (Anand et al., 2019a). The GTC spectrum taken (Castro-Tirado et al., 2019) about 18 hours after the initial detection was too low signal-to-noise ratio to merit a classification, but an H-α emission line at z[s] = 0 revealed that the transient was galactic, and therefore unrelated.

ZTF19abyfazm/AT2019pvz - Amongst the other candidates identified in Anand et al. 2019a, we highlighted this one as being blue (g-r$\sim$0.4), with its last non-detection one day before the merger, and a faint source in PS1 about 2.5 arcsec from the transient position. Our imaging and spectroscopy with LT showed that the transient remained bright and blue, with no obvious emission or absorption lines in the spectrum, suggesting that this was likely a cataclysmic variable (Perley & Copperwheat, 2019); this conclusion was further supported by a GTC spectrum (Castro-Tirado et al., 2019).

ZTF19abyfbii/AT2019pwa - During the same initial search we identified ZTF19abyfbii, whose proximity to an SDSS galaxy with photometric redshift of z[p] = 0.124 placed it within the distance uncertainty for S190910d (Anand et al., 2019a). Our candidate was classified as a SN Ia at z[s] = 0.1286 ± 0.0005 less than 20 hours later by GTC using the Hα, Hβ and O II lines in its spectrum (Castro-Tirado et al., 2019). Further spectroscopy with the William Hershel Telescope provided a detailed clas-

sification that this transient was a SN Ia 91T-like, five days before the peak, at z[s]=0.118 (Cannizzaro et al., 2019).

A.2.6 S190910h

We summarize the candidate counterparts to S190910h in Table A.4 and follow-up photometry in Table A.13. Next, we discuss why we conclude that each one is unrelated.

A.2.6.1 Spectroscopically Classified

ZTF19abyheza/AT2019pxi - We initially detected ZTF19abyheza at g = 19.14 ± 0.13 with ZTF with heavy galactic extinction of ∼0.8 in the direction of the transient. One day later, Valeev et al. (2019) imaged the transient, reporting that it had brightened to r = 18.74 ± 0.05. GTC spectroscopy revealed Hα in emission and Hβ in absorption at z[s] = 0. Synthesizing this information along with the lightcurve shape suggesting that this was likely a CV.

ZTF19abyhhml/AT2019pxj - According to our machine-learning algorithms derived from the PS1 DR2 catalog, we could not clearly determine whether this source was of stellar origin. Similar to the previous transient, GTC imaging demonstrated that the lightcurve had risen to r = 19.26 ± 0.04, and spectra exhibited the He II and He I lines, and a double-peaked Hα line, confirming that it was also a galactic CV.

ZTF19abyirjl/AT2019pxe - We highlighted ZTF19abyirjl as being of interest due to its photometric redshift, 0.1 ± 0.017. Having no other information about the transient, we monitored the lightcurve for several days and determined

it was too slow to be associated with the GW event, with an average flat evolution. One month later, we obtained a spectrum using P200+DBSP which clearly demonstrated, through Si II lines that it was a SN Ia.

ZTF19abygvmp/AT2019pzg - This candidate was amongst those candidates reported in our second set of transients (Stein et al., 2019b). We highlighted ZTF19abygvmp, a transient detected one hour after the merger time, in a slightly offset position from the galaxy, as it had appeared to have risen by 0.5 mag since the last non-detection. Cannizzaro et al. acquired a WHT spectrum of the source about two days later, but the spectrum, dominated by host galaxy light, yielded only a redshift of z[s] = 0.049, exactly consistent with the LVC distance estimate. Two weeks later, we obtained an LRIS spectrum of the source, classifying it as a SN II (also consistent with its slow photometric evolution).

A.2.6.2 Slow Photometric Evolution

ZTF19abylleu/AT2019pyu - 23 hours after the merger we detected this bright (r = 19.25 mag) transient with an upper limit of r = 20.4 mag from the day before. Though we could not obtain any spectra, we continued tracking the evolution of the transient over a period of $\sim$ 25 days; the r-band lightcurve remained relatively flat, while the g-band lightcurve exhibited a gradual decline. We concluded that the evolution was too slow ($\alpha_g = 0.03$) to be associated with the GW event.

ZTF19abyjfiw - (Valeev et al., 2019) obtained a spectrum with GTC about two days later which appeared to be a featureless blue continuum, from which they could not derive a conclusive classification. However, the transient presents a flat

evolution, with a coefficient $\alpha < 0.1$. Another detection by ZTF (four months after merger) suggests that it could be a CV.

ZTF19abyiwiw/AT2019pzi - We identified this transient in spatial and temporal coincidence with both S190910d and S190910h, at 3.1 degrees galactic latitude and 2.3 mags of extinction in the direction of the transient. It was first discovered at r = 20.16 mag, but photometric follow-up determined that its evolution was too slow to be relevant, with $\alpha_g = 0.20$.

ZTF19abymhyi/AT2019pzh - ZTF19abymhyi was faint and hostless, with detections in the g-band two hours after the merger (Stein et al., 2019b) and upper limits of g = 20.65 mag from the day before. The transient rose by ∼0.3 mags one day later. However, it was ruled out as its photometric evolution does not pass our threshold, as it faded slower than expected with an $\alpha_g = 0.03$.

ZTF19abyjcoo/AT2019pxm This orphan transient was discovered at r = 20.28 mag and we rule it out due to its slow evolution ($\alpha_r = 0.06$).

A.2.6.3 Artifacts

ZTF19abyjcom/AT2019pxk, ZTF19abyjcon/AT2019pxl - On the first night of observations following this GW event we detected two hostless transients within the same exposure, detected within the same sky region. Imaging with the Liverpool telescope about one day later resulted in non-detections of both transients, despite the fact that other transients of a similar magnitude, discovered within the same exposure, were detected. Furthermore, despite clear detections initially in the r- and g- bands, we could not detect these transients in future serendipitous observations

of the sky region with ZTF. We posit that these three transients are likely cross-talk artifacts that occurred within the same exposure, and therefore are unrelated.

A.2.7 S190923y

We summarize one candidate counterpart to S190923y in Table A.5. Despite the small sky localization, the position of S190923y on the sky made it particularly challenging to access. For that reason we chose to conduct a fully serendipitous search in ZTF data.

ZTF19acbmopl/AT2019rob - We found this transient with a photometric redshift of $\lesssim$0.03, consistent with the LVC distance reported, slightly off the nucleus of its host galaxy. ZTF19acbmopl showed a slow evolution in both the r- and g-bands: $\alpha_r = 0.03$ and $\alpha_g = 0.03$.

A.2.8 S190930t

We summarize the candidate counterparts to S190930t in Table A.6 and follow-up photometry in Table A.14. Next, we discuss why we conclude that each one is unrelated.

A.2.8.1 Spectroscopically Classified

ZTF19acbpqlh/AT2019rpn - We first detected this candidate 13.4 hours after the merger using our `AMPEL` pipeline, with a magnitude of g = 20.36 mag and upper limits of g = 20.77 mag from three days before the merger. The transient was at a galactic latitude of b = -8.49 degrees. Using its spectroscopic host galaxy redshift, z[s] = 0.026, we derived an absolute magnitude of -14.91 mag (Stein et al.,

2019c). The same night we obtained a spectrum with P200+DBSP revealing a mostly featureless blue continuum with a weak broad feature around Hα suggesting that the transient could be a young core-collapse SN. Using the ZTSh 2.6m telescope in CrAO observatory, Mazaeva et al. 2019 imaged the supernova, and found that its B-R color of 0.5 mag was unlike expected of any optical transient associated with a GW event. We followed up by taking a second spectrum with DBSP on October 5, 2019, and confirmed that the candidate was indeed a SN II.

ZTF19acbwaah/AT2019rpp - 22 hours after the merger we detected this transient, whose slight offset from a potential galaxy host at z[s] = 0.032 would lend it an absolute magnitude of -18.069 (Stein et al., 2019c). The next night, we conducted observations of this candidate with DBSP; the spectrum was consistent with a SN Ia a few weeks post-peak SN light located at z[s] = 0.03 (Karambelkar et al., 2019).

ATLAS19wyn/AT2019rpj - With ZTF we independently detected a candidate first reported by ATLAS (Smartt et al., 2019) (ZTF19acbpsuf) 13.8 hours after the merger; ATLAS detected it four hours later. The transient had a deep upper limit of 20.92 from about 6 days before the merger, and its association with a host at z[s] = 0.0297 translated to an absolute magnitude of -15.987. The strong Balmer P-Cygni features in our DBSP spectrum, taken the same night as the initial detection clearly indicated that the transient was a supernova (Karambelkar et al., 2019).

A.2.9 S191205ah

We summarize the candidate counterparts to S191205ah in Table A.7 and follow-up photometry in Table A.15. Next, we discuss why we conclude that each

one is unrelated.

A.2.9.1 Spectroscopically Classified

ZTF19acyiflj/AT2019wmy - This transient was discovered at $r = 20.09$ mag and observed by GTC at a magnitude of $r = 19.79$ mag hours after the trigger. A faint host is visible in the PS1 images of the field. However, the GTC spectrum showed a SN Ia at redshift of z[s] = 0.081 (Hu et al., 2019a).

ZTF19acxowrr/AT2019wib - The first detection of this transient was ~ 4 days after the GW event at $r = 19.054 \pm 0.13$ mag. It rose over the first ~ 15 days, during which several spectra were taken. The first classification came from GTC (Hu et al., 2019b): a SN II at redshift of z[s] = 0.05.

ZTF19acyitga/AT2019wmn - This transient was located in a galaxy at a redshift z[s] = 0.071 and was first detected at $r = 19.26$ mag. We obtained an LT spectrum of ZTF19acyitga a 14 days after the discovery and which showed it was a SN Ia.

A.2.9.2 Slow Photometric Evolution

ZTF19acxpnvd/AT2019wkv - This transient was reported in Andreoni et al. (2019b) after its discovery at r = 19.4 mag. The transient was located in the outskirts of a galaxy located at a photometric SDSS redshift of z[p] $\lesssim 0.03$ and it was ruled out due to the slow evolution showed after peaking, with $\alpha_g = 0.06$.

ZTF19acxoywk/AT2019wix - Similarly, this transient was reported in Andreoni et al. (2019b) with a discovery magnitude of r = 19.75 mag. It was located in the outer regions of a galaxy with spectroscopic redshift of z[s] = 0.05, however,

the evolution of this transient was only of $\alpha_g = -0.15$.

ZTF19acxoyra/AT2019wid - This slow evolving transient was highlighted in Andreoni et al. (2019b), after being discovered at r = 19.20 mag in the nucleus of a galaxy at z[s] = 0.09. However it had an almost flat evolution after reaching its peak ($\alpha_g = 0.05$).

ZTF19acxpwlh/AT2019wiy - This transient was located in a galaxy at a SDSS photometric redshift of z[p] = 0.12. Discovered at g = 19.84, it showed an almost flat evolution over the days after reaching its peak ($\alpha_r = 0.07$).

A.2.10 S191213g

We summarize the candidate counterparts to S191213g in Table A.8 and follow-up photometry in Table A.16. Next, we discuss why we conclude that each one is unrelated.

A.2.10.1 Spectroscopically Classified

ZTF19acykzsk/SN2019wqj - This transient was discovered at g = 19.25 mag in a galaxy at z[s] = 0.021. It was not detected in the ultra-violet by the Swift telescope (Oates et al., 2019). The spectrum taken with the Spectrograph for the Rapid Acquisition of Transients (SPRAT) on the LT (Perley & Copperwheat, 2019a) and with the Gemini Multi-Object Spectrograph (GMOS-N) mounted on the Gemini-North 8-meter telescope (Fremling et al., 2019) showed prominent Hydrogen lines and was classified as a SN II. This was later confirmed by a GTC spectrum that showed similar features (Elias-Rosa et al., 2019). Furthermore, this transient had PS1 detections $\sim$ 1 day after the event (Smith et al., 2019). Part of the evolution of

this transient was followed-up by the Lulin One-meter Telescope (LOT; Tan et al. 2019).

ZTF19acymaru/AT2019wnh - This transient was discovered at r = 20.03 mag and highlighted in Andreoni et al. (2019c). The ZTF reference image did not show a visible host. Finally, the GTC spectrum revelaed a SN Ia at redshift z[s] = 0.167 (Castro-Tirado et al., 2019).

ZTF19acykzsp/AT2019wne - This candidate was first highlighted in Andreoni et al. (2019c), as it was discovered at r = 20.18 mag. The LT/SPRAT spectrum showed a SN Ia at maximum light at z[s] = 0.16 (Perley & Copperwheat, 2019a).

ZTF19acyfoha/AT2019wkl - Similarly, ZTF19acyfoha was reported in Andreoni et al. (2019c) at a g = 17.49 mag. It was located in one of the arms of an spiral galaxy, with a CLU redshift of z[p] = 0.04. The candidate was observed with the SEDM at the P60, and its spectra showed clear features of a SN Ia at z[s] = 0.044.

ZTF19acymcwv/AT2019wni - This transient was discovered at r = 20.24 mag and reported in Andreoni et al. (2019c). The candidates is in the outskirts of an elliptical galaxy and spectrum taken with WHT revealed a SN Ia at z[s] = 0.09 (Brennan et al., 2019).

ZTF19acymixu/AT2019wrr - This candidate was first reported in Stein et al. (2019a), as it was discovered at r = 19.87 mag on top of a faint diffuse source. After $\sim$ 1.6 days observations with the Neil Gehrels Swift Observatory showed a source at b = 20.1 mag. However, it was later classified as a SN Ia at z[s] = 0.14 with a spectrum taken with DBSP at the P200.

ZTF19acylvus/AT2019wnk - This transient was discovered at r = 19.60 mag, sitting on top of a faint galaxy without known redshift. It was classified by the GTC as a SN Ia at z[s] = 0.1 (Castro-Tirado et al., 2019).

ZTF19acymcna/AT2019wnn - This transient was detected at r = 20.74 mag in the nucleus of an elliptical galaxy. The GTC spectrum showed broad Hydrogen features at z= 0.2, consistent with an AGN.

ZTF19acyldun/AT2019wrt - This candidate was reported with an initial magnitude of g = 19.8. The follow-up with the Swift telescope shown an active source in the ultraviolet (Oates et al., 2019). The observations performed by GTC discovered a source at z[s] = 0.057 with narrow Balmer lines consistent with a Luminous Blue Variable (LBV) (Castro-Tirado et al., 2019), as it was also detected in 2012 by PS1. However, the source brightened to a peak absolute magnitude of ≈ -18 mag and we revise its classification to be a SN IIn. It additionally faded at a rate much slower than our $\alpha = 0.3$ magnitude evolution threshold, with a coefficient of $\alpha_r = 0.09$.

A.2.10.2 Slow Photometric Evolution

ZTF19acykyzj/AT2019wrg - This candidate was discovered at g = 20.55 and was reported in Stein et al. (2019a). ZTF19acykyzj was located in the outskirts of a spiral galaxy at unknown redshift, however, its slow magnitude evolution ($\alpha_r = -0.03$) make this transient not relevant.

ZTF19acymapa/AT2019wro - This source was detected at g = 20.31 and reported in Stein et al. (2019a). To calculate the evolution of this object we have only used the first 2 nights of data, as there are no more data on this transient. Using

this Δt, we obtain a slow evolving transient with an $\alpha_r = -0.06$. Additionally, we note that the first two data points make a color consistent with g-r = 0.

ZTF19acymaxu/AT2019wrp - This candidate was highlighted in Stein et al. (2019a) at r = 18.70 mag. It is on top of a faint PS1 source and its slow magnitude evolution of $\alpha_r = 0.03$ allows us to rule it out.

ZTF19acymlhi/AT2019wrs - The first detection of this candidate was of r = 19.54 mag and its initial color was consistent with g-r = 0 mag. Similar to ZTF19acymapa, the baseline used in this case was of $\Delta t = 2$ days and the evolution showed a slow rise of $\alpha_r = -0.17$.

A.2.10.3 Artifacts

ZTF19acykwsd/AT2019wnl - This transient was highlighted as an orphan source with two detections in different bands: r = 19.42 mag and g = 19.39 mag. We proceed to obtain an LT/SPRAT spectrum, however the source was not present in the acquisition image. Further investigation showed more sources around ZTF19acykwsd consistent with cross-talk.

A.2.10.4 Stellar sources

ZTF19acykyqu/AT2019wre - This transient was detected at g = 21.13 mag and it has a second detection 3.5 hours later at r = 20.86 mag. There are no more ZTF data on this object, however there is a faint point source underneath the transient and a PS1-DR2 detection $\sim$ a month before the GW event. We then consider ZTF19acykyqu to be related to a stellar background source.

ZTF19acykyrz/AT2019wrf - Similar to ZTF19acykyqu, this source sits on a

PS1 source, that has previous variability history. The first PS1 reported detection was in 2010, while the last PS1 reported detection was in 2014. As ZTF only detected this source twice, at g = 20.97 mag and r = 20.16 mag, we posit that this candidate is related to the PS1 source underneath.

ZTF19acykzfy/AT2019wrh - This orphan transient was first discovered at g = 20.56, and was detected $\sim$ 3.5 hours later at r = 20.96 mag. The galactic latitude of ZTF19acykzfy (b = -15.73 deg) and a nearby (<3 arcsec) detection in the PS1-DR2 catalog back the stellar origin of this transient.

ZTF19acyldum/AT2019wrn - The candidate was first reported by Stein et al. (2019a) with a magnitude of g = 19.78 mag. It was later detected twice: 3 hours later at r = 19.82 mag and 5 hours later at g = 19.84 mag. However, there is a PS1-DR2 detection within 1 arcsec in 2010 and a faint source in the ZTF reference images. Therefore, we posit this candidate as a stellar variable and thus, unrelated.

A.2.11 S200105ae and S200115j

For candidates identified within the skymap of S200105ae and S200115j, see Anand, Coughlin et al. 2020.

A.2.12 S200213t

We summarize the candidate counterparts to S200213t in Table A.9 and follow-up photometry in Table A.17. Next, we discuss why we conclude that each one is unrelated. All the transients described for this event (S200213t) were reported in Kasliwal et al. (2020a).

A.2.12.1 Spectroscopically Classified

ZTF20aamvqxl/AT2020ciy - This transient was first reported in Kasliwal et al. (2020a) as it was discovered at g = 20.45 mag, in the outskirts of a potential host. With the spectra taken with GTC Valeev et al. (2020), the candidate was classified as a SN Ia at z[s] = 0.1.

ZTF20aamvnth/AT2020cjb - Similarly, this candidate was first reported in Kasliwal et al. (2020a), however it potential host was a faint and diffuse galaxy visible in the PS1 image of the field. A spectrum from GTC classified this candidate as a SN II at z[s] = 0.061 (Castro-Tirado et al., 2020).

ZTF20aamvoxx/AT2020cjg - This transient was first observed at g = 19.99 mag, close to the nucleus of an elliptical galaxy. Data taken with GTC classified this candidate as a SN Ia at z[s] = 0.097 (Valeev et al., 2020).

ZTF20aamvtip/AT2020cje - The first detection of ZTF20aamvtip was at g = 20.7 mag, and faded 0.2 mag in the r-band after a day. The SDSS photometric redshift of the faint host was of z[p] = 0.225. The GTC spectra classified it as a SN Ia at z[s] = 0.15 (Valeev et al., 2020).

ZTF20aamvnat/AT2020ciz - This transient was discovered at a g = 18.93 mag and while originally thought orphan, a faint red counterpart in the PS1 and ZTF reference image suggested an stellar origin. Additionally, it is located at b = -5.62 deg, backing up the stellar hypothesis. Finally, GTC spectra showed strong Hydrogen lines at z[s] = 0, thus consistent with a galactic cataclysmic variable (Castro-Tirado et al., 2020).

ZTF20aamvodd/AT2020cjf - Similarly, this transient sits at b = -9.53 deg and has a faint red PS1 counterpart. ZTF20aamvodd was later classified as a stellar flare at z[s] = 0.0 (Castro-Tirado et al., 2020), due to its H-alpha features.

ZTF20aamvoeh/AT2020cjc - This transient was discovered at g = 20.56 mag on top of an elliptical galaxy. We classified the candidate as a SN Ia at z[s] = 0.14 using the spectrum taken with the DBSP at the P200 telescope.

ZTF20aanaltd/AT2020clt - This transient was first reported on Andreoni et al. (2020a), as it was discovered at g = 20.81 mag in the outskirts of a faint red galaxy. Spectrum from LRIS at the Keck observatory revealed a SN Ia at z[s] = 0.2 (De, 2020).

ZTF20aanaoyz/AT2020clw - This transient was discovered at g = 21.50 mag on top of a faint PS1 elongated source. It was classified by GTC as a SN Ia at redshift z[s] = 0.276 (Hu et al., 2020).

ZTF20aamvpvx/AT2020clx - The first observation of this transient was at g = 20.30 mag in the nucleus of an elliptical galaxy. The GTC spectrum showed a SN II at redshift z[s] = 0.074 with prominent Hydrogen features (De, 2020).

ZTF20aanakcd/AT2020cmr - This candidate was discovered in the outskirts of an elongated, bright elliptical galaxy at g = 20.70 mag. The spectrum taken with the Double Beam Spectrograph at P200 classified it as a SN IIn at z[s] = 0.077 (Andreoni et al., 2020).

ZTF20aanamcs/AT2020crc - This object was discovered close to the nucleus of an edge-on galaxy, at g = 21.25 mag z[s] = 0.093 and subsequently classified as a SN II (De, 2020).

ZTF20aanakge/AT2020crd - This candidate was detected as an orphan at g = 20.64 mag. The spectrum taken with OSIRIS at the GTC classified it as a SN Ia at z[s] = 0.1272 (Hu et al., 2020).

A.2.12.2 Stellar

ZTF20aanaksk/AT2020clu - This candidate was first reported at $g = 20.48$ mag as an orphan transient. We rule out ZTF20aanaksk as it has 2 previous detections in 2010 in the PS1-DR2 catalog and we posit it is related to a faint star in the background.

ZTF20aanakes/AT2020cly - This candidate was first detected $g = 21.11$ mag, and with a color consistent with $g - r = 0$. Follow-up with ARTIC and GTC left only upper limits for this fast transient (Bellm & Graham, 2020; Hu et al., 2020). However, there is an archival detection in the PS1-DR2 catalog 1.5 arcsec from the ZTF source. Thus we reject this candidate.

A.2.12.3 Slow Photometric Evolution

ZTF20aamvmzj/AT2020cja - This transient sits at b = -10.43 deg, however, it does not seem to have a PS1 or ZTF counterpart as the previous stellar sources. The spectra taken with Keck I+LRIS and P200 only showed a featureless blue continuum (De, 2020). It was first observed (Oates et al., 2020a) by the Ultraviolet/Optical Telescope (UVOT; Roming et al. 2005) at the Neil Gehrels Swift Observatory 6.7 days after the merger, and it was only detected in the u-band at u = 19.05 mag. It was later followed-up, but not detected in any band-pass (Oates et al., 2020b). Nonetheless, the magnitude evolution of the transient, was otherwise flat and it

slowly faded over time with an $\alpha_r = 0.04$.

ZTF20aanaqhe/AT2020cre - This transient was detected at g = 20.88 mag on an elliptical galaxy at a photometric redshift of z[p] = 0.16. It slow rise of $\alpha_g = -0.08$ was inconsistent with the rise of a fast transient.

ZTF20aanakwb/AT2020cls - This transient was first reported in Andreoni et al. (2020a) g = 21.03 mag offset from a bright Gaia point source (g = 15.27 mag). This transient was detected by LOT 12 hours later at an r-band magnitude consistent with no evolution. The initial color g - r is consistent with 0 mag. In the ZTF reference image, there is a faint point source which indicates stellar activity.

A.2.12.4 Outside the GW map

ZTF20aanallx/AT2020clv - This transient was first reported in Andreoni et al. (2020a) g = 21.11 mag and was discovered at galactic latitude of b = -11.43 deg. It is offset from an elliptical galaxy, however, it falls in a fairly crowded region. The rejection criteria we used for this transient is the fact that it is not within the 95% credible level of the latest LALInference map for S200213t.

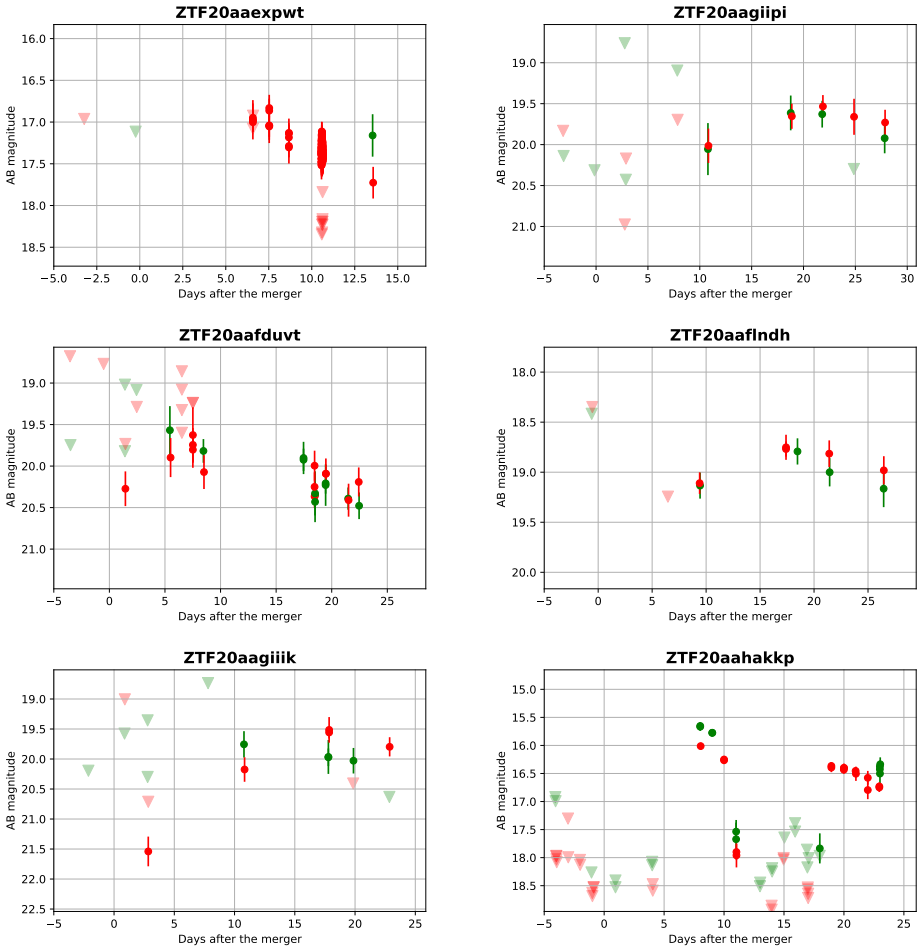

Figure A.1: The light curves for the objects ruled out photometrically are shown in this figure. In each panel, filled circles represent ZTF forced photometry and the photometry from the ZTF alert production pipeline. Filled triangles display upper limits for non-detections. The r-, g-, and i-band data is presented in red, green and yellow respectively.

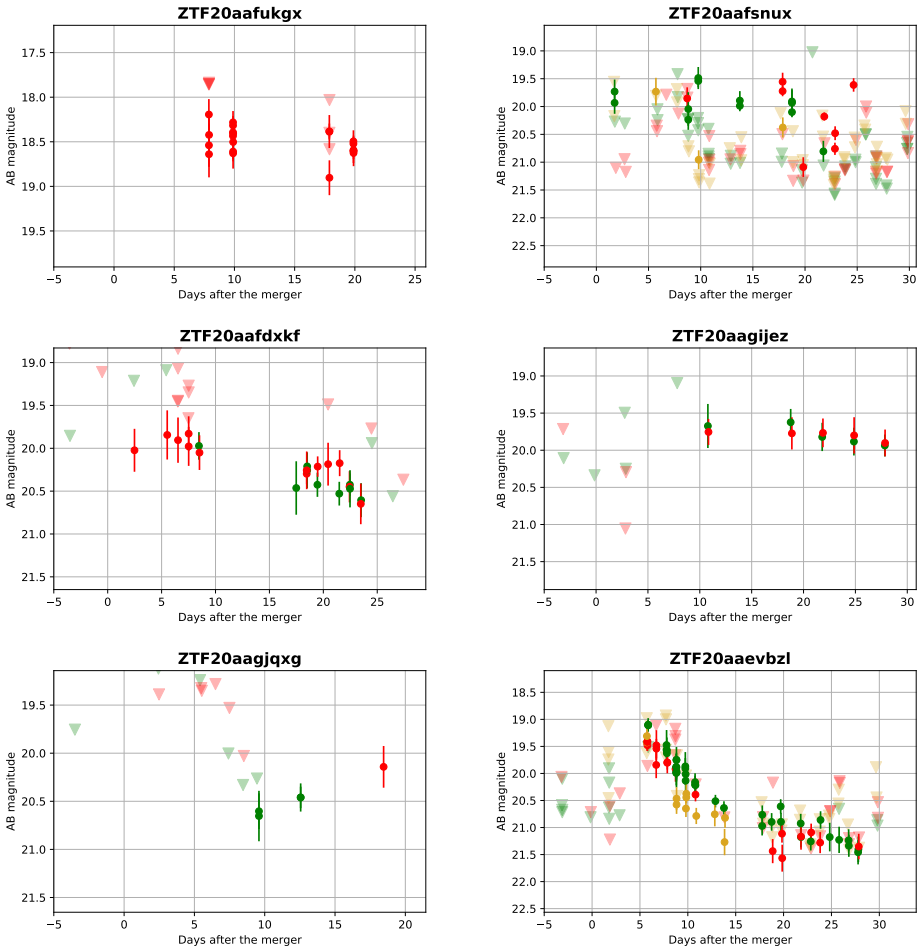

Figure A.2: The light curves for the objects ruled out photometrically are shown in this figure. Same as in Fig. A.1

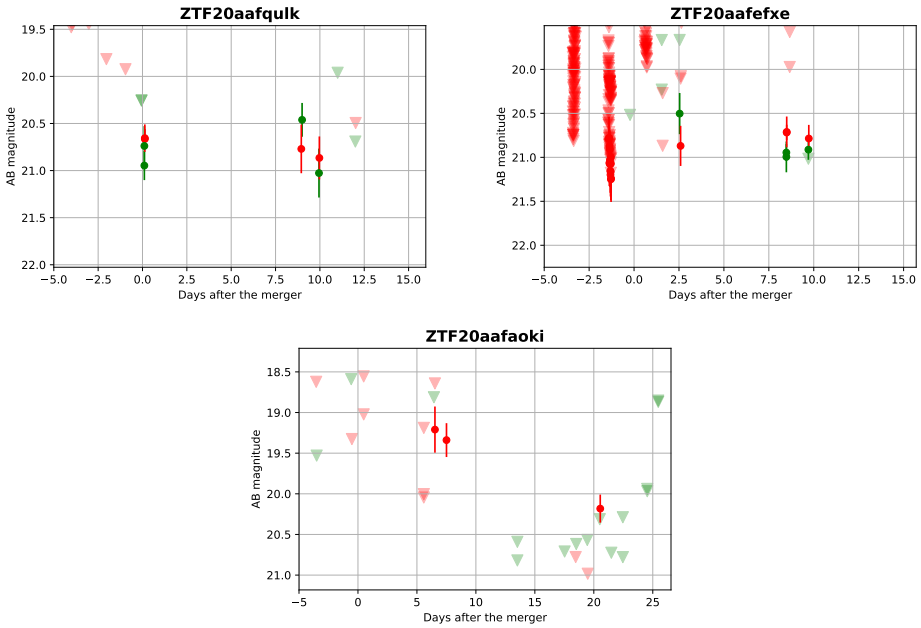

Figure A.3: The light curves for the objects ruled out photometrically are shown in this figure. Same as in Fig. A.1-A.2

Name	TNS	RA	DEC	Host/Redshift	Discov. Mag	Rejection Crit.
ZTF19aasmftm	AT2019sne	325.9004479	77.8315634	0.156 [s]	g = 18.78±0.19	SN Ia
ZTF19aaslzjf	AT2019snh	320.6262982	65.8134516	0.028 [s]	g = 19.45±0.14	SN Ia
ZTF19aasmddt	SN2019fht	299.25055	9.7016748	0.028 [s]	g = 18.6±0.11	SN II
ZTF19aasmekb	AT2019snl	300.6013987	14.2873159	-	g = 17.33±0.04	$\alpha_g = 0.24$
ZTF19aassfws	AT2019fuc	298.6678611	61.2400121	-	r = 21.35±0.21	artifact
ZTF19aaslszp	AT2019snj	301.3434628	53.3990477	0.084 [s]	g = 20.12±0.15	$\alpha_r = 0.01$, AGN
ZTF19aaslolf	AT2019snn	288.7838539	79.4357187	-	r = 21.12±0.18	$\alpha_r < 0.01$, AGN, PS1
ZTF19aaslozu	AT2019snr	306.3144981	65.1093759	-	r = 20.59±0.21	$\alpha_g = 0.06$, AGN, PS1
ZTF19aasshpf	AT2019snt	315.4768651	70.2055771	-	r = 19.99±0.23	$\alpha_r < 0.01$
ZTF19aaslphi	AT2019sno	297.3809977	61.9605925	-	r = 21.26±0.20	$\alpha_r = -0.08$
ZTF19aaslpds	AT2019snq	306.2625186	61.521461	-	r = 19.9±0.14	$\alpha_r = 0.03$
ZTF19aasmzqf	AT2019aaco	353.5204911	78.9577781	-	r = 19.86±0.09	$\alpha_r = 0.01$
ZTF19aaslzfk	AT2019snd	308.968271	72.3536353	-	g = 20.0±0.26	$\alpha_g = -0.02$
ZTF19aaslvwn	AT2019snf	299.059846	46.463559	-	g = 20.68±0.17	$\alpha_r < 0.01$
ZTF19aasmdir	AT2019sng	300.2360007	9.504002	-	g = 20.07±0.11	$\alpha_r < 0.01$

Table A.1: List of candidate counterparts to S190426c

Name	TNS	RA	DEC	Host/Redshift	Discov. Mag	Rejection Crit.
ZTF19abvizsw	AT2019pim	279.47282	61.497984	1.26 [s]	r = 19.89±0.16	long GRB afterglow
ZTF19abwvals	AT2019pni	73.250555	12.69303	0.091 [s]	r = 18.96±0.30	SN Ia
ZTF19abvixoy	AT2019pin	279.552972	27.420935	-	r = 18.93±0.10	$\alpha_r = 0.23$, CV
ZTF19abvionh	AT2019pip	253.750924	14.05133	0.0985 [s]	g = 20.57±0.31	$\alpha_g = 0.10$, CV
ZTF19abwsmmd	AT2019pnc	22.666409	-19.712405	0.0972 [s]	g = 19.78±0.18	$\alpha_g = 0.03$
ZTF19abvislp	AT2019pnx	220.349708	54.151153	0.10 [s]	r = 19.98±0.20	$\alpha_r = 0.05$
ZTF19abxdvcs	AT2019qev	252.010477	41.920087	-	g = 20.64±0.28	$\alpha_g = 0.03$

Table A.2: List of candidate counterparts to S190901ap

Name	TNS	RA	DEC	Host/Redshift	Discov. Mag	Rejection Crit.
ZTF19abyfhov	AT2019pvu	260.693429	11.424436	0.13 [s]	g = 19.92±0.22	SN Ia
ZTF19abyfbii	AT2019pvz	255.44162	11.602254	0.118 [s]	r = 19.60±0.16	SN Ia-91T
ZTF19abyfazm	AT2019pwa	290.535876	48.069162	0.38 [s]	g = 17.53±0.03	CV, $\alpha_r = 0.09$
ZTF19abyfhaq	AT2019pvv	303.148593	49.392607	0 [s]	g = 18.01±0.31	$\alpha_r = 0.15$, Galactic

Table A.3: List of candidate counterparts to S190910d

Name	TNS	RA	DEC	Host/Redshift	Discov. Mag	Rejection Crit.
ZTF19abyheza	AT2019pxi	332.913391	60.395816	0 [s]	r = 16.14±0.13	CV, $\alpha_r = 0.08$
ZTF19abyhhml	AT2019pxj	339.691635	55.936649	0 [s]	r = 17.36±0.12	CV, $\alpha_r = 0.13$
ZTF19abyirjl	AT2019pxe	30.471176	30.73355	0.1 [s]	r = 19.45±0.13	SN Ia
ZTF19abyjcom	AT2019pxk	32.936353	12.033344	-	r = 19.63±0.24	artifact
ZTF19abyjcon	AT2019pxl	33.252469	12.472604	-	r = 19.87±0.19	artifact
ZTF19abyjcoo	AT2019pxm	33.089712	12.297698	<0.03 [p]	r = 19.95±0.24	$\alpha_r = 0.06$
ZTF19abyjfiw	AT2019pxn	39.186807	34.647299	-	g = 20.13±0.21	$\alpha_r < 0.01$
ZTF19abygvmp	AT2019pzg	28.976258	41.090979	0.049 [s]	r = 20.13±0.25	SN II
ZTF19abyiwiw	AT2019pzi	340.521441	55.220244	-	r = 18.58±0.30	$\alpha_g = 0.20$
ZTF19abylleu	AT2019pyu	355.338225	-23.450706	-	r = 19.19±0.24	$\alpha_g = 0.03$
ZTF19abymhyi	AT2019pzh	340.85572	34.186344	<0.03 [p]	g = 20.36±0.23	$\alpha_g = -0.13$

Table A.4: List of candidate counterparts to S190910h

Name	TNS	RA	DEC	Host/Redshift	Discov. Mag	Rejection Crit.
ZTF19acbmopl	AT2019rob	114.040207	28.487381	<0.03 [p]	g = 19.64±0.27	$\alpha_g = 0.01$

Table A.5: List of candidate counterparts to S190923y

Name	TNS	RA	DEC	Host/Redshift	Discov. Mag	Rejection Crit.
ZTF19acbpqlh	AT2019rpn	319.9216636	37.5220721	0.026 [s]	g = 19.47±0.18	SN II
ZTF19acbwaah	AT2019rpp	162.3277489	22.9827302	0.031 [s]	r = 17.61±0.08	SN Ia
ATLAS19wyn	AT2019rpj	339.8367397	31.4916262	0.0297 [s]	g = 19.32±0.11	SN II

Table A.6: List of candidate counterparts to S190930t

Name	TNS	RA	DEC	Host/Redshift	Discov. Mag	Rejection Crit.
ZTF19acxpnvd	AT2019wkv	175.361851	8.241201	<0.03 [p]	i = 19.58±0.20	$\alpha_g = 0.06$
ZTF19acxoywk	AT2019wix	149.896148	13.915051	0.05 [s]	r = 19.69±0.21	$\alpha_g = -0.15$
ZTF19acxoyra	AT2019wid	153.093775	8.609330	0.09 [s]	r = 19.14±0.19	$\alpha_g = 0.05$
ZTF19acxpwlh	AT2019wiy	155.712970	23.603273	<0.24 [p]	g = 19.77±0.19	$\alpha_r = 0.07$
ZTF19acyiflj	AT2019wmy	152.899874	23.943843	0.081 [s]	r = 20.05±19.63	SN Ia
ZTF19acxowrr	AT2019wib	154.871458	27.883738	0.05 [s]	r = 19.00±0.13	SN II
ZTF19acyitga	AT2019wmn	159.796830	5.161942	0.071 [s]	r = 19.20±0.16	SN Ia

Table A.7: List of candidate counterparts to S191205ah

Name	TNS	RA	DEC	Host/Redshift	Discov. Mag	Rejection Crit.
ZTF19acykzsk	SN2019wqj	32.904547	34.041346	0.021 [s]	g = 19.0±0.06	SN II
ZTF19acymaru	AT2019wnh	80.461954	-19.266401	0.167 [s]	r = 19.92±0.16	SN Ia
ZTF19acykzsp	AT2019wne	28.359144	31.801012	0.16 [s]	r = 20.08±0.31	SN Ia
ZTF19acyfoha	AT2019wkl	85.104365	-18.097630	0.04 [s]	g = 17.31±0.08	SN Ia
ZTF19acymcwv	AT2019wni	36.248920	47.497844	0.09 [s]	r = 19.76±0.24	SN Ia
ZTF19acykwsd	AT2019wnl	33.088072	41.388708	-	r = 19.3±0.25	artifact
ZTF19acylvus	AT2019wnk	83.631136	-19.420244	0.104 [s]	r = 19.45±0.24	SN Ia
ZTF19acymcna	AT2019wnn	33.207899	40.999726	0.138 [s]	r = 20.48±0.22	$\alpha_r = -0.01$, AGN
ZTF19acykyqu	AT2019wre	38.819646	38.319851	-	g = 20.94±0.21	Stellar - PS1-DR2
ZTF19acykyrz	AT2019wrf	36.064972	38.080388	-	g = 20.83±0.17	Stellar - PS1-DR2
ZTF19acykyzj	AT2019wrg	36.056624	51.367126	-	g = 19.75±0.20	$\alpha_r = -0.03$
ZTF19acykzfy	AT2019wrh	43.115194	41.660303	-	g = 20.34±0.20	Stellar - PS1-DR2
ZTF19acyldum	AT2019wrn	79.681883	-7.185279	-	g = 19.41±0.13	PS1-DR2 detection
ZTF19acyldun	AT2019wrt	79.199993	-7.478682	0.057 [s]	g = 19.42±0.17	$\alpha_r = 0.09$, LBV
ZTF19acymapa	AT2019wro	78.207321	-5.948936	-	g = 18.54±0.22	$\alpha_r^{\ddagger} = -0.06$
ZTF19acymaxu	AT2019wrp	82.952485	-26.694523	<0.13 [p]	r = 18.65±0.06	$\alpha_r = 0.03$
ZTF19acymixu	AT2019wrr	90.913936	60.728245	0.14 [s]	r = 19.66±0.32	SN Ia
ZTF19acymlhi	AT2019wrs	91.592426	-18.804727	-	r = 17.99±0.26	$\alpha_r^{\ddagger} = -0.17$

Table A.8: List of candidate counterparts to S191213g reported in GCN 26424 and 26437. The candidates for which its photometric evolution has been calculated with a baseline (Δt) between 2 and 3 days are marked with a ‡

Name	TNS	RA	DEC	Host/Redshift	Discov. Mag	Rejection Crit.
ZTF20aamvqxl	AT2020ciy	29.237921	53.668882	0.102 [s]	g = 19.44±0.17	SN Ia
ZTF20aamvnth	AT2020cjb	18.337721	49.645539	0.061 [s]	g = 19.95±0.17	SN II
ZTF20aamvoxx	AT2020cjg	39.399095	26.920616	0.097 [s]	g = 19.47±0.12	SN Ia
ZTF20aamvtip	AT2020cje	38.082538	27.810094	0.151 [s]	g = 20.3±0.16	SN Ia
ZTF20aamvnat	AT2020ciz	27.239552	56.354579	0.0 [s]	g = 17.42±0.05	CV
ZTF20aamvmzj	AT2020cja	27.189195	51.430481	-	g = 19.46±0.11	$\alpha_r = 0.04$
ZTF20aamvoeh	AT2020cjc	33.502011	38.936317	0.14 [s]	g = 20.25±0.12	SN Ia
ZTF20aamvodd	AT2020cjf	37.482387	50.319427	0.0 [s]	g = 18.92±0.11	Stellar flare
ZTF20aanakwb	AT2020cls	6.5215391	42.7737224	–	g = 20.75±0.27	stellar
ZTF20aanaltd	AT2020clt	9.7406716	43.4410695	0.2 [s]	g = 20.57±0.23	SN Ia
ZTF20aanaksk	AT2020clu	19.4356399	31.1744954	<0.03 [p]	g = 20.27±0.10	PS1
ZTF20aanallx	AT2020clv	6.3666608	51.2233877	–	g = 20.58±0.28	Outside the LALInfernce map
ZTF20aanaoyz	AT2020clw	24.5940995	23.3822569	0.276 [s]	g = 21.28±0.27	SN Ia
ZTF20aamvpvx	AT2020clx	31.9402981	20.0306147	0.074 [s]	g = 19.95±0.14	SN II
ZTF20aanamcs	AT2020crc	13.7433345	43.4980245	0.093 [s]	g = 20.98±0.28	SN II
ZTF20aanakge	AT2020crd	12.6306233	41.484178	0.1272 [s]	g = 20.38±0.33	SN Ia
ZTF20aanaqhe	AT2020cre	17.0425796	45.5256583	-	g = 20.63±0.27	$\alpha_g = -0.08$
ZTF20aanakes	AT2020cly	2.0985443	38.0441264	–	g = 20.79±0.21	PS1
ZTF20aanakcd	AT2020cmr	8.1571223	41.3156371	0.077 [s]	g = 20.48±0.17	SN IIn

Table A.9: List of candidate counterparts to S200213t

Name	IAU Name	Date	Telescope	Filter	m (AB)	σ_m	$m_{\rm lim}$
ZTF19aasmftm	AT2019sne	2458602.6514	LT	g	21.33	0.15	21.71
ZTF19aasmftm	AT2019sne	2458602.6528	LT	r	21.06	0.10	21.51
ZTF19aasmftm	AT2019sne	2458602.6542	LT	i	20.90	0.17	21.03
ZTF19aassfws	AT2019fuc	2458603.6605	LT	g	99.0	99.0	22.32
ZTF19aassfws	AT2019fuc	2458603.6619	LT	r	99.0	99.0	22.04
ZTF19aassfws	AT2019fuc	2458603.6633	LT	i	99.0	99.0	21.50
ZTF19aaslszp	AT2019snj	2458603.6654	LT	g	20.80	0.07	22.25
ZTF19aaslszp	AT2019snj	2458603.6668	LT	r	20.51	0.07	22.12
ZTF19aaslszp	AT2019snj	2458603.6682	LT	i	19.19	0.06	22.00
ZTF19aaslzjf	AT2019snh	2458603.6703	LT	g	20.94	0.18	21.75
ZTF19aaslzjf	AT2019snh	2458603.6717	LT	r	20.40	0.10	22.00
ZTF19aaslzjf	AT2019snh	2458603.6731	LT	i	20.30	0.10	22.00
ZTF19aasmddt	SN2019fht	2458603.7113	LT	g	19.79	0.10	22.77
ZTF19aasmddt	SN2019fht	2458603.7127	LT	r	19.43	0.11	21.54
ZTF19aasmddt	SN2019fht	2458603.7141	LT	i	19.41	0.09	21.10
ZTF19aasmddt	SN2019fht	2458604.7237	LT	g	19.69	0.06	21.61
ZTF19aasmddt	SN2019fht	2458604.7251	LT	r	19.51	0.03	22.29
ZTF19aasmddt	SN2019fht	2458604.7265	LT	i	19.55	0.07	20.63

Table A.10: Follow-Up Photometry for S190426c candidates

Table A.11: Follow-Up Photometry for S190901ap candidates

Name	IAU Name	Date	Telescope	Filter	m (AB)	σ_m	$m_{\rm lim}$
ZTF19abvizsw	AT2019pim	2458729.229	GIT	i	20.14	0.1	20.41
ZTF19abvizsw	AT2019pim	2458729.126	GIT	i	20.13	0.09	20.41
ZTF19abvizsw	AT2019pim	2458729.303	GIT	g	21.19	0.06	21.43
ZTF19abvizsw	AT2019pim	2458729.103	GIT	r	20.57	0.11	20.65
ZTF19abvizsw	AT2019pim	2458730.4481	LT	g	22.02	0.10	22.00
ZTF19abvizsw	AT2019pim	2458730.4420	LT	r	21.62	0.09	22.0
ZTF19abvizsw	AT2019pim	2458730.4541	LT	i	21.16	0.07	22.00
ZTF19abvizsw	AT2019pim	2458730.4621	LT	z	20.87	0.12	22.00
ZTF19abvizsw	AT2019pim	2458731.14	GIT	i	99.0	99.0	20.29
ZTF19abvizsw	AT2019pim	2458731.134	GIT	i	99.0	99.0	20.29
ZTF19abvizsw	AT2019pim	2458731.118	GIT	r	99.0	99.0	20.98
ZTF19abvizsw	AT2019pim	2458731.125	GIT	r	99.0	99.0	21.14
ZTF19abvizsw	AT2019pim	2458731.3862	LT	g	22.50	0.20	22.50
ZTF19abvizsw	AT2019pim	2458731.3802	LT	r	22.05	0.10	22.50
ZTF19abvizsw	AT2019pim	2458731.3923	LT	i	21.60	0.10	22.50
ZTF19abvizsw	AT2019pim	2458731.3983	LT	z	21.20	0.20	22.50
ZTF19abvizsw	AT2019pim	2458731.5172	LT	g	22.54	0.16	23.00
ZTF19abvizsw	AT2019pim	2458731.5112	LT	r	22.10	0.12	23.00
ZTF19abvizsw	AT2019pim	2458731.5232	LT	i	21.64	0.11	23.00
ZTF19abvizsw	AT2019pim	2458731.5293	LT	z	21.55	0.22	23.00
ZTF19abvizsw	AT2019pim	2458732.102	GIT	r	99.0	99.0	19.32
ZTF19abvizsw	AT2019pim	2458732.119	GIT	i	99.0	99.0	20.4
ZTF19abvizsw	AT2019pim	2458732.125	GIT	i	99.0	99.0	20.43
ZTF19abvizsw	AT2019pim	2458738.3819	WHT	r	22.60	0.12	24.00
ZTF19abvizsw	AT2019pim	2458739.3839	WHT	i	22.43	0.12	24.10
ZTF19abvizsw	AT2019pim	2458740.4939	WHT	i	22.51	0.15	23.50
ZTF19abvizsw	AT2019pim	2458740.5219	WHT	r	23.38	0.25	23.70
ZTF19abvizsw	AT2019pim	2458750.7337	Keck1	g	23.99	0.10	26.00
ZTF19abvizsw	AT2019pim	2458750.7342	Keck1	i	23.80	0.09	25.00
ZTF19abvionh	AT2019pip	2458729.166	GIT	r	20.8	0.05	21.27
ZTF19abvionh	AT2019pip	2458729.206	GIT	r	20.77	0.06	21.17
ZTF19abvionh	AT2019pip	2458729.213	GIT	r	20.68	0.08	21.15
ZTF19abvionh	AT2019pip	2458730.166	GIT	r	20.63	0.04	21.22
ZTF19abvionh	AT2019pip	2458730.18	GIT	r	20.66	0.05	21.23
ZTF19abvionh	AT2019pip	2458731.204	GIT	g	20.56	0.06	21.16
ZTF19abvionh	AT2019pip	2458731.4331	LT	u	20.47	0.11	21.86
ZTF19abvionh	AT2019pip	2458731.4208	LT	g	20.51	0.29	22.55
ZTF19abvionh	AT2019pip	2458731.4168	LT	r	20.36	0.09	22.35
ZTF19abwsmmd	AT2019pnc	2458731.5587	LT	g	19.86	0.16	20.41
ZTF19abwsmmd	AT2019pnc	2458731.5641	LT	r	20.02	0.07	22.02
ZTF19abwsmmd	AT2019pnc	2458731.5614	LT	i	20.26	0.06	22.47
ZTF19abwvals	AT2019pni	2458731.7095	LT	g	20.42	0.07	22.63
ZTF19abwvals	AT2019pni	2458731.7149	LT	r	20.04	0.08	22.96
ZTF19abwvals	AT2019pni	2458731.7122	LT	i	20.23	0.24	22.30
ZTF19abvixoy	AT2019pin	2458729.144	GIT	r	18.97	0.03	21.16
ZTF19abvixoy	AT2019pin	2458729.182	GIT	r	18.73	0.02	21.17
ZTF19abvixoy	AT2019pin	2458729.238	GIT	i	18.97	0.05	20.35
ZTF19abvixoy	AT2019pin	2458729.245	GIT	i	19.06	0.05	20.38
ZTF19abvixoy	AT2019pin	2458729.285	GIT	i	19.02	0.1	20.27
ZTF19abvixoy	AT2019pin	2458729.292	GIT	i	18.94	0.1	20.23
ZTF19abvislp	AT2019pnx	2458734.171	GIT	g	99.0	99.0	20.42

continued ...

. . . continued

Name	IAU Name	Date	Telescope	Filter	m (AB)	σ_m	$m_{\rm lim}$
ZTF19abvislp	AT2019pnx	2458734.178	GIT	g	99.0	99.0	20.29
ZTF19abvislp	AT2019pnx	2458735.113	GIT	g	99.0	99.0	20.34
ZTF19abvislp	AT2019pnx	2458735.181	GIT	r	99.0	99.0	19.91
ZTF19abvislp	AT2019pnx	2458733.111	GIT	g	99.0	99.0	20.45
ZTF19abvislp	AT2019pnx	2458733.118	GIT	g	99.0	99.0	20.36
ZTF19abvislp	AT2019pnx	2458735.174	GIT	r	99.0	99.0	19.89
ZTF19abxdvcs	AT2019qev	2458733.133	GIT	g	19.93	0.03	20.7
ZTF19abxdvcs	AT2019qev	2458733.173	GIT	r	20.18	0.05	20.72
ZTF19abxdvcs	AT2019qev	2458733.179	GIT	r	20.28	0.03	20.82
ZTF19abxdvcs	AT2019qev	2458734.242	GIT	g	19.83	0.03	20.55
ZTF19abxdvcs	AT2019qev	2458734.249	GIT	g	19.9	0.05	20.38
ZTF19abxdvcs	AT2019qev	2458734.258	GIT	r	20.03	0.05	20.31
ZTF19abxdvcs	AT2019qev	2458734.264	GIT	r	20.11	0.05	20.32
ZTF19abxdvcs	AT2019qev	2458735.206	GIT	r	19.8	0.05	19.94
ZTF19abxdvcs	AT2019qev	2458735.213	GIT	r	19.84	0.05	19.89

Name	IAU Name	Date	Telescope	Filter	m (AB)	σ_m	$m_{\rm lim}$
ZTF19abyfazm	AT2019pwa	2458736.8848	P60	r	18.17	0.04	20.48
ZTF19abyfazm	AT2019pwa	2458737.3704	LT	g	17.95	0.03	21.00
ZTF19abyfazm	AT2019pwa	2458737.3704	LT	g	17.96	0.01	21.81
ZTF19abyfazm	AT2019pwa	2458737.3715	LT	r	18.30	0.03	21.00
ZTF19abyfazm	AT2019pwa	2458737.3715	LT	r	18.30	0.01	22.36
ZTF19abyfazm	AT2019pwa	2458737.3725	LT	i	18.65	0.05	21.00
ZTF19abyfazm	AT2019pwa	2458737.3725	LT	i	18.62	0.01	22.16

Table A.12: Follow-up Photometry for S190910d candidates

Name	IAU Name	Date	Telescope	Filter	m (AB)	σ_m	$m_{\rm lim}$
ZTF19abyjcom	AT2019pxk	2458737.5558	LT	g	99.0	99.0	20.75
ZTF19abyjcom	AT2019pxk	2458737.5569	LT	r	99.0	99.0	20.71
ZTF19abyjcom	AT2019pxk	2458737.5579	LT	i	99.0	99.0	20.21
ZTF19abyjcon	AT2019pxl	2458737.6142	LT	g	99.0	99.0	21.29
ZTF19abyjcon	AT2019pxl	2458737.6152	LT	r	99.0	99.0	21.44
ZTF19abyjcon	AT2019pxl	2458737.6163	LT	i	99.0	99.0	21.33
ZTF19abyjcoo	AT2019pxm	2458737.6234	LT	g	99.0	99.0	20.84
ZTF19abyjcoo	AT2019pxm	2458737.6245	LT	r	99.0	99.0	20.89
ZTF19abyjcoo	AT2019pxm	2458737.6255	LT	i	99.0	99.0	21.30

Table A.13: Follow-up Photometry for S190910h candidates

Name	IAU Name	Date	Telescope	Filter	m (AB)	σ_m	$m_{\rm lim}$
ATLAS19wyn	AT2019rpj	2458758.0974	LOT	g	19.65	0.08	99.0
ATLAS19wyn	AT2019rpj	2458758.0974	LOT	r	19.58	0.09	99.0
ATLAS19wyn	AT2019rpj	2458758.0974	LOT	i	19.55	0.12	99.0
ATLAS19wyn	AT2019rpj	2458758.8562	LDT	r	19.6	0.1	22.8
ZTF19acbpqlh	AT2019rpn	2458758.0937	LOT	g	20.80	0.25	99.0
ZTF19acbpqlh	AT2019rpn	2458758.0937	LOT	r	20.67	0.33	99.0
ZTF19acbpqlh	AT2019rpn	2458758.0937	LOT	i	20.80	0.39	99.0
ZTF19acbpqlh	AT2019rpn	2458758.8548	LDT	r	19.80	0.10	22.8

Table A.14: Follow-up Photometry for S190930t candidates

Name	IAU Name	Date	Telescope	Filter	m (AB)	σ_m	$m_{\rm lim}$
ZTF19acxowrr	AT2019wib	2458850.0554	P60	r	18.91	0.16	99.0
ZTF19acxowrr	AT2019wib	2458852.7504	P60	i	99.0	99.0	20.00
ZTF19acyitga	AT2019wmn	2458837.8427	P60	r	18.21	0.07	99.0

Table A.15: Follow-up Photometry for S191205ah candidates

Name	IAU Name	Date	Telescope	Filter	m (AB)	σ_m	$m_{\rm lim}$
ZTF19acykzsk	SN2019wqj	2458831.8323	P60	r	19.06	0.08	20.34
ZTF19acykzsk	SN2019wqj	2458831.928	LOT	g	19.37	0.10	99.0
ZTF19acykzsk	SN2019wqj	2458831.931	LOT	r	19.11	0.16	99.0
ZTF19acykzsk	SN2019wqj	2458831.935	LOT	i	19.10	0.11	99.0
ZTF19acykzsk	SN2019wqj	2458832.223	LOT	g	19.51	0.11	99.0
ZTF19acykzsk	SN2019wqj	2458832.231	LOT	r	19.10	0.14	99.0
ZTF19acykzsk	SN2019wqj	2458832.233	LOT	i	19.06	0.24	99.0
ZTF19acykzsk	SN2019wqj	2458832.2910	UVOT	v	99.0	99.0	17.2
ZTF19acykzsk	SN2019wqj	2458832.2910	UVOT	b	99.0	99.0	17.8
ZTF19acykzsk	SN2019wqj	2458832.2910	UVOT	u	99.0	99.0	17.5
ZTF19acykzsk	SN2019wqj	2458832.2910	UVOT	w1	99.0	99.0	17.5
ZTF19acykzsk	SN2019wqj	2458832.2910	UVOT	m2	99.0	99.0	18.0
ZTF19acykzsk	SN2019wqj	2458832.2910	UVOT	w2	99.0	99.0	18.1
ZTF19acymixu	AT2019wrr	2458832.2910	UVOT	v	99.0	99.0	19.5
ZTF19acymixu	AT2019wrr	2458832.2910	UVOT	b	20.10	0.4	99.0
ZTF19acymixu	AT2019wrr	2458832.2910	UVOT	u	99.0	99.0	19.7
ZTF19acymixu	AT2019wrr	2458832.2910	UVOT	w1	99.0	99.0	19.7
ZTF19acymixu	AT2019wrr	2458832.2910	UVOT	m2	99.0	99.0	19.7
ZTF19acymixu	AT2019wrr	2458832.2910	UVOT	w2	99.0	99.0	20.3
ZTF19acymaru	AT2019wnh	2458831.9682	LCOGT1m	g	19.83	0.04	21.00
ZTF19acymaru	AT2019wnh	2458831.9706	LCOGT1m	i	20.23	0.15	21.00
ZTF19acymaru	AT2019wnh	2458831.9755	LCOGT1m	r	20.11	0.05	21.00
ZTF19acyfoha	AT2019wkl	2458831.7544	P60	r	17.29	0.05	19.19
ZTF19acyldun	AT2019wrt	2458853.7823	P60	i	18.99	0.10	19.87
ZTF19acyldun	AT2019wrt	2458832.2910	UVOT	v	99.0	99.0	17.9
ZTF19acyldun	AT2019wrt	2458832.2910	UVOT	b	18.83	0.13	99.0
ZTF19acyldun	AT2019wrt	2458832.2910	UVOT	u	18.18	0.12	99.0
ZTF19acyldun	AT2019wrt	2458832.2910	UVOT	w1	17.62	0.11	99.0
ZTF19acyldun	AT2019wrt	2458832.2910	UVOT	m2	17.71	0.13	99.0
ZTF19acyldun	AT2019wrt	2458832.2910	UVOT	w2	18.19	0.12	99.0

Table A.16: Follow-up Photometry for S191213g candidates

Name	IAU Name	Date	Telescope	Filter	m (AB)	σ_m	$m_{\rm lim}$
ZTF20aamvqxl	AT2020ciy	2458893.3371	LT	i	20.17	0.15	21.61
ZTF20aamvqxl	AT2020ciy	2458893.3406	LT	g	99.0	99.0	19.54
ZTF20aamvoxx	AT2020cjg	2458893.3733	LT	i	20.29	0.21	21.30
ZTF20aamvoxx	AT2020cjg	2458893.3751	LT	r	21.47	0.19	22.49
ZTF20aamvoxx	AT2020cjg	2458893.3768	LT	g	20.26	0.03	23.36
ZTF20aamvtip	AT2020cje	2458893.3457	LT	i	20.68	0.07	22.73
ZTF20aamvtip	AT2020cje	2458893.3475	LT	r	20.73	0.11	22.52
ZTF20aamvtip	AT2020cje	2458893.3493	LT	g	20.80	0.06	23.14
ZTF20aamvmzj	AT2020cja	2458893.3559	LT	g	20.45	0.05	23.10
ZTF20aamvmzj	AT2020cja	2458906.7200	LCO2m	g	20.79	0.09	20.91
ZTF20aamvmzj	AT2020cja	2458906.7350	LCO2m	r	20.32	0.09	21.30
ZTF20aamvmzj	AT2020cja	2458893.9607	LOT	g	20.37	0.10	99.0
ZTF20aamvmzj	AT2020cja	2458893.9607	LOT	r	20.58	0.14	99.0
ZTF20aamvmzj	AT2020cja	2458893.9607	LOT	i	21.02	0.51	99.0
ZTF20aamvoeh	AT2020cjc	2458893.3559	LT	g	20.45	0.05	23.10
ZTF20aamvoeh	AT2020cjc	2458906.7200	LCO2m	g	20.79	0.09	20.91
ZTF20aamvoeh	AT2020cjc	2458906.7350	LCO2m	r	20.32	0.09	21.30
ZTF20aanakwb	AT2020cls	2458893.9607	LOT	g	99.0	99.0	18.9
ZTF20aanakwb	AT2020cls	2458893.9607	LOT	r	21.12	0.32	99.0
ZTF20aanakwb	AT2020cls	2458893.9607	LOT	i	20.97	0.37	99.0
ZTF20aanaltd	AT2020clt	2458893.9607	LOT	g	21.47	0.24	99.0
ZTF20aanaltd	AT2020clt	2458893.9607	LOT	r	19.34	0.04	99.0
ZTF20aanaltd	AT2020clt	2458893.9607	LOT	i	19.98	0.12	99.0
ZTF20aanaksk	AT2020clu	2458893.9607	LOT	g	20.80	0.14	99.0
ZTF20aanaksk	AT2020clu	2458893.9607	LOT	r	20.79	0.15	99.0
ZTF20aanaksk	AT2020clu	2458893.9607	LOT	i	21.19	0.47	99.0
ZTF20aanaoyz	AT2020clw	2458893.9607	LOT	g	21.46	0.42	99.0
ZTF20aanaoyz	AT2020clw	2458893.9607	LOT	r	21.09	0.22	99.0
ZTF20aanaoyz	AT2020clw	2458893.9607	LOT	i	20.75	0.37	99.0
ZTF20aanakes	AT2020cly	2458894.5992	APO	g	99.0	99.0	23.50
ZTF20aanakes	AT2020cly	2458894.6012	APO	i	99.0	99.0	21.50
ZTF20aanakes	AT2020cly	2458894.6031	APO	r	99.0	99.0	23.00

Table A.17: Follow-Up Photometry for S200213t candidates

Appendix B: Facilities and software

A summary of the facilities, instruments and software used in this thesis is listed below.

B.1 Facilities and instruments

Fermi	Gamma-ray Burst Monitor (GBM)
Neil Gehrels *Swift* Observatory	X-ray Telescope (XRT)
Neil Gehrels *Swift* Observatory	UV/Optical Telescope (UVOT)
P48	Zwicky Transient Facility (ZTF)
P60	Spectral Energy Distribution Machine (SEDM)
P200	Double Spectrograph (DBSP)
P200	Wide field IR Camera (WIRC)
Kitt Peak 84 inch	Kitt Peak Electron multiplying CCD Demonstrator (KPED)
LCOGT	Sinistro
LCOGT	Spectral
Gemini Observatory	Gemini Multi-Object Spectrograph (GMOS) - North
Gemini Observatory	Gemini Multi-Object Spectrograph (GMOS) - South
LDT	Large Monolithic Imager (LMI)
LDT	DeVeny
Keck	Low Resolution Imaging Spectrograph (LRIS)
LT	Infrader-Optical suite: Optical (IO:O)
GIT	GIT camera
GTC	Optical System for Imaging and low-Intermediate-Resolution Integrated Spectroscopy (OSIRIS)
uGMRT	GMRT Wideband Backend (GWB)
Blanco	Dark Energy Camera (DECam)

B.2 Software

`ipython`	Pérez & Granger 2007
`jupyter`	Kluyver et al. 2016
`matplotlib`	Hunter 2007
`python`	Van Rossum & Drake 2009
`NumPy`	Harris et al. 2020
`astropy`	Robitaille et al. 2013
`afterglowpy`	Ryan et al. 2020
`simsurvey`	Feindt et al. 2019
`pysedm`	Rigault et al. 2019

SNID	Blondin & Tonry 2007
PyRAF-dbsp	Bellm & Sesar 2016
DRAGONS	Labrie et al. 2019
HOTPANTS	Becker 2015
ForcePhotZTF	Yao et al. 2019
ZTF FP	Masci et al. 2019
ligo.skymap	Singer et al. 2016
Prospector	Johnson et al. 2019
pPXF	Cappellari 2017
fsps	Conroy et al. 2009
gwemopt	Coughlin et al. 2018

Bibliography

Aasi, J., Abadie, J., Abbott, B., et al. 2016, Living Reviews in Relativity, 19

Aasi et al. 2015, Classical and Quantum Gravity, 32, 074001

Abbott, B. P., Abbott, R., Adhikari, R., et al. 2009, Reports on Progress in Physics, 72, 076901

Abbott, B. P., Abbott, R., Abbott, T. D., et al. 2016, PhRvL, 116, 061102

—. 2017a, ApJL, 848, L12

—. 2017b, ApJL, 848, L13

—. 2017c, PhRvL, 119, 161101

—. 2017d, Nature, 551, 85

—. 2018, PhRvL, 121, 161101

Abbott, B. P., Abbott, R., Abbott, T., et al. 2018, Living Reviews in Relativity, 21, 3

Abbott, B. P., Abbott, R., Abbott, T. D., et al. 2019a, Physical Review X, 9, 031040

—. 2019b, PhRvL, 123, 011102

Abbott, B. P., Abbott, R., Abbott, T. D., et al. 2019, Phys. Rev. X, 9, 031040. https://link.aps.org/doi/10.1103/PhysRevX.9.031040

Abbott, R., Abbott, T., Abraham, S., et al. 2020, arXiv:2010.14527

Abbott, R., Abbott, T. D., Abraham, S., et al. 2021, Physical Review X, 11, 021053

Abbott et al. 2017a, Nature, 551, 85. http://dx.doi.org/10.1038/nature24471

—. 2017b, Phys. Rev. Lett., 119, 161101. https://link.aps.org/doi/10.1103/PhysRevLett.119.161101

—. 2017c, ApJL, 848, L13. http://stacks.iop.org/2041-8205/848/i=2/a=L13

—. 2017d, Phys. Rev. Lett., 118, 221101

—. 2017e, ApJL, 850, L39. http://stacks.iop.org/2041-8205/850/i=2/a=L39

—. 2018, Living Reviews in Relativity, 21, 3. https://doi.org/10.1007/s41114-018-0012-9

Acernese et al. 2015, Classical and Quantum Gravity, 32, 024001

Ade, P. A. R., Aghanim, N., Arnaud, M., et al. 2016, Astron. Astrophys., 594, A13

Aghanim, N., et al. 2018, arXiv:1807.06209

Ahumada, R., Allende Prieto, C., Almeida, A., et al. 2020a, ApJS, 249, 3

Ahumada, T., Coughlin, M., & Anand, S. 2020b, GRB Coordinates Network, 26817, 1

Ahumada, T., Coughlin, M. W., Staats, K., et al. 2019a, GCN, 24198

—. 2019b, GCN, 24320

Ahumada, T., Kumar, H., Fremling, C., et al. 2020c, GRB Coordinates Network, 29029, 1

Ahumada, T., Coughlin, M. W., Cenko, S. B., et al. 2018, GRB Coordinates Network, 23515, 1

Ahumada, T., Coughlin, M. W., Staats, K., et al. 2019c, GRB Coordinates Network, 24343, 1

Ahumada, T., Anand, S., Andreoni, I., et al. 2020, GRB Coordinates Network, 27737, 1

Ahumada, T., Anand, S., Stein, R., et al. 2020a, GRB Coordinates Network, 28295, 1

Ahumada, T., Andreoni, I., Karambelkar, V., et al. 2020b, GRB Coordinates Network, 26810, 1

Ahumada, T., et al. 2020, GCN, 26822, 1

Ahumada, T., Singer, L. P., Anand, S., et al. 2021, Nature Astronomy, 5, 917

Ahumada, T., Anand, S., Coughlin, M. W., et al. 2022, ApJ, 932, 40

Akiyama, K., Alberdi, A., Alef, W., et al. 2022, ApJL, 930, L12

Alard, C. 2000, A&AS, 144, 363

Alexander, K. D., Fong, W., Paterson, K., & Rastinejad, J. 2020, GRB Coordinates Network, 28302, 1

Alexander, K. D., Berger, E., Fong, W., et al. 2017, ApJL, 848, L21

Allington-Smith, J., Murray, G., Content, R., et al. 2002, Publications of the Astronomical Society of the Pacific, 114, 892

Almualla, M., Coughlin, M. W., Anand, S., et al. 2020, Mon. Not. R. Astron. Soc., 495, 4366. https://doi.org/10.1093/mnras/staa1498

Amati, L. 2021, Nature Astronomy, 5, 877

Amati, L., Frontera, F., Tavani, M., et al. 2002, Astronomy & Astrophysics, 390, 81

Anand, S., Andreoni, I., Khandagale, M., et al. 2019a, GRB Coordinates Network, 25706, 1

Anand, S., Kasliwal, M. M., M.W. Coughlin, T. A., et al. 2019b, GCN, 24311

Anand, S., Coughlin, M., Singer, L., et al. 2020a, GRB Coordinates Network, 26662, 1

Anand, S., Kumar, H., Reusch, S., et al. 2020b, GRB Coordinates Network, 26767, 1

Anand, S., Coughlin, M. W., Kasliwal, M. M., et al. 2021, Nature Astronomy, 5, 46

Anand, S., Andreoni, I., Ahumada, T., et al. 2021, GRB Coordinates Network, 30005, 1

Andreoni, I., Anand, S., & Kasliwal, M. 2019a, GRB Coordinates Network, 24349, 1

Andreoni, I., & Bellm, E. 2019, GCN, 24356

Andreoni, I., Cenko, S. B., Masci, F., & Graham, M. 2019b, GCN, 24302

Andreoni, I., De, K., Kasliwal, M., Huang, Y., & Liu, X. 2020, GCN, 27075, 1

Andreoni, I., Kasliwal, M. M., Cenko, S. B., & Yao, Y. 2020, GRB Coordinates Network, 26863, 1

Andreoni, I., Kumar, H., Karambelkar, V., et al. 2020a, GCN, 27065, 1

Andreoni, I., Anand, S., Bianco, F. B., et al. 2019, Publications of the Astronomical Society of the Pacific, 131, 068004

Andreoni, I., Goldstein, D. A., Anand, S., et al. 2019, ApJL, 881, L16

Andreoni, I., Goldstein, D. A., Anand, S., et al. 2019a, ApJL, 881, L16

Andreoni, I., Anand, S., Coughlin, M. W., et al. 2019b, GCN, 26416, 1

Andreoni, I., Anand, S., Bellm, E., et al. 2019c, GCN, 26424, 1

Andreoni, I., Kool, E. C., Carracedo, A. S., et al. 2020b, ApJ, 904, 155

Andreoni, I., Goldstein, D. A., Kasliwal, M. M., et al. 2020, ApJ, 890, 131

Andreoni, I., Coughlin, M. W., Kool, E. C., et al. 2021, ApJ, 918, 63

Andreoni, I., Margutti, R., Salafia, O. S., et al. 2022a, ApJS, 260, 18

Andreoni, I., Coughlin, M., Ahumada, T., et al. 2022b, GRB Coordinates Network, 31590, 1

Antier, S., Agayeva, S., AlMualla, M., et al. 2020, arXiv:2004.04277

Antonelli, L. A., D'Avanzo, P., Perna, R., et al. 2009, Astronomy & Astrophysics, 507, L45

Arcavi, I., Howell, D. A., McCully, C., et al. 2019, GRB Coordinates Network, 24307, 1

Arcavi, I., Hosseinzadeh, G., Howell, D. A., et al. 2017, Nature, 551, 64

Arcavi, I., McCully, C., Hosseinzadeh, G., et al. 2017, The Astrophysical Journal Letters, 848, L33. http://stacks.iop.org/2041-8205/848/i=2/a=L33

Arcavi et al. 2017, Nature, 551, 64 EP . http://dx.doi.org/10.1038/nature24291

Ascenzi, S., Oganesyan, G., Branchesi, M., & Ciolfi, R. 2021, Journal of Plasma Physics, 87, 845870102

Ascenzi, S., Coughlin, M. W., Dietrich, T., et al. 2019, MNRAS, 486, 672

Assef, R. J., Stern, D., Noirot, G., et al. 2018, ApJS, 234, 23

Baade, W., & Zwicky, F. 1934, Proceedings of the National Academy of Science, 20, 259

Band, D., Matteson, J., Ford, L., et al. 1993, ApJ, 413, 281

Barbary, K., Barclay, T., Biswas, R., et al. 2016, SNCosmo: Python library for supernova cosmology, , , ascl:1611.017

Bauswein, A., Baumgarte, T. W., & Janka, H.-T. 2013, Phys. Rev. Lett., 111, 131101. https://link.aps.org/doi/10.1103/PhysRevLett.111.131101

Bauswein et al. 2017, ApJL, 850, L34. http://stacks.iop.org/2041-8205/850/i=2/a=L34

Becker, A. 2015, HOTPANTS: High Order Transform of PSF ANd Template Subtraction, , , ascl:1504.004

Belkin, S., Zhornichenko, A., Pozanenko, A., et al. 2020, GRB Coordinates Network, 28306, 1

Bellm, E. C., Burke, C. J., Coughlin, M. W., et al. 2022, ApJS, 258, 13

Bellm, E. C., & Graham, M. 2020, GCN, 27118, 1

Bellm, E. C., & Sesar, B. 2016, pyraf-dbsp: Reduction pipeline for the Palomar Double Beam Spectrograph, , , ascl:1602.002

Bellm, E. C., Kulkarni, S. R., Graham, M. J., et al. 2019a, PASP, 131, 018002

Bellm, E. C., Kulkarni, S. R., Barlow, T., et al. 2019b, PASP, 131, 068003

Berger, E. 2014, ARA&A, 52, 43

Berger, E., Fong, W., & Chornock, R. 2013, ApJL, 774, L23

Berger, E., Price, P. A., Cenko, S. B., et al. 2005, Nature, 438, 988

Berti, E. 2006, Class. Quantum Grav., 23, S785

Bertin, E. 2006, in Astronomical Society of the Pacific Conference Series, Vol. 351, Astronomical Data Analysis Software and Systems XV, ed. C. Gabriel, C. Arviset, D. Ponz, & S. Enrique, 112

Bertin, E. 2011, in Astronomical Society of the Pacific Conference Series, Vol. 442, Astronomical Data Analysis Software and Systems XX, ed. I. N. Evans, A. Accomazzi, D. J. Mink, & A. H. Rots, 435

Bertin, E., & Arnouts, S. 1996, A&AS, 117, 393

—. 2010, SExtractor: Source Extractor, Astrophysics Source Code Library, , , ascl:1010.064

Bertin, E., Mellier, Y., Radovich, M., et al. 2002, in Astronomical Society of the Pacific Conference Series, Vol. 281, Astronomical Data Analysis Software and Systems XI, ed. D. A. Bohlender, D. Durand, & T. H. Handley, 228

Bhalerao, V., Kumar, H., Karambelkar, V., et al. 2019, GCN, 24201

Bhalerao, V., Bhattacharya, D., Vibhute, A., et al. 2017, Journal of Astrophysics and Astronomy, 38, 31

Blagorodnova, N., Neill, J. D., Walters, R., et al. 2018, PASP, 130, 035003

Blondin, S., & Tonry, J. L. 2007, ApJ, 666, 1024

Blondin, S., & Tonry, J. L. 2007, Astrophys. J., 666, 1024

Bloom, J. S., Zucker, C., Schlafly, E., et al. 2019, GCN, 24337

Bloom, J. S., Kulkarni, S. R., Djorgovski, S. G., et al. 1999, Nature, 401, 453–456. http://dx.doi.org/10.1038/46744

Boella, G., Butler, R. C., Perola, G. C., et al. 1997, A&AS, 122, 299

Bolton, C. T. 1972, Nature Physical Science, 240, 124

Breeveld, A. A., Kuin, N. P. M., Marshall, F. E., et al. 2019, GCN, 24296

Brennan, S., Killestein, T., Fraser, M., et al. 2019, GCN, 26429, 1

Bromberg, O., Nakar, E., Piran, T., & Sari, R. 2013, ApJ, 764, 179. http://stacks.iop.org/0004-637X/764/i=2/a=179

Bromberg, O., Tchekhovskoy, A., Gottlieb, O., Nakar, E., & Piran, T. 2018, MNRAS, 475, 2971

Brown, T. M., Baliber, N., Bianco, F. B., et al. 2013, PASP, 125, 1031. https://doi.org/10.1086%2F673168

Brown, T. M., Baliber, N., Bianco, F. B., et al. 2013, PASP, 125, 1031

Buchner, J., Georgakakis, A., Nandra, K., et al. 2014, A&A, 564, A125

Buckley, D., Jha, S. W., Cooke, J., & Mogotsi, M. 2019, GCN, 24205

Buckley, D. A. H., Hearnshaw, J. B., Nordsieck, K. H., & O'Donoghue, D. 2003, in Society of Photo-Optical Instrumentation Engineers (SPIE) Conference Series, Vol. 4834, Proc. SPIE, ed. P. Guhathakurta, 264–275

Bulla, M. 2019, MNRAS, 489, 5037

Burdge, K., Perley, D. A., & Kasliwal, M. 2019, GRB Coordinates Network, 25639, 1

Burgess, J. M., Yu, H.-F., Greiner, J., & Mortlock, D. J. 2016, arXiv e-prints, arXiv:1610.07385

Burgh, E. B., Nordsieck, K. H., Kobulnicky, H. A., et al. 2003, in Society of Photo-Optical Instrumentation Engineers (SPIE) Conference Series, Vol. 4841, Proc. SPIE, ed. M. Iye & A. F. M. Moorwood, 1463–1471

Burke, J., Hiramatsu, D., Arcavi, I., et al. 2019, GRB Coordinates Network, 24206, 1

Burns, E., Svinkin, D., Hurley, K., et al. 2021, ApJL, 907, L28

Burrows, D. N., Hill, J. E., Nousek, J. A., et al. 2005, SSRv, 120, 165

Calzetti, D., Armus, L., Bohlin, R. C., et al. 2000, ApJ, 533, 682

Cannizzaro, G., Pastor-Marazuela, I., Jonker, P., Maguire, K., & Fraser, M. 2019, GRB Coordinates Network, 25725, 1

Cannizzaro, G., Pastor-Marazuela, I., Jonker, P., Maguire, K., & Fraser, M. 2019, GCN, 25730, 1

Cannizzo, J. K., & Gehrels, N. 2009, ApJ, 700, 1047. http://stacks.iop.org/0004-637X/700/i=2/a=1047

Cano, Z., Wang, S.-Q., Dai, Z.-G., & Wu, X.-F. 2017, Advances in Astronomy, 2017

Cao, Y., Nugent, P. E., & Kasliwal, M. M. 2016, PASP, 128, 114502

Cappellari, M. 2017, MNRAS, 466, 798

Carini, R., Izzo, L., Palazzi, E., et al. 2019, GRB Coordinates Network, 24252, 1

Cash, W. 1979, ApJ, 228, 939

Castro-Tirado, A., Hu, Y.-D., Valeev, A., et al. 2020, GCN, 27063, 1

Castro-Tirado, A., Valeev, A., Sokolov, V., et al. 2019, GRB Coordinates Network, 25721, 1

Castro-Tirado, A., Hu, Y.-D., Valeev, A., et al. 2019, GCN, 26492, 1

Castro-Tirado, A. J., Valeev, A. F., Hu, Y.-D., et al. 2020, GRB Coordinates Network, 26703

Castro-Tirado, A. J., de Ugarte Postigo, A., Gorosabel, J., et al. 2005, A&A, 439, L15

Castro-Tirado, A. J., Hu, Y. D., Li, X. Y., et al. 2019, GRB Coordinates Network, 24214, 1

Cenko, S. B., Fox, D. B., Moon, D.-S., et al. 2006, Publications of the Astronomical Society of the Pacific, 118, 1396

Cenko, S. B., Kulkarni, S., Horesh, A., et al. 2013, ApJ, 769, 130

Cenko, S. B., Urban, A. L., Perley, D. A., et al. 2015, ApJL, 803, L24

Cenko, S. B., Coughlin, M. W., Ghosh, S., et al. 2018, GRB Coordinates Network, 22969, 1

Cenko et al. 2018, GRB Coordinates Network, Circular Service, No. 22969, #1 (2018/July-0), 22969

Cepa, J., Aguiar, M., Castañeda, H., et al. 2005, Revista Mexicana de Astronomía y Astrofísica, 24, 1

Chabrier, G. 2003, PASP, 115, 763

Chadwick, J. 1932, Nature, 129, 312

Chambers, K. C., Magnier, E. A., Metcalfe, N., et al. 2016a, arXiv e-prints, arXiv:1612.05560

—. 2016b, arXiv e-prints, arXiv:1612.05560

Chandra, P., Purkayastha, S., Bhalerao, V., Kumar, H., & Kasliwal, M. 2020, GRB Coordinates Network, 28410, 1

Chang, S.-W., Wolf, C., Onken, C. A., Luvaul, L., & Scott, S. 2019a, GCN, 24325

Chang, S. W., Wolf, C., Onken, C. A., et al. 2019b, GRB Coordinates Network, 24260, 1

Chatterjee, D., Ghosh, S., Brady, P. R., et al. 2019a, A Machine Learning Based Source Property Inference for Compact Binary Mergers, ,

Chatterjee, D., Nugent, P. E., Brady, P. R., et al. 2019b, ApJ, 881, 128

Chornock, R., Berger, E., Kasen, D., et al. 2017, ApJL, 848, L19

Chornock et al. 2017, ApJL, 848, L19. http://stacks.iop.org/2041-8205/848/i=2/a=L19

Chu, M., Dahiwale, A., & Fremling, C. 2022, Transient Name Server Classification Report, 2022-1011, 1

Clocchiatti, A., Suntzeff, N. B., Covarrubias, R., & Candia, P. 2011, The Astronomical Journal, 141, 163

Connaughton, V., Briggs, M. S., Goldstein, A., et al. 2015, The Astrophysical Journal Supplement Series, 216, 32. http://dx.doi.org/10.1088/0067-0049/216/2/32

Conroy, C., & Gunn, J. E. 2010, ApJ, 712, 833

Conroy, C., Gunn, J. E., & White, M. 2009, ApJ, 699, 486

Cook, D. O., Kasliwal, M. M., Van Sistine, A., et al. 2017, ArXiv e-prints, arXiv:1710.05016

—. 2019, ApJ, 880, 7

Costa, E., Frontera, F., Heise, J., et al. 1997, Nature, 387, 783

Côté, B., Fryer, C. L., Belczynski, K., et al. 2018, ApJ, 855, 99

Coughlin, M. W., Ahumada, T., Cenko, B., et al. 2018a, GRB Coordinates Network, 23379, 1

Coughlin, M. W., Anand, S., & Ahumada, T. 2019a, GCN, 24223

Coughlin, M. W., Dietrich, T., Margalit, B., & Metzger, B. D. 2018b, arXiv e-prints, arXiv:1812.04803

Coughlin, M. W., Singer, L. P., Cenko, S. B., et al. 2018c, GRB Coordinates Network, 22739, 1

Coughlin, M. W., Tao, D., Chan, M. L., et al. 2018, Monthly Notices of the Royal Astronomical Society, 478, 692. http://dx.doi.org/10.1093/mnras/sty1066

Coughlin, M. W., Singer, L. P., Ahumada, T., et al. 2018a, GRB Coordinates Network, 22871, 1

Coughlin, M. W., Cenko, S. B., Ahumada, T., et al. 2018b, GRB Coordinates Network, 23324, 1

Coughlin, M. W., Dietrich, T., Doctor, Z., et al. 2018, Mon. Not. Roy. Astron. Soc., 480, 3871

Coughlin, M. W., Ahumada, T., Anand, S., et al. 2019b, ApJL, 885, L19

Coughlin, M. W., Antier, S., Corre, D., et al. 2019a, Mon. Not. R. Astron. Soc., http://oup.prod.sis.lan/mnras/advance-article-pdf/doi/10.1093/mnras/stz2485/29808472/stz2485.pdf, stz2485. https://doi.org/10.1093/mnras/stz2485

Coughlin, M. W., Dekany, R. G., Duev, D. A., et al. 2019b, Monthly Notices of the Royal Astronomical Society, 485, 1412–1419. http://dx.doi.org/10.1093/mnras/stz497

Coughlin, M. W., Ahumada, T., Cenko, S. B., et al. 2019c, PASP, 131, 048001

Coughlin, M. W., Ahumada, T., Anand, S., et al. 2019d, ApJL, 885, L19

Coughlin, M. W., Dekany, R. G., Duev, D. A., et al. 2019e, Monthly Notices of the Royal Astronomical Society, 485, 1412

Coughlin, M. W., Kasliwal, M. M., Perley, D. A., et al. 2019, GRB Coordinates Network, 24283, 1

Coughlin, M. W., Dietrich, T., Antier, S., et al. 2020a, Mon. Not. Roy. Astron. Soc., 492, 863

Coughlin, M. W., Dietrich, T., Heinzel, J., et al. 2020b, Phys. Rev. Research, 2, 022006. https://link.aps.org/doi/10.1103/PhysRevResearch.2.022006

Coughlin et al. 2018a, GRB Coordinates Network, Circular Service, No. 23324, #1 (2018/October-0), 23324

—. 2018b, GRB Coordinates Network, Circular Service, No. 22739, #1 (2018/May-0), 22739

Coulter, D. A., Foley, R. J., Kilpatrick, C. D., et al. 2017, Science, 358, 1556

Cowley, A. P., Crampton, D., Hutchings, J. B., Remillard, R., & Penfold, J. E. 1983, ApJ, 272, 118

Cowperthwaite, P., Villar, V., Scolnic, D., & Berger, E. 2019, The Astrophysical Journal, 874, 88

Cowperthwaite, P. S., Berger, E., Villar, V. A., et al. 2017, ApJL, 848, L17

Crawford, S. M., Still, M., Schellart, P., et al. 2010, in Society of Photo-Optical Instrumentation Engineers (SPIE) Conference Series, Vol. 7737, Society of Photo-Optical Instrumentation Engineers (SPIE) Conference Series, 25

Cunningham, V., Cenko, S. B., Ryan, G., et al. 2020, arXiv preprint arXiv:2009.00579

Cushing, M. C., Vacca, W. D., & Rayner, J. T. 2004, PASP, 116, 362

Cutri, R. M., Wright, E. L., Conrow, T., et al. 2013, Explanatory Supplement to the AllWISE Data Release Products, Explanatory Supplement to the AllWISE Data Release Products, ,

D'Ai, A., Sbarufatti, B., Oates, S. R., et al. 2020, GRB Coordinates Network, 28300, 1

D'Avanzo, P. 2015, Journal of High Energy Astrophysics, 7, 73

De, K. 2020, GCN, 27140, 1

De, K., Hankins, M., & Kasliwal, M. M. 2020a, GRB Coordinates Network, 26814, 1

De, K., Hankins, M., Adams, S. M., et al. 2019, GCN, 24306

De, K., Hankins, M. J., Kasliwal, M. M., et al. 2020b, PASP, 132, 025001

De, K., Kasliwal, M. M., Tzanidakis, A., et al. 2020c, arXiv e-prints, arXiv:2004.09029

Dekany, R., Smith, R. M., Riddle, R., et al. 2020, PASP, 132, 038001

Dermer, C. D., Chiang, J., & Böttcher, M. 1999, ApJ, 513, 656

Dey, A., Schlegel, D. J., Lang, D., et al. 2019, The Astronomical Journal, 157, 168. https://doi.org/10.3847%2F1538-3881%2Fab089d

Dichiara, S., Gatkine, P., Durbak, J., et al. 2019, GCN, 24220

Dichiara, S., Troja, E., O'Connor, B., et al. 2020, Monthly Notices of the Royal Astronomical Society, 492, 5011

Dietrich, T., Coughlin, M. W., Pang, P. T. H., et al. 2020, Science, 370, 1450

Dimitriadis, G., Jones, D. O., Siebert, M. R., et al. 2019, GRB Coordinates Network, 24358, 1

Djorgovski, S. G., Drake, A. J., Mahabal, A. A., et al. 2011, arXiv e-prints, arXiv:1102.5004

Dong, D. Z., Hallinan, G., Nakar, E., et al. 2021, Science, 373, 1125

Drake, A., Djorgovski, S., Mahabal, A., et al. 2009, ApJ, 696, 870

Drout, M. R., Piro, A. L., Shappee, B. J., et al. 2017, Science, 358, 1570

Duev, D. A., Mahabal, A., Masci, F. J., et al. 2019, Monthly Notices of the Royal Astronomical Society, 489, 3582

Duffell, P. C., & MacFadyen, A. I. 2015, ApJ, 806, 205. http://stacks.iop.org/0004-637X/806/i=2/a=205

Eichler, D., Livio, M., Piran, T., & Schramm, D. N. 1989, Nature, 340, 126

Einstein, A. 1922, in The Meaning of Relativity (Springer), 54–75

Elias-Rosa, N., Benetti, S., Piranomonte, S., et al. 2019, GCN, 26428, 1

Evans, P., Beardmore, A., Page, K. L., et al. 2007, Astronomy & Astrophysics, 469, 379

Evans, P., Beardmore, A., Page, K., et al. 2009, Monthly Notices of the Royal Astronomical Society, 397, 1177

Evans, P. A., Cenko, S. B., Kennea, J. A., et al. 2017, Science, 358, 1565

Evans, P. A., Page, K. L., Kennea, J. A., et al. 2020, GRB Coordinates Network, 26798, 1

Feindt, U., Nordin, J., Rigault, M., et al. 2019, Journal of Cosmology and Astroparticle Physics, 2019, 005

Fermi GBM Team. 2020, GRB Coordinates Network, 28284, 1

Finn, L. S., & Chernoff, D. F. 1993, Phys. Rev. D, 47, 2198. https://link.aps.org/doi/10.1103/PhysRevD.47.2198

Fishbach, M., Gray, R., Magaña Hernandez, I., et al. 2019, ApJL, 871, L13

Fishman, G. J., Meegan, C. A., Wilson, R. B., et al. 1989, in Bulletin of the American Astronomical Society, Vol. 21, 860

Flaugher, B., Diehl, H. T., Honscheid, K., et al. 2015, AJ, 150, 150

Flesch, E. W. 2019, arXiv e-prints, arXiv:1912.05614

Flewelling, H. 2018, in American Astronomical Society Meeting Abstracts, Vol. 231, American Astronomical Society Meeting Abstracts #231, 436.01

Fong, W., Berger, E., Margutti, R., & Zauderer, B. A. 2015, ApJ, 815, 102. http://stacks.iop.org/0004-637X/815/i=2/a=102

Fong, W., Margutti, R., Chornock, R., et al. 2016, ApJ, 833, 151

Fong, W., Laskar, T., Rastinejad, J., et al. 2021, ApJ, 906, 127

Fong, W.-f., Nugent, A. E., Dong, Y., et al. 2022, arXiv e-prints, arXiv:2206.01763

Foreman-Mackey, D., Hogg, D. W., Lang, D., & Goodman, J. 2013, PASP, 125, 306

Förster, F., Cabrera-Vives, G., Castillo-Navarrete, E., et al. 2021, AJ, 161, 242

Foucart, F., Hinderer, T., & Nissanke, S. 2018, Phys. Rev., D98, 081501

Foucart, F., Deaton, M. B., Duez, M. D., et al. 2014, PhRvD, 90, 024026

Fox, D. B., Frail, D. A., Price, P. A., et al. 2005, Nature, 437, 845

Frail, D. A., Kulkarni, S. R., Nicastro, L., Feroci, M., & Taylor, G. B. 1997, Nature, 389, 261

Fremling, C., Ahumada, T., Singer, L. P., De, K., & Kasliwal, M. M. 2019, GCN, 26427

Fremling, C., Sollerman, J., Taddia, F., et al. 2016, A&A, 593, A68

Fremling, C., Miller, A. A., Sharma, Y., et al. 2020, ApJ, 895, 32

Fremling, U. C., Miller, A. A., Sharma, Y., et al. 2019, arXiv e-prints, arXiv:1910.12973

Frontera, F., Costa, E., Piro, L., et al. 1998, ApJL, 493, L67

Fynbo, J. P., Watson, D., Thöne, C. C., et al. 2006, Nature, 444, 1047

Gaia Collaboration, Brown, A. G. A., Vallenari, A., et al. 2018, A&A, 616, A1

Gal-Yam, A., Fox, D., & MacFayden, A. 2006, Nature, 1053. https://doi.org/10.1038/nature05373

Gal-Yam, A., Maoz, D., Guhathakurta, P., & Filippenko, A. V. 2008, ApJ, 680, 550

Galama, T. J., Vreeswijk, P., Van Paradijs, J., et al. 1998, Nature, 395, 670

Gehrels, N., Chincarini, G., Giommi, P., et al. 2004, ApJ, 611, 1005

Gehrels, N., Sarazin, C. L., O'Brien, P. T., et al. 2005, Nature, 437, 851

Gimeno, G., Roth, K., Chiboucas, K., et al. 2016, in Ground-based and Airborne Instrumentation for Astronomy VI, Vol. 9908, International Society for Optics and Photonics, 99082S

Goldstein, A., Preece, R. D., & Briggs, M. S. 2010, ApJ, 721, 1329–1332. http://dx.doi.org/10.1088/0004-637X/721/2/1329

Goldstein, A., Veres, P., Burns, E., et al. 2017, ApJLetters, 848, L14

Goldstein, A., Fletcher, C., Veres, P., et al. 2020, ApJ, 895, 40

Goldstein, D. A., Andreoni, I., Nugent, P. E., et al. 2019, ApJL, 881, L7

Golkhou, V. Z., Butler, N. R., Strausbaugh, R., et al. 2018, The Astrophysical Journal, 857, 81

Gompertz, B., et al. 2020, arXiv:2004.00025

Gompertz, B. P., Levan, A. J., Tanvir, N. R., et al. 2018, ApJ, 860, 62

Gompertz, B. P., Ravasio, M. E., Nicholl, M., et al. 2022, arXiv e-prints, arXiv:2205.05008

Graham, J. F., & Schady, P. 2016, ApJ, 823, 154

Graham, M. J., Kulkarni, S., Bellm, E. C., et al. 2019, PASP, 131, 078001

Granot, J., Gill, R., Guetta, D., & De Colle, F. 2018, MNRAS, 481, 1597

Granot, J., & Sari, R. 2002, ApJ, 568, 820

Green, R. M. 1985, Spherical Astronomy

Grindlay, J., Portegies Zwart, S., & McMillan, S. 2006, Nature Physics, 2, 116

Gruber, D., Goldstein, A., von Ahlefeld, V. W., et al. 2014, The Astrophysical Journal Supplement Series, 211, 12

Guevel, D., & Hosseinzadeh, G. 2017, Dguevel/Pyzogy: Initial Release, vv0.0.1, Zenodo, doi:10.5281/zenodo.1043973

Guiriec, S., Briggs, M. S., Connaugthon, V., et al. 2010, The Astrophysical Journal, 725, 225. https://doi.org/10.1088%2F0004-637x%2F725%2F1%2F225

Gupta, S., Sharma, V., Vibhute, A., et al. 2020, GRB Coordinates Network, 28288, 1

Gupta, Y., Ajithkumar, B., Kale, H., et al. 2017, Curr. Sci, 113, 707

H. E. S. S. Collaboration, Abdalla, H., Aharonian, F., et al. 2021, Science, 372, 1081

Haggard, D., Nynka, M., Ruan, J. J., et al. 2017, ApJL, 848, L25

Hallinan, G., Corsi, A., Mooley, K. P., et al. 2017, Science, 358, 1579

Hamburg, R., Veres, P., & Meegan, C. 2018, GCN, 23057, 1

Hammerstein, E., van Velzen, S., Gezari, S., et al. 2022, arXiv e-prints, arXiv:2203.01461

Han, X. H., Wei, J. Y., Guillot, S., Wang, J., & Basa, S. 2020, GRB Coordinates Network, 26786, 1

Harris, C. R., Millman, K. J., van der Walt, S. J., et al. 2020, Nature, 585, 357–362

Hewish, A., Bell, S. J., Pilkington, J. D. H., Scott, P. F., & Collins, R. A. 1968, Nature, 217, 709

Hewish, A., & Okoye, S. E. 1965, Nature, 207, 59

Hinshaw, G., Larson, D., Komatsu, E., et al. 2013, ApJS, 208, 19

Hiramatsu, D., Arcavi, I., Burke, J., et al. 2019, GRB Coordinates Network, 24194, 1

Hjorth, J., & Bloom, J. S. 2012, in Chapter 9 in "Gamma-Ray Bursts, 169–190

Hjorth, J., Watson, D., Fynbo, J. P. U., et al. 2005, Nature, 437, 859

Ho, A. Y., Perley, D. A., Beniamini, P., et al. 2020, arXiv:2006.10761

Ho, A. Y. Q., Kulkarni, S. R., Nugent, P. E., et al. 2018, ApJL, 854, L13

Ho, A. Y. Q., Perley, D. A., Kulkarni, S. R., et al. 2020, ApJ, 895, 49

Ho, A. Y. Q., Perley, D. A., Gal-Yam, A., et al. 2021, arXiv e-prints, arXiv:2105.08811

Ho, A. Y. Q., Perley, D. A., Yao, Y., et al. 2022, arXiv e-prints, arXiv:2201.12366

Hook, I., Jørgensen, I., Allington-Smith, J., et al. 2004, Publications of the Astronomical Society of the Pacific, 116, 425

Hosseinzadeh, G., Cowperthwaite, P. S., Gomez, S., et al. 2019, ApJL, 880, L4

Hotokezaka, K., Nakar, E., Gottlieb, O., et al. 2019, Nature Astronomy, doi:10.1038/s41550-019-0820-1. https://doi.org/10.1038/s41550-019-0820-1

Hu, Y., Valeev, A., Castro-Tirado, A., et al. 2019a, GRB Coordinates Network, 26502, 1

Hu, Y.-D., Valeev, A., Castro-Tirado, A., et al. 2019b, GCN, 26422, 1

Hu, Y. D., Castro-Tirado, A. J., Li, X. Y., et al. 2019a, GRB Coordinates Network, 24324, 1

Hu, Y. D., Castro-Tirado, A. J., Valeev, A. F., et al. 2019b, GRB Coordinates Network, 24359, 1

Hu, Y.-D., Castro-Tirado, A., Valeev, A., et al. 2020, GCN, 27154, 1

Huang, K., Urata, Y., Ip, W., et al. 2005, Nuovo Cim. C, 28, 731

Huehnerhoff, J., Ketzeback, W., Bradley, A., et al. 2016, in Ground-based and Airborne Instrumentation for Astronomy VI, Vol. 9908, International Society for Optics and Photonics, 99085H

Hulse, R. A., & Taylor, J. H. 1975, ApJL, 195, L51

Hunter, J. D. 2007, Computing in Science Engineering, 9, 90

Hurley, K., & et al. 2020, GCN, 28291

Im, M., Kim, J., Paek, G. S. H., et al. 2019, GRB Coordinates Network, 24318, 1

Ivezic, Z., Tyson, J. A., Acosta, E., et al. 2008, arXiv:0805.2366

Ivezić, Ž., Kahn, S. M., Tyson, J. A., et al. 2019, ApJ, 873, 111

Izzo, L., Leloudas, G., Bruun, S., et al. 2019a, GRB Coordinates Network, 25675, 1

Izzo, L., Carini, R., Benetti, S., et al. 2019b, GRB Coordinates Network, 24208, 1

Jedicke, R., Bolin, B., Granvik, M., & Beshore, E. 2016, Icarus, 266, 173

Jencson, J., De, K., Anand, S., et al. 2019, GCN, 24233

Johnson, B. D., Leja, J. L., Conroy, C., & Speagle, J. S. 2019, Prospector: Stellar population inference from spectra and SEDs, , , ascl:1905.025

Jones, R. L., Yoachim, P., Chandrasekharan, S., et al. 2015, in American Astronomical Society Meeting Abstracts, Vol. 225, American Astronomical Society Meeting Abstracts #225, 336.40

Jonker, P., et al. 2019, GCN, 24221

Just, O., Bauswein, A., Pulpillo, R. A., Goriely, S., & Janka, H.-T. 2015, Monthly Notices of the Royal Astronomical Society, 448, 541. +http://dx.doi.org/10.1093/mnras/stv009

Kaiser, N., Burgett, W., Chambers, K., et al. 2010, in SPIE Proceedings, Vol. 7733, Ground-based and Airborne Telescopes III, 77330E

Kann, D. A., Thoene, C., Stachie, C., et al. 2019, GRB Coordinates Network, 24459, 1

Karambelkar, V., De, K., Van Roestel, J., & Kasliwal, M. 2019, GCN, 25921, 1

Karambelkar, V., De, K., van Roestel, J., & Kasliwal, M. M. 2019, GRB Coordinates Network, 25931, 1

Kasen, D., Metzger, B., Barnes, J., Quataert, E., & Ramirez-Ruiz, E. 2017, Nature, 551, 80 EP . http://dx.doi.org/10.1038/nature24453

Kasliwal, M., Cannella, C., Bagdasaryan, A., et al. 2019a, PASP, 131, 038003

Kasliwal, M. M., Korobkin, O., Lau, R. M., Wollaeger, R., & Fryer, C. L. 2017a, ApJL, 843, L34

Kasliwal, M. M., & Nissanke, S. 2014, ApJL, 789, L5. http://stacks.iop.org/2041-8205/789/i=1/a=L5

Kasliwal, M. M., Perley, D., Kumar, H., et al. 2020a, GCN, 27051, 1

Kasliwal, M. M., Nakar, E., Singer, L. P., et al. 2017b, Science, 358, 1559

Kasliwal, M. M., Kasen, D., Lau, R. M., et al. 2019b, Monthly Notices of the Royal Astronomical Society: Letters, http://oup.prod.sis.lan/mnrasl/advance-article-pdf/doi/10.1093/mnrasl/slz007/27503647/slz007.pdf. https://doi.org/10.1093/mnrasl/slz007

Kasliwal, M. M., Anand, S., Ahumada, T., et al. 2020b, ApJ, 905, 145

Kasliwal et al. 2019, GCN, 24191

Kerr, R. P. 1963, PhRvL, 11, 237

Kilpatrick et al. 2017, Science, 358, 1583. http://science.sciencemag.org/content/358/6370/1583

Klebesadel, R. W., Strong, I. B., & Olson, R. A. 1973, ApJL, 182, L85

Klose, S., Schmidl, S., Kann, D., et al. 2019, å, 622, A138

Kluyver, T., Ragan-Kelley, B., Pérez, F., et al. 2016, in Positioning and Power in Academic Publishing: Players, Agents and Agendas, ed. F. Loizides & B. Scmidt (Netherlands: IOS Press), 87–90. https://eprints.soton.ac.uk/403913/

Kong, A., Tan, H.-J., Yu, P.-C., Ngeow, C.-C., & Ip, W.-H. 2019, GCN, 24301

Kostrzewa-Rutkowska, Z., Hodgkin, S., Delgado, A., et al. 2019, GCN, 24354

Kotani, T., Kawai, N., Yanagisawa, K., et al. 2005, Nuovo Cimento C Geophysics Space Physics C, 28, 755

Kouveliotou, C., Meegan, C. A., Fishman, G. J., et al. 1993, ApJ, 413, L101

Kremer, K., Lu, W., Piro, A. L., et al. 2021, ApJ, 911, 104

Kulkarni, S. R. 2005, ArXiv Astrophysics e-prints, astro-ph/0510256

Kulkarni, S. R., Frail, D. A., Wieringa, M. H., et al. 1998, Nature, 395, 663

Kumar, H., Bhalerao, V., Anupama, G. C., et al. 2022, arXiv e-prints, arXiv:2206.13535

Kumar, P., & Granot, J. 2003, ApJ, 591, 1075

Labrie, K., Anderson, K., Cárdenes, R., Simpson, C., & Turner, J. E. H. 2019, in Astronomical Society of the Pacific Conference Series, Vol. 523, Astronomical Data Analysis Software and Systems XXVII, ed. P. J. Teuben, M. W. Pound, B. A. Thomas, & E. M. Warner, 321

Lattimer, J. M., & Schramm, D. N. 1974, ApJL, 192, L145

Law, N. M., Kulkarni, S. R., Dekany, R. G., et al. 2009, PASP, 121, 1395

Lazzati, D., López-Cámara, D., Cantiello, M., et al. 2017, ApJL, 848, L6. http://stacks.iop.org/2041-8205/848/i=1/a=L6

Leibler, C. N., & Berger, E. 2010, ApJ, 725, 1202

Levesque, E. M., Bloom, J. S., Butler, N. R., et al. 2010, Monthly Notices of the Royal Astronomical Society, 401, 963

Li, L.-X., & Paczynski, B. 1998, ApJL, 507, L59. http://stacks.iop.org/1538-4357/507/i=1/a=L59

Ligo Scientific Collaboration, & VIRGO Collaboration. 2019, GRB Coordinates Network, 24228, 1

LIGO Scientific Collaboration, & Virgo Collaboration. 2020a, GRB Coordinates Network, 26640

—. 2020b, GRB Coordinates Network, 26657

—. 2020c, GRB Coordinates Network, 26688

—. 2020d, GRB Coordinates Network, Circular Service, No. 26759, #1 (2020/Jan-0), 26759

—. 2020e, GRB Coordinates Network, 26807, 1

LIGO Scientific Collaboration, Aasi, J., Abbott, B. P., et al. 2015, Classical and Quantum Gravity, 32, 074001

Lipunov, V., Kornilov, V., Krylov, A., et al. 2005, Astrophysics, 48, 389

Lipunov, V., Kornilov, V., Gorbovskoy, E., et al. 2010, Advances in Astronomy, 2010, 349171

Lipunov, V., N.Tyurina, Gorbovskoy, E., et al. 2019a, GCN, 24326

Lipunov, V., Gorbovskoy, E., Tyurina, N., et al. 2019b, GRB Coordinates Network, 24241, 1

Lipunov, V., Gorbovskoy, E., Kornilov, V., et al. 2020, GRB Coordinates Network, 28285, 1

Lipunov, V., Gorbovskoy, E., Kornilov, V., et al. 2020a, GRB Coordinates Network, 26646, 1

—. 2020b, GRB Coordinates Network, 26755

Lipunov et al. 2017, ApJL, 850, L1. http://stacks.iop.org/2041-8205/850/i=1/a=L1

Littlejohns, O. M., Butler, N. R., Cucchiara, A., et al. 2015, MNRAS, 449, 2919

Lloyd-Ronning, N. M., & Zhang, B. 2004, ApJ, 613, 477

LSST Dark Energy Science Collaboration (LSST DESC), Abolfathi, B., Alonso, D., et al. 2021, ApJS, 253, 31

Lü, H.-J., Liang, E.-W., Zhang, B.-B., & Zhang, B. 2010, ApJ, 725, 1965

MacFadyen, A. I., Woosley, S. E., & Heger, A. 2001, ApJ, 550, 410

MacFarlane, M. J., & Dunham, E. W. 2004, Optical design of the Discovery Channel Telescope, Society of Photo-Optical Instrumentation Engineers (SPIE) Conference Series, doi:10.1117/12.550633

Mahabal, A., Rebbapragada, U., Walters, R., et al. 2019, PASP, 131, 038002. https://doi.org/10.1088%2F1538-3873%2Faaf3fa

Mangan, J., Dunwoody, R., Meegan, C., & Fermi GBM Team. 2020, GRB Coordinates Network, 28287, 1

Margutti, R., Berger, E., Fong, W., et al. 2017, ApJL, 848, L20

Masci, F. J., Laher, R. R., Rebbapragada, U. D., et al. 2017, PASP, 129, 014002

Masci, F. J., Laher, R. R., Rusholme, B., et al. 2019, PASP, 131, 018003

Massey, P., Dunham, E., Bida, T., et al. 2013, in American Astronomical Society Meeting Abstracts# 221, Vol. 221

Mazaeva, E., Pozanenko, A., Belkin, S., Klunko, E., & Volnova, A. 2020, GRB Coordinates Network, 26819, 1

Mazaeva, E., Pozanenko, A., Rumyantsev, V., Belkin, S., & Volnova, A. 2019, GCN, 25943, 1

McBrien, O., Smartt, S., Smith, K. W., et al. 2019, GCN, 24197

McBrien, O. R., Smartt, S. J., Huber, M. E., et al. 2021, MNRAS, 500, 4213

McCully, C., Hiramatsu, D., Howell, D. A., et al. 2019, GCN, 24295

—. 2017, ApJL, 848, L32

McMullin, J. P., Waters, B., Schiebel, D., Young, W., & Golap, K. 2007, in Astronomical data analysis software and systems XVI, Vol. 376, 127

Meegan, C., et al. 2009, ApJ, 702, 791

Mészáros, P., & Rees, M. J. 1997, The Astrophysical Journal, 476, 232

—. 1998, ApJL, 502, L105. http://stacks.iop.org/1538-4357/502/i=2/a=L105

Metzger, B. D. 2017, Living Rev. Rel., 20, 3

Metzger, B. D., Giannios, D., Thompson, T. A., Bucciantini, N., & Quataert, E. 2011, Monthly Notices of the Royal Astronomical Society, 413, 2031. http://dx.doi.org/10.1111/j.1365-2966.2011.18280.x

Metzger, B. D., Martínez-Pinedo, G., Darbha, S., et al. 2010, Monthly Notices of the Royal Astronomical Society, 406, 2650

Metzger, M., Djorgovski, S., Kulkarni, S., et al. 1997, Nature, 387, 878

Möller, A., Peloton, J., Ishida, E. E. O., et al. 2021, MNRAS, 501, 3272

Mong, Y., Ackley, K., Galloway, D., et al. 2021, Monthly Notices of the Royal Astronomical Society, 507, 5463

Mooley, K. P., Nakar, E., Hotokezaka, K., et al. 2017, Nature, 554, 207 EP . http://dx.doi.org/10.1038/nature25452

Mooley, K. P., Frail, D. A., Dobie, D., et al. 2018, ApJL, 868, L11

Morihana, K., Jian, M., & Nagayama, T. 2019a, GRB Coordinates Network, 24219, 1

—. 2019b, GRB Coordinates Network, 24328, 1

Morokuma, T., Ohta, K., Yoshida, M., et al. 2019, GRB Coordinates Network, 24230, 1

Morrissey, P., Conrow, T., Barlow, T. A., et al. 2007, ApJS, 173, 682

Muthukrishna, D., Parkinson, D., & Tucker, B. E. 2019, ApJ, 885, 85

Nagakura, H., Hotokezaka, K., Sekiguchi, Y., Shibata, M., & Ioka, K. 2014, ApJL, 784, L28. http://stacks.iop.org/2041-8205/784/i=2/a=L28

Nakar, E. 2007, Phys. Rept., 442, 166

Nakar, E. 2007, PhR, 442, 166

—. 2015, ApJ, 807, 172

Narayan, R., Paczynski, B., & Piran, T. 1992, ApJL, 395, L83

Nicholl, M., Cartier, R., Pelisoli, I., et al. 2019, GCN, 24321

Nicholl et al. 2017, ApJL, 848, L18. http://stacks.iop.org/2041-8205/848/i=2/a=L18

Nissanke, S., Sievers, J., Dalal, N., & Holz, D. 2011, ApJ, 739, 99

Nordin, J., Brinnel, V., Van Santen, J., et al. 2019, Astronomy & Astrophysics, 631, A147

Norris, J. P., & Bonnell, J. T. 2006, The Astrophysical Journal, 643, 266

Norris, J. P., Marani, G. F., & Bonnell, J. T. 2000, ApJ, 534, 248

Noysena, K., Antier, S., Blazek, M., et al. 2020, GRB Coordinates Network, 26820, 1

Nugent, A. E., Fong, W.-f., Dong, Y., et al. 2020, arXiv preprint arXiv:2007.10372

Nugent, A. E., Fong, W.-f., Dong, Y., et al. 2022, arXiv e-prints, arXiv:2206.01764

Oates, S., Page, K., De Pasquale, M., et al. 2019, GCN, 26471, 1

Oates, S., Page, K., Breeveld, A., et al. 2020a, GCN, 27153, 1

Oates, S., Klingler, N., Page, K., et al. 2020b, GCN, 27400, 1

O'Brien, P. 2018, in COSPAR Meeting, Vol. 42, 42nd COSPAR Scientific Assembly, E1.15–18–18

O'Connor, B., & Troja, E. 2022, GRB Coordinates Network, 32065, 1

O'Connor, B., Troja, E., Dichiara, S., et al. 2021, MNRAS, 502, 1279

—. 2022, arXiv e-prints, arXiv:2204.09059

Oke, J., Cohen, J., Carr, M., et al. 1995, PASP, 107, 375

Paczynski, B., & Rhoads, J. E. 1993, ApJL, 418, L5

Palmese, A., Soares-Santos, M., Santana-Silva, L., et al. 2019, GCN, 24312

Panaitescu, A., & Kumar, P. 2002, ApJ, 571, 779

Pang, P. T. H., Dietrich, T., Coughlin, M. W., et al. 2022, arXiv e-prints, arXiv:2205.08513

Paterson, K., Fong, W., Nugent, A., et al. 2020, ApJL, 898, L32

Patterson, M. T., Bellm, E. C., Rusholme, B., et al. 2019, PASP, 131, 018001

Pavana, M., Kiran, B., Anupama, G., & Bhalerao, V. 2019, GCN, 24200

Pei, Y. C. 1992, ApJ, 395, 130

Pérez, F., & Granger, B. E. 2007, Computing in Science and Engineering, 9, 21. `https://ipython.org`

Perley, D., & Copperwheat, C. 2019, GRB Coordinates Network, 25720, 1

Perley, D., & Copperwheat, C. 2019a, GCN, 26426, 1

Perley, D. A. 2019, PASP, 131, 084503

Perley, D. A., & Copperwheat, C. M. 2019b, GCN, 24202

Perley, D. A., Copperwheat, C. M., & Taggart, K. L. 2019a, GCN, 24204

—. 2019b, GCN, 24314

Perley, D. A., Ho, A. Y. Q., & Copperwheat, C. M. 2019c, GRB Coordinates Network, 25643, 1

Perley, D. A., Mazzali, P. A., Yan, L., et al. 2018, Monthly Notices of the Royal Astronomical Society, 484, 1031

Perley, D. A., Goobar, A., Kasliwal, M. M., et al. 2019d, GRB Coordinates Network, 24331, 1

Perley, D. A., Fremling, C., Sollerman, J., et al. 2020, ApJ, 904, 35

Pian, E., D'Avanzo, P., Benetti, S., et al. 2017, Nature, 551, 67

Piascik, A., Steele, I. A., Bates, S. D., et al. 2014, in Ground-based and Airborne Instrumentation for Astronomy V, Vol. 9147, International Society for Optics and Photonics, 91478H

Piran, T., Bromberg, O., Nakar, E., & Sari, R. 2013, Philosophical Transactions of the Royal Society of London Series A, 371, 20120273

Piro, A. L., Haynie, A., & Yao, Y. 2021, ApJ, 909, 209

Pittori, C., Verrecchia, F., Ursi, A., et al. 2020, GRB Coordinates Network, 28289, 1

Radice, D., Perego, A., Zappa, F., & Bernuzzi, S. 2018, ApJL, 852, L29. http://stacks.iop.org/2041-8205/852/i=2/a=L29

Rana, J., Anand, S., & Bose, S. 2019, The Astrophysical Journal, 876, 104. http://dx.doi.org/10.3847/1538-4357/ab165a

Rana, J., Singhal, A., Gadre, B., Bhalerao, V., & Bose, S. 2017, ApJ, 838, 108

Rastinejad, J. C., Fong, W., Kilpatrick, C. D., et al. 2021, ApJ, 916, 89

Rastinejad, J. C., Gompertz, B. P., Levan, A. J., et al. 2022, arXiv e-prints, arXiv:2204.10864

Rau et al. 2009, PASP, 121, 1334. http://stacks.iop.org/1538-3873/121/i=886/a=1334

Reusch, S., Ahumada, T., Anand, S., et al. 2020a, GRB Coordinates Network, 27745, 1

Reusch, S., Andreoni, I., Kumar, H., et al. 2020b, GRB Coordinates Network, 28981, 1

Rhoads, J. E. 1999, ApJ, 525, 737

—. 2003, ApJ, 591, 1097

Rhodes, L., Fender, R., Williams, D., et al. 2019, GRB Coordinates Network, 24226, 1

Rhodes, L., Fender, R., Williams, D. R. A., & Mooley, K. 2021, MNRAS, 503, 2966

Richardson, D., Jenkins III, R. L., Wright, J., & Maddox, L. 2014, The Astronomical Journal, 147, 118

Ricker, G. R., & Vanderspek, R. K. 2003, AIPC, 662

Ridnaia, A., Golenetskii, S., Aptekar, R., et al. 2020, GRB Coordinates Network, 28294, 1

Rigault, M., Neill, J. D., Blagorodnova, N., et al. 2019, A&A, 627, A115

Roberts, L. F., Kasen, D., Lee, W. H., & Ramirez-Ruiz, E. 2011, ApJL, 736, L21. http://stacks.iop.org/2041-8205/736/i=1/a=L21

Roberts, L. F., Lippuner, J., Duez, M. D., et al. 2017, Monthly Notices of the Royal Astronomical Society, 464, 3907. +http://dx.doi.org/10.1093/mnras/stw2622

Robitaille, T. P., Tollerud, E. J., Greenfield, P., et al. 2013, A&A, 558, A33

Roming, P. W. A., Kennedy, T. E., Mason, K. O., et al. 2005, SSRv, 120, 95

Rosell, M. J. B., Rostopchin, S., Zimmerman, A., et al. 2019, GRB Coordinates Network, 25622, 1

Rossi, A., Stratta, G., Maiorano, E., et al. 2020, MNRAS, 493, 3379

Rossi, A., Rothberg, B., Palazzi, E., et al. 2021, arXiv e-prints, arXiv:2105.03829

Rosswog, S. 2005, ApJ, 634, 1202

—. 2015, International Journal of Modern Physics D, 24, 1530012

Rosswog, S., Feindt, U., Korobkin, O., et al. 2017, Class. Quant. Grav., 34, 104001

Rothberg, B., Kuhn, O., Veillet, C., & Allanson, S. 2020, GRB Coordinates Network, 28319, 1

Ryan, G., Eerten, H. v., Piro, L., & Troja, E. 2020, ApJ, 896, 166

Ryan, G., Van Eerten, H., Piro, L., & Troja, E. 2020, ApJ, 896, 166

Sagués Carracedo, A., Bulla, M., Feindt, U., & Goobar, A. 2020, arXiv e-prints, arXiv:2004.06137

Sagues Carracedo, A., Kumar, H., Ahumada, T., et al. 2020, GRB Coordinates Network, 28293, 1

Sakamoto, T., Barthelmy, S. D., Baumgartner, W. H., et al. 2011, ApJS, 195, 2

Salmaso, I., Tomasella, L., Benetti, S., et al. 2019, GCN, 25619, 1

Salsamo, I., Tomasella, L., Benetti, S., D'Avanzo, P., & Cappellaro, E. 2019, GRB Coordinates Network, 25618, 1

Salvaterra, R., Cerutti, A., Chincarini, G., et al. 2008, MNRAS, 388, L6

Sari, R., Piran, T., & Halpern, J. P. 1999, ApJL, 519, L17

Sari, R., Piran, T., & Narayan, R. 1998, ApJL, 497, L17

Savchenko, V., Ferrigno, C., Kuulkers, E., et al. 2017, ApJL, 848, L15

Schady, P. 2015, Journal of High Energy Astrophysics, 7, 56

Schady, P., Chen, T. W., Schweyer, T., Malesani, D. B., & Bolmer, J. 2019, GRB Coordinates Network, 24229, 1

Schaffer, S. 1979, Journal for the History of Astronomy, 10, 42

Schlafly, E. F., & Finkbeiner, D. P. 2011, ApJ, 737, 103

Schmidt, M. 1963, Nature, 197, 1040

Schulze, S., Irani, I., Zimmerman, E., et al. 2020, Transient Name Server AstroNote, 13, 1

Schwarzschild, K. 1916, Sitzungsberichte der Königlich Preußischen Akademie der Wissenschaften (Berlin, 189

Setzer, C. N., Biswas, R., Peiris, H. V., et al. 2019, Monthly Notices of the Royal Astronomical Society, 485, 4260

Shappee, B. J., Prieto, J. L., Grupe, D., et al. 2014, The Astrophysical Journal, 788, 48

Shappee, B. J., Simon, J. D., Drout, M. R., et al. 2017, Science, 358, 1574

Shappee, B. J., Kochanek, C. S., Stanek, K. Z., et al. 2019, GCN, 24313

Sharma, Y., Marathe, A., Bhalerao, V., et al. 2020, arXiv preprint arXiv:2011.07067

Shibata, M., Fujibayashi, S., Hotokezaka, K., et al. 2017, PhRvD, 96, 123012

Shivvers, I., & Berger, E. 2011, ApJ, 734, 58

Shklovsky, I. S. 1967, ApJL, 148, L1

Singer, L. P., & Price, L. R. 2016, Phys. Rev. D, 93, 024013. https://link.aps.org/doi/10.1103/PhysRevD.93.024013

Singer, L. P., Cenko, S. B., Kasliwal, M. M., et al. 2013, ApJL, 776, L34

Singer, L. P., Chen, H.-Y., Holz, D. E., et al. 2016, The Astrophysical Journal Supplement Series, 226, 10. https://doi.org/10.3847/0067-0049/226/1/10

Singer et al. 2013, ApJL, 776, L34. http://stacks.iop.org/2041-8205/776/i=2/a=L34

—. 2015, ApJ, 806, 52

—. 2019a, GRB Coordinates Network, Circular Service, No. 24168, #1 (2019/April-0), 24168

—. 2019b, GRB Coordinates Network, Circular Service, No. 24228, #1 (2019/May-0), 24228

Sironi, L., Keshet, U., & Lemoine, M. 2015, SSRv, 191, 519

Skrutskie, M. F., Cutri, R. M., Stiening, R., et al. 2006, AJ, 131, 1163

Smartt, S., Srivastav, S., Smith, K., et al. 2019, GCN, 25922, 1

Smartt, S. J., Valenti, S., Fraser, M., et al. 2015, A&A, 579, A40

Smartt et al. 2017, Nature, 551, 75 EP . http://dx.doi.org/10.1038/nature24303

Smith, K., Smartt, S., Young, D., et al. 2019, GCN, 26430, 1

Smith, K. W., Williams, R. D., Young, D. R., et al. 2019a, Research Notes of the American Astronomical Society, 3, 26

Smith, K. W., Young, D. R., McBrien, O., et al. 2019b, GCN, 24210

Smith, M. P., Nordsieck, K. H., Burgh, E. B., et al. 2006, in Proc. SPIE, Vol. 6269, Society of Photo-Optical Instrumentation Engineers (SPIE) Conference Series, 62692A

Soares-Santos, M., Holz, D. E., Annis, J., et al. 2017, ApJL, 848, L16

Sobacchi, E., Granot, J., Bromberg, O., & Sormani, M. 2017, Monthly Notices of the Royal Astronomical Society, 472, 616

Soderberg, A. M., Kulkarni, S. R., Nakar, E., et al. 2006, Nature, 442, 1014

Soumagnac, M. T., & Ofek, E. O. 2018, PASP, 130, 075002

Speagle, J. S. 2020, Monthly Notices of the Royal Astronomical Society, 493, 3132

Sravan, N., Marchant, P., & Kalogera, V. 2019, ApJ, 885, 130

Stalder, B., Tonry, J., Smartt, S., et al. 2017, ApJ, 850, 149

Steeghs, D., Ulaczyk, K., Lyman, J., et al. 2020, GRB Coordinates Network, 26794, 1

Steele, I. A., Smith, R. J., Rees, P. C., et al. 2004, 5489, 679

Stein, R., Kool, E., Kumar, H., et al. 2019, GRB Coordinates Network, 25656, 1

Stein, R., & Reusch, S. 2020, robertdstein/ampel_followup_pipeline: V1.1 Release, vv1.1, Zenodo, doi:10.5281/zenodo.4048336. https://doi.org/10.5281/zenodo.4048336

Stein, R., Reusch, S., & Necker, J. 2021, desy-multimessenger/nuztf: v2.4.1, vv2.4.1, Zenodo, doi:10.5281/zenodo.5758176. https://doi.org/10.5281/zenodo.5758176

Stein, R., Reusch, S., Perley, D., Andreoni, I., & Coughlin, M. 2019a, GCN, 26437, 1

Stein, R., Andreoni, I., Coughlin, M., et al. 2019b, GCN, 25727, 1

Stein, R., Kasliwal, M. M., Kool, E., et al. 2019c, GCN, 25899, 1

Stein, R., Anand, S., Coughlin, M., et al. 2020, GRB Coordinates Network, 26673, 1

Stein, R., Velzen, S. v., Kowalski, M., et al. 2021, Nature Astronomy, 5, 510

Stern, D., Assef, R. J., Benford, D. J., et al. 2012, ApJ, 753, 30. http://stacks.iop.org/0004-637X/753/i=1/a=30

Svinkin, D., Golenetskii, S., Aptekar, R., et al. 2020, GRB Coordinates Network, 27755, 1

Svinkin, D. S., Aptekar, R. L., Golenetskii, S. V., et al. 2019, in Journal of Physics Conference Series, Vol. 1400, Journal of Physics Conference Series, 022010

Svinkin, D. S., Frederiks, D. D., Aptekar, R. L., et al. 2016, ApJS, 224, 10

Tachibana, Y., & Miller, A. A. 2018, PASP, 130, 128001

Tan, H.-J., Kong, A., Ngeow, C.-C., & Ip, W.-H. 2019, GCN, 26431, 1

Tan, H.-J., Yu, P.-C., Kong, A., et al. 2019a, GCN, 24274

Tan, H.-J., Yu, P.-C., Ngeow, C.-C., & Ip, W.-H. 2019b, GCN, 24193

Tanvir, N. R., Gonzalez-Fernandez, C., Levan, A. J., Malesani, D. B., & Evans, P. A. 2019, GRB Coordinates Network, 24334, 1

Tanvir, N. R., Levan, A. J., Fruchter, A. S., et al. 2013, Nature, 500, 547

Tanvir, N. R., Levan, A. J., González-Fernández, C., et al. 2017, ApJL, 848, L27

Taylor, J. H., & Weisberg, J. M. 1982, ApJ, 253, 908

The LIGO Scientific Collaboration, the Virgo Collaboration, the KAGRA Collaboration, et al. 2021a, arXiv e-prints, arXiv:2111.03606

The LIGO Scientific Collaboration, the Virgo Collaboration, Abbott, R., et al. 2021b, arXiv e-prints, arXiv:2108.01045

The LIGO Scientific Collaboration and the Virgo Collaboration. 2020, arXiv, 2001.01761

The LSST Dark Energy Science Collaboration, Mandelbaum, R., Eifler, T., et al. 2018, arXiv e-prints, arXiv:1809.01669

Tonry, J. L. 2011, Publ. Astron. Soc. Pac., 123, 58

Tonry, J. L., Stubbs, C. W., Lykke, K. R., et al. 2012, ApJ, 750, 99

Tonry, J. L., Denneau, L., Heinze, A. N., et al. 2018, PASP, 130, 064505. http://stacks.iop.org/1538-3873/130/i=988/a=064505

Troja, E., Piro, L., van Eerten, H., et al. 2017, Nature, 551, 71 EP . http://dx.doi.org/10.1038/nature24290

Troja, E., Piro, L., Ryan, G., et al. 2018, MNRAS, 478, L18

Troja, E., Castro-Tirado, A. J., Becerra González, J., et al. 2019, Monthly Notices of the Royal Astronomical Society, 489, 2104

Troja, E., Watson, A. M., Becerra, R. L., et al. 2019, GRB Coordinates Network, 24335, 1

Tsutsui, R., Yonetoku, D., Nakamura, T., Takahashi, K., & Morihara, Y. 2013, Monthly Notices of the Royal Astronomical Society, 431, 1398

Tsvetkova, A., Frederiks, D., Svinkin, D., et al. 2021, ApJ, 908, 83

Turpin, D., Coleiro, A., Karpov, S., et al. 2020, GRB Coordinates Network, 26687, 1

Utsumi, Y., Tanaka, M., Tominaga, N., et al. 2017, PASJ, 69, 101

Vacca, W. D., Cushing, M. C., & Rayner, J. T. 2003, PASP, 115, 389

Valeev, A., Hu, Y., Castro-Tirado, A., et al. 2020, GCN, 27060, 1

Valeev, A., Hu, Y.-D., Castro-Tirado, A., et al. 2019, GCN, 25731, 1

Valeev, A. F., Castro-Tirado, A. J., Hu, Y.-D., et al. 2020, GRB Coordinates Network, 26702

Valenti et al. 2017, ApJL, 848, L24. http://stacks.iop.org/2041-8205/848/i=2/a=L24

van Eerten, H. 2018, International Journal of Modern Physics D, 27, 1842002

van Paradijs, J., Groot, P. J., Galama, T., et al. 1997, Nature, 386, 686

Van Rossum, G., & Drake, F. L. 2009, Python 3 Reference Manual (Scotts Valley, CA: CreateSpace)

Veitch, J., Raymond, V., Farr, B., et al. 2015, PhRvD, 91, 042003

Vieira, N., Ruan, J. J., Haggard, D., et al. 2020, ApJ, 895, 96

Villar, V. A., Guillochon, J., Berger, E., et al. 2017, ApJL, 851, L21. http://stacks.iop.org/2041-8205/851/i=1/a=L21

Villasenor, J., Lamb, D., Ricker, G., et al. 2005, Nature, 437, 855

von Kienlin, A., Meegan, C. A., Paciesas, W. S., et al. 2020, ApJ, 893, 46

Waratkar, G., Kumar, H., Bhalerao, V., Stanzin, J., & Anupama, G. C. 2019, GCN, 24304

Watson, D., Hansen, C., Selsing, J., et al. 2019, Nature, 574, 497

Webster, B. L., & Murdin, P. 1972, Nature, 235, 37

Wei, J., Xin, L., Antier, S., et al. 2019, GCN, 25640, 1

Weisskopf, M. C., Tananbaum, H. D., Van Speybroeck, L. P., & O'Dell, S. L. 2000, in Society of Photo-Optical Instrumentation Engineers (SPIE) Conference Series, Vol. 4012, X-Ray Optics, Instruments, and Missions III, ed. J. E. Truemper & B. Aschenbach, 2–16

West, A. A., Morgan, D. P., Bochanski, J. J., et al. 2011, AJ, 141, 97

Wiersema, K., Levan, A. J., Fraser, M., et al. 2019, GRB Coordinates Network, 24209, 1

Wijers, R. A. M. J., Rees, M. J., & Mészáros, P. 1997, Monthly Notices of the Royal Astronomical Society, 288, L51. http://dx.doi.org/10.1093/mnras/288.4.L51

Willingale, R., Starling, R., Beardmore, A. P., Tanvir, N. R., & O'Brien, P. T. 2013, Monthly Notices of the Royal Astronomical Society, 431, 394

Willingale, R., O'Brien, P. T., Osborne, J. P., et al. 2007, ApJ, 662, 1093

Wilson, J. C., Eikenberry, S. S., Henderson, C. P., et al. 2003, in Society of Photo-Optical Instrumentation Engineers (SPIE) Conference Series, Vol. 4841, Instrument Design and Performance for Optical/Infrared Ground-based Telescopes, ed. M. Iye & A. F. M. Moorwood, 451–458

Woosley, S. E., & Bloom, J. S. 2006, ARA&A, 44, 507

Wright, E. L., Eisenhardt, P. R. M., Mainzer, A. K., et al. 2010, The Astronomical Journal, 140, 1868. http://stacks.iop.org/1538-3881/140/i=6/a=1868

Wu, M.-R., Fernández, R., Martinez-Pinedo, G., & Metzger, B. D. 2016, Monthly Notices of the Royal Astronomical Society, 463, 2323. +http://dx.doi.org/10.1093/mnras/stw2156

Yang, B., Jin, Z.-P., Li, X., et al. 2015, Nature Communications, 6, 1

Yang, J., Zhang, B. B., Ai, S. K., et al. 2022, arXiv e-prints, arXiv:2204.12771

Yao, Y., Miller, A. A., Kulkarni, S. R., et al. 2019, The Astrophysical Journal, 886, 152. http://dx.doi.org/10.3847/1538-4357/ab4cf5

Yonetoku, D., Murakami, T., Nakamura, T., et al. 2004, ApJ, 609, 935

Yu, H.-F., Preece, R. D., Greiner, J., et al. 2016, arXiv:1601.05206

Zackay, B., Ofek, E. O., & Gal-Yam, A. 2016, ApJ, 830, 27

Zackay, B., Ofek, E. O., & Gal-Yam, A. 2016, ApJ, 830, 27. http://stacks.iop.org/0004-637X/830/i=1/a=27

Zafar, T., Watson, D., Møller, P., et al. 2018, Monthly Notices of the Royal Astronomical Society, 479, 1542

Zhang, & Choi. 2008, å, 484, 293. https://doi.org/10.1051/0004-6361:20079210

Zhang, B., Fan, Y. Z., Dyks, J., et al. 2006, ApJ, 642, 354

Zhang, B., Zhang, B.-B., Virgili, F. J., et al. 2009, ApJ, 703, 1696

Zhang, B. B., Liu, Z. K., Peng, Z. K., et al. 2021, Nature Astronomy, 5, 911

Zhang, Z., Chen, D., & Huang, Y. 2012, ApJ, 755, 55

Zhou, R., Newman, J. A., Mao, Y.-Y., et al. 2021, MNRAS, 501, 3309

Zhu, J.-P., Yang, Y.-P., Zhang, B., Gao, H., & Yu, Y.-W. 2021, arXiv preprint arXiv:2110.10468